FAILURE MECHANISMS OF CONCRETE MASONRY

By

CHICHAO YAO

B. ENG. Tong Ji University, 1983

A THESIS SUBMITTED IN PARTIAL FULFILLMENT OF

THE REQUIREMENTS FOR THE DEGREE OF

DOCTOR OF PHILOSOPHY

in

THE FACULTY OF GRADUATE STUDIES

DEPARTMENT OF CIVIL ENGINEERING

We accept this thesis as conforming

to the required standard

THE UNIVERSITY OF BRITISH COLUMBIA

April 1989

In presenting this thesis in partial fulfilment of the requirements for an advanced degree at the University of British Columbia, I agree that the Library shall make it freely available for reference and study. I further agree that permission for extensive copying of this thesis for scholarly purposes may be granted by the head of my department or by his or her representatives. It is understood that copying or publication of this thesis for financial gain shall not be allowed without my written permission.

Department of Civil Engineering

The University of British Columbia
Vancouver, Canada

Date April 26, 1989

ABSTRACT

The behaviour of concrete masonry under in-plane compression combined with out-of-plane bending was examined both experimentally and analytically.

Ungrouted and grouted masonry, both fully bedded or face-shell bedded, were included in the study. It was found that the masonry under the above stated loading conditions may suffer loss of capacity either due to splitting or shear type of material failure, or by instability. Different loading conditions yield different failure mechanisms, which in turn correspond to different apparent strengths. Theoretical developments are presented leading to estimates of capacity for each of these cases. An extensive experimental program involving 104 masonry prism specimens, was conducted to assist and to verify these analyses.

Theoretical developments include those directed to explain splitting failure phenomena, to investigate the mortar joint effect, the deformation compatibility of grouted masonry, and to examine the slenderness of tall masonry wall. Experimental measurements and observations made on the specimens include capacity, deformation and failure pattern.

TABLE OF CONTENTS

LIST OF TABLES

TABLE PAGE

LIST OF FIGURES

FIGURE PAGE

FIGURE PAGE

FIGURE PAGE

FIGURE PAGE

NOTATION

A, B, C, D = constants in various contexts;

A_g,A_n = gross area and net area of block unit, respectively;

a, b = constants used for dimensions;

a, b = pre-existing half crack length and half spacing, respectively, in (Chapter III);

a, b = half width of hollow core and block unit, respectively;

c, c_m, c_f, c_c = bedding joint crack depths of a wall cross-section, defined in Fig. 11.2;

c_1, c_2 = constants;

E, E' = modulus of elasticity;

E_u, E_g, E_j, = modulus of elasticity of block unit, grout, mortar joint, respectively;

e, e_o = loading eccentricities;

e_c, e_f, e_m = virtual eccentricities corresponding to different bedding joint crack depths;

F = compressive force;

F_1, F_2 = functions of bedding joint cracking defined in Appendix F;

f = friction between pre-existing crack surfaces;

f'_c , f_t = compressive and tensile strength, respectively;

f'_{mp}, f'_{mg} = compressive strength of plain masonry and grouted masonry, respectively;

f'_u, f'_g, f'_j = compressive strength of block unit, grout (prism strength), mortar (cube strength), respectively;

f_{ju} = unconfined strength of mortar joint;

f_{jc}, f_{je} = confined strengths of mortar joint;

f'_{ut} = tensile strength of block;

G_1, G_2 = functions of bedding joint cracking defined in Appendix F;

G_I, G_{IC} = energy release rate of crack extension and its critical value;

H = parametric function defined in Appendix B;

h = height of wall or specimen;

h_c, h_f = wall heights corresponding to different bedding joint crack depths;

h_o = height of block unit;

I, I_g = moment of inertia of wall corresponding to net cross-section and gross-section, respectively;

K_I, K_{IC} = stress intensity factor at crack tips and its critical value;

k = crack configuration factor (in Chapter III);

k, k_1, k_2 = constants;

l, l_o = extending crack (half) length and its initial value (in Chapter III);

l = length of wall or specimen;

M = number of cracks in specimen, (in Chapter III);

M = bending moment;

m = modulus of Weibull distribution;

m_1, m_2 = modular ratio of E_u/E_g and E_u/E_j, respectively;

n = modular ratio of reinforcing steel to block shell;

P, P_1 = tensile splitting force (in Chapter III);

P = applied compressive load;

P_{cr}, P_k = Euler load (corresponding to gross section), and buckling load of wall, respectively;

p = contact pressure between grout and block shell;

Q_i, Q_n, Q_t, T_i = traction components on internal boundary and external boundary of an elastic body containing cracks, respectively;

R = energy dissipated by friction;

S = shear force;

s = contour length;

T = effective crack induced shear sliding force;

t = thickness of wall;

t_o = thickness of mortar joint;

U = strain energy;

u, v = dispacement variables;

u_i, v_i, v_n, v_t = displacement components on internal boundary and external boundary of an elastic body containing cracks, respectively;

$\mathcal{V}$ = volume;

V = work done by external load;

W = energy dissipated to form new crack

w = specimen width (in Chapter III);

w, w_g = sum of the mortared web dimension and grout dimension along wall length, respectively;

x, y = variables under different context;

Z = cumulative function of a Weibull distribution;

α = inclining angle of pre-existing cracks (in Chapter III);

α = release angle of block inner core;

Γ_1, Γ_2 = external and internal boundaries;

Δ, δ = displacements;

δ, δ_1 = crack opening and its value at the starting ponit of transitional interval (in Chapter III);

ϵ = compressive strain;

ϵ_1 = extreme fiber strain on compression side of wall;

ϵ_u, ϵ_g, ϵ_j = compressive strain in block unit, grout and mortar joint, respectively;

ϵ_{ij}, σ_{ij} = strain and stress components;

η = net area to gross area ratio of block unit A_n/A_g;

Θ, Θ_o, Θ_1 = cracking phase and its values at the starting points of crack extension and transitional interval;

θ = Weibull distribution parameter;

κ = constant related to Poisson's ratio, defined in Chapter IV;

λ = parameter defining grout and bedding extent, given by Eq. 10.3;

μ = coefficient of friction (in Chapter III);

μ = effective Poisson's ratio: $\nu/(1-\nu)$;

ν = Poisson's ratio;

ν_u, ν_g, ν_j = Poisson's ratio of block unit, grout and mortar, respectively;

ξ = average defect size-spacing ratio (a/b, in Chapter III);

ξ = ratio of moment of inertia I/I_g;

ρ = steel ratio with respect to gross section of wall;

σ, σ_t = compressive and tensile stress, respectively;

σ_{ij}, τ_{ij} = normal and shear stress components, respectively;

σ_o, σ_1, σ_2 = threshold stress for crack extension, stresses at the starting and finishing points, of transitional interval (in Chapter III); respectively;

σ_1, σ_2 = outer fibre stresses of wall;

σ_l = lateral confining stress in joint;

σ_m, σ_s = compressive stress in masonry (average) and in masonry shell, respectively;

σ_u, σ_g, σ_j = compressive stress in block unit, grout and mortar joint, respectively;

σ_{ut} = lateral tensile stress in block unit;

φ = rotation (slope) of wall section;

φ_c, φ_f = rotations of wall section corresponding to different bedding joint crack depths;

Φ = Airy stress function;

ϕ = density function of Weibull distribution;

Ω_1, Ω_2 = functions of bedding joint crack depth defined by Eqs. 11.19 and 11.21.

ACKNOWLEDGEMENT

The author wishes to express his gratitude to Dr. N. D. Nathan, who supervised the research for this program, for his continued interest, unfailing help and much valuable advice during preparation of this thesis. The author also wishes to thank Drs. D. L. Anderson and R. F. Foschi for their many constructive comments and suggestions.

The scholarships, i.e. I. W. Killam Memorial Fellowship and the University Graduate Fellowship, received by the author are also gratefully appreciated.

The research project is partially supported by the National Science and Engineering Research Council. The masonry units for the experimental program were kindly donated by Ocean Construction Supplies Limited.

DEDICATION

TO THE MEMORY OF MY FATHER

CHAPTER I

INTRODUCTION

1.1 General Remarks

Masonry construction is basically an assembly of blocks. The blocks can be natural stone, clay bricks or precast concrete units. They are jointed with cementitious material called mortar. The history of masonry building may be as old as human civilization, but the interest in masonry is still increasing today because of the economy of construction and the pleasing appearence of masonry structures.

Serious studies of structural masonry have been carried out for the last two decades. While knowledge of the structural behaviour of masonry has been greatly improved, many questions still remain unanswered in this area, and the design rests largely on an empirical base.

This study will focus on the failure and capacity of the concrete masonry under in-plane compression combined with out-of-plane bending. The study extends from a background investigation of material failure to a rational analysis of masonry stability. The behaviour of masonry prisms with various bedding and grouting combinations under various loading conditions is carefully observed through experiments.

This thesis is organized in the following manner. The experimental program is first reported in Chapter II; the results will be quoted and studied in detail in the subsequent chapters. The background study on material failure under axial compression, which will be used to explain some behaviour of concrete masonry in later chapters, follows in Chapter III. Chapters IV to VII focus on the behaviour of plain concrete masonry; Chapters VIII to X on grouted masonry. The study on the slenderness and the stability of concrete masonry is presented in Chapter XI. Finally, Chapter XII concludes this study.

It is hoped that the theoretical findings and the experimental observations presented in this study will enhance existing knowledge of the failure of concrete masonry, and assist in the formulation of design rules for concrete masonry structures.

1.2 Object and Scope

The object of this thesis will be:

a) To review and develop the background for material failure theory.

b) To observe the behaviour including deformation, fracture pattern, failure mode and ultimate capacity of concrete masonry prisms with different loading conditions, joint conditions and grouting conditions.

c) To examine and develop the existing theories for failure of concrete masonry under various conditions.

d) To investigate the slenderness and stability of concrete masonry.

CHAPTER II

EXPERIMENTAL PROGRAM

2.1 Purpose and Scope

Extensive experimental work on concrete masonry has been conducted previously. In this program, however, efforts were made to observe more closely the deformation and fracture pattern of masonry prisms under concentric and eccentric compression. Prism specimens were designed to cover various combinations of bedding and grouting conditions.

In order to re-examine the Hilsdorf model of mortar expansion, for plain prisms under concentric loading, particular emphasis will lie on observation of splitting failure, and the effect of joints on deformation and capacity of masonry. For grouted prisms under concentric compression, attention will be paid to the cracks induced by the different deformation properties of the masonry unit and the grout, and the forces shared by these two materials before and after cracking. For masonry prisms under eccentric loading, failure modes will be observed and the joint bond on the unloaded side will be monitored through deformation gauges.

The experimental results concerning the properties of the masonry constituents are concisely reported in this chapter. The characteristic results for masonry specimen are summarized. The detailed results will be reported and studied in the context of related analysis in later chapters.

2.2 Materials

All materials used in making the test specimens are commercially available and typical of those commonly used in local construction.

2.2.1 Masonry Units

All the masonry prisms tested were built by using 8 inch standard concrete block units with double end (in accordance with CSA-A165-M85, C-20). The units were kindly donated by Ocean Construction Supplies Ltd, Vancouver, B. C. The dimensions are shown schematically in Fig. 2.1.

To determine the compressive strength of the units, 16 blocks were tested with a Baldwin Tate-Emery testing machine. In accordance with ASTM C140, 8 blocks were capped with hydrostone (a gymsum cement). In order to observe the effect of the capping condition, another 8 blocks were tested with fibreboard capping. Table 2.1 gives the results of failure loads. As can be seen, although there is a statistical difference, it is not sufficient to suggest a different failure mechanism. This is consistent with the fact that the two test conditions exhibited similar shear failure patterns, as typically shown in Fig. 2.2. 16 block units with two different capping conditions all exhibited conical type failure, owing to the low height to width ratio. The average failure load is 200.5 kips, which corresponds to an average strength of about 3250 psi based on the net area of the unit (the ratio of net area to gross area of the unit η is 0.51).

Attempts were also made to obtain the deformation properties by measuring the relative displacement of the loading head. However, due to the compliance of the testing machine (the dial gauge was not mounted directly against the loading platens) and the variation in the cappings, the results were not accurate compared with those measured by LVDTs directly mounted on the blocks in prism tests. The latter are given by Fig. 2.3. The initial modulus of the units is about 3.42×10^6 psi.

The concrete units were very brittle in the sense that they often failed totally in an explosive manner as soon as the peak load was reached. It was not possible to measure the deformation after the peak strain with the standard test procedure.

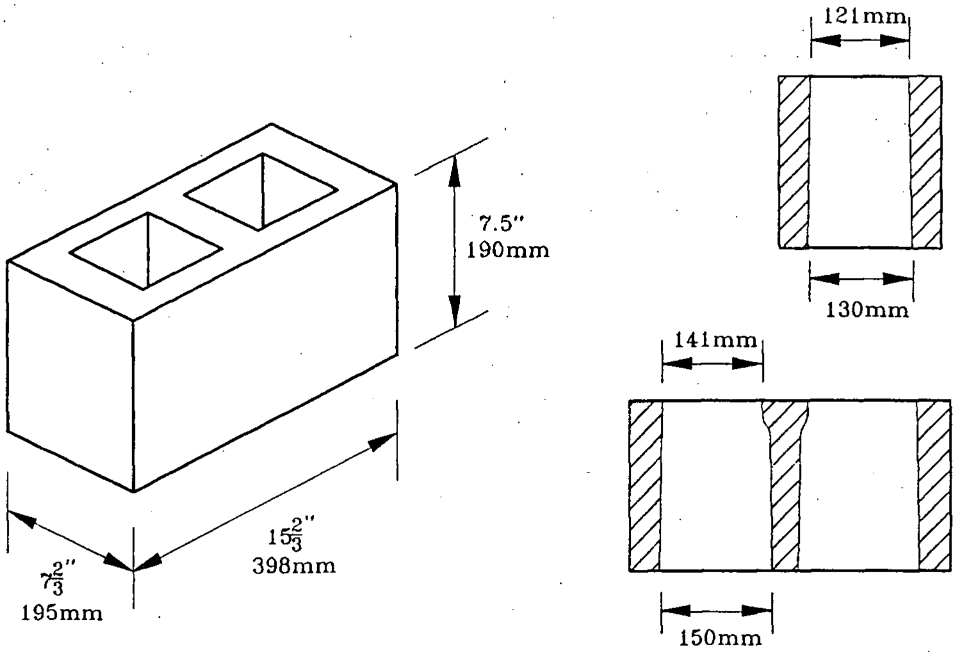

FIG. 2.1 Masonry Unit

SPECIMEN	1	2	3	4	5	6	7	8	AVG	COV
GROUP 1	169	188	194	196	207	186	213	189	193.0	6.5%
GROUP 2	219	186	232	205	208	187	220	203	208.0	7.2%

Table 2.1 Failure Loads of Block Unit (kips)

GROUP 1: Hydro-stone cap; GROUP 2: Fiber board cap

FIG. 2.2 Conical Failure of Masonry Unit

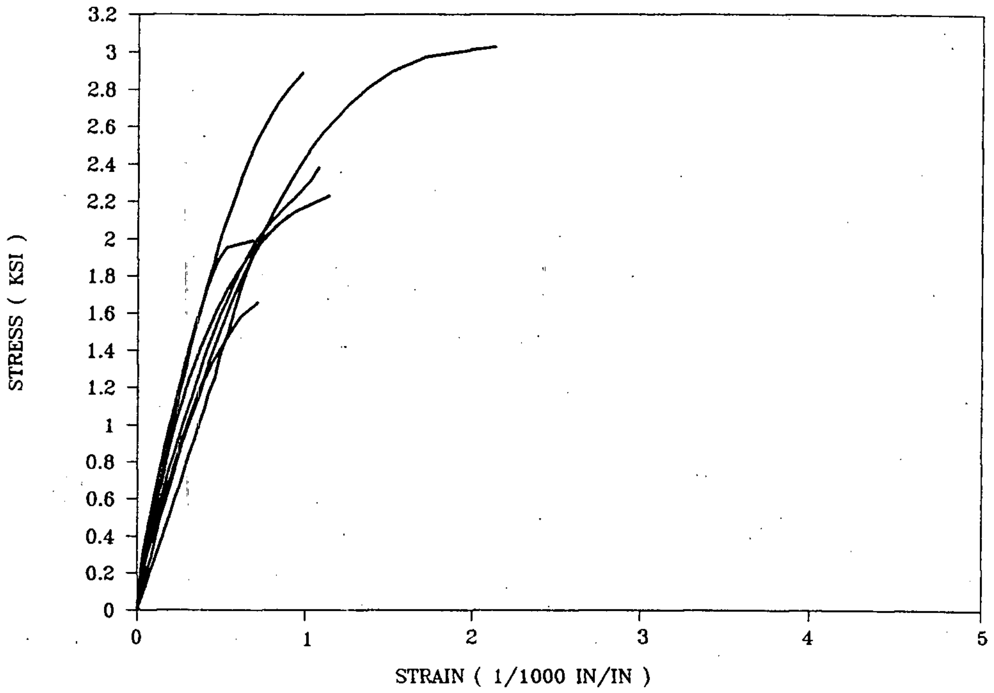

FIG. 2.3 Stress-Strain Relation of Masonry Unit under Compression

2.2.2 Mortar

Three types of mortar were used, i.e. type M, S, and N in accordance with CSA-179M-1976. The mortars were mixed by an experienced mason, with a small electrically driven mixer, during the construction of the specimens. The mix proportions are given in Table 2.2. Mortar cubes were sampled for every batch. The 28-day cube strengths are given in Table 2.3. At the same time, the stress-strain relationships were measured for type N and some of the type S mortar, as shown in Fig. 2.4. The results indicate that the mortars are much softer than normal concrete, and that they have very large peak strains. The initial moduli are about 0.4×10^6psi for type N mortar, and 0.5×10^6psi for type S mortar. The peak strains are about 0.006 for the former and 0.009 for the latter. The high compliance of the mortar was also indicated by deformation measurements across the joints of prism specimens. As typically shown in Fig. 2.5, the ratio of the initial modulus of three types of mortar to that of the concrete units is about 1 to 6-8. The deformation properties measured directly from mortar cube tests and the unit tests are very close to these results.

Mortar Type	Proportion by Volume			
	Cement(Type III)	Masonry Cement	Fine Sand	Water
M	1	1	2.5	1
S	1/2	1	3	1
N	---	1	3	0.68

Table 2.2 Mix Proportions of Mortar

SPECIMEN	1	2	3	4	5	6	AVG	COV
M TYPE	4188	4835	4625	5100			4690	7.1%
S TYPE	3985	4320	3875	4075	3750		4000	4.8%
N TYPE	1450	1710	1560	1650	1325	1730	1570	9.2%

Table 2.3 28 Day Mortar Cube (2 in) Strength (psi)

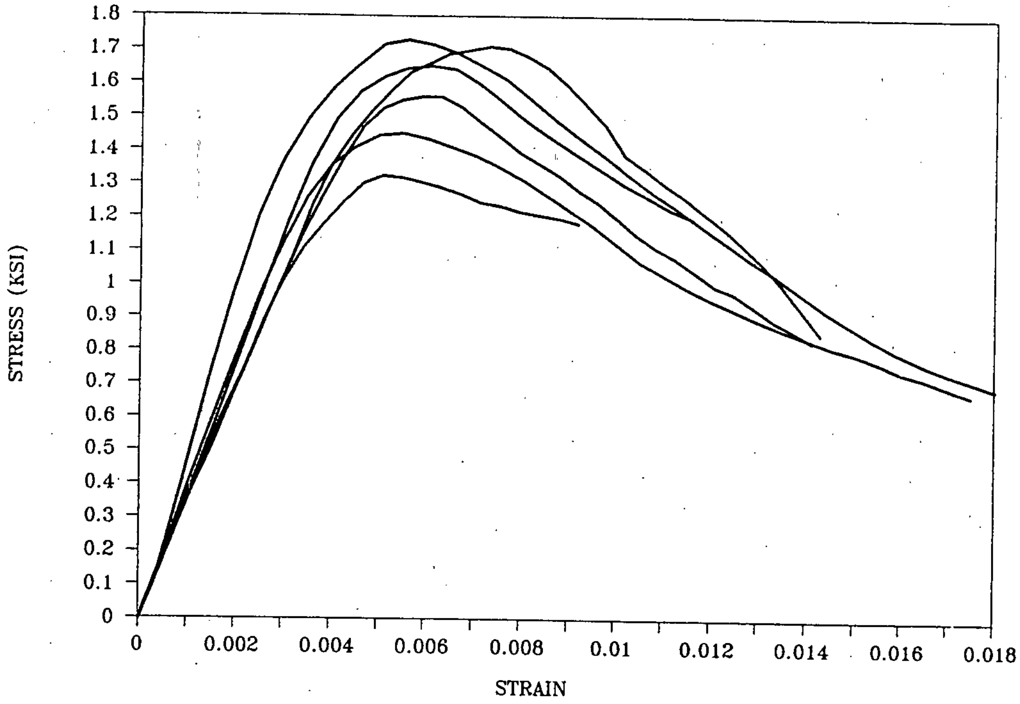

(a)

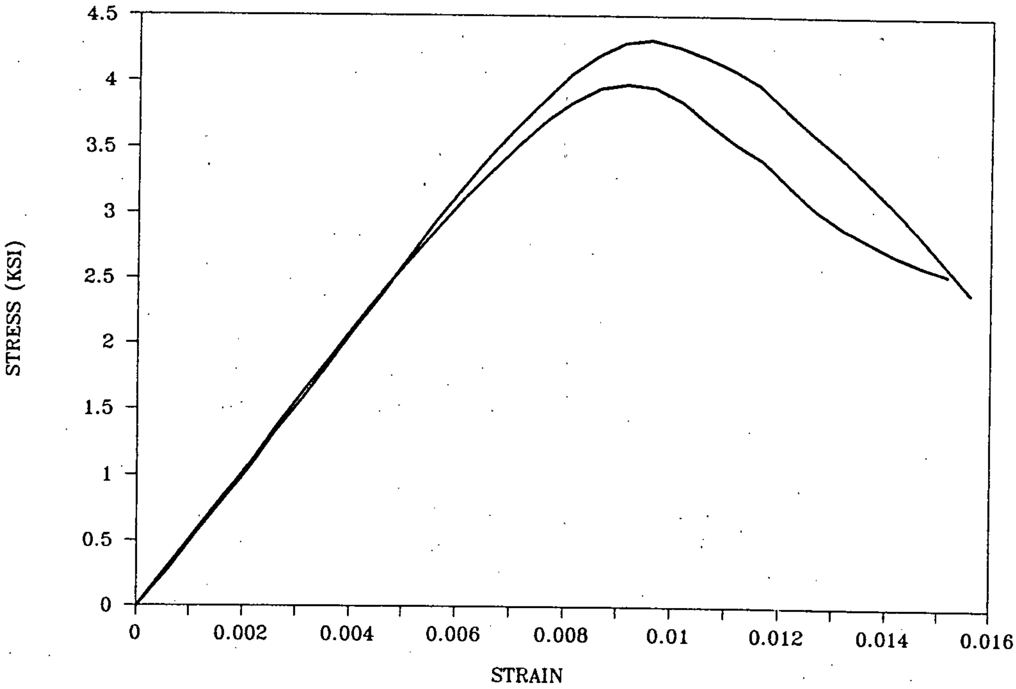

(b)

FIG.2.4 Stress-Strain Relation of Mortar: a) Type N, b) Type S.

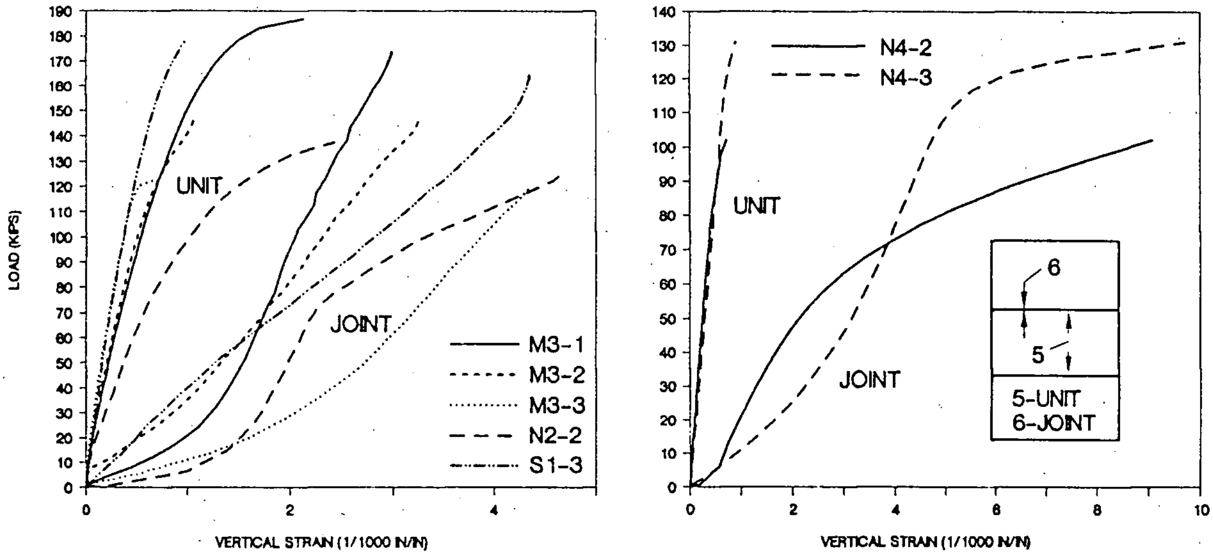

FIG. 2.5 Measured Vertical Compressive Strains along Block Units and across Mortar Joint of Plain Prisms under Uniaxail Compression.

2.2.3 Grout

Three types of grout with different strengths were designed for the specimens. They are denoted by GS, GN and GW. The mix proportions are listed in Table 2.4. The water content was adjusted slightly to achieve 3-5 inch slump. For every mix batch, two or three standard prisms were cast and cured in accordance to CSA-179M-1976. The compressive strengths are given in Table 2.5.

To examine the correlation between the strength obtained by the standard test and that actually grouted in the masonry, 20 grout prisms taken from the cores of failed masonry specimens were tested. The cores were cut by a diamond saw and capped with sulfur before testing. The results are shown in Table 2.6. As is seen, the strength of the grout prisms taken from failed masonry specimens is substantially higher than that of the standard prisms. This may be partly due to the different height to width ratios of the specimens (1.4:1 for the former, 2:1 for the latter, approximately), partly to the difference in curing time (the former were tested about a year later). This suggests that the strength obtained by the standard test is only meaningful as a reference parameter.

The deformation properties were measured on the cores taken from tested grouted masonry prisms. The deformation curves are given by Fig. 2.6. The initial modulus is 2.8×10^6 psi for type S grout, 2.6×10^6 psi for type N grout and 1.9×10^6 psi for type W grout.

Grout	Proportion by Volume			
Type	Cement(Type III)	Coarse Sand	Pea Gravel	Water
GS	1	2.5	2.5	0.6
GN	1	2	2	0.8
GW	1	5	---	1.0

Table 2.4 Mix Proportions of Grout

SPECIMEN	1	2	3	4	5	6	7	8	9	AVG	COV
S−TYPE	4720	5445	4890	5320	4705					5015	6.1%
N−TYPE	3685	3885	3720	4015	3390	3425	3745	3600	3815	3700	5.1%
W−TYPE	3165	3500	3305	3375	3285					3325	3.2%

Table 2.5 Grout Strength, by Standard Prism Tests (psi)

SPECIMEN	1	2	3	4	5	6	7	8	9	AVG	COV
S−TYPE	6305	4170	5530	6690	5245					5590	15.7%
N−TYPE	6180	5625	5970	6350	5810	6310	5870	6660	6215	6110	4.9%
W−TYPE	4530	4725	4330	4450	4050	4210				4385	5.0%

Table 2.6 Grout Strength, by Tests on Cores Taken from Failed Prisms (psi)

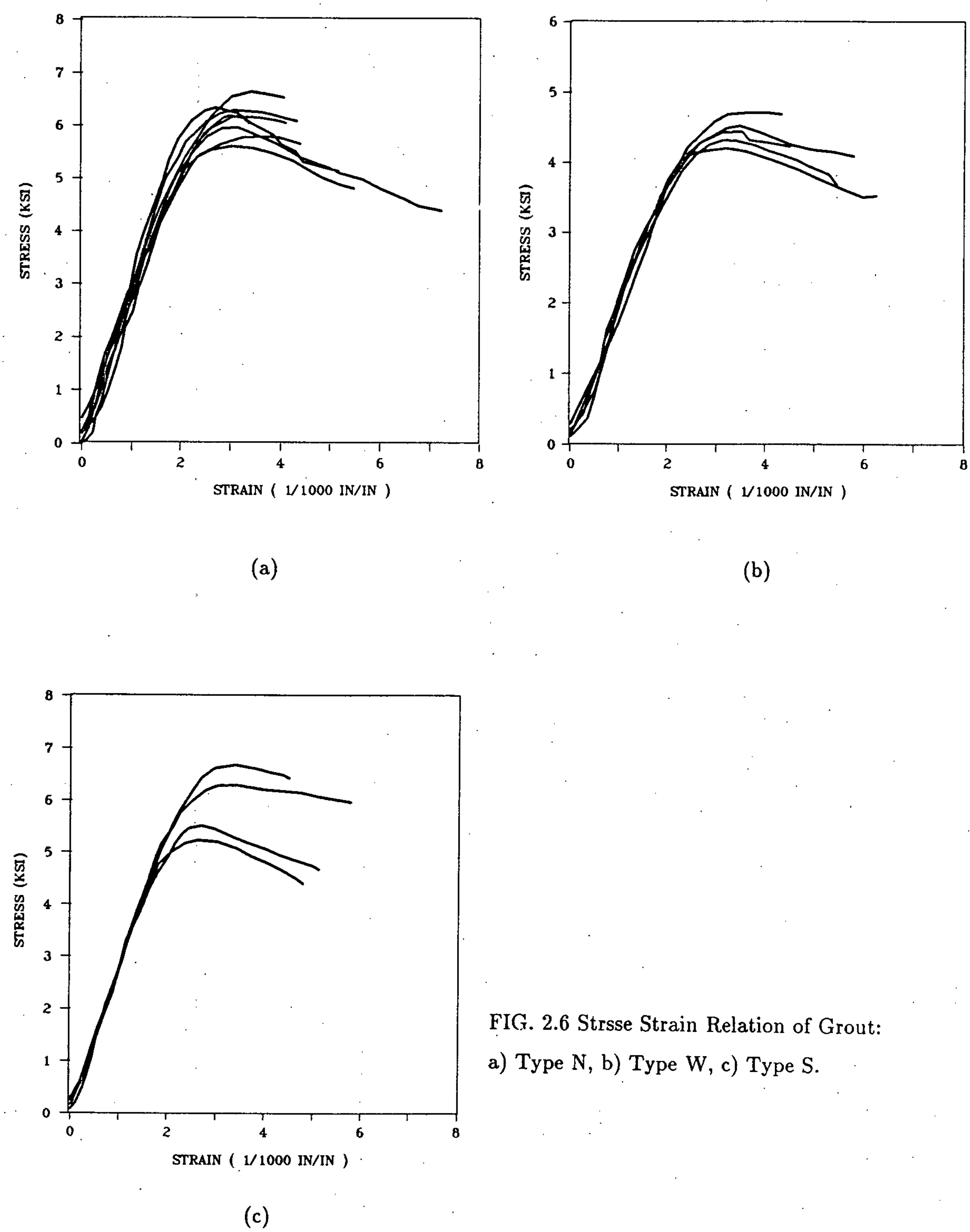

FIG. 2.6 Strsse Strain Relation of Grout:
a) Type N, b) Type W, c) Type S.

2.3 Prism Specimens

104 3-high prisms were built with different bedding, and grouting conditions, designed to be tested under different eccentricities. Three high specimens were chosen because it is believed that the end effect of the loading device can be eliminated in the middle course where all the measurements were made. The specifications of the specimens are listed in Table 2.7.

All the plain prisms were built by an experienced mason. All the mortar joints were cut flush on the prism faces. The prisms were then grouted 4-5 days later (for grouted prisms). The specimens were stored in the structures laboratory at the University of British Columbia for about a year until they were tested. A few specimens were discarded because of the debonding of the mortar joint (the debonding happened because specimens were moved once, due to other experimental activities, during the storing period, and because of setup handling).

For the grouted prisms, hydrostone was used to finish the top ends prior to testing. All the prisms were transported by using a small trolley to the testing device and then capped (top and bottom) with fibreboard before they were positioned between the loading platens.

Specimen	No. of Prisms	Joint Conditions	Grouting Conditions	Load Eccent.	Additional Description
S1	4	S Mortar	---	0	Joint thickness is 3/8
N2	4	N Mortar	---	0	inch except otherwise
M3	4	M Mortar	---	0	specified.
N4	4	NJ, t_o=6/8"	---	0	NJ=N Mortar.
P5	4	t_o=0	---	0	Contact faces were grinded
G7	4	4mm glass plate	---	0	jointed by cement paste.
S8	4	S Mortar	N Grout	0	
M9	4	M Mortar	N Grout	0	
N10	4	NJ, t_o=6/8"	N Grout	0	NJ=N Mortar.
P11	4	t_o=0	N Grout	0	
N12	4	N Mortar	S Grout	0	
N13	4	N Mortar	N Grout	0	
N14	4	N Mortar	W Grout	0	
N15	4	NJ, face-shell	---	0	NJ=N Mortar.
S16	4	SJ, face-shell	---	0	SJ=N Mortar.
N17	4	NJ, face-shell	N Grout	0	NJ=N Mortar.
N18	4	N Mortar	---	t/6	
N19	4	N Mortar	---	t/3	
M20	4	M Mortar	---	t/3	
S21	4	S Mortar	---	t/3	
N22	4	NJ, face-shell	---	t/3	
N23	4	N Mortar	N Grout	0	Half block
S25	4	S Mortar	N Grout	t/3	
N26	4	N Mortar	N Grout	t/6	
M26	4	M Mortar	N Grout	t/3	
M27	4	MJ, face-shell	---	0	MJ=M Mortar.

Table 2.7 Prism Specimens

2.4 Testing Device

Since it was expected that for the grouted prisms the failure loads would be higher than the capacity of the existing testing facilities in the structures laboratory (up to 400 kips), a loading device was built as shown in Fig. 2.7. It was formed basically with a girder serving as a lever, with appropriate supporting members; it had a mechanical advantage of 2. The device was connected to a hydraulic jack with 400 kips capacity, and so that it could apply a load up to 800 kips. It was calibrated up to 600 kips, but, in the event, the failure loads of the specimens never exceeded 400 kips.

The specimens were designed to be compressed with pin-ended conditions. The top and bottom loading platens, therefore, were designed with cylindrical bearings, as shown in Figs. 2.7 and 2.8. The platens were designed for three loading eccentricities, i.e. $e=0$, $e=t/6$ and $e=t/3$. The supporting devices were built with high strength steel.

The hydraulic jack was controlled by an MTS control console (Model 483.02), with force control mode (displacement control not available). The load was set to increase automatically so that a specimen would fail in about 3 minutes, for plain specimens, and 5 minutes for grouted ones. The load was read through an electronic load cell mounted in the jack.

2.5 Instrumentation

To measure the deformations of the prisms, about half of the specimens were instrumented wirh six quarter-inch linear variable differential transformers (LVDT, Trans-Tek Series 240). The arrangement and locations of the LVDTs were different for concentric and for eccentric compression conditions, and are denoted by 1 to 6 in the figures showing the measured curves (cf. Fig. 4.3, for example). The LVDT across the mortar joint had a gauge length of 1.8 inches (45 mm), while all rest were 5 inch (125 mm). The LVDTs were clamped to aluminum supports which were then mounted on small disc screw nuts glued in advance by fast setting epoxy, typically as shown in Fig. 2.9.

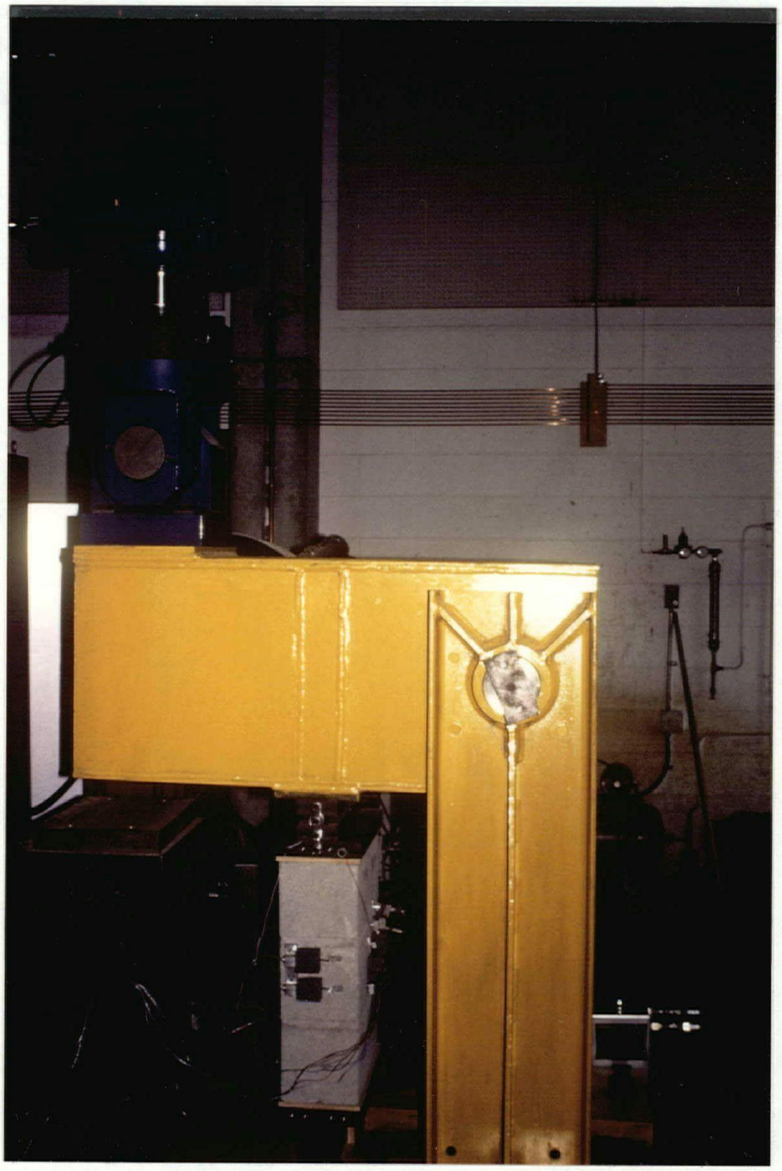

FIG. 2.7 Testing Device

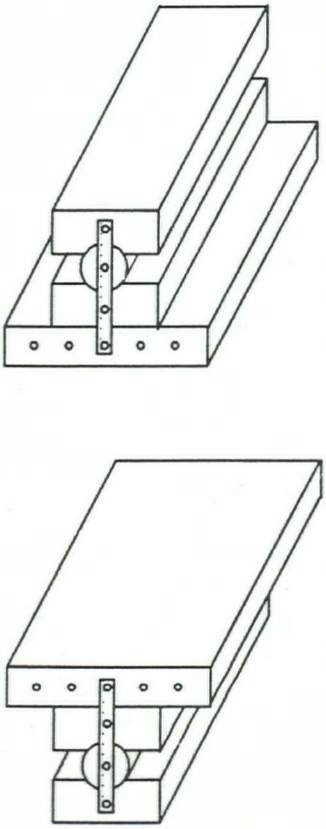

Fig. 2.8 Loading Platens

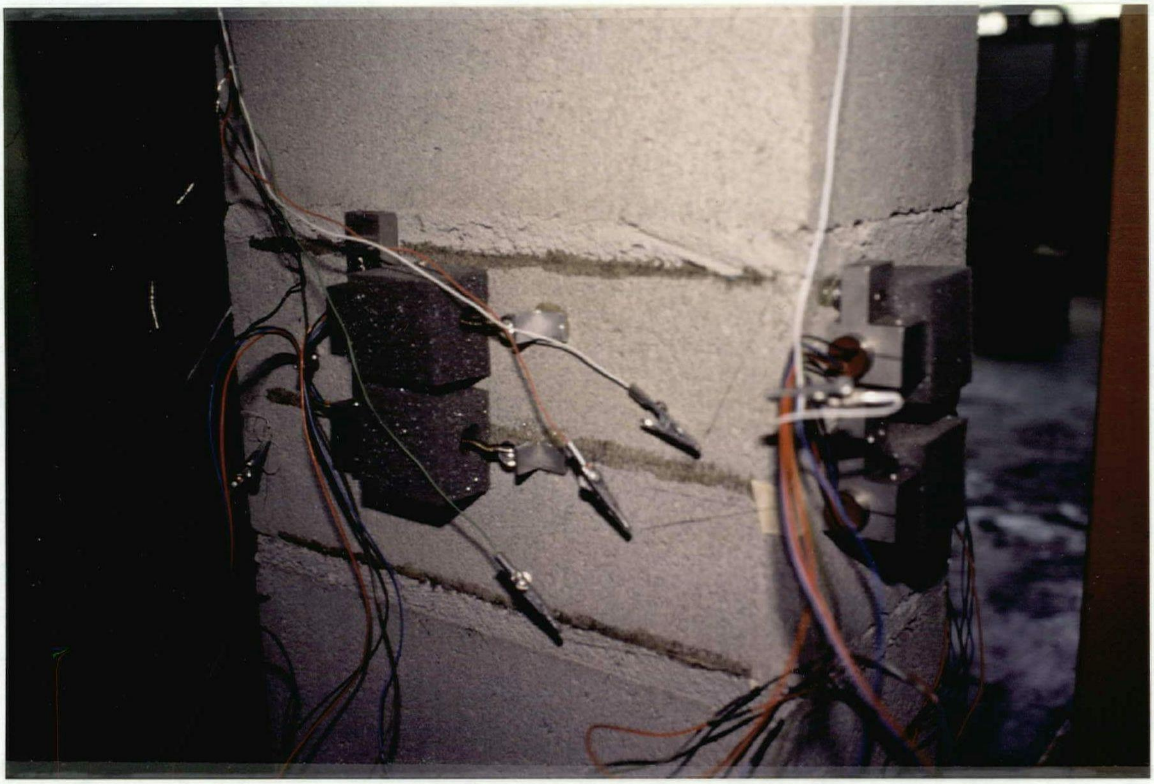

Fig. 2.9 Instrumentaion: LVDTs and Glued Wires

Because of the destructive nature of the experiments, it was expected that the specimen would fail in a sudden, explosive pattern, especially with the load controlled testing machine. To reduce the impact of the failing specimen, the LVDTs were surrounded with plexiglass sleeves and sponges as can be seen in Fig. 2.9. To monitor the effect of the impact, they were checked for normal functioning after every test and calibrated against gauge thickness for every two tests, or whenever the central core of a transducer was bent (this happened several times during the tests, straightening was often necessary). Fortunately, the outer coils survived for the whole testing program, although the linking wires broke several times.

According to the manufacturer, the LVDTs have an infinite resolution. However, when the displacement measured is too small, the readings may be buried in the noise. It turned out that when the displacement was larger than 0.0025 inch (corresponding to 0.5 milli-strain of the given gauge length), this was not a big problem, and the readings were satisfactory for most cases.

For plain prisms under axial compression, an electronic circuit was designed to study the macroscopic splitting of plain prisms under uniaxial compression. Four very thin copper wires (gauge 42, ϕ 0.08 mm) were glued with epoxy to different locations on the prisms. These wires served as electrical conductors which give electrical pulses when they break. Since the wires were fully surrounded by the hardened glue and adhering to the surface of the specimen, they were supposed to break when the specimen split. By detecting the order of the wires breaking, we obtain the running direction of a crack which runs across the wires. The crack propagation speed in concrete is about 180m/sec (Bhargava and Rehnstorm 1975) so that a split would run through the block height in about 0.001 second. The electronic circuit (see appendix) was designed by an experienced electrician in the civil engineering department, which was capable of detecting the break order for intervals less than 5×10^{-6} second. Basically, it recorded the electrical pulses given by open circuits due to breakages of the wires in an ordered way. The circuit was built and then tested in the electrical engineering department at UBC. To gain more confidence with the method, it was first used in face-shell bedded prisms and gave consistent results. It was then tried with fully bedded masonry with lines glued to the face-shells as well as the webs, and again gave consistent results (webs split in contrast to face-shells). The wires were then all glued to the webs, where splitting always occurred. The device is shown in Fig. 2.10 (also see Fig. 2.9 for glued wires), and it is seen that the breaking order is indicated by four rows of light emission diodes (LED).

To give better insight into the failure processes, a VHS standard video camera was used to record most of the tests. This was found very useful for later observation since, as the testing machine was load controlled, many specimens were totally destroyed (often in an explosive manner) as soon as ultimate load was reached. The camera was installed to face one of the webs, because fractures were more often observed to occur in webs than in face-shells (compare the deformations measured at locations 3, 4 with those at locations 1, 2 given in following chapters).

The camera was able to record visible cracks on the web faces, usually immediately before final failure. However, LVDTs were more sensitive to smaller cracks occurring at earlier stages (as inferred by a sudden increase in measured displacement). For the majority of the specimens, the overall failure pattern could be examined by slow playback of the recorder. For a few specimens that failed in a highly explosive manner, however, the recording was not very satisfactory. Usually there was no warning, such as cracking or spalling, that failure was approaching in these specimens.

2.6 Data Acquisition

The data, i.e. six displacements and one load, were read by an Optilog system, an electronic data acquistion unit, which is basically a microprocessor digitizing and recording the analog signals. It was controlled by an IBM personal computer with Optilog software. The whole setup is shown in Fig. 2.11.

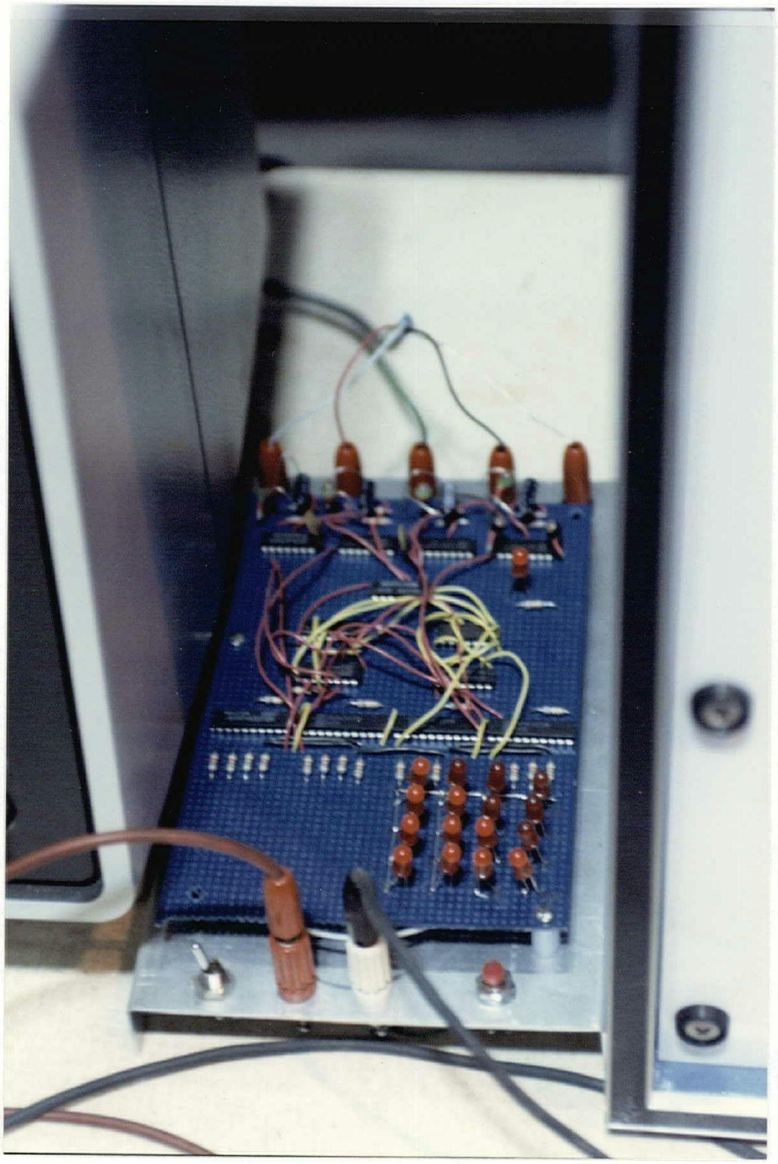

FIG. 2.10 Electronic Device Detecting Wire Break Order

The load cell and all the LVDTs were calibrated through the unit. The system was set so that the load and the displacements were read every two seconds for plain prisms and four seconds for grouted ones. The recorded data were often reviewed during the tests to prevent any abnormal readings. They were then converted to standard format for later processing.

FIG. 2.11 Data Acquisition Setup

2.7 Summary of Characteristic Results

Since the prism specimens cover a wide range and each group has its own emphasis, it may be inappropriate to give all the detailed results at this stage. Therefore, the results will be reported and studied in the context of analysis in the related chapters.

In order to have an overall view of the test results, we give a short, descriptive summary of some of the important experimental characteristics. They are outlined in terms of the failure mode and capacity, which are of common interest but which are yet generally distinct between different specimens.

The specimens may be roughly characterized into 6 major groups according to their bedding, grouting, loading conditions, as well as their failure characteristics. They are: plain masonry with full bedding under concentric compression; plain masonry with face-shell bedding under concentric compression; plain masonry (with both bedding conditions) under eccentric compression; grouted masonry with full bedding under concentric compression; grouted masonry with face-shell bedding under concentric compression; grouted masonry (with both bedding conditions) under eccentric compression.

The summary is organized in Table 2.8. Figs. 2.12 to 2.16 give some typical failure modes.

SPECIMEN	FAILURE MODE	CAPACITY CHARACTERISTICS
1) Plain masonry with full bedding under concentric compression.	Often one major split ran through specimen within middle third of webs, immediately before final failure. Splits did not consistently initiate from the mortar joint. Splits were continuous.	Joint conditions had a significant influence on the capacity.
2) Plain masonry with face-shell bedding under concentric compression.	One or two splits in webs occured at or immediately before final failure. Splits consistently initiated from joints, at locations near two joint ends and wandered afterwards. Splits were discontinuous at joints.	Joint strength had a relatively significant influence on the capacity. Capping conditions had a substantial influence on the capacity.
3) Plain masonry under eccentric compression.	Failure was characterized by shear, i.e. by spalling and crushing on the loaded side; and was often localized in part of the specimen. Joints on unloaded side did not effectively transfer tension.	Joint strength and bedding pattern had a relatively minor effect on the capacity.
4) Grouted masonry with full bedding under concentric compression.	Splits both in webs and face-shells were observed well before final failure, some at as low as 40% of failure loads. Block shells still carried substantial load after cracking. Final failure brought by spalling of the shells, followed by crushing of grout at the midheight.	Joint strength and grout strength had a relatively minor effect on the capacity.
5) Grouted prism with face-shell bedding under concentric compression.	Splits in webs occured well before final faiure. Block shells carried little load after cracking.	Capacity was not much higher than that of grout alone.
6) Grouted masonry under eccentric compr.	As described in 3).	Both grout and joint have a minor effect on the capacity.

Table 2.8 A Summary of Failure and Capacity Characteristics

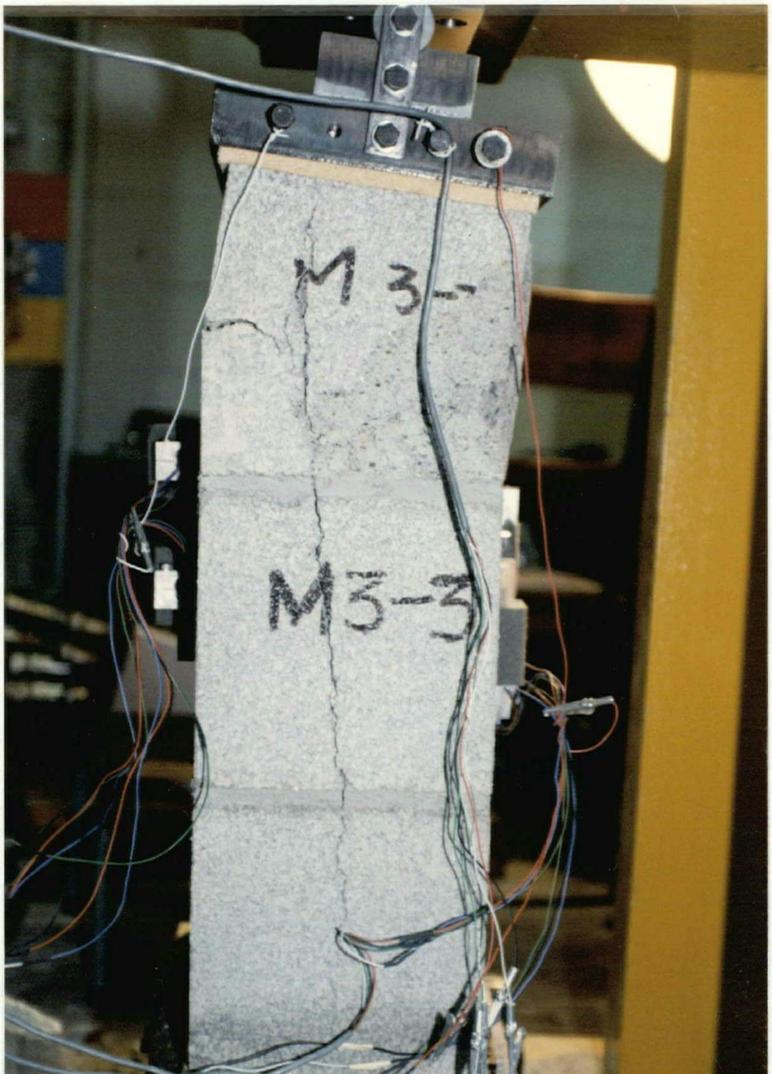

FIG. 2.12 Splitting Failure of Plain Concrete Masonry with

Full Bedding under Uniaxial Compression

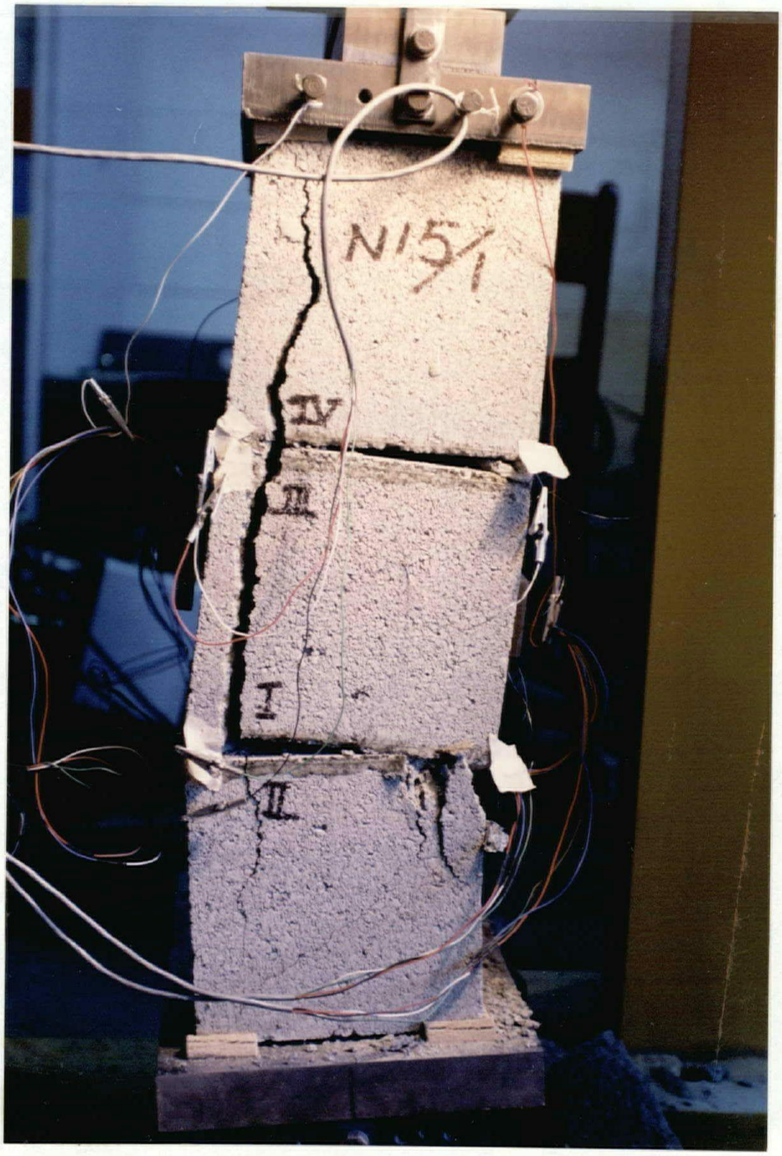

FIG. 2.13 Failure of Plain Masonry with Face-Shell Bedding under Uniaxial Compression

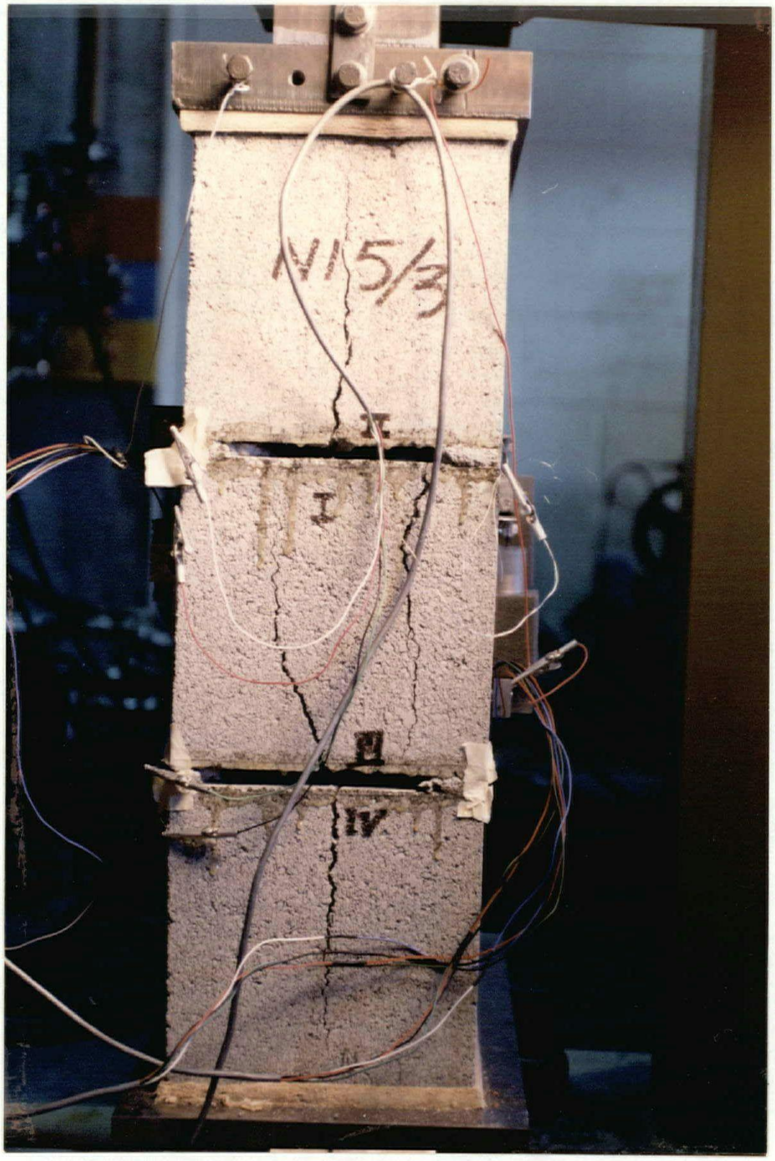

FIG. 2.14 Failure of Face-Shell Bedded, Fully Capped Masonry under Uniaxial Compression

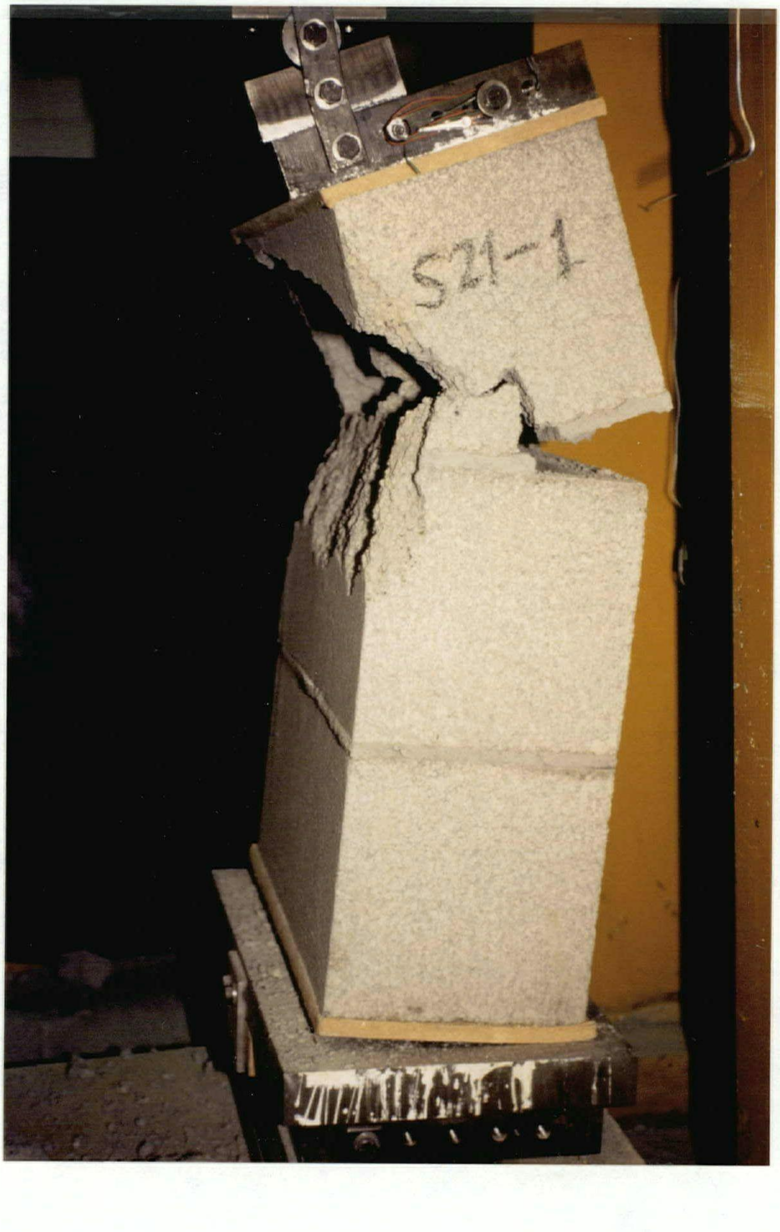

FIG.2.15 Failure of Plain Masonry under Eccentric Compression

FIG. 2.16 Failure of Grouted Masonry under Eccentric Compression

CHAPTER III

SOME BACKGROUND TO COMPRESSION FAILURE OF CONCRETE

3.1 Purpose

Concrete masonry is basically a concrete member with discontinuity in material properties. In structural design, it is usually used to sustain compressive force.

In traditional analysis for concrete structures, a phenomenological approach has been used: experimentally observed stress-strain relationships, usually from uniaxial tests, have been applied. Failure has been defined as the stress or strain in the member which reaches some critical value (strength or ultimate strain), which is obtained from uniaxial tests and assumed to be constant in a general stress state.

However, this approach is subject to certain limitations. The compressive strength of a material such as concrete, whose failure is characterized by brittle cleavage fracture, is not a very meaningful parameter. It varies with the stress state due to the so-called strain gradient effect, a phenomenon which is more obvious for concrete masonry. The approach also fails to give an explanation for the splitting failure mechanism often observed in concrete masonry as well as concrete under uniaxial compression. These problems have been partially recognized but never been fully explained.

The study presented in this chapter will attempt to raise the question and to shed some light on the problems by examining brittle materials under uniaxial compression. The intention is to present an explanation of the behaviour of these materials based on a failure mechanism at the fundamental level.

The principles of this study will be used to explain some behaviour of concrete masonry and to support an alternative approach in later chapters. It is hoped that this study will also help to develop a better understanding of the nature of the strain gradient effect and the splitting failure phenomenon commonly exhibited in brittle material testing, and lead to more general and consistent failure criteria for these materials.

3.2 Brittle Failure under Uniaxial Compression

Although concrete may exhibit high nonlinearity at working compressive stress, it is essentially a brittle material. This is so mainly because the failure of concrete is characterized by brittle cleavage fracture and the plastic deformation due to viscous behaviour of the hardened cement is rather limited (Hsu et al 1963, Ziegeldorf 1983).

Extensive research work at both structural and phenomenological levels has indicated that under compression, concrete experiences three distinct stages before its final failure: initiation of the cracks; slow stable crack growth accompanied by crack arrest; a critical condition characterized by unstable crack propagation and an extensive crack network formation (for example, see Mindess 1983). The cracking process is reflected in the global nonlinearity of the material, which appears in spite of the fact that both aggregate and hardened cement paste are, individually, essentially linear up to the failure stress of the concrete. Another indication is the apparent volume increase of concrete under compression.

An important feature is that globally, the fractures in the material coincide with the direction of the maximum principal compressive stress (Kotsovos 1979). For the case of uniaxial compression, this corresponds to the well known splitting failure occurring overwhelmingly in careful experiments. The conical failure mode frequently observed in concrete compression tests is due to the lateral confining effect of the loading platen; it will change to a splitting mode if the friction between the specimen and the loading platen is reduced.

Although shear stress does develop on inclined planes in uniaxial compression tests, the classical theories based on shear fracture proposed by Coulomb, Navier, and Mohr are simply not born out by experiment. Fracture mechanics based on Griffith's theory provides a powerful methodology in brittle failure analysis. Unfortunately, its success in application to concrete, compared with metals, is rather moderate. This is largely because, as a cement-based composite, concrete is essentially a discontinuous, anisotropic, heterogeneous, multiphase system. There is no clearly defined front for a major crack and the energy dissipating mechanism is not merely confined to the surface energy. Direct application of the single crack model in Linear Elastic Fracture Mechanics does not lead to satisfactory quantitative results.

However, recent developments in the application of fracture mechanics to concrete have been more encouraging. This involves the use of a proper, nonlinear form of fracture mechanics in which a finite nonlinear zone at the fracture front is taken into account, for example see Bažant (1985). This finite zone can model strain-localization due to strain softening of concrete (in an average sense over a smeared crack band) at the crack front and provide an energy criterion for crack extension. Concrete outside of this finite zone can be considered to behave essentially elastically. It is found that the detailed distributions of stress and strain at the fracture front have little effect globally, since fracture propagation depends essentially on the flux of energy into the fracture process zone, which is a global characteristic of the entire structure. Although these findings were obtained in the study of concrete under tension, some of the basic principles should also be applicable to the case of uniaxial compression.

In the case of uniaxial compression, experiments on different brittle materials such as ceramics, glass and especially on natural rocks, have again revealed the same splitting failure mode and a similar stable-unstable failure process. For relatively homogeneous materials, often only one or a few splits are observed, while for less homogeneous materials, more visible vertical cracks are found to accompany the main splitting. (Seldenrath et al 1958, Fairhurst and Cook 1966, Brace and Byerlee 1966, Paterson 1978). This has led to relatively extensive model studies, at a fundamental level, in these areas. The most frequently studied models are grounded in the idea that frictional sliding of a pre-existing crack produces, at the crack tips, tension cracks that grow in the direction of compression, as shown in Fig. 3.1.

It may be worth giving a brief description of the effect of the presence of a sliding crack. Consider a block in which a crack appears as in Fig. 3.2(a). Before the crack appeared, the stress

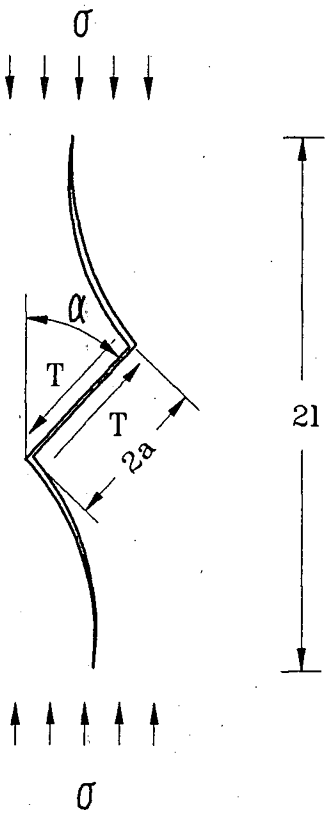

FIG. 3.1 A Sliding Frictional Crack in a Compressive Stress Field, Showing the Original Defect and its Extension

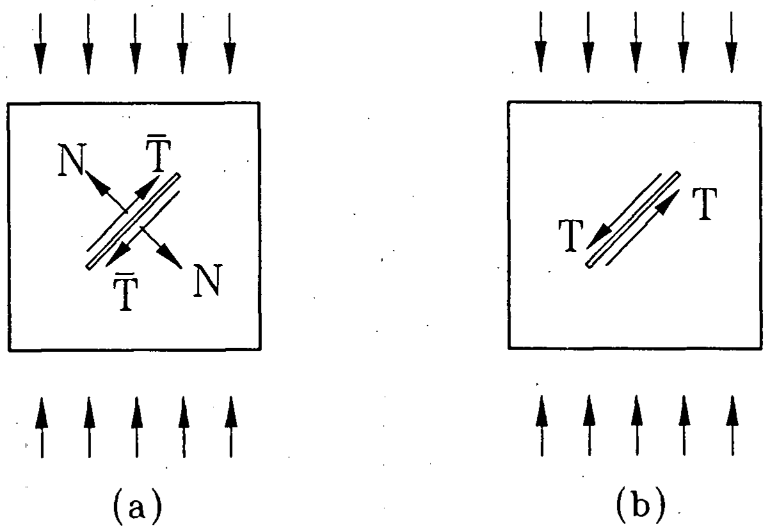

FIG. 3.2 Depiction of the Effect of a Crack

field was such that a pair of normal forces N and shear forces $\overline{T}$ were transferred across the space now occupied by the crack. When the crack forms, N is still transferred, but $\overline{T}$ can no longer be carried. Thus the effect of the crack on the original stress field is the same as the application of two opposite shear forces T on the crack zone, as depicted in Fig. 3.2(b) and Fig. 3.1 (i.e. the removal of $\overline{T}$). Similar argument may also apply for material defects with other configurations.

Although this model is a radical idealization of reality, it does capture some of the basic features of the observations made at the microscopic level on rocks and concrete. Frictional sliding does occur along the pre-existing interface cavities or cleavage cracks, and for concrete this often takes place at the matrix-aggregate interface. The sliding-induced tension cracks tend to grow in the direction of the compression, in spite of local inhomogeniety, in an initially stable manner.

Although material defects are also found in the form of cavities without contact faces, it has been observed that the induced tension cracking has a much lower tendency to grow than does the sliding case (Ziegeldorf 1983). This can also be inferred from the analytical work of Panasjuk (1976), Zaitsev(1983), or Sammis and Ashby (1986), which indicates that under compressive stress σ, the energy release rate for a crack with extended length l is in the order of $\sigma^2/\ l$ if the defect is an inclined pre-existing crack, and $\sigma^2/\ l^5$ if the defect is a void (see Fig. 3.3). Thus defects in the approximate form of sliding cracks will dominate the crack extension unless the distribution of defects in other forms is overwhelming.

Additionally, the idealization of material defects appears to be necessary if we are to reach an analytically manageable approach. Probably for all these reasons, since it was first proposed by McClintock and Walsh (1963), the model of a sliding crack with kinks has received considerable attention. It has been studied both analytically and by model experiment; the latter is often achieved by carrying out tests on some synthetic brittle material with man-made sliding crack(s). The most notable work includes Brace and Bombolaksi (1963), Hoek and Bieniawski (1965), Santiago and Hilsdorf (1973), Kachanov (1982), Nemat-Nasser and Horii (1982), Zaitsev

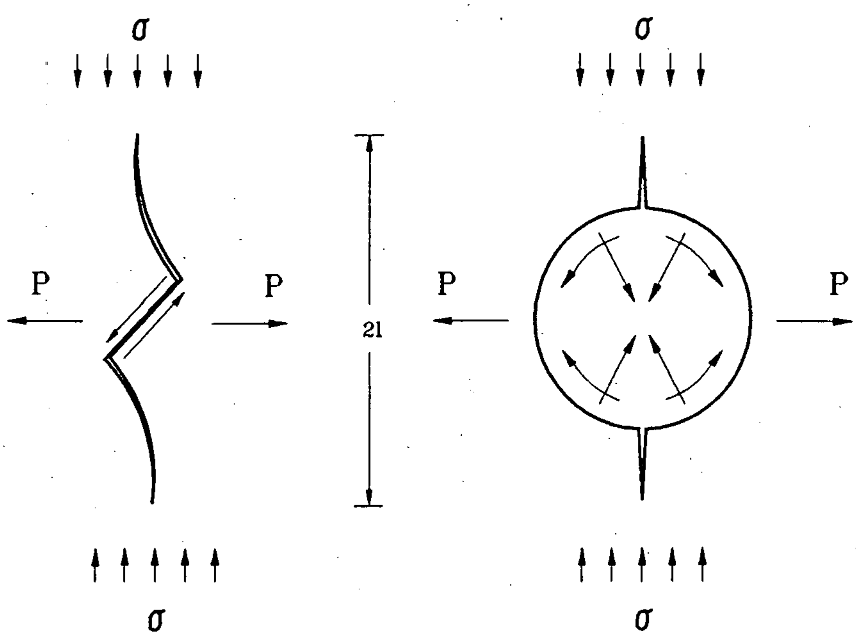

FIG. 3.3 Models of Material Defects. (The Missing Force Acts on Each Side in a Direction Opposite to that Shown. The Effect of the Defect is Therefore to Apply Forces in the Direction Shown.)

(1983), Steiff (1984), Horii and Nemat-Nasser (1985), Ashby and Cooksley (1986), and Horii and Nemat-Nasser (1986).

Because of the complexity of the problem, almost all the analytical studies have been based on plain elasticity. This is, of course, closer to the behaviour of homogeneous brittle materials such as ceramics and glass than to rocks and concrete. Nevetherless, they appear to give reasonable explanations of some of the characteristics of these inhomogeneous materials.

In this chapter, some aspects of previous model studies will be briefly reviewed, and a simplified model based on interaction of the sliding cracks will be presented. The focus will be on the transition from stable to unstable cracking under uniaxial compression; and the latter will be shown to manifest the well known splitting failure. The model will be shown to reveal the characteristics of the compressive strength, and of the stress-strain relation of brittle materials under uniaxial compression.

The model will be based on plane elasticity and an idealized crack pattern. When it is applied to the behaviour of concrete and rock, it may be subject to the same limitations as the previous analytical work, but, in view of the limited plastic deformation of these materials under uniaxial compression, and of the successful application of fracture mechanics to concrete under tension, this approach should reveal some of the basic features of compression. However, as indicated above, local nonlinear behaviour must be included to give correct quantitative predictions for concrete. Thus, although some quantitative conclusions drawn from the proposed model will be presented, the basic objective is to illustrate rather than quantify. It is hoped, that this theoretical treatment, based on a hypothesis for the failure mechanism, will shed some light on the actual failure process, and lead to a better understanding of the problem.

3.3 Models of Internal Brittle Failure

Brittle failure under uniaxial compression is distinct from that in tension in that there exists a stable cracking process before final unstable fracture. This has been observed experimentally (for instance, as we reviewed for concrete in the introduction), and has been identified from the fracture mechanics point of view (for example, see Kostovos and Newman 1981). With crack growth, the strain-energy concentration at a crack front tends to increase in the case of tension, but decrease in the case of compression. Thus in compression, the fracture occurs initially in a discrete, stable manner with increasing load; failure occurs when the stable cracking reaches a certain extent, but not at the initiation of these cracks. Overlooking the subcritical crack growth will lead to erroneous results, such as Griffith's prediction of 1:8 for the ratio of tensile to compressive strength - a substantial underestimate for many brittle materials (Obert 1972). (In the case of concrete under tension, fracture may appear to be temporarily stabilized; but this is due to arrest by the aggregate rather than the release of the strain-energy concentration.)

The model of a single crack with kinks certainly exhibits this stable feature. Referring to Fig. 3.1, the sliding shear force, which represents the effect of an inclined crack with length $2a$ in an otherwise compressive stress field, is the resultant of the driving shear stress along the crack (for example, see Zaitsev 1983)

$$T = 2a\,\sigma\,(\sin\alpha\cos\alpha - \mu\sin^2\alpha) \qquad 3.1$$

where μ is the coefficient of friction of the material. When the extended crack length $2l$ is long compared with $2a$, the horizontal components of these shear forces may, as far as splitting is concerned, be considered as a pair of tension forces of magnitude $P = T\sin\alpha$. As the crack extends in the direction of the applied stress, these forces remain approximately constant, and the well-known fracture mechanics solution (Broek 1978) for this case shows that the stress intensity at the crack tip attenuates with extension ($K_I = P/\sqrt{\pi l}$). It is for this reason that the crack is initially stable. An exact formulation of the problem has been given by Horii and Nemat-Nasser (1985), which gives results very close to this approximation. Since the stable extension does not lead to immediate failure, the detailed turning path of the wing cracks appears to be unimportant.

Model experiments on brittle materials with a man-made sliding crack have indeed indicated this stable, tensile crack extension, turning into the direction of the loading (Brace and Bombolakis 1963, Hoek and Bieniawski 1965, Santiago and Hilsdorf 1973, Nemat-Nasser and Horii 1982, Horii and Nemat-Nasser 1985). This direction is favored because this is the orientation in which the least work is required to open the crack. Although Mode II stress intensity appears in the crack tips, shear fracture in the plane of the prepared sliding crack was never observed unless the width of the specimen was close to the crack length.

However, since final failure is brought about by unstable fracture, there must be a transition from stability to instability in the cracking. Recognizing this point, Ashby and Cooksley (1985) developed a model based on the wing crack interaction. They hypothesize that when stable cracks are relatively long, the branches between cracks tend to bend, which intensifies the stress concentrations at the crack tips and leads to instability. However, this bending interaction mechanism appears to be insufficient to explain an unstable split in a relatively short specimen. It may be worth mentioning that Kendall (1978) has also developed a similar beam bending model to explain axial splitting; but this one requires an indented (i.e. a load which does not cover the outer edges of the loaded face) compressive load acting on a vertical crack, forcing the two struts separated by the crack to bend outwards. Obviously, this model fails to give an explanation when the global compressive stress is uniform.

Based on their analytical work, Horii and Nemat-Nasser (1982, 1985) concluded that the sliding-induced tensile crack is very sensitive to lateral stress. The crack extension soon becomes unstable if a small lateral tension exists. Their model experiments on a barrel-shaped specimen gave an excellent illustration of this point. However, an explanation is still needed for the case of uniaxial compression corresponding to zero lateral stress.

3.4 Proposed Model

It is clear that the model of a single crack with kinks only provides the source of the splitting. Other effects must be included to explain the unstable transition. We now present a relatively simple model to show that this transition can be a consequence of the extension of a group of stable cracks. Some interesting results will follow immediately.

3.4.1 Crack Interactions and Critical State

Since, as indicated above, crack extension in compression is initially stable, there is a high probability that, with increasing stress, cracks will extend from all defects with similar configurations. As a result, compressive failure is usually not governed by any individual defect; this contrasts with tension failure, which is governed by the defect with critical configuration, and in which fracture is highly localized. Thus it appears necessary to consider all the defects which govern the behaviour. By the same argument, it may also be reasonable, as will be discussed later, to treat the cracking process in an average sense. By using the model of the sliding crack with kinks and the described approximation, every defect in a material corresponds to a pair of splitting forces

$$P_i = k_i \; a_i \; \sigma \tag{3.2}$$

where

$$k_i = 2 \; (\sin\alpha_i \cos\alpha_i \; - \; \mu \sin^2\alpha_i \;) \; \sin\alpha_i \tag{3.3}$$

Note that P_i depends on the initial, inclined, length of the crack and not on the extended length.

k_i a_i takes account of the configuration of the crack. For concrete, a_i may be in the order of the aggregate particle size; the coefficient of friction μ is about 0.36 (Troxell et al. 1968), so that k for the worst angle is about 0.45 (i.e. the angle corresponding to the biggest force).

Let us examine an idealized case where a series of defects lies in a line as shown in Fig. 3.4(a). By the stated approximations, the situation in Fig. 3.4(a) is equivalent to Fig. 3.4(b): a series of cracks with an average length of $2l$ and an average spacing $2b$ acted on by pairs of point forces.

For an infinite medium, the problem has been studied by Irwin (1957). The stress intensity factor at the crack tips for this case is available from the Westergaard stress function given by him:

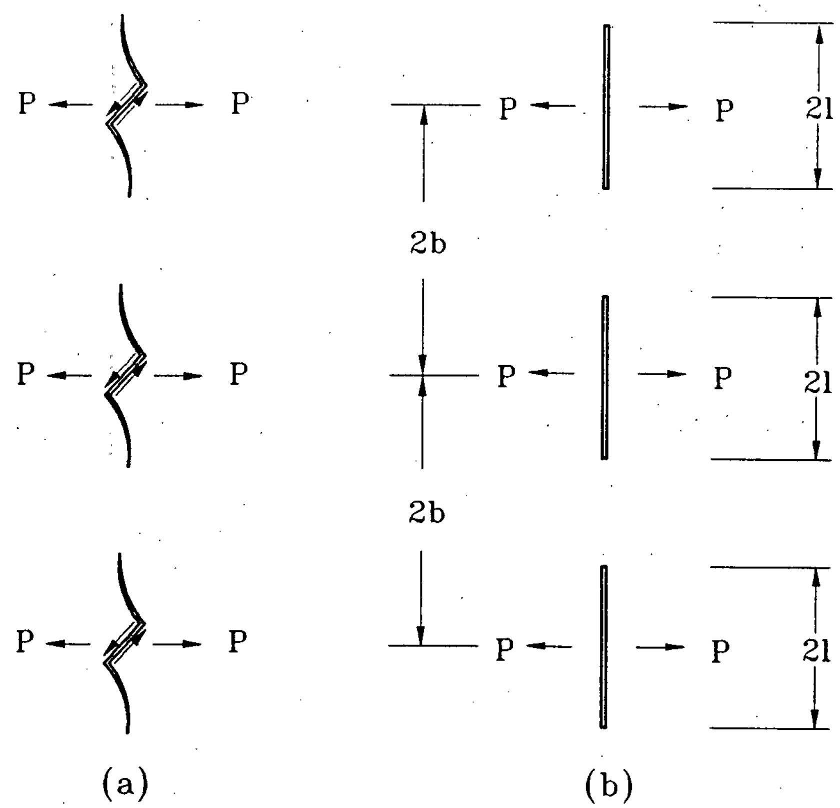

FIG. 3.4 A Series of Cracks in a Compressive Stress Field: Two Levels of Idealization

$$K_I = \frac{P}{\sqrt{b \sin(\pi l/b)}} \quad 3.4$$

or, in terms of energy release rate for plane strain conditions:

$$G_I = \frac{P^2(1-\nu^2)}{Eb \sin(\pi l/b)} \quad 3.5$$

where E = Young's modulus; ν = Poisson's ratio.

Cracks extend when Eqs. 3.4 or 3.5 reach some critical value, which is a material constant. The solution indicates that, when $l/b < 1/2$, $dP/dl > 0$, cracks propagate stably; the propagation becomes unstable when $l/b > 1/2$, $dP/dl < 0$. Once l/b reaches 1/2, cracks will propagate extensively, and one or more will run through the material immediately. This point may therefore be defined as the critical state. This relatively simple model clearly reveals the characteristics of the stable-unstable fracture process. It shows that critical instability can be the result of the stable crack growth itself.

In reality, pre-existing defects may rarely exist exactly colinearly. However, model experiments by Horii and Nemat-Nasser (1985), in which plates of Columbia resin CR39 containing a number of pre-existing sliding cracks were tested under uniaxial compression, have indicated that the vertically distributed cracks do indeed tend to join each other to form the final fracture, even though they are not in a vertical line.

For a relatively homogeneous specimen (without man-made cracks), surface cracks at the top and bottom will be likely to govern the behaviour, i.e. vertical cracks will initiate from top and bottom instead of from inside of material (this can easily be verified by testing, say, a plexiglass strut). The model still applies if we consider the specimen height as $2b$, referring to Fig. 3.4(b), and recognize the fact that the solution is symmetric with respect to every line of splitting forces. Physically, it means that the equivalent splitting forces are applied at the top and the bottom of the specimen, and the fractures become unstable when the vertical cracks initiating from the top and the bottom both reach approximately one quarter of the specimen height.

A similar argument applies in the case where the height of a specimen is small compared to the size of a pre-existing crack inside the material, so that the final fracture is governed by a split from this defect. In this case, the specimen height can be still considered as $2b$, but the pair of splitting forces is applied inside. The fracture becomes unstable when the split reaches approximately half of the specimen height. Thus it appears that the model is useful in many cases.

3.4.2 Some Consequences of the Model: Peak Stress

Putting Eq. 3.2 into Eq. 3.4, with $l/b = 1/2$, and solving for σ, we can estimate the failure stress (or the so-called compressive strength) of concrete, or any other brittle material, as

$$f'_c = \frac{K_{IC}}{k\xi\sqrt{b}} \qquad 3.6$$

where K_{IC} = critical stress intensity factor; k = average configuration factor; b = average half spacing of defects; ξ = average value of a/b. These quantities are all considered to be fundamental material constants. Note that f'_c is used here to denote the failure stress of a brittle material, not necessarily concrete. Note that all the terms on the right hand side of Eq. 3.6 should be understood in an effective sense when they are not clearly defined by microscopic observation. For concrete and rocks, the term K_{IC} or G_{IC} should be understood as the energy dissipated by all the mechanisms when a crack propagates, not merely the surface energy.

It can be easily shown that, based on this model, the stress intensity at the crack tips will be drastically reduced even if a small lateral compressive stress is present. Thus such a stress will lead to a different failure mode corresponding a higher failure stress. This may explain the shear failure mode, which is accompanied by a significant increase in strength, that is exhibited in a compression test on a confined specimen. In practice, the lateral stress is often introduced by the loading platen in uniaxial compression tests.

Equation 3.6 may need modification for specimens of finite size and for the interlock and crack arrest mechanisms that are present in concrete and rocks; and for concrete, inclusion of the nonlinear behaviour at the crack front appears to be necessary for precise analysis. Nevertheless, the equation should give a reasonable estimate of the compressive strength.

3.4.3 Relation to Tensile Strength

Brittle tension failure is relatively well understood. It is governed directly by the pre-existing cracks, because extension is unstable under tensile loading. The tensile strength can be estimated, based on the pre-existing crack configuration and distribution (see Fig. 3.5) using the solution (Broek 1978)

$$K_I = [\ \sigma_t \sqrt{\pi a}\ ]\ [(2b/\pi a)\ \tan(\pi a/2b)]^{1/2} \qquad 3.7$$

where the term in the first bracket is the well-known solution for an isolated crack in a background tensile stress field; the term in the second bracket is included to provide an estimate of the effect of adjacent cracks. Although cracks would rarely exist in the configuration of Fig. 3.5, tension failure is governed by a single crack with critical configuration, so that Eq. 3.7 need only hold for a very small region.

Equation 3.7 may be rearranged to give the tensile strength as

$$f_t = \frac{K_{IC}}{\sqrt{2b\ \tan(\pi\xi/2)}} \qquad 3.8$$

so that, in view of Eq. 3.6

$$\frac{f_t}{f_c} = \frac{k\xi}{\sqrt{2\ \tan(\pi\xi/2)}} \qquad 3.9$$

This implies that the ratio of tensile to compressive strength of a brittle material is solely dependent on the configuration and distribution of the pre-existing defects, and the internal friction of the material. This ratio for concrete is plotted against ξ in Fig. 3.6. The ratio for the extreme case, $\mu = 0$ (e.g. for some ceramics) is shown as well.

Experiment shows that f_t/f_c ranges from 0.06 to 0.13 for concrete, suggesting a range of ξ from 0.05 to 0.25. The model also suggests that the lower strength ratio is associated with a smaller ξ, which tends to indicate a higher strength material. This agrees with the well-known non-proportional relationship between tensile strength and compressive strength of concrete

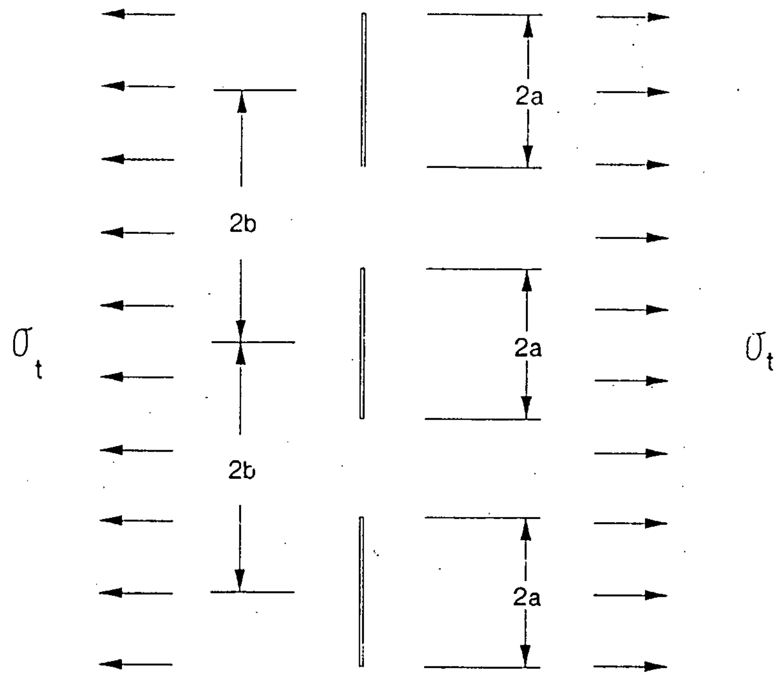

FIG. 3.5 A Series of Cracks in a Tensile Stress Field

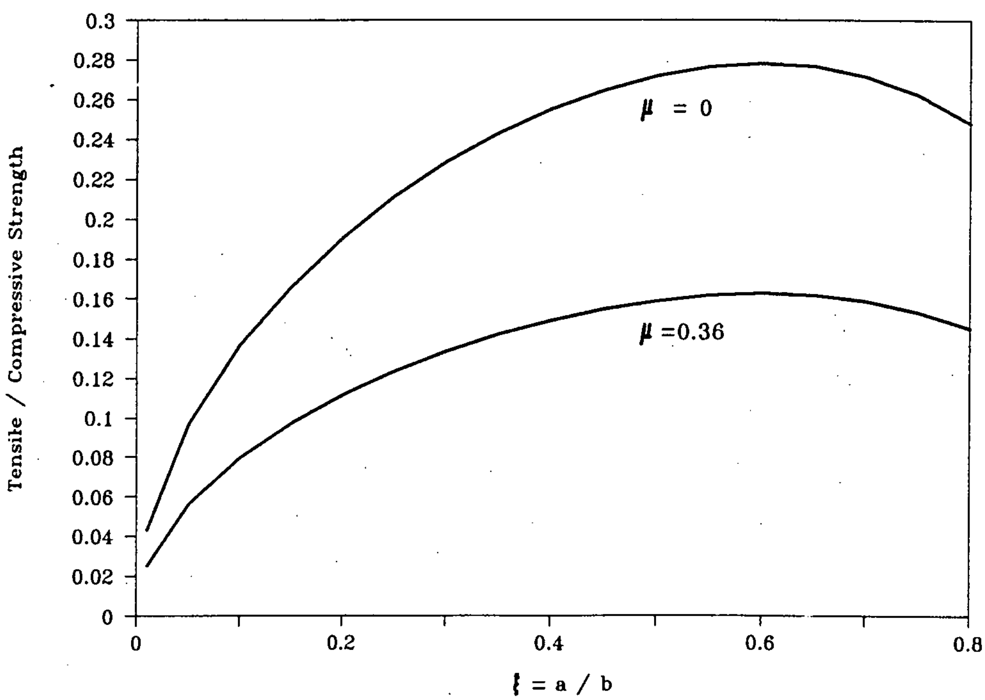

FIG. 3.6 Predicted Relation between Tensile Strength and Compressive Strength versus Size/Spacing Ratio for Brittle Materials

(Park and Pauley 1975). The model also predicts an upper bound of about 0.16 for this ratio. To the author's knowledge, this extreme case has never been surpassed.

An explanation is provided for the wide range in strength ratio observed in other brittle materials. Rocks, for example, exhibit values from 0.02 to 0.10 (Obert 1972), which are covered by the model when the pre-existing cracks range from short to long relative to their average spacing.

The model also predicts that no brittle material can have a tensile strength exceeding 28% of its compressive strength.

3.5 The Stress-Strain Curves for Brittle Materials under Uniaxial Compression

We first review existing knowledge of the force-deformation relationship, which may be divided into two parts: the pre- and post-peak branches.

Although the word brittle implies limited deformation before failure, it appears that, even for very brittle materials, there is some nonlinearity immediately before the peak stress. For less brittle materials such as concrete, there is an essentially linear response up to a certain stress level, then nonlinearity becomes apparent, and increasingly so as the material approaches failure (Wawersik and Fairhurst 1970; Obert 1972; Mindess 1983; Brady 1985).

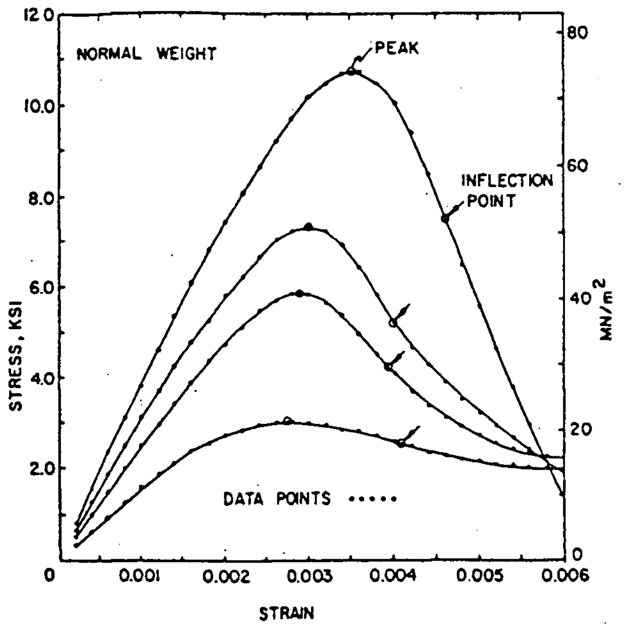

FIG. 3.7 Experimental Stress-Strain Relations of Concrete, under Normal Test Conditions (Wang 1978)

The post-peak behaviour is still more complicated. Less brittle materials, such as concrete, exhibit a pronounced long tail (Wang 1978) in the stress-strain curve under normal testing conditions, as shown in Fig. 3.7.

However, Kotsovos (1983) indicates that this widely held view may be misleading. His experiments show that end conditions significantly affect the post-peak behaviour, especially for high strength concrete. He placed various "anti-friction" media between the specimen and load platen, and found very different behaviour (Fig. 3.8). He concludes that, if the frictional restraint is eliminated, the material will suffer a complete and immediate loss of load-carrying capacity. His results show an apparent recovery of compressive strain after the peak load, but he does not comment at any length on this surprising phenomenon. It is seldom observed, even in tests of more brittle materials, since recording in this range is very difficult without special arrangements.

Wawersik and Fairhurst (1970), using very careful test procedures, were able to follow, in part, the descending branch for some fine-grained rocks. Some strain was clearly recovered as the load was reduced beyond the peak stress, and the stress-strain curve turned towards the origin (Fig. 3.9).

The long tail, with decreasing stress accompanied by increasing strain (assuming that it is not merely a result of imprecise test procedures), is known as class I response. The alternative observation, when the strain is recovered, is known as class II response; it has the defining characteristics that "the fracture process is unstable or self-sustaining; to control fracture, energy must be extracted from the material" (Brady 1985). The classification has been based entirely on experimental observation, and it is hoped that the following analysis, based on the proposed model, will shed some light on the observed phenomena.

3.5.1 The Pre-Peak Branch

The initial deformation, before the cracks begin to extend, can be calculated from Young's modulus. A second phase, which will now be studied, is entered when crack propagation begins.

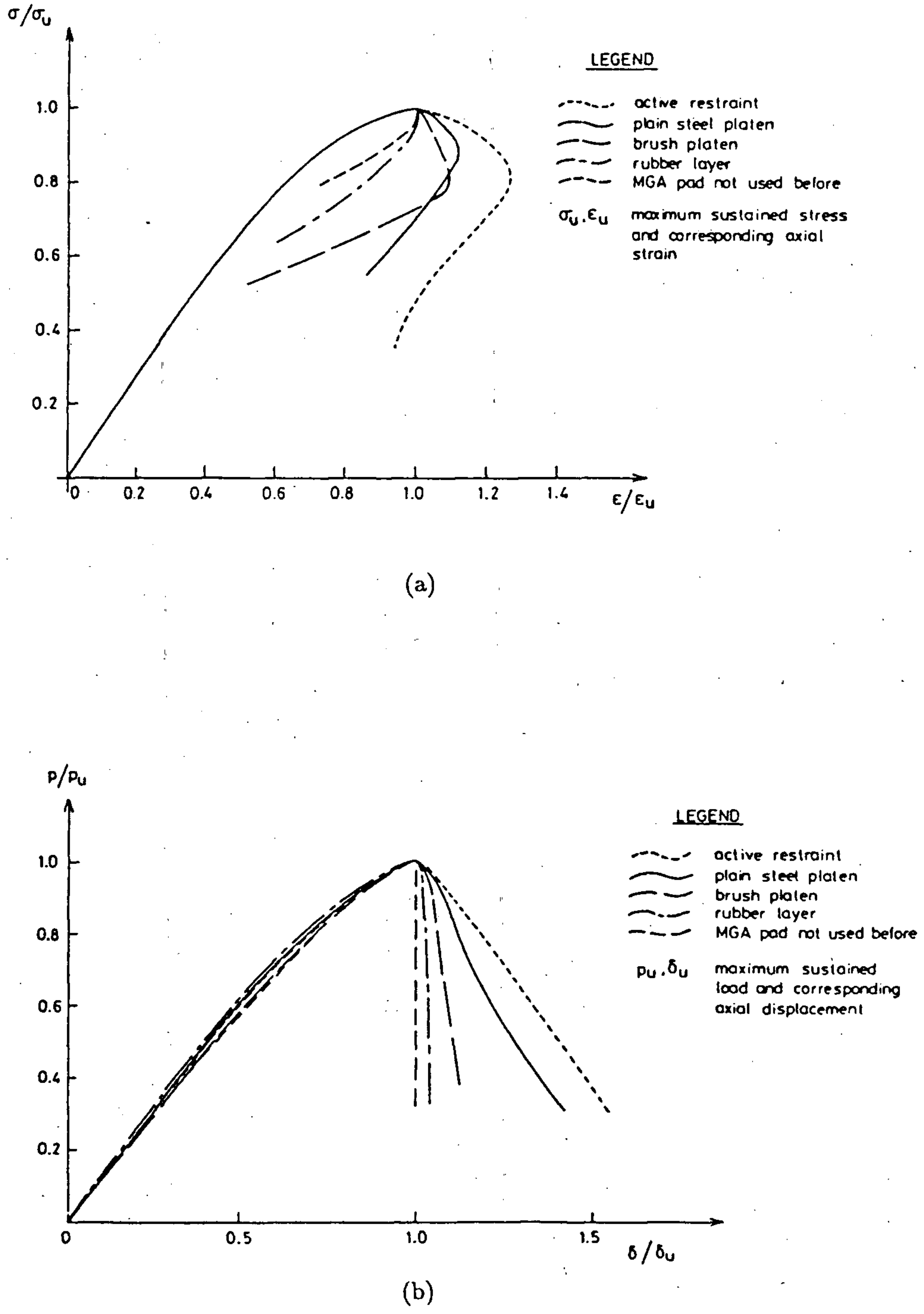

FIG. 3.8 Experimental Stress-Strain Relations of Concrete, Specimens with "Anti-Friction" Capping (Kotsovos 1983): (a) Stress versus Strain Measured on the Specimens; (b) Load versus Displacement

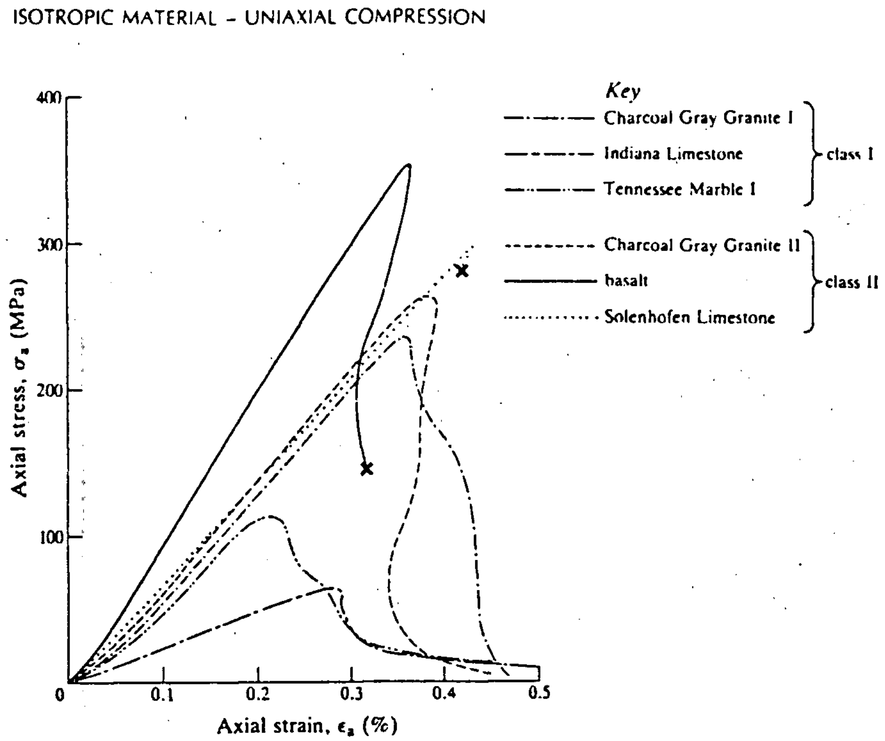

FIG. 3.9 Experimental Stress-Strain Relations of some Natural Rocks (Wawersik and Fairhurst 1970)

Consider a rectangular region of height h and width w under uniaxial compression; assume the cracking process is quasi-static. When the cracks extend dl we have, for energy conservation,

$$dV - dU = dW + dR \qquad 3.10$$

where dV = work done by external load; dU = increase of the strain energy; dW = energy dissipated to form new crack extensions; dR = energy dissipated by the friction between the contact surfaces of pre-existing cracks.

Clearly

$$dV = F d\Delta \tag{3.11}$$

where F = external load; Δ = associated displacement.

Since in a brittle material the plastic deformation is limited, the material will remain essentially linearly elastic regardless of the cracking. It can be shown (see appendix) that as long as overall fracture does not occur, so that the region is still connected, the strain energy can be expressed in terms of the external load and the associated displacement, as

$$U = 1/2\ F\Delta \tag{3.12}$$

If the friction between the pre-existing crack surfaces is included, this expression becomes

$$U \approx \frac{1}{2}\left[\ F\Delta\ -\ MAF^2 \log\left(\frac{\tan(\pi l/2b)}{\tan(\pi l_o/2b)}\right)\right] \tag{3.13}$$

where M is the number of pre-existing cracks in the region, l_o may be called the effective initial extending crack length, which is a function of the crack configuration, and A is a constant expressed as

$$A = \frac{8(1\text{-}\nu^2)\mu k a^2 \sin\alpha}{\pi E w^2} \tag{3.14}$$

Thus dU is readily available by differentiation of this expression:

$$\mathrm{d}U = \frac{1}{2}\left[F\Delta' + F'\Delta\ -\ 2MAFF' \log\left(\frac{\tan(\pi l/2b)}{\tan(\pi l_o/2b)}\right)\ -\ MAF^2 \frac{\pi}{b}\mathrm{cosec}\frac{\pi l}{b}\right] dl \tag{3.15}$$

The new crack surface energy can be expressed as

$$dW = 2M\ G_{IC}\ dl \tag{3.16}$$

Finally, the energy dissipated by the friction can be approximated as (see appendix)

$$dR \approx M\,\frac{8\mu G_{IC}\sin\alpha}{k}\left[\,1 + \frac{1}{2}\cos\!\left(\frac{\pi l}{b}\right)\log\left(\frac{\tan(\pi l/2b)}{\tan(\pi l_o/2b)}\right)\right] dl \tag{3.17}$$

These equations are valid when cracks are extending, i.e., when K_I or G_I defined by Eqs. 3.4 or 3.5 have reached the critical values. They give the relationship between load F and the displacement Δ in terms of the independent parameter l, the crack length. For a given load, the equations can be solved for Δ by substituting Eqs. 3.11, 3.15, 3.16 and 3.17 into Eq. 3.10, and using the initial condition

$$\Delta = \sigma_o h/E \qquad \text{when} \quad l = l_o \tag{3.18}$$

where σ_o may be called the threshold stress for the crack extension; the relation to l_o is obtained in view of Eqs. 3.4 and 3.6:

$$\sigma_o/f_c' = \sqrt{\sin(\pi l_o/b)} \tag{3.19}$$

Now, the load $F = \sigma w$ is related to l by Eqs. 3.2, and 3.4; and

$$\Delta = \epsilon h \tag{3.20}$$

where ϵ = longitudinal strain.

Thus we are able to extract an expression for strain in terms of stress. Assuming the average spacing of the cracks is the same horizontally and vertically,

$$\frac{M}{wh} = \frac{1}{(2b)^2} \qquad 3.21$$

we get

$$\epsilon = \left\{ \frac{G_{IC}}{\pi b f_c'} \left[1 + \frac{2\mu \sin\alpha}{k} \right] \log \frac{\tan(\Theta/2)}{\tan(\Theta_o/2)} + \frac{f_c'}{E} \right\} \frac{\sigma}{f_c'} \qquad 3.22$$

where $\Theta_o = \text{arc}\ \sin(\sigma_o/f_c')^2$; $\Theta = \text{arc}\ \sin(\sigma/f_c')^2$.

Phase II of the pre-peak branch covers the range $\sigma_o \leq \sigma \leq f_c'$, with $\Theta_o \leq \Theta \leq \pi/2$.

3.5.2 The Post-Peak Branch

The model discussed above is found to represent behaviour of class II materials into the post-peak branch. When $\mu = 0$, Eq. 3.22 is valid for the full range $\Theta_o \leq \Theta \leq \pi$. When friction is included, however, the equation applies only until the cracks stop opening somewhere in the descending branch. There is then a complicated situation as the cracks begin to close and the friction to change direction; a more elaborate treatment is given in the appendix. After an interval, the crack widths decrease and the friction force is reactivated in the opposite direction; Eq. 3.22 is again applicable, but with opposite sign on the terms containing μ in the bracket. There is also a different constant of integration in this range.

This application to class II behaviour is predicated on the assumption that cracks extend vertically in isolation from each other, so that the region is still connected. Further, it is assumed that the cracks are regular, so that horizontal fracture does not occur, and that the crack surfaces are relatively smooth, so that they close during the descending branch without interlocking. These assumptions, necessary for continued application of Eq. 3.22, are good for a relatively homogeneous brittle material.

For less homogeneous materials such as concrete and coarse grained rocks these assumptions may be expected to be approximately fulfilled during the loading stage, when the cracks are less extensive, and still opening. On the descending branch, however, the cracks tend to propagate through weak grain boundaries or aggregate-cement matrix bonds (Ziegeldorf 1983; Brady 1985), and the zig-zag crack paths have a tendency to interconnect parallel fractures. This leads to type I response as will be discussed below.

But, even in this case, the experiments of Kotsovos (1983) suggest that the type I response may merely be due to the end frictional constraints inhibiting vertical crack extension and leading to this type of failure. With "anti-friction" capping, he observed that vertical cracking of the higher strength specimens always extended in both directions, while, for the lower strength ones, it extended in one direction only, indicating that the restraining action of at least one end zone was still present.

Thus it appears that the validity of the assumptions of Eq. 3.22 depends upon the material properties and the loading conditions.

3.5.3 The Predicted Stress-Strain Curve

Eq. 3.22 is plotted for $\sigma_o/f_c' = 0.3$, with $\mu = 0$ and $\mu = 0.36$, in Fig. 3.10. The shape of the Type II curve is characterized by 4 points as indicated on the figure. From O to A, below the threshold stress, $l = l_o$, the cracks do not extend, and displacement is due solely to the linear elastic response.

In reality, of course, the onset of stable crack extension is difficult to identify; it is a gradual process rather than a sudden one, because of the variety of defect configurations. Thus there is a transition rather than a well-defined point A.

From A to B, additional deformation occurs due to crack extension, and the curve becomes more non-linear as f_c' is approached. Inclusion of friction increases both peak stress and

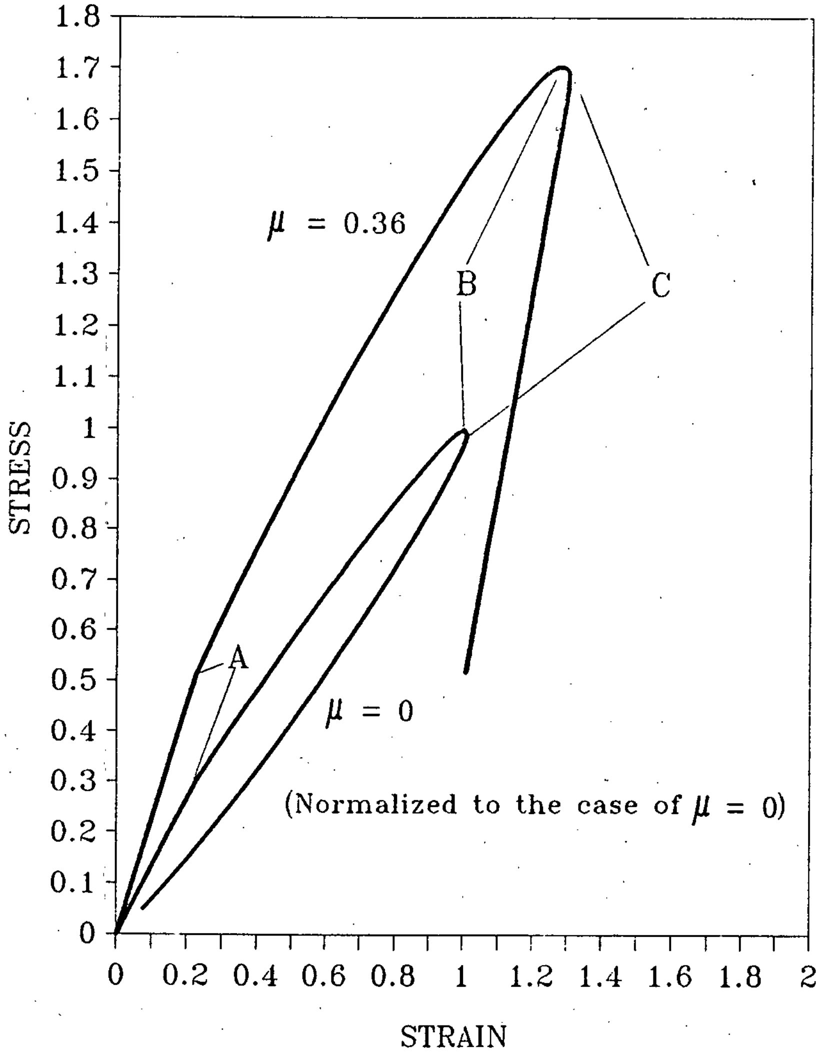

FIG. 3.10 Predicted Stress-Strain Relations of Brittle Materials

strain. Greater non-linearity appears due to energy dissipation through friction.

After the peak, the cracks continue to propagate as the applied stress decreases, in an unstable extension process. At point C the strain reaches its maximum value, and then begins to reduce; the work required for the cracking process beyond C is provided by part of the strain energy released from the material, but surplus energy must be extracted by the loading device. The area enclosed by the complete curve is, of course, equal to the energy dissipated in creating new crack surfaces.

A "less brittle" material may have a lower threshold stress for crack extension, and a higher coefficient of friction. A "more brittle" material, on the contrary, may have a very high threshold and low friction coefficient, so that it gives the appearance of a linear stress-strain curve. But the model implies that, since failure is caused by cracking, there must always be some non-linearity before it occurs.

Note that failure is finally brought about by the unstable crack extension splitting the specimen into pieces which are individually unstable, thus reducing the load capacity.

With conventional test arrangements, a load controlled testing machine will cause material failure at point B; displacement control will lead to failure at C if the machine is stiff enough. Failure will be explosive because of the sudden release of strain energy. Most reported results for more brittle materials are incomplete in this sense, but Wawersik and Fairhurst showed complete curves that agreed, qualitatively, with the model prediction, as did the post-peak curves for high strength concrete obtained by Kotsovos. Note that, during unstable crack extension, one or a few cracks will propagate preferentially, so that the model may lose some validity.

However, for less homogeneous materials, such as concrete and coarse-grained rocks, the assumption of regular vertical crack extension may not be valid in the post-peak range, as discussed earlier. This would explain the frequently observed class I response. Wawersik and Fairhurst (1970) found that, in class I behaviour of rocks, vertical fracture is, indeed,

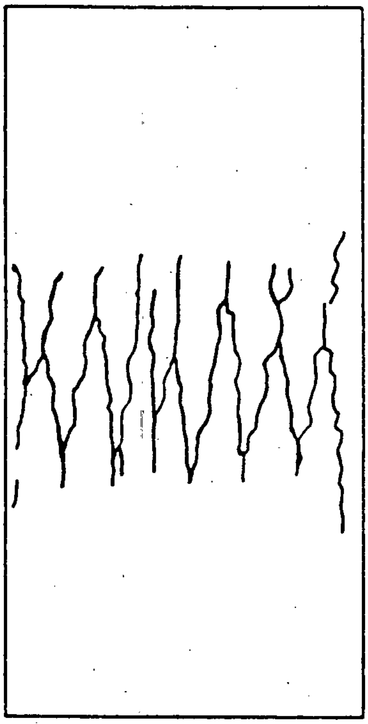

FIG. 3.11 Depiction of Irregular Cracking Pattern

accompanied by gradual development of shear fracture in the post-peak range; a similar description is given by Kotsovos for his lower strength specimens.

During this range, the ratchet-like mechanism of Fig. 3.11 forms, vertical deformation involves the wedges being driven into each other, and the energy of the load is converted to strain energy in the wedges, and friction losses between them, as well as surface energy in new cracks. The first two are clearly nonlinear, requiring that the vertical load decrease less rapidly with increasing deformation, and causing the load-deformation curves to be concave upward. Hence the inflection point observed by Wang et al. (1978) and the long tail thereafter.

From the above analysis one may conclude that the fracture pattern determines the post-peak stress-strain relation. Vertical fracture through the material will lead to "more brittle" failure, while the development of shear faults will give the appearance of more ductile behaviour. The fracture pattern, in turn, may often be governed by the loading conditions; friction in the loading platen, for example, may cause shear cracks and, more ductile behaviour.

3.6 Statistical Considerations

We now consider briefly the sensitivity of the model predictions to statistical variations in the parameters, which have hitherto been treated in an average sense.

Assume that the defects are uniformly distributed spatially but that the configurations have a random character described by some probability distribution, with density function

$$\Phi = \Phi(ka) \qquad 3.23$$

and cumulative function

$$Z = Z(ka) \qquad 3.24$$

with ka in some range

$$(ka)_{min} \leq ka \leq (ka)_{max} \qquad 3.25$$

Equation 3.6 can be modified by these assumptions to give

$$f_c' = \frac{K_{IC}\sqrt{b_o}}{ka[1-Z(ka)]^{1/4}} = \left[\frac{K_{IC}\sqrt{\bar{b}}}{\overline{ka}}\right] \cdot \left[\frac{\overline{ka}}{ka}\left(\frac{1-Z(\overline{ka})}{1-Z(ka)}\right)^{1/4}\right] \qquad 3.26$$

where b_o is the average half spacing of total defects under consideration, and the barred quantities denote the mean values.

Assuming a normal distribution for defect configuration, and approximating by a Weibull distribution, we write

$$Z(ka) = 1 - \exp\left[\, -(ka/\theta)^m\right] \qquad 3.27$$

The Weibull modulus $m = 3.6$ best represents a normal distribution; θ is taken corresponding to a coefficient of variation of ka of about 0.32. the second term of Eq. 3.26, which accounts for the statistical considerations, is plotted in Fig. 3.12, and shows the variation of f_c' as predicted by the model, against the variation in crack configuration.

If only a few defects with larger configuration factor *ka* (i.e. with wider crack spacing) have extended to govern specimen behaviour, the failure stress will be higher. This is because these defects are sparsely distributed, the stress required to bring them to interact upon each other to reach the critical state will be high, as indicated at the right end of the graph.

Although defects with smaller configuration are more densely distributed, the stress needed to cause them to extend will still be higher, as shown at the left end of the graph.

The minimum value is reached when *ka* is close to the mean value, around which the variation is small for a wide range of *ka*. Thus the average parameters do yield a reasonable approximation. This conclusion should be valid as long as the distribution is not extremely distorted.

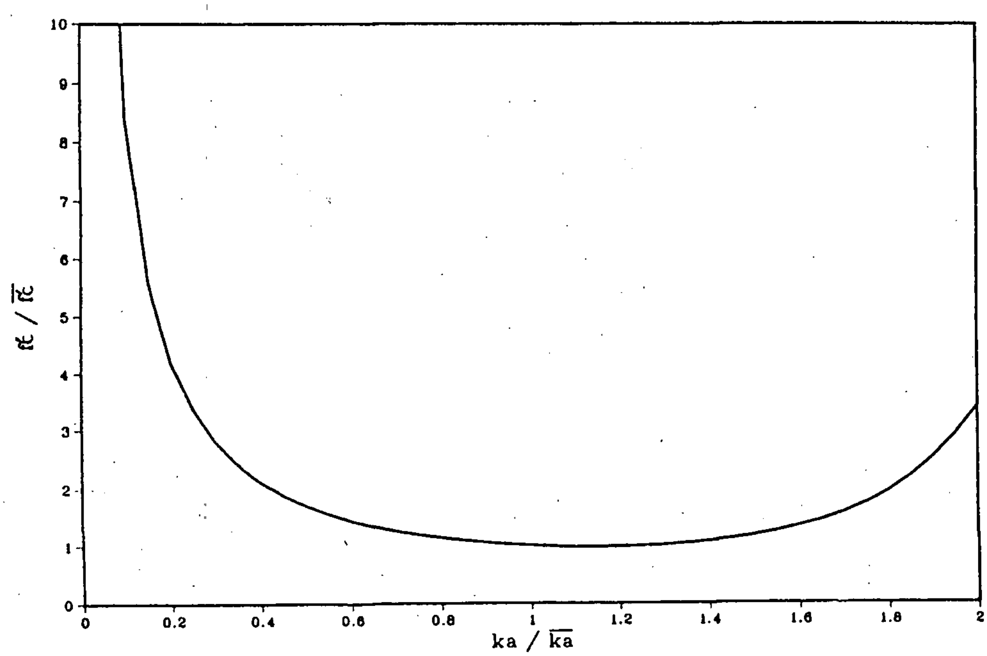

FIG. 3.12 Sensitivity of Compressive Strength to Crack Configuration Factor: the Normalized Strength Predicted by the Model is Plotted against the Configuration Factor, Which Depends on Crack Configuration and Internal Friction

3.7 Summary and Corollary

The failure mechanism of brittle materials under uniaxial compression has been examined at the fundamental level. A failure model based on the internal mechanism has been proposed to reveal the characteristics of the compressive strength, and stress-strain relation of these materials. The observed splitting failure has been shown to be the result of the cumulative, subcritical, stable crack growth. The underlying concepts of the model have been justified by reported observations.

It may be further inferred from the study that the failure stress, or the so-called compressive strength of a brittle material is closely dependent on the internal failure mechanism. The internal mechanism, however, depends not only on the material texture, but is also affected by the testing or loading conditions. Splitting failure corresponds to the lowest failure stress. Any conditions which prevent this failure mode from being realized will lead to an apparently higher failure stress. These conditions may be lateral confinement such as that introduced by the end friction, or a strain gradient which causes unequal compression in the material.

Although the compressive strength as a function of these conditions is difficult to determine, one may expect the failure stresses to be better correlated if the internal failure mechanisms are similar. This is of practical significance. In the later chapters, separate treatments for concrete masonry under different loading conditions will be proposed and it will be seen that this leads to better correlations in terms of the failure stresses.

CHAPTER IV

PLAIN MASONRY WITH FULL BEDDING

4.1 Two Basically Different Failure Modes

In concrete masonry compression tests, the specimens fail basically in two modes. One is splitting in the direction of the load; the other shows conical failure planes (see Chapter II). The significance of these two different mechanisms arises from the fact that the different failure modes yield different apparent strengths, as indicated in the preceding chapter.

It has been found repeatedly in previous experimental studies (for example, Fattal and Cattaneo 1976; Turkstra and Thomas 1978) that when the eccentricity of the load on masonry specimens is increased, there is a significant apparent increase in compressive strength. This phenomenon is also revealed in the tests conducted by the author, as depicted in Fig. 4.1 by comparing a theoretical load-moment interaction curve for a masonry prism with experimental results. Although this strength increase was attributed in some earlier studies (Turkstra and Thomas 1978) to the stress gradient effect, it is now generally accepted that it is essentially due to a difference in the failure mechanism.

When masonry is under uniaxial compression, splitting failure dominates, whether the masonry is fully or face-shell bedded. The failure mode changes to the shear type when the masonry is under eccentric loading.

Two obvious questions arise: 1) what is the cause of these two different failure mechanisms? 2) what is the implication of these failure mechanisms for the compressive strength, the parameter of most practical concern.

In this study, the failure mechanism is carefully re-examined, and some of the existing theory is revised, in the light of both experimental and analytical work. We start with the case of fully bedded plain concrete masonry under uniaxial compression.

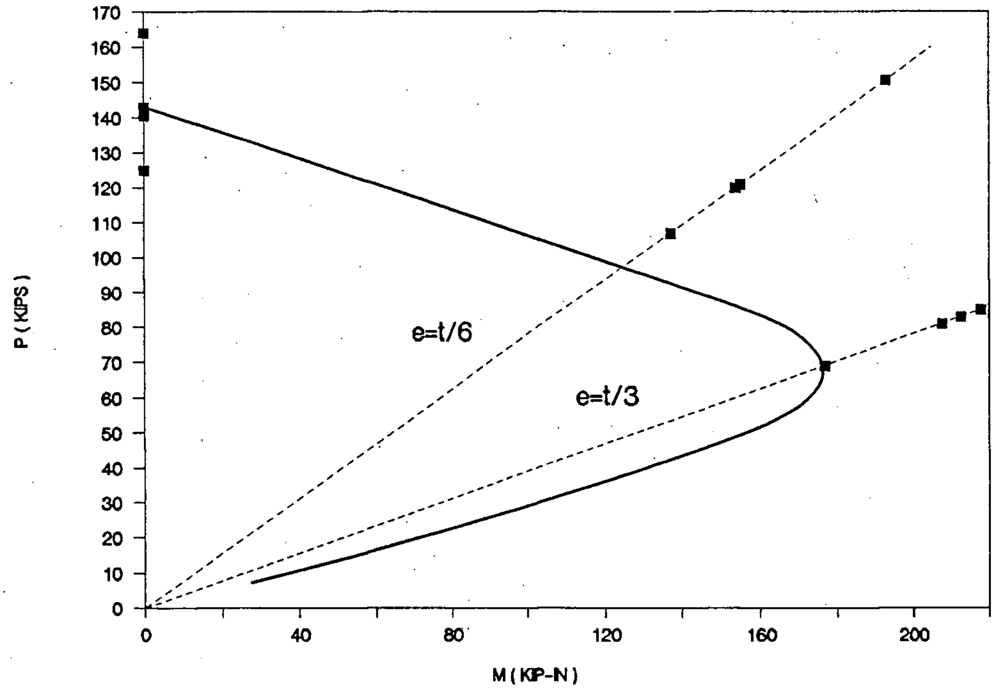

FIG. 4.1 Apparent Strength Increase Phenomenon under Eccentric Compression

Splitting failure under uniaxial compression has been indicated by numerous previous experiments, and the experiments conducted by the author have also revealed this phenomenon (see Fig. 2.12).

Under uniaxial compression, the only apparent disturbance in the uniaxial compression field is the joint. We shall discuss the effect of the joint on the strength of masonry, and consider whether the presence of the joint is the cause of the splitting failure.

4.2 Joint Effect— A Revision of Hilsdorf's Model

The main function of mortar joints is to provide structural continuity, wind and water tightness, as well as architectural effect. The joints can be in various patterns, such as running bond or stack bond, and they can be raked or flush. However, for reasons of simplicity, the study in this chapter is confined to stack bonded, fully bedded masonry with unraked joints. It is believed that the bond pattern does not have a significant effect on masonry strength (Maurenbrecher 1980; Shrive 1982), and that the analysis to be presented is generally applicable.

To achieve cohesiveness and workability, mortar contains certain proportions of cement, sand and lime. Mechanically, it is usually weaker and less stiff than the surrounding concrete units (see Chapter II).

It is widely accepted that the mortar joints affect the masonry strength, stronger mortar making stronger masonry. The most influential theory for the joint effect was proposed by Hilsdorf (1969). His theory postulates that when masonry prisms are under uniaxial compression, the less stiff mortar has a tendency to expand laterally; this lateral expansion of the mortar is confined by the masonry units, giving rise to lateral compressive stress in the mortar and to lateral tensile stresses in the units, thereby causing tensile splitting failure of the blocks. Using the Coulomb-Navier failure criterion and some rather coarse assumptions about equilibrium and compatibility, Hilsdorf derived an equation relating the compressive strength of masonry to the strengths of unit and mortar. This, of course, is very practical, since the strengths of the unit and the mortar are comparatively easy to measure.

However, there has been a lot of controversy about the correctness of Hilsdorf's model in the subsequent literature. On the one hand, Hatzinikolas et al (1978) made a numerical analysis based on Hilsdorf's model and concluded that the magnitude of the tensile stress in the block units due to the lateral expansion of the mortar was sufficient to exceed the tensile strength of concrete blocks and thus was responsible for the splitting failure of concrete masonry. Priestley et al (1983) extended Hilsdorf's equation to grouted concrete masonry and claimed good agreement (in terms of masonry strength) with the existing experimental data. Most recently, Biolzi (1988) applied the failure model in an approximate plastic analysis for brick masonry. On the other hand, Shrive (1980, 1983) strongly opposed the notion that the lateral expansion of mortar was the main cause of splitting failure. He noted that 1) splitting failure of compression specimens is not unique to masonry. 2) the tensile stress caused by mortar expansion in the block is too small to exceed the tensile strength of the block. The latter conclusion was based on the numerical analyses of Smith et al (1971), Turkstra et al (1978), Hamid (1978) and of Shrive himself with Jessop (1980), which indicate that the tensile stress is much less than that required to break the tensile bonds in the block. Drysdale and Hamid (1979) suggested that the mechanism of the lateral expansion of mortar needed reconsideration because in their experiments the mortar joints had a relatively minor influence on the capacity of concrete masonry.

The emergence of these controversies is not surprising, since some points were not clarified in the previous studies. When postulating a tensile stress which will initiate a crack, it is important to indicate the location where it will occur. This provides a logical way to check the correctness of the model by examining whether the location is correctly predicted in experimental studies. This was somehow overlooked in the previous work. The arbitrariness involved in the assumption of the material constants used in numerical analyses may also have contributed to the controversial nature of some previous findings. And so far, there has been no direct experimental evidence which could lead to a conclusive assessment of the model. Because of that, some experimental and analytical work is directed here to evaluation of this theory.

It should be indicated that all the previous work implicitly takes one notion for granted: that failure is a localized effect. Whether masonry fails depends on whether tensile stress at some point exceeds the tensile bonds of the material. In the light of the study in Chapter III, we know that in the case of compression, local tensile cracking is only a necessary condition for global failure; it may not be sufficient. In our approach, we will consider both the causes of tensile cracking, and whether this is tantamount to failure.

4.2.1 Experimental Results

The experimental results indicate:

1) for all fully bedded plain concrete masonry prisms tested under uniaxial compression, vertical splitting (parallel to the direction of loading) was the predominant failure mode. The splitting occurs in the middle third of the web, continuously runs through the specimen, as typically illustrated in Fig. 2.12. Similar observations were reported in previous experimental work (for example, Hatzinikolas et al 1978).

2) There is a lateral expansion effect due to the mortar, as evidenced by the strain measurements on the block units. Fig 4.2 shows some typical results recorded in experiments. The average lateral strain at location #3, which is closer to the mortar joint, is appreciably larger than that measured at location #4, which is at the mid-height of the web.

3) However, there is some randomness in where the macrocrack is initiated. By detecting the order of breaking of the wires crossing splits (A detailed description of this procedure was given in Chapter II), cracks were found to initiate at a location close to the mortar joint only in about two thirds of the fully bedded specimens, as depicted in Fig. 4.3. This does not support Hilsdorf's model, since the model suggests that crack should initiate consistently from the joint. If we assume that a crack which initiated from this location is a random event and relax Hilsdorf's hypothesis such that there is only a 90% chance of this event occurring, then this hypothesis is rejected at a 0.1 level of significance. We also note the test result is in sharp contrast to that observed in face-shell bedded plain concrete masonry, where cracks initiated consistently at a location close to the joint. (cf. Fig. 5.2) This strengthens the assertion that the test result does not support Hilsdorf's postulation that the splitting is due to the lateral expansion of the mortar joint.

4) The joint conditions have a big influence on the capacity of a masonry prism (see Table 4.1). It is noted that stronger mortar does not necessarily make a stronger prism, as indicated by comparing the failure loads of the prisms with type S mortar with those with type M mortar. The lower failure loads of the prisms with type M mortar are believed to be due to the poorer adhesion of that type of mortar, which appeared during the experiments. The effect of the

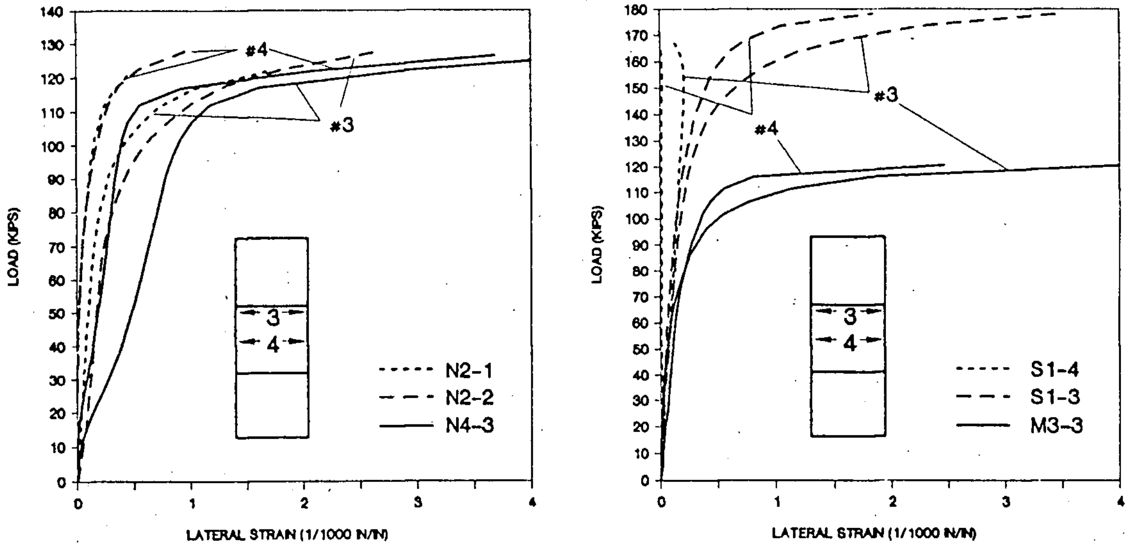

FIG. 4.2 Measured Lateral Strains in Webs of Middle Courses of Plain Masonry Prism under Uniaxial Compression

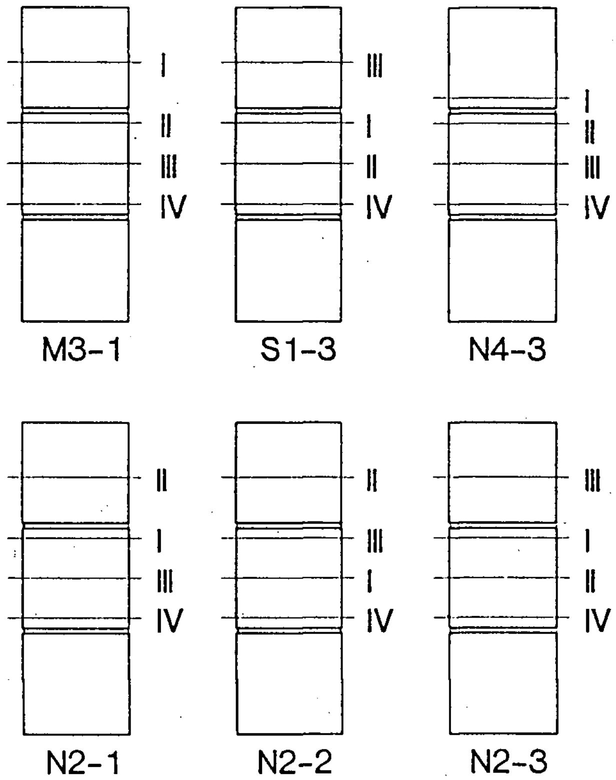

FIG. 4.3 Detected Orders of Macroscopic Splitting, in Terms of 4 Sections along Prisms.

SPECIMEN	1	2	3	4	AVG	COV
M3 (M−MORTAR)	187.0	147.0	123.0	140.0	149.0	15.7%
S1 (S−MORTAR)	204.0	194.0	178.0	168.0	186.0	7.5%
N2 (N−MORTAR)	125.0	140.5	143.0	164.0	143.0	9.7%
N4 (t_o = 3/4in)	120.0	105.0	133.0		119.0	9.6%
P5 (t_o = 0 in)	103.0	123.0	112.0	103.0	110.0	7.5%

Table 4.1 Failure Loads of Plain Prisms with Full Bedding (kips)

adhesion on masonry strength will be discussed later.

5) Vertical strain measurements indicate that the mortar joints are much softer than the concrete units. The ratio of the initial modulus of concrete to that of three mortar types is about 6-8 to 1. (See Figs. 2.3, 2.4 and 2.5 in Chapter II.)

To study joint effects, some of the prisms were built with zero joint thickness, and one group with glass plate. The glass was chosen because of its high modulus of elasticity and relatively low rupture strength (E=8×10^{6}psi, f'_{rup} = 5000 psi, obtained by experiment). It was expected that the glass plate filled joints would minimize the Poisson's effect and at the same time provide little lateral confinement. However, these specimens without mortar bedded joints failed at relatively low loads (see Tables 4.1, and 8.1 for grouted prisms); the experiments were not conclusive. The low failure loads are believed to have been caused by stress concentrations in the vicinity of the joints without a mortar cushion. The indications are that vertical cracks occurred during the loading stage of these prisms; and for the specimens with glass plates, the cracking noise of the glass was also heard.

4.2.2 Theoretical Analysis

We proceed now to revise Hilsdorf's model in the light of a stress analysis. Although numerous stress analyses (mentioned above) including some based on 3 dimensional modeling (Hamid and Chukwunenye, 1986) of this problem have been conducted, they were all based on numerical approaches. To gain some direct insight into the problem, we derive some analytical solutions based on plane elasticity for the configuration of a mortar joint being sandwiched between concrete block units.

Consider the case shown in Fig. 4.4(a), which depicts a view of either web face or face-shell face (joint length a may be either equal to web width or face-shell width). The mortar joint, being much softer than the concrete block, as indicated by experimental observation, may be considered as squeezed by two rigid platens, and by the principle of superposition, the loading situation may be decomposed as shown in Fig. 4.4(b) and (c). It is case (c) which will cause interface shear between the mortar and the masonry unit and hence cause tensile stress in the unit. By symmetry, we only need to consider half of the joint, as shown in Fig. 4.5

Since the joint is bounded by two rigid platens, the lateral strains due to the traction must be localized at its ends. Thus the vertical displacements v in the middle region of the joint, which are mainly caused by to Poisson's effect, will be small (recall we are considering case c) alone here). Further, since a is much larger than t_o, the variation of the vertical displacements with x must also be small. Therefore we assume

$$v \approx 0 \qquad \text{throughout the region}$$

$$u = u(x,y)$$

Assuming that the mortar joint in the plane of the cross-web or the face-shell is in a state of plane stress, Lame's equations (solving the problem in terms of displacements, Xu 1979) reduce to

$$\frac{\partial^2 u}{\partial x^2} + \frac{1-\nu}{2}\frac{\partial^2 u}{\partial y^2} = 0 \qquad \begin{array}{l} 0 < x < a/2 \\ 0 < y < t_o \end{array} \qquad 4.1$$

with boundary conditions

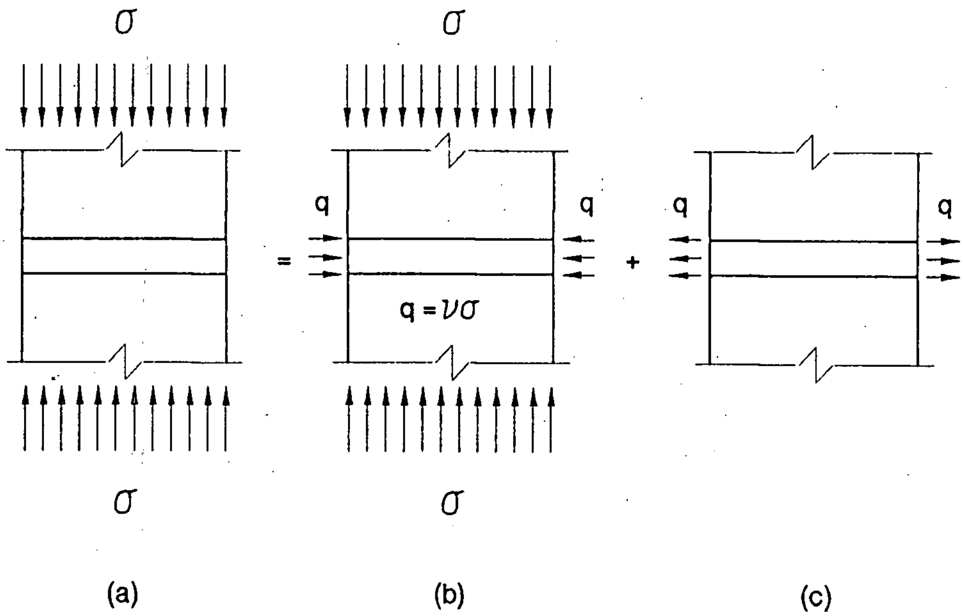

FIG. 4.4 A Mortar Joint Sandwiched by Block Units: a) under Axial Compression; b) under Biaxial Compression c) under Lateral Traction.

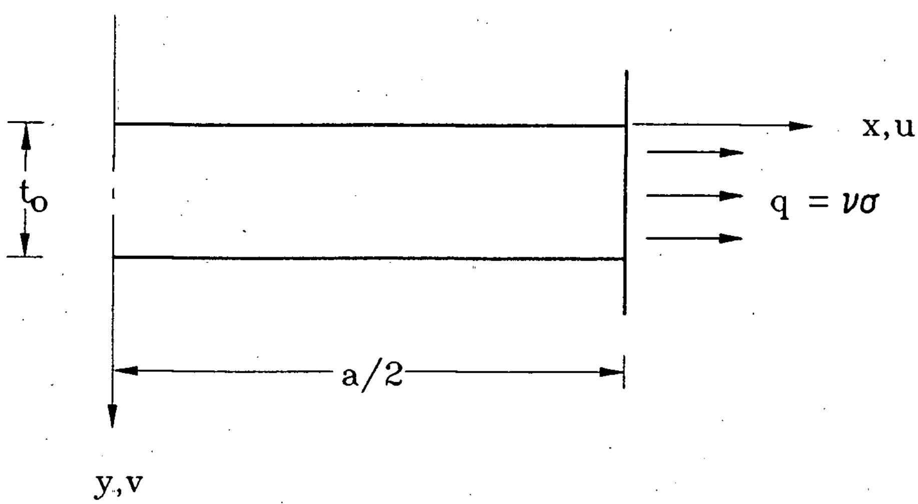

FIG 4.5 A Mortar Joint under Lateral Traction

$$u(0,y) = 0 \qquad 0 \le y \le t_o \quad \text{(by symmetry)} \qquad 4.2$$

$$u(x,0) = 0 \qquad 0 \le x \le a/2 \qquad 4.3$$

$$u(x,t_o) = 0 \qquad 0 \le x \le a/2 \qquad 4.4$$

$$\frac{E}{1-\nu^2}\, u_x\,(a/2,y) = q \qquad 0 \le y \le t_o \qquad 4.5$$

where E is Young's modulus and ν is Poisson's ratio.

A series solution for this boundary value problem can be found (see appendix)

$$u(x,y) = \frac{4(1-\nu^2)qt_o}{\pi^2\kappa E}\sum_{n=1}^{\infty}\frac{\sinh[(2n-1)\kappa\pi x/t_o]\,\sin[(2n-1)\pi y/t_o]}{(2n-1)^2\cosh[(2n-1)\kappa\pi a/2t_o]} \qquad 4.6$$

where $\kappa = \sqrt{(1-\nu)/2}$

From which we deduce the shear stress along the joint

$$\tau_{xy} = \frac{E}{2(1+\nu)}\, u_y(\,x,\,0\,)$$

$$= \frac{4\kappa q}{\pi}\sum_{n=1}^{\infty}\frac{\sinh[(2n-1)\kappa\pi x/t_o]}{(2n-1)\cosh[(2n-1)\kappa\pi a/2t_o]} \qquad 4.7$$

with the resultant force

$$S = \int_0^{a/2}\tau_{xy}\ dx = \frac{4qt_o}{\pi^2}\sum_{n=1}^{\infty}\frac{1}{(2n-1)^2}\left[1-\frac{1}{\cosh[(2n-1)\kappa\pi a/2t_o]}\right] \qquad 4.8$$

Since $a \gg t_o$, $\cosh[(2n-1)\kappa\pi a/2t_o] \gg 1$, the second term in the bracket of Eq. 4.8, which represents the vanishingly small force transferred by the middle of the joint, can be neglected. Further, by noting that $q = \nu\sigma$ and

$$\sum_{n=1}^{\infty} \frac{1}{(2n\text{-}1)^2} = \frac{\pi^2}{8}$$

we obtain

$$S = \frac{\nu \sigma t_o}{2} \tag{4.9}$$

The point of action of this resultant is

$$x_s = \frac{\int_0^{a/2} x\, \tau_{xy}\, dx}{S}$$

$$= \frac{8}{\pi^2} \sum_{n=1}^{\infty} \left[\frac{a}{2(2n\text{-}1)^2} - \frac{t_o}{\kappa\pi(2n\text{-}1)^3} \right] > \frac{a}{2} - \frac{t_o}{\kappa\pi} \tag{4.10}$$

which lies near the end of the joint.

By inspecting Eqs. 4.7 and 4.10, it is concluded that the interface shear must be highly concentrated near two ends of the joint. It is also clear in view of Eq. 4.9, that this shear is directly proportional to the applied compressive stress, the thickness and the Poisson's ratio of the mortar joint. It is these shear forces acting like lateral point loads which introduce the tensile stresses in the web and face-shell.

Eq. 4.7 is compared with a numerical solution using the boundary element method. The computer program (TWOFS) is given by Crouch et al (1983), and 67 elements were used for this problem. For ν=0.3 and t_o/a=3/64, the solutions are plotted in Fig. 4.6, together with a depiction of how these shears act on a web. The analytical solution is in good agreement with the numerical one, which supports the assumption that the vertical displacement can be neglected.

We proceed to perform stress analysis for a web or a face-shell under the action of these shear forces. As shown in Fig. 4.7, this is a plane problem in a rectangular domain with stress specified boundary conditions. The shear distributions on the boundaries are given by Eq. 4.7.

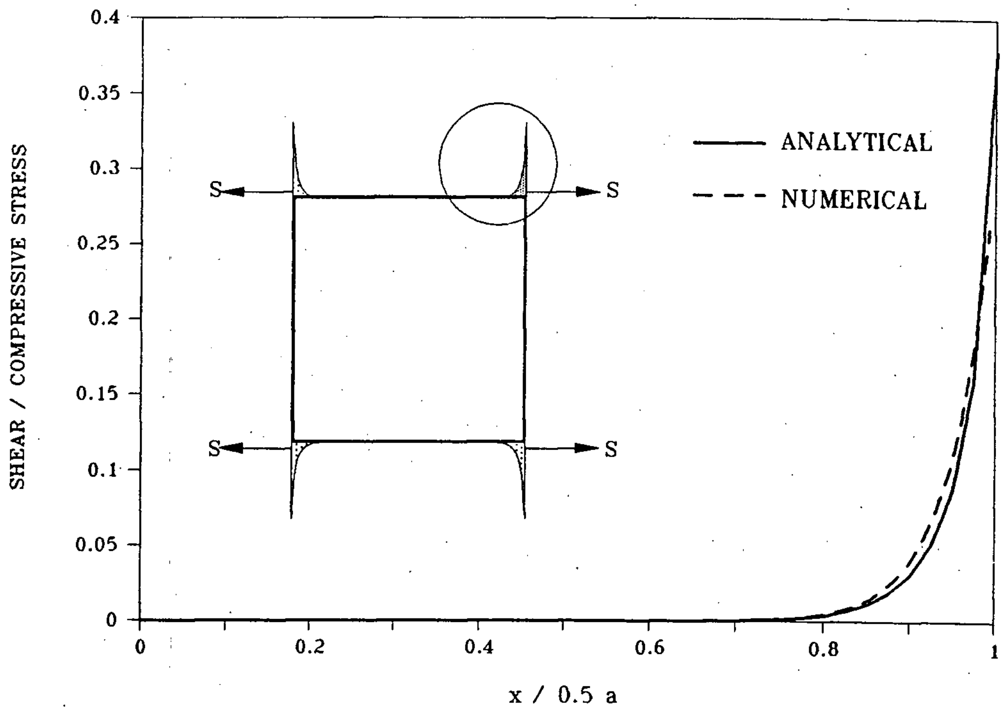

FIG 4.6 Lateral Interface Shear Distribution between Mortar Joint and Block Units.

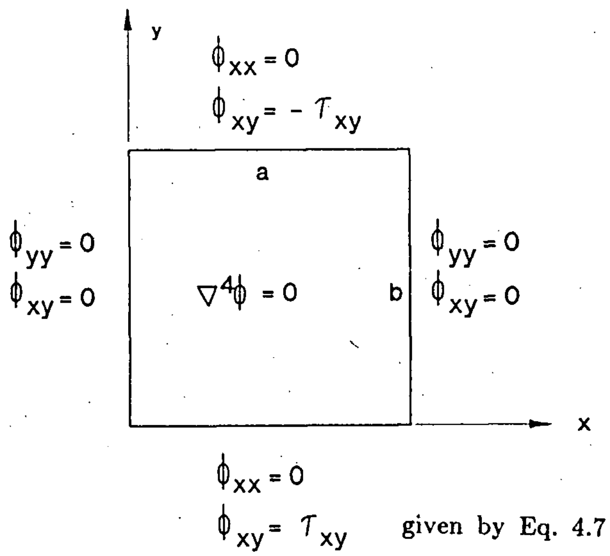

FIG 4.7 Depiction of Boundary Conditions of a Web (or Face-Shell)

under Action of Interface Shears.

The common approach for this kind of problem is to find a stress function (Airy stress function). For this particular case we can write the stress function in a series form as

$$\Phi = \sum_{m=1}^{\infty} A_m \left(\frac{m\pi(y\text{-}b/2)}{a} \sinh \frac{m\pi(y\text{-}b/2)}{a} - \alpha_m \tanh\alpha_m \cosh \frac{m\pi(y\text{-}b/2)}{a} \right) \sin\frac{m\pi x}{a}$$

$$+ B_m \left(\frac{m\pi(x\text{-}a/2)}{b} \sinh \frac{m\pi(x\text{-}a/2)}{b} - \beta_m \tanh\beta_m \cosh \frac{m\pi(x\text{-}a/2)}{b} \right) \sin\frac{m\pi y}{b} \qquad 4.11$$

where $\alpha_m = \frac{m\pi b}{2a}$, $\beta_m = \frac{m\pi a}{2b}$, and A_m, B_m are determined by having Eq. 4.11 satisfy the boundary conditions depicted in Fig. 4.7 (for detailed derivation see appendix). By inspection, the maximum tensile stress will occur at the top and bottom boundaries of the domain. So finally, the tensile stress distribution we are interested in is

$$\begin{aligned} \sigma_x &= \Phi_{yy} \\ &= 2 \sum_{m=1}^{\infty} A_m \left(\frac{m\pi}{a}\right)^2 \cosh\alpha_m \sin\frac{m\pi x}{a} \qquad 4.12 \end{aligned}$$

For a square domain, as in the geometry of the web, the series solution is plotted in Fig. 4.8, together with a numerical solution. A numerical solution for the more realistic case of $(\nu_j/E_j)/(\nu_u/E_u)=9$, where subscripts j and u denote mortar joint and block unit respectively, is also included in the graph. The changes of this distribution due to variations in Poisson's ratio and the thickness of the joint, the aspect ratio of the rectangular domain (corresponding to a web and a face-shell) are plotted in Fig. 4.9, Fig. 4.10 and Fig. 4.11 respectively.

The above stress analysis clearly indicates that the tensile stress reaches its <u>maximum</u> at a location close to the two ends of the top or bottom edge of the domain and a <u>minimum</u> in the middle of the edge; changing the parameters in the stress analysis does not alter the basic features of this stress distribution. This is not surprising in view of the point load like shear

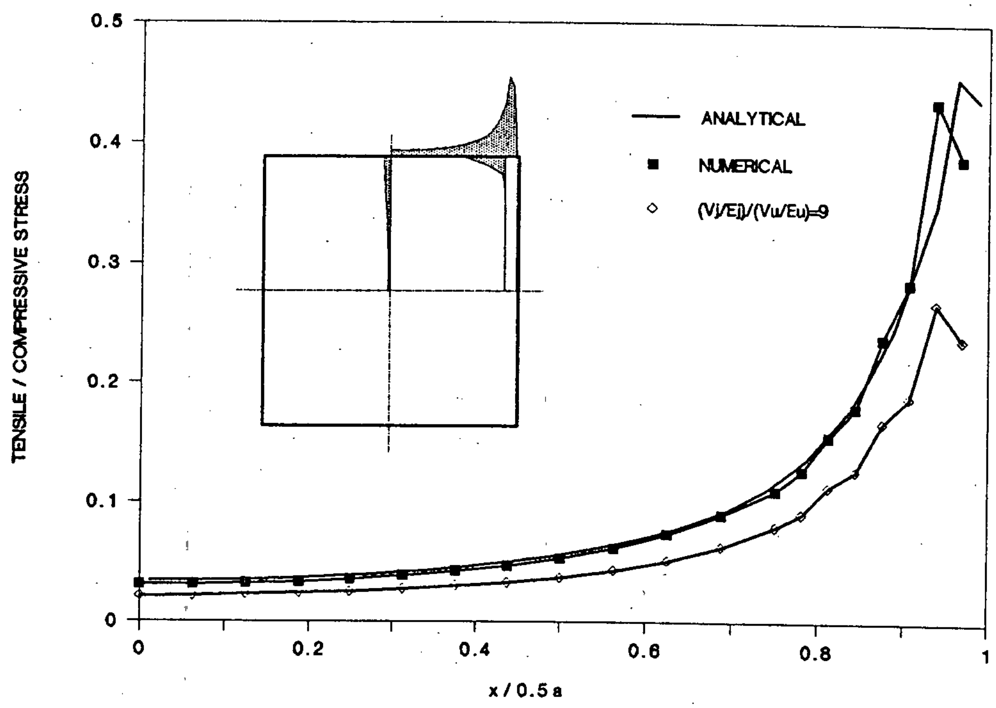

FIG 4.8 Lateral Tensile Stress along Top of Block Introduced by the lateral Shears

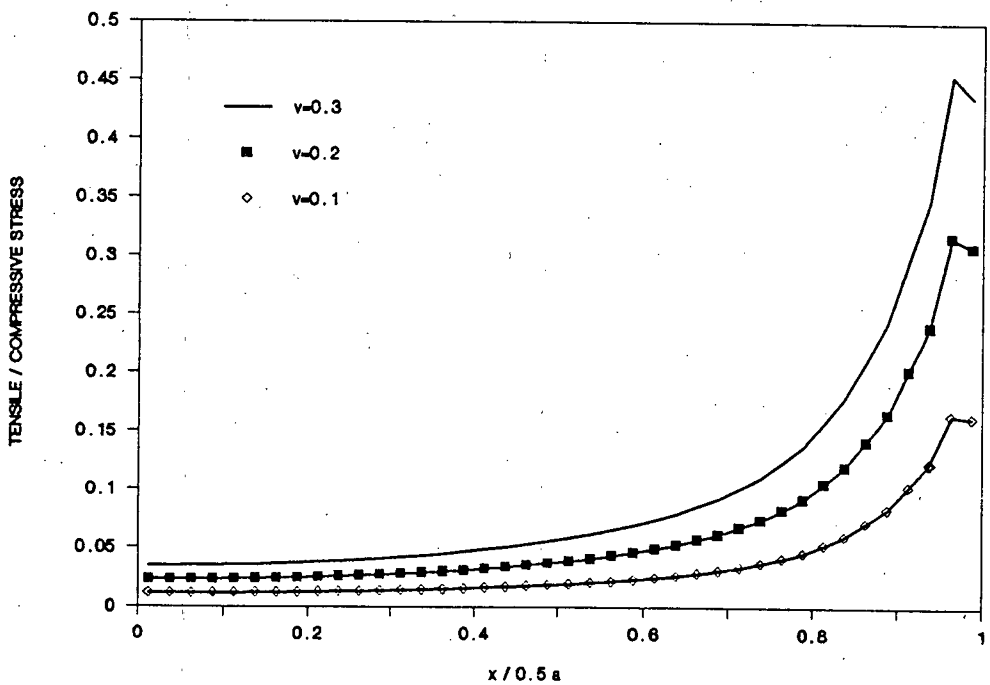

FIG 4.9 Lateral Tensile Stress along Top of Block, with Variation in Poisson's Ratio of Joint

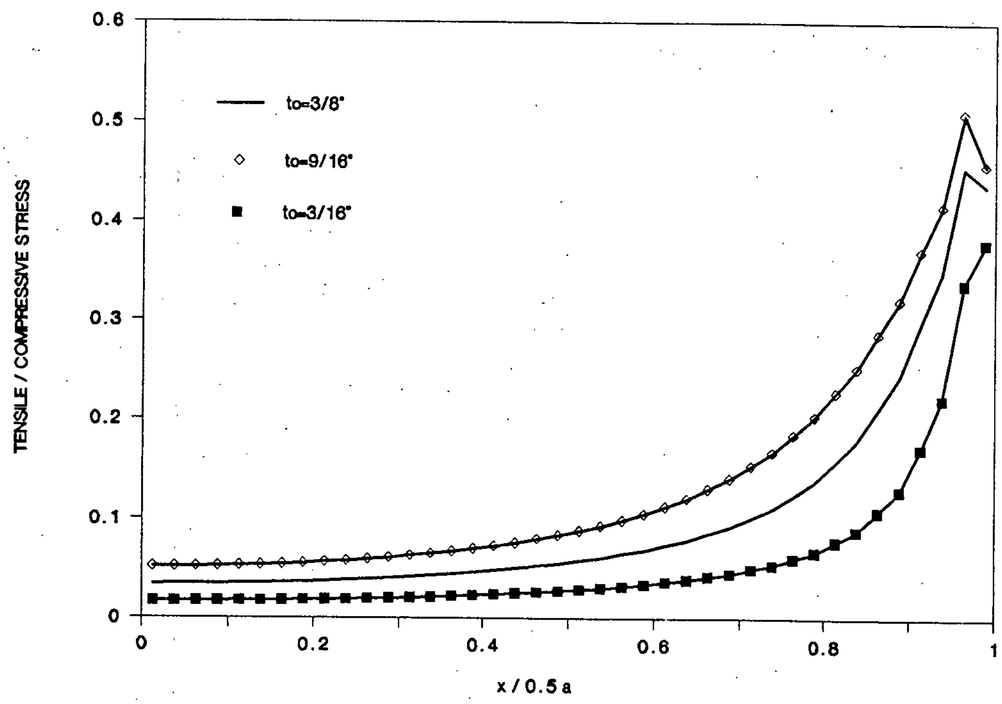

FIG 4.10 Lateral Tensile Stress along Top of Block, with Variation in Joint Thichness

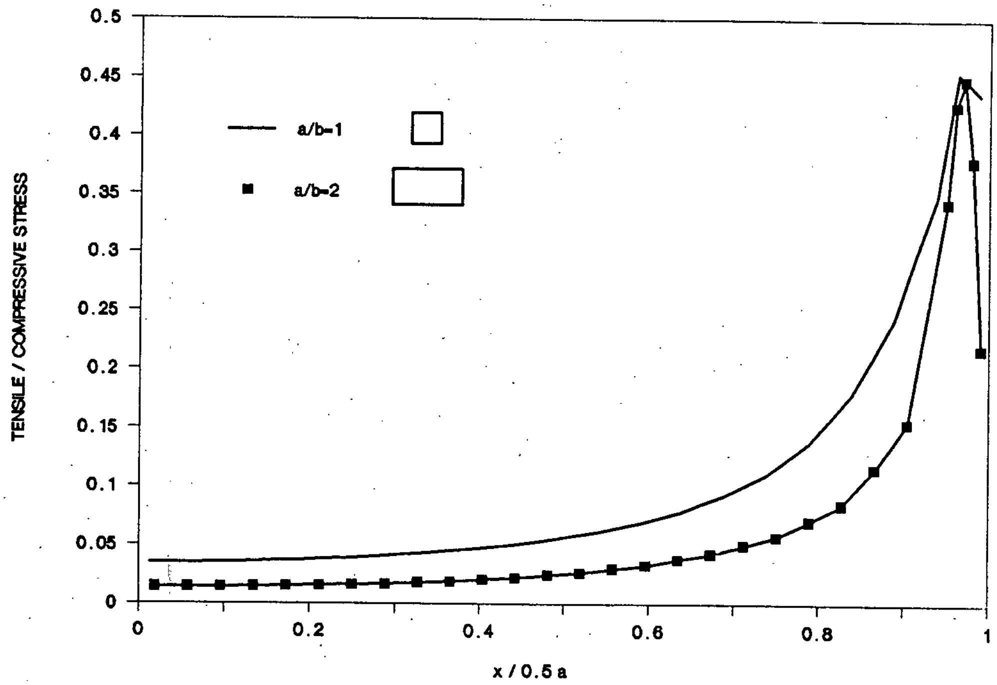

FIG 4.11 Lateral Tensile Stress along Top of Block, with Variation in Domain Aspect Ratio

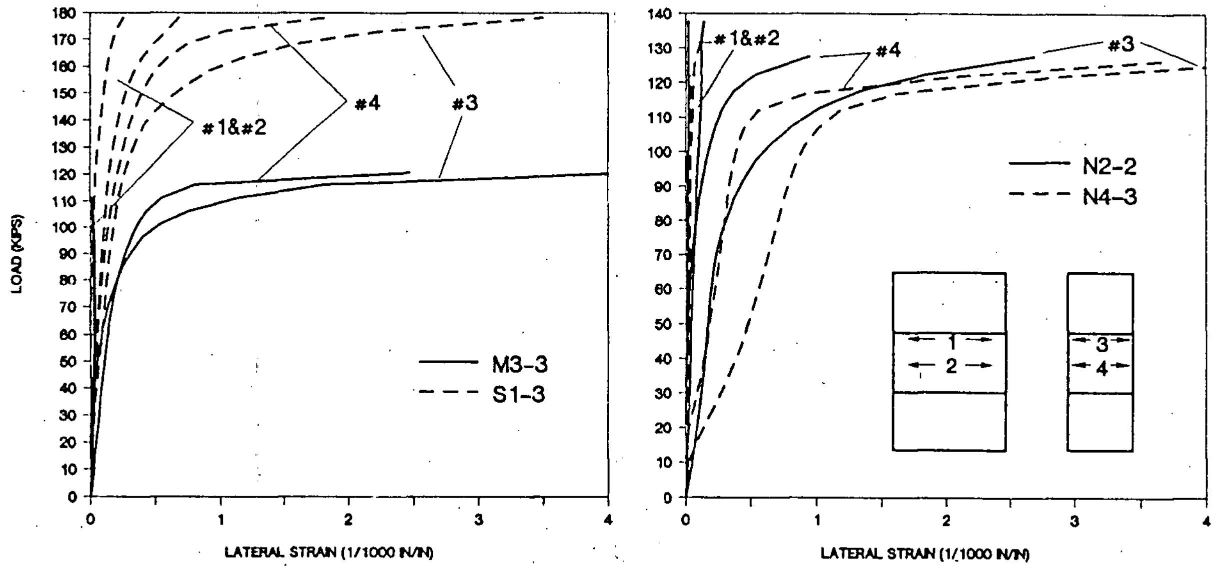

FIG 4.12 Lateral Strains Measured along webs and Face-shells of

Plain Prisms under Uniaxial Compression

distribution specified by Eq. 4.7. And it is consistent with the experimental observation that the strains parallel to the joint were higher at the ends than in the middle of the joint, as indicated by gauges in these locations. Fig. 4.12 gives the typical results of this measurement. No appreciable strain was measured at location #1 or at location #2, which are in the middle of a face-shell and does not cover two ends of the joint. This is in contrast to those measured in locations #3 and #4, which cross the whole length of the web. In other words, the tensile strain is highly concentrated near two ends of the joint where tensile stress reaches maximum.

4.2.3 Conclusion on Hilsdorf's Model

Based on above study, the conclusion is obvious, that splitting in masonry can not be simply attributed to the lateral expansion of the mortar. First, if lateral expansion of the mortar were the main cause of the splitting, it would occur somewhere near two edges of a web or a face-shell where the tensile stress reaches its maximum. (see Fig. 4.8 – Fig. 4.11) If the thickness changes of the face-shell and the web in the fillets near the corner of a unit are taken into account, one may conclude that splitting would occur somewhere near the web — face-shell joint, a conclusion which is not supported by experimental observation. Second, the interface shear, which is responsible for the tensile stresses in the web and the face-shell, is a monotonically increasing function of the mortar joint length a, as clearly indicated by Eq. 4.8. Thus the shear forces along the face-shell are not less than those along the web. If mortar expansion were the main cause for the splitting of a masonry prism, the splitting would be more likely to occur or at least have an equal probability of occurring, in the face-shell, a conclusion which contradicts the experimental observations. Third, the experimental monitoring of crack initiation, as we have shown earlier, indicates that the lateral expansion of the mortar being the cause of the splitting mechanism is not acceptable. These points alone are sufficient to rule out the correctness of Hilsdorf's model, since even the necessary conditions for failure can not be justified by his model.

Moreover, rigorously speaking, the underlying concepts of Hilsdorf's model may be misleading. As indicated at the beginning, it is not sufficient to focus on a local tensile event in the case of compression. Even if the vertical splitting were initiated by joint expansion, for this to lead to direct catastrophic failure of the masonry needs further justification. From a fracture mechanics point of view, the energy required to open this crack would come from the strain energy released in the mortar joint, as a result of partial relaxation of the lateral confining stress. It can be shown that the amount of this energy is limited, so that the crack would stabilize. Even if we assume this crack could run through a masonry block, the latter would still not lose vertical load transfer ability; it would have failed only in the sense of the serviceability condition.

Certainly, the above stress analysis may be subject to some limitations because it is based on two-dimensional elasticity, which does not take account of the material nonlinearity or of the complete specific geometry of the concrete block. Nevertheless, this does not detract from the useful conclusions deduced from the above study. Nor would nonlinear behaviour in the joint itself change the essential feature of the stress distribution; it would only cause limited shifting in the locations where maximum tensile stress occurs.

4.3 Some Comments on Splitting Failure and Mode Transition Phenomena

It is clear that the splitting failure of masonry cannot be attributed to the lateral expansion of the mortar joint alone; rather, it is inherent in the failure of the material as we explained in Chapter III.

Although it is difficult at this stage to explain fully the splitting failure for the specific geometry of masonry, or the transition to the shear mode with an increase of loading eccentricity, certain hypotheses may be made in the light of the concepts illustrated in Chapter III.

a) The main splitting probably develops in the web rather than the face-shell because this leads to the weakest structure.

b) Under eccentric loading, vertical crack surfaces tend to be forced into contact by the transfer of shear from the loaded to the unloaded side. This contacting may in turn increase the friction across the crack, which may prevent splitting failure from occurring.

c) Because two different failure mechanisms are involved, the apparent strengths will be different, and a one parameter failure criterion will not be satisfactory.

4.4 Joint Effect on Axial Capacity

It has been demonstrated that a plain mortar joint is not the governing factor for the failure pattern of concrete masonry. Hilsdorf's model is not appropriate for assessing the effect of the joints on masonry strength.

Available experimental results on the joint effect, including the tests done by the author, appear to be scattered. A possible way to assess this effect would be to compare tests on prisms with mortar joints and with dry joints—— not a very practical approach. The masonry unit strength is not a good reference, since under standard testing conditions, it will exhibit a conical failure mechanism as a result of the end friction, with a substantially higher apparent strength. Because of these difficulties, in most experimental work, the joint effect has been examined by varying the joint conditions.

Some experimental observations may be worth reviewing.

a) Usually the compressive strength of unit is higher than that of prism, which is in turn higher than that of mortar. However, although the mortar strength is lower than the prism strength (calculated on the mortared area), joint failure has never been observed. It should be noted that, when talking about mortar strength, we implicitly assume the unconfined compressive strength. The strength obtained by the standard cube test is actually partly confined since its height to width ratio is small. Experiments by Hatzinikolas et al (1978) have shown that the unconfined strength can be as low as 63% of the cube strength. The mortar in the joint could have even lower strength due to poorer curing conditions.

This observation is also revealed by the author's tests. The average unit strength f_u' is 3250 psi. For most prisms N type mortar was used, which has an average cube strength of 1570 psi. The average failure load of masonry prisms with this mortar is 143 kips, corresponding to an f_m' of about 2320 psi. (cf. Table 4.1) Although the exact correlation between the strength of the mortar cube and that of the mortar in the joint is unknown, and type M and S mortars appear to have very high cube strengths, it seems reasonable, to accept that $f_u' > f_m' > f_{ju}$, where f_{ju} denotes the unconfined mortar strength. For all the prisms tested, no joint failure was observed. This is also evidenced by the deformation measured across the joint (see Fig. 2.5 in Chapter II).

b) Both mortar type and joint thickness have an influence on the masonry strength, although there is still an uncertainty about the degree and nature of this influence. This is reflected in that the tests done by Drysdale and Hamid (1979) have shown the influence to be relatively minor, while in the author's tests the influence is significant (see Table 4.1 and Fig. 4.16); and although the available test data tend to indicate that stronger mortar makes stronger masonry, both experiments have indicated that this is not always true.

c) This influence becomes relatively minor with increase of loading eccentricity. (see Table 6.1 in Chapter VI)

d) Reinforcement by metal plates enhances both the capacity and ductility of masonry (Priestley and Elder 1982), while reinforcement by steel bars in the joint reduces the strength (Hatzinikolas 1978).

It can be conjectured that the mortar joint affects the strength of masonry basically in that the joint introduces discontinuities in the material properties, such as strength and stiffness. These discontinuities will complicate the stress distribution in the vicinity of the joint and thus affect the vertical load transfer ability.

It may be reasonable to assume that as long as the joint conditions do not provide lateral confinement to prevent splitting failure, as in the case of plate reinforcement (observation d), the joint will generally have a negative effect on the masonry strength in the presence of uniaxial compression. This is because the joint will generally alter the otherwise uniform compressive stress in its vicinity, and thus the force is effectively transferred by a smaller area. This can be illustrated by following analysis.

4.5 Stress in Joint Vicinity

As shown by the stress analysis in section 4.2.2, when masonry is under uniaxial compression, the less stiff mortar joint is subject to vertical compressive force as well as lateral interface shear. Although the problem was solved in a plane coinciding with webs or face-shells, the principle can be extended to the perpendicular plane representing the cross-section of webs or face-shells. Thus the mortar is actually confined bilaterally; and because of that, the apparent strength (the confined strength) is increased. This explains why joint failure is not observed in tests although $f'_m > f_{ju}$.

An indication of this confinement is found in the vertical deformation curves of mortar joints recorded in the tests, which reveal that the joints became stiffer with increase of load (cf. Fig. 2.5). As a consequence of this confinement, the otherwise uniform compressive stress distribution in the vicinity of the joint is changed.

Fig. 4.13 depicts a cross-sectional view of a mortar joint and a free body diagram of the joint. It is obvious that lateral confining stress results from the interface shear and that it reaches a maximum in the middle of the joint. As an estimation of the confining stress distribution, we use the simplified approach as presented in section 4.2.2. The problem approximates plane strain conditions, since the joint is almost fully confined in the direction along its length. Recalling the form of solution for the lateral displacement u as given in Eq. 4.6, we may write the confining stress as (referring to the cross-sectional plane shown in Fig. 4.13):

$$\sigma_l = q - \sigma_x = q - \frac{E'}{1\text{-}\mu^2}\frac{\partial u}{\partial x} \qquad \left(\begin{array}{c} \mu = \nu/1\text{-}\nu, \quad E'=E/1\text{-}\nu^2 \\ \text{for plane strain conditions} \end{array} \right)$$

$$= q\left(1 - \frac{4}{\pi} \sum_{n=1}^{\infty} \frac{\cosh[(2n\text{-}1)\kappa\pi x/t_o]\,\sin[(2n\text{-}1)\pi y/t_o]}{(2n\text{-}1)\,\cosh[(2n\text{-}1)\kappa\pi a_o/2t_o]} \right) \qquad 4.13$$

Taking the average of this stress over the joint thickness leads to

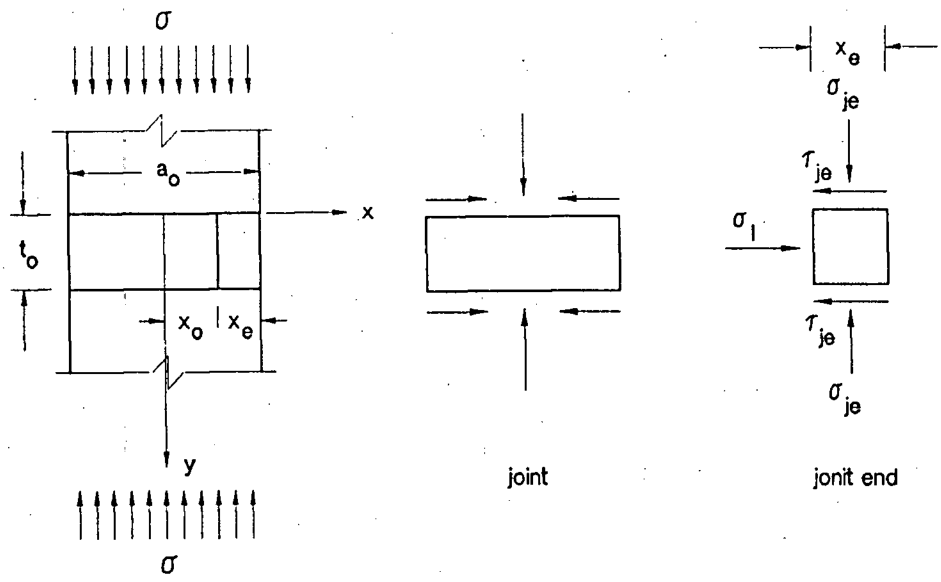

FIG 4.13 A Cross-Sectional View (along the Depth of Block Shells) of Mortar Joint

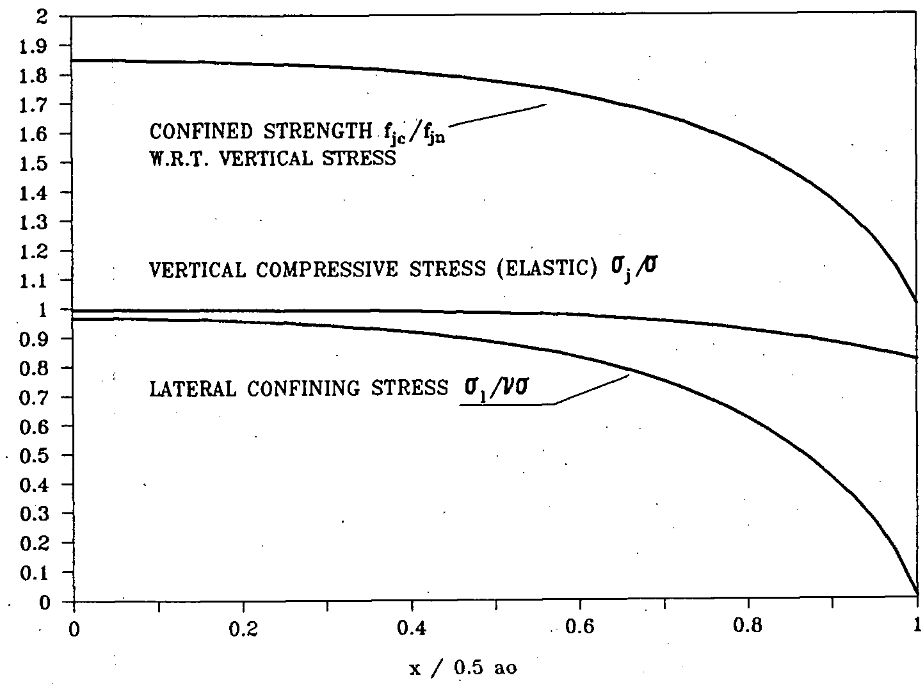

FIG 4.14 Compressive Stress, Lateral Confining Stress and Confined Strength in Mortar Joint

$$\sigma_l(x) = \frac{1}{t_o} \int_0^{t_o} \sigma_l\ (x,y)\ dy$$

$$= q\left(1 - \frac{8}{\pi^2} \sum_{n=1}^{\infty} \frac{\cosh[(2n\text{-}1)\kappa\pi x/t_o]}{(2n\text{-}1)^2 \cosh[(2n\text{-}1)\kappa\pi a_o/2t_o]}\right) \qquad 4.14$$

where t_o and a_o are the thickness and the width (the transverse dimension of the block face-shell or web) of a joint. To correspond to plane strain conditions, q and κ become

$$q = \frac{\sigma\nu}{1-\nu} \qquad 4.15$$

$$\kappa = \sqrt{\frac{1-2\nu}{2(1-\nu)}} \qquad 4.16$$

For $t/a_o \approx 1/4$, typical of the geometry of concrete masonry conditions, and $\nu = 0.3$, this confining stress distribution is plotted in Fig. 4.14. It is clear that the joint is not uniformly confined. Under this non-uniform confinement, the joint will develop a varying confined strength. Since the joint is more confined in the direction along its length, the increase in mortar compressive strength will mainly depend on the confining stress in the joint width direction (the x direction in Fig. 4.13). Thus, we may use the known empirical relation (Park and Pauley 1975)

$$f_{jc} = f_{ju} + 4.1\ \sigma_l \qquad 4.17$$

with $\sigma_l = \sigma_l(x)$ here. The confined compressive strength f_{jc} of the joint, based on the confining stress given by Eq. 4.14, is also plotted in Fig. 4.14. This may underestimate the strength somewhat in view of the full confinement along the length of the joint.

When the applied compressive stress is small compared to f_{ju}, the unconfined compressive strength of mortar, a good approximation for the compressive stress distribution in the joint will be given by the elastic case[1]:

$$\sigma_j \approx \sigma - \frac{\mu E'}{1-\mu^2}\frac{\partial u}{\partial x}$$

$$= \sigma\left(1 - \frac{8\mu^2}{\pi^2}\sum_{n=1}^{\infty}\frac{\cosh[(2n\text{-}1)\kappa\pi x/t_o]}{(2n\text{-}1)^2\cosh[(2n\text{-}1)\kappa\pi a_o/2t_o]}\right) \qquad 4.18$$

which departs slightly from uniform distribution, as plotted in Fig. 4.14.

When σ exceeds f_{ju}, the end part of the joint will "yield", because the confined strength of the end part is less than σ. The stress distribution in the joint is then dramatically complicated. The lateral confining stress given by Eq. 4.14 is no longer valid since the end parts of the joint have developed substantial nonlinearity. A precise stress analysis for the joint is difficult, but we shall give an approximate approach to this problem.

Because the inner part of the joint is more confined, it develops higher strength and therefore transfers more stress. Thus we may divide the joint into two parts with the dividing point x_o, within which the material remains elastic in the sense that it does not fail or develop substantial nonlinearity, as shown in Fig. 4.13. We assume, as is suggested by Fig. 4.14, that the compressive stress is approximately uniformly distributed within this range.

Since the end part is subjected to compressive stress as well as highly concentrated shear force and lateral confining force as indicated in the preceding stress analysis, it will fail under the combination of these forces. The known empirical failure curve of concrete under shear and compression, as shown in Fig. 4.15 (Park and pauley, 1975), may serve as a good approximation only for the very end of the joint, where the lateral confining stress is negligible.

In the presence of large lateral confining stress, we may modify the failure curve by assuming that it is characterized by the confined strength instead of the uniaxial compressive

[1]For equilibrium, the peak value would be slightly higher than the average stress σ given by Eq. 4.18.

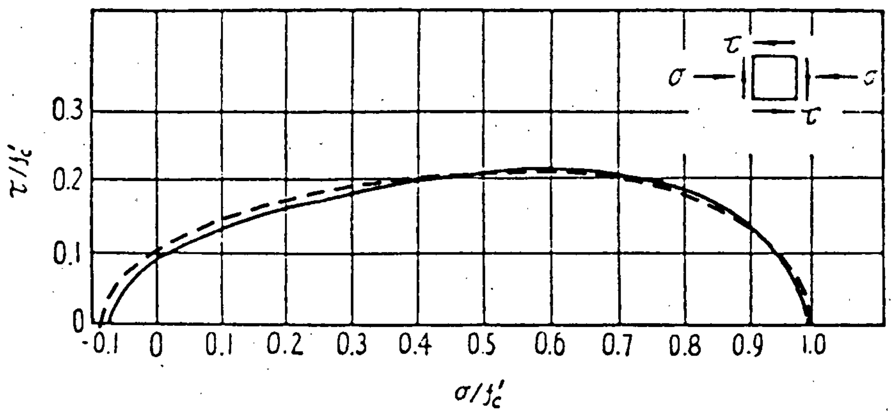

FIG. 4.15 Failure Curve of Concrete under Shear and Compression: Solid Line, after Park and Pauley (1975); Dashed Line, Fitted by Eq. 4.19

strength. This basically enlarges the failure curve in an absolute stress space. The left and right ends of this curve can be fitted by segments of two ellipses.

For ease of analysis, we further simplify the situation by considering only the average failing compressive and shear stresses in the joint. It may be useful to list here the notations that will be used in the following paragraphs: (see Fig. 4.13)

a_o = width of the joint

x_o = half width of the middle part of the joint

x_e = width of the end part of the joint

t_o = thickness of the joint

f_{ju} = unconfined strength of the mortar joint

f_{jc} = confined strength of the mortar joint in the centre part

f_{je} = confined strength of the mortar joint in the end part

σ = average compressive stress in entire joint

σ_l = lateral confining stress in joint

σ_{je} = average compressive failing stress in the end part

τ_{je} = average shear failing stress in the end part

Thus the failure criterion for the end part is

$$\left(\frac{\sigma_{je}/f_{je} - 0.6}{0.7} \right)^2 + \left(\frac{\tau_{je}}{0.22 f_{je}} \right)^2 = 1 \qquad 4.19a$$

for $\sigma_{je}/f_{je} < 0.6$. And for $\sigma_{je}/f_{je} \geq 0.6$

$$\left(\frac{\sigma_{je}/f_{je} - 0.6}{0.4} \right)^2 + \left(\frac{\tau_{je}}{0.22 f_{je}} \right)^2 = 1 \qquad 4.19b$$

f_{je} can be written

$$f_{je} = \frac{f_{ju} + f_{jc}(x_o)}{2} \qquad 4.20$$

We assume a loading path by noting the relation given by Eq. 4.9 and $S \approx x_e \tau_{je}$, from which it follows that, at failure

$$\tau_{je} = \frac{\mu t_o}{2 x_e} \sigma_{je} \qquad 4.21$$

Vertical equilibrium requires

$$\frac{\sigma a_o}{2} = x_o f_{jc}(x_o) + x_e \sigma_{je} \qquad 4.22$$

where f_{jc} is defined by

$$f_{jc} = f_{ju} + 4.1\ \sigma_l \qquad 4.23$$

and σ_l can be found by lateral equilibrium of the end part

$$\sigma_l\ t_o = 2\tau_{je}x_e \qquad 4.24$$

Eq. 4.19 to Eq. 4.24 together with the relation that $x_o + x_e = a_o/2$ can be used to find the 7 unknowns; namely, x_e, x_o, f_{jc}, σ_l, f_{je}, σ_{je} and τ_{je}.

As an example, we use this approach to examine the prisms with type N mortar. Recall that the cube strength of this type mortar is 1570 psi; we set it equal to f_{ju}. This may underestimate the distortion of the uniform stress, since the actual value for f_{ju} is even lower. At failure of the N type masonry, $\sigma = f_m' = 2320$ psi, then $f_{ju}/\sigma = 0.677$, leading to $x_o/(a_o/2) = 0.84$, $f_{jc}/\sigma = 1.15$, $\sigma_{je}/\sigma = 0.27$. i.e., about 16% of the joint (outer part) failed with an average failing stress 27% of the average stress σ. As a consequence, the outer part of the joint sheds forces to the inner part, leading to an increase in stress to 1.15 times σ in that part.

4.6 Capacity Estimation

The above study indicates that the mortar joints can alter the otherwise uniform compressive stress distribution considerably when masonry is under uniaxial compression. According to the approximation, at failure of the masonry with N type mortar tested by the author, about 97% of the compressive force is transferred through a strip with 84% of the width of the web or face-shell. This means that the compressive force is only transferred by part of the joints and the masonry units are actually not fully loaded, which will certainly have a negative effect on the strength of the masonry.

However, if one wishes to generalize the joint effect on masonry strength by correlating the mortar cube strength and the unit strength with the prism strength, as is often desired in practice, some uncertainties have to be recognized:

1) The correlation between mortar cube strength and the strength of the mortar placed in the joint.

2) The correlation between unit strength and the strength of "a prism with dry joints", a desired reference parameter.

3) Uncertainties in failure criteria of concrete.

4) Material properties such as those governing deformation and adhesion, which are often assumed but not measured. They are by no means unimportant to masonry strength.

Based on above analysis and arguments, we present here a semi-empirical approach. Since no better failure criterion is available, we assume that the masonry unit will fail when the average compressive stress in the middle part of the mortar joint, which will be higher than the average stress in the masonry, reaches some critical value; and this critical value may be linearly correlated to the masonry unit strength. Thus we may write the failure condition

$$f_{jc}(x_o) = k_1 f'_u \qquad 0 < k_1 < 1 \qquad 4.25$$

Further, we assume that the unconfined strength of the mortar placed in joints is proportional to the cube mortar strength

$$f_{ju} = k_2 f'_j \qquad 0 < k_2 < 1 \qquad 4.26$$

where f'_j denotes the cube mortar strength, and k_1 and k_2 are some assumed correlation factors.

At failure, equations from 4.19 to 4.24 are assumed to be satisfied. Thus the masonry strength, i.e. the average failure stress in masonry, is actually expressed in Eq. 4.22, from which we can write

$$\frac{f_m'}{f_u'} = k_1 \left(1 - \mu \frac{t_o}{a_o} \frac{\sigma_{je}}{\tau_{je}} \right) + \frac{t_o}{a_o} \frac{\sigma_{je}}{\tau_{je}} \; \frac{k_1 - k_2(f_j'/f_u')}{4.1} \qquad 4.27$$

where σ_{je} and τ_{je} can be explicitly expressed in terms of f_j' and f_u' in view of Eqs. 4.19 – 4.21, 4.23 and 4.24. For $k_1 = 0.95$, $k_2 = 0.75$, $t/a_o = 0.25$ and Poisson's ratio $\nu = 0.3$, Eq. 4.27 is plotted in Fig. 4.16 and compared with the experimental data. The value of the correlation factor k_2 is very close to the conversion factor between concrete cylinder strength and cube strength recommended by L'Hermite (Neville 1965). For the cube strength ranging from 2000 psi to 3000 psi, this factor is between 0.73 and 0.76. The model curve is essentially identical to a linear regression curve of the data, i.e.

$$\frac{f_m'}{f_u'} = 0.68 + 0.19 \frac{f_j'}{f_u'} \qquad 4.28$$

The four points on the right have been excluded from this analysis; they were type M mortar, and are believed to represent a different phenomenon — failure of the adhesion between block mortar.

The model also gives a reasonable correlation with the limited data on masonry capacity when the mortar joint is doubled (t=3/4 inch), as shown in Fig. 4.17.

The model may be used to estimate the masonry strength. However, as indicated before, some uncertainties need further investigation. One of them, is of course, the correlation between the cube mortar strength and the strength of mortar placed in the joint, since the curing conditions are so different. The other is the effect of the joint adhesion.

We may conclude from the above analysis that since the load transfer capability of mortar joints depends largely on the existence of the lateral confining stress, introduced basically by the interface shear between the joint and block unit, that the adhesion between joint and unit

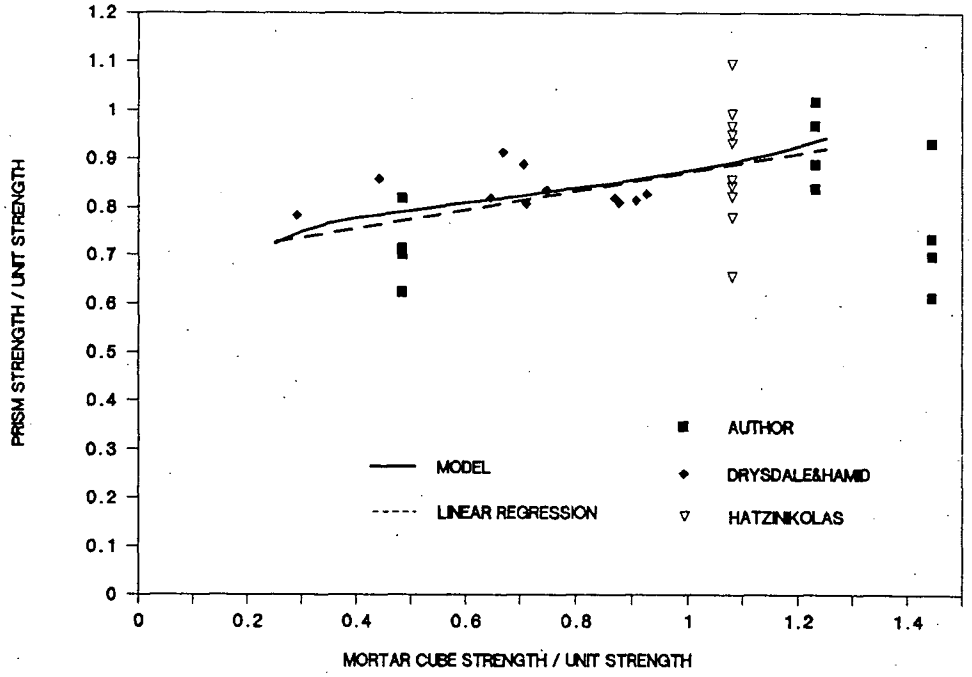

FIG. 4.16 Prism Strength versus Mortar Cube Strength

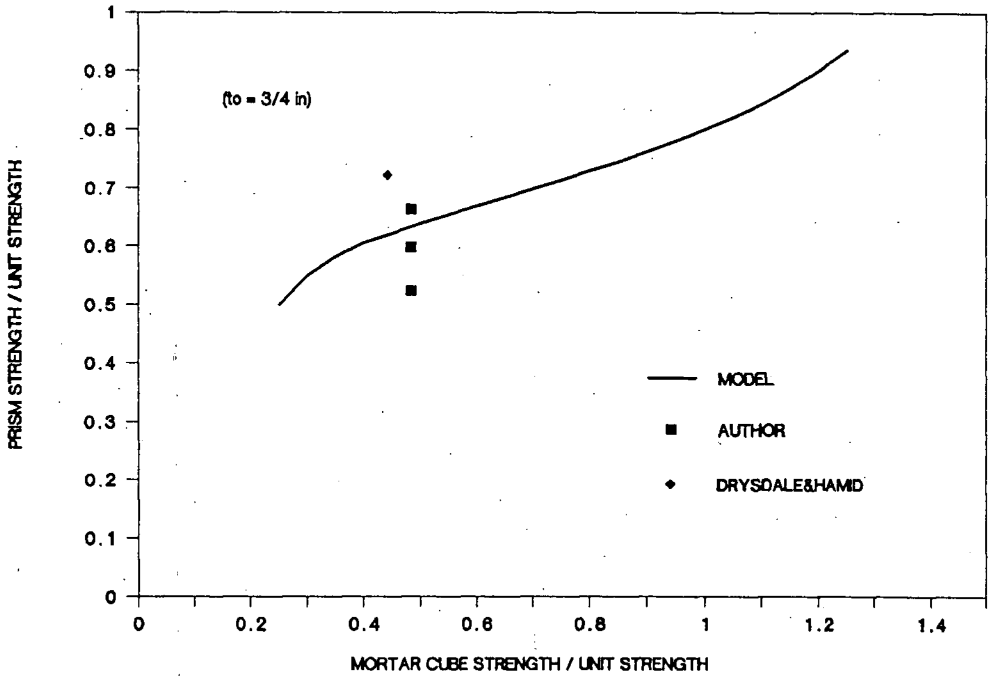

FIG. 4.17 Prism Strength versus Mortar Cube Strength, with Joint Thickness Doubled

should be important for masonry strength.

These uncertainties may have contributed to the experimental observation that stronger mortar does not necessarily make stronger masonry.

In the experiments conducted by the author, the stronger mortar, here type M, did not make a stronger prism, probably because it contains less lime than does type S mortar. This not only causes poorer adhesion to the blocks, (a phenomenon noticed by the author in his experiments), but also may lead to poorer water retaining ability. In other words, type M prisms not only had poorer adhesion between joint and unit, but also may actually have a lower joint strength due to poorer curing conditions.

Therefore, it is recommended that, in practice, attention should be paid to the overall quality of the mortar. Proper mix design should be specified and the cohesive requirement should be enforced.

4.7 Summary

In this chapter, the failure and capacity of plain concrete masonry under concentric compression has been studied. Hilsdorf's model of splitting failure has been reviewed in the light of both experimental and analytical work. It is concluded that the splitting failure mode cannot simply be attributed to the lower stiffness of the mortar joints; it is a manifestation of compression failure as discussed in Chapter III.

The less stiff mortar joint tends to be confined laterally, developing higher compressive strength in the inner part. On the one hand, it prevents joint failure. On the other hand, it tends to alter the uniform compressive stress in the vicinity of the joint, i.e. more compressive force tends to be transferred by the inner part of the joint. A failure criterion based on failure of masonry unit under this intensified compressive stress was proposed, which gives reasonable capacity estimation.

CHAPTER V

PLAIN MASONRY WITH FACE-SHELL BEDDING

5.1 Introduction

In North America concrete masonry is often mortared only on the face-shells. Even when a mason attempts to apply mortar to the cross-webs as well, he may not be able to ensure vertical alignment so that the webs can transmit force effectively. The mechanical properties of face-shell bedded masonry, therefore, have been studied extensively.

The splitting failure of face-shell bedded masonry is relatively well understood. Shrive (1982) concluded that tensile stress is developed at the centre of the webs, by a mechanism somewhat analogous to deep beam bending, i.e. the top and bottom halves of the web are taken as deep beams, bending up and down respectively (see Fig. 5.1), thus causing the splitting failure in face-shell bedded masonry.

The author is in full agreement with the reasoning in Shrive's paper. The present study of face-shell bedded masonry was intended to confirm his model experimentally, to study the transition to a failure mechanism for eccentrically loaded specimens, to explore the relationship to fully bedded masonry, and to develop some related quantitative results.

5.2 Experimental Work

Sixteen face-shell bedded prisms were built and twelve of them were tested under uniaxial compression including two with full capping. Table 5.1 summarizes the failure loads of these specimens.

Under uniaxial compression, splitting of the webs was again revealed by the tests. By observing the wire breaking order as previously described, cracks were found to initiate consistently from the top or bottom of the webs in middle course (see Fig. 5.2). This supports Shrive's model. Both the failure process recorded on video and the lateral deformation

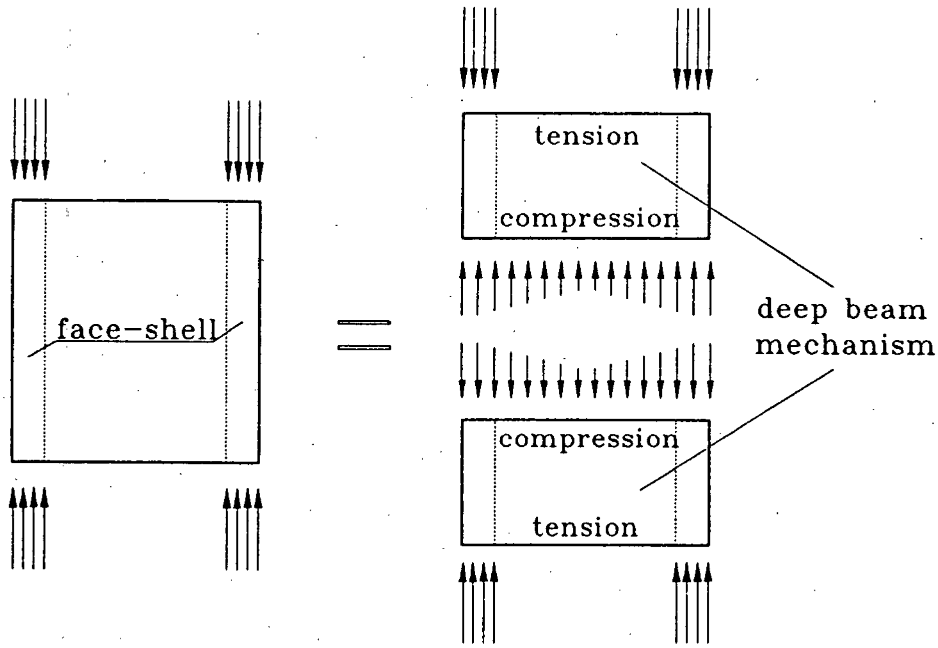

FIG. 5.1 Depiction of Deep Beam Mechanism

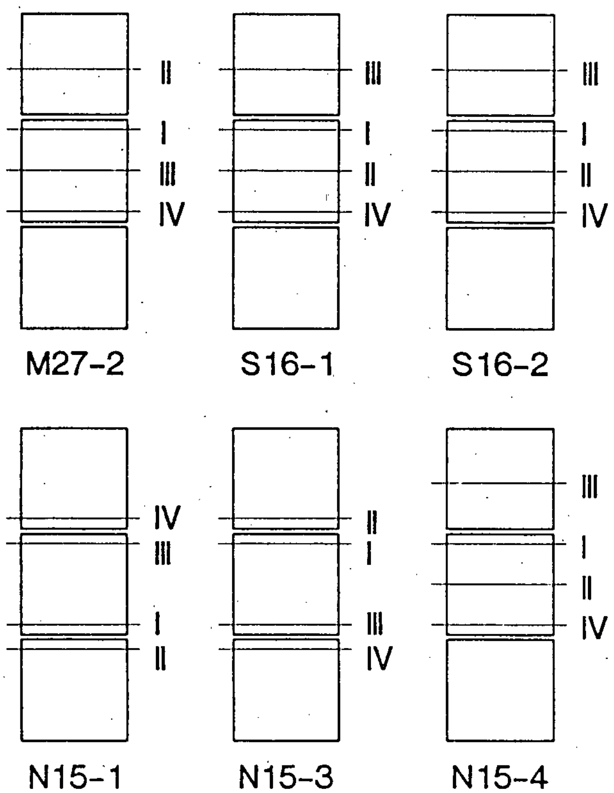

FIG. 5.2 Detected Orders of Macroscopic Splitting, in Terms of

4 Sections along Prisms. (Face-Shell Bedded Prisms)

SPECIMEN	1	2	3	4	AVG	COV
M27 (M−MORTAR)	118.0	99.0	86.0	75.0	94.5	19.9%
S16 (S−MORTAR)	119.0	127.0	140.0	109.0	123.8	9.2%
N15 (N−MORTAR)	100.0	115.0			107.5	7.0%
N15 (N−MORTAR)			53.0*	48.0*	50.5	5.0%

Table 5.1 Failure Loads of Plain Prisms with Face-Shell Bedding (kips)

* Tested with full capping

measurements indicated that splitting occurs at or immediately before final failure. Figs. 5.3, 5.4 give the deformation curves. A deep beam mechanism is suggested by the substantial difference in the deformation measurement at locations #3 #4; splitting is clearly evidenced by the jumps in these curves. The final failure is characterized by peeling off (fully or partly) of the face-shells, as shown in Fig. 2.13 in Chapter II.

However, for most of the specimens with face-shell capping cracks were found to initiate in the web somewhere near two ends of the mortar joints, and tended to wander afterwards, as typically illustrated in Fig. 2.13. This appears somewhat different from what one would expect by the deep beam bending model, which suggests that splitting would occur in the centre of the web.

Splitting in the centre of webs was found in the specimens tested with full capping (see Fig. 2.14), usually occurring in the top course. These specimens failed at very low loads (about 50% of that of the face-shell capping, see Table 5.1), immediately after web splitting; the two halves of blocks collapsed by hinging about the inside toes of the mortar joints. The hinging mechanism is implied by the vertical displacement measured across the outside of the joint of specimen N15-3, which contracted first because of compression then tended to open due to the joint rotation.

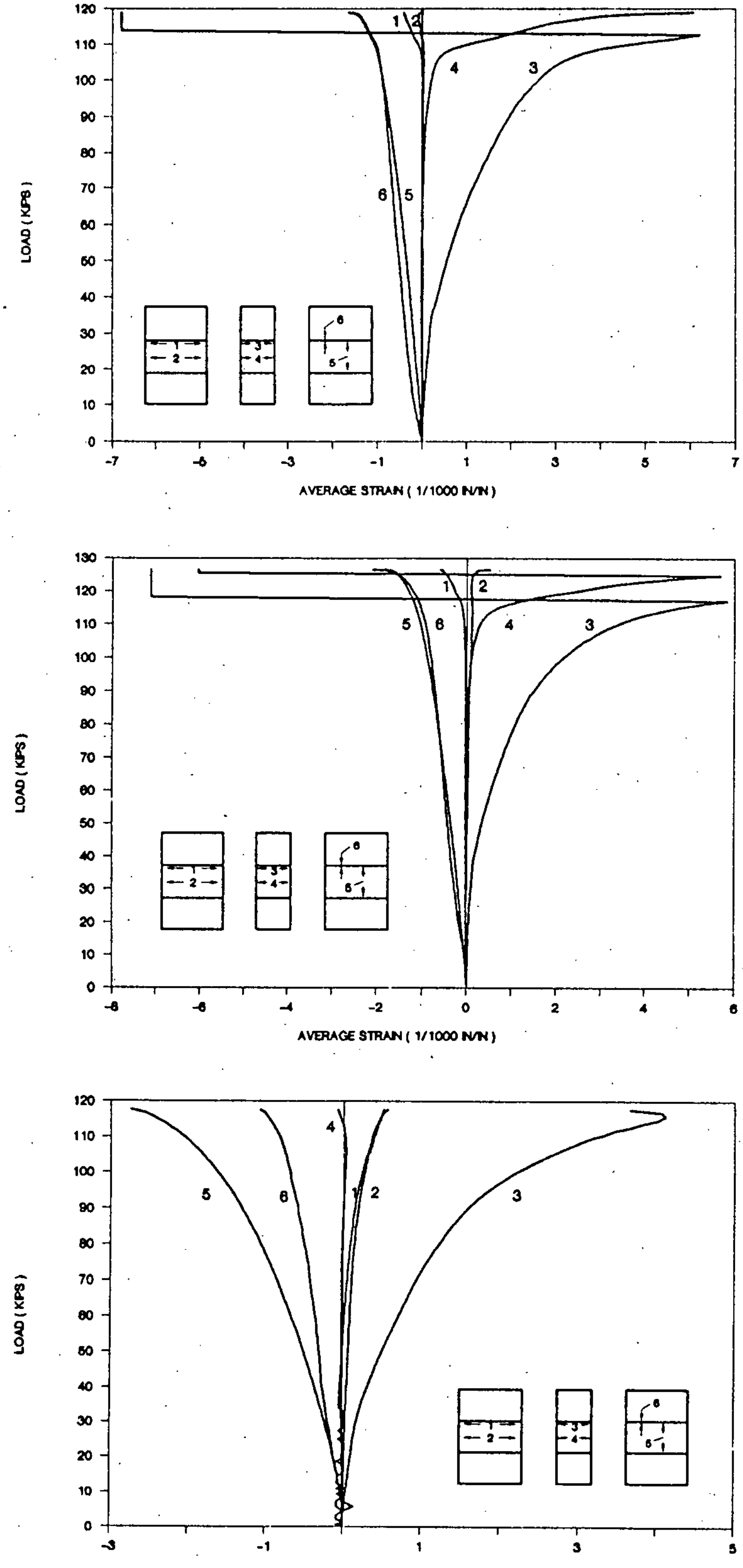

a) S16-1

b) S16-2

c) M27-1

FIG. 5.3 Measured Deformations at Certain Locations of Face-Shell Bedded Prisms

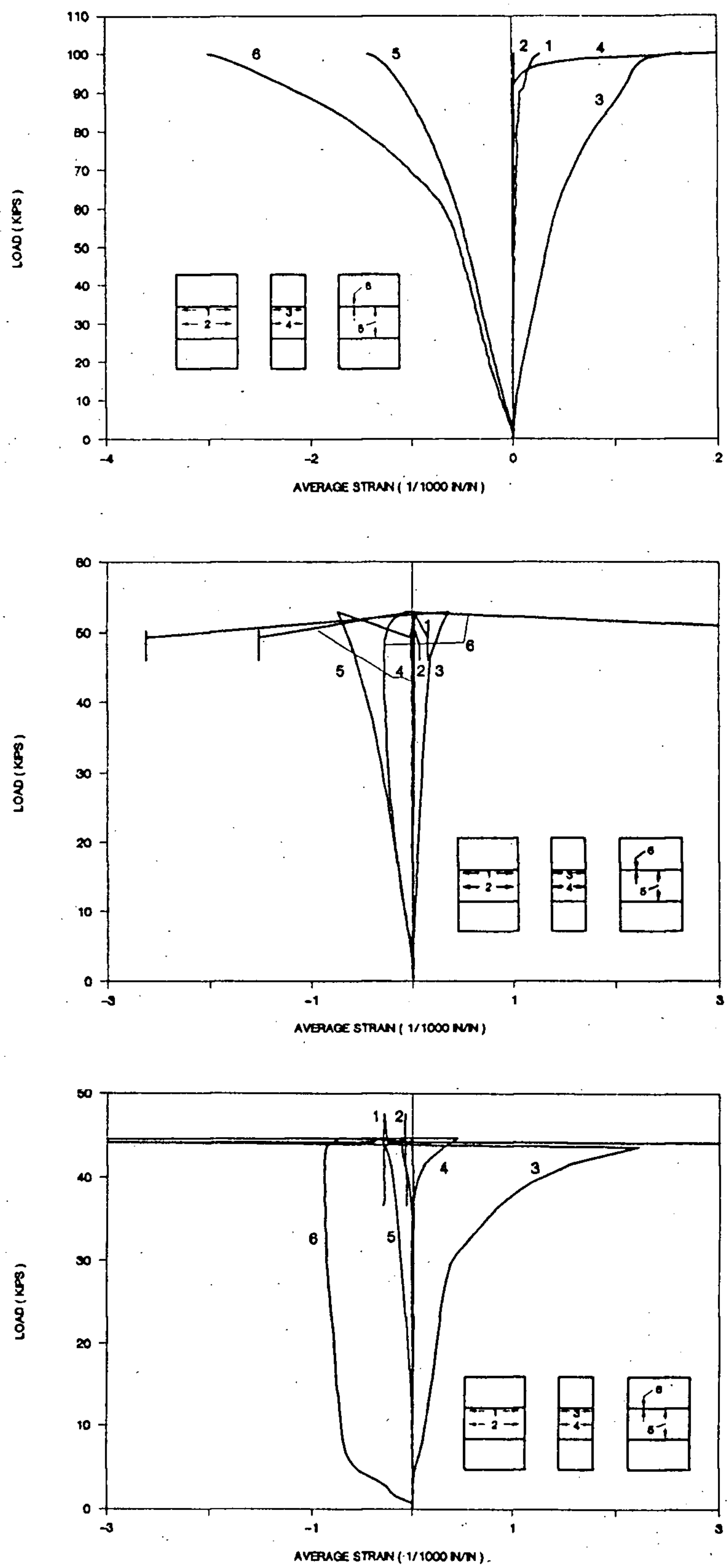

a) N15-1

b) N15-3

c) N15-4

FIG. 5.4 Measured Deformations at Certain Locations of Face-Shell Bedded Prisms

5.3 Stress Analysis

Shrive did a 3-dimensional stress analysis by modeling a 2-high face-shell bedded prism using the finite element method. However, the analysis was only for the case of uniaxial compression and the results given in his paper are limited to certain locations. Therefore, some additional numerical stress analysis is performed here.

We model a web as a plane elastic problem for simplicity. The author believes the 2−dimensional model has some value, although this is actually a 3−dimensional problem requiring the exact geometry of the prism. The stress field was solved by using the boundary element method (Crouch 1983). Thirty four elements per edge length were used, and the results given on the boundaries in the following figures are the stresses evaluated at the centre of each element.

The stress distributions determined for certain locations in the face-shell loaded web are given in Fig. 5.5. It is interesting to note that lateral tensile stress in the top of the web remains approximately constant within the middle range and reaches its maximum at about the quarter points instead of in the centre. The high lateral tension at the quarter points can be attributed to the local stress concentration arising from the compressive forces in the face-shell, while the centre part is stressed in tension because of the beam bending mechanism (cf. Fig. 5.1). This is implied by the tensile stress distributions along the depth at these two corresponding locations; the former has a much sharper stress gradient, as shown in Fig. 5.5. The elastic analysis gives the astonishingly high value of the maximum tensile stress, read as 49% of the vertical compressive stress acting on the face-shell. This result is comparable to that given by Shrive (1982). However, we may argue that, since nonlinear developments in the concrete allow some degree of stress redistribution, the tensile stress may be expected not to reach such a high value at the moment of failure.

The stress analysis suggests that the two sides of the web are not only carrying higher local tensions than the centre part, but are also under a complex stress state, i.e, under tension,

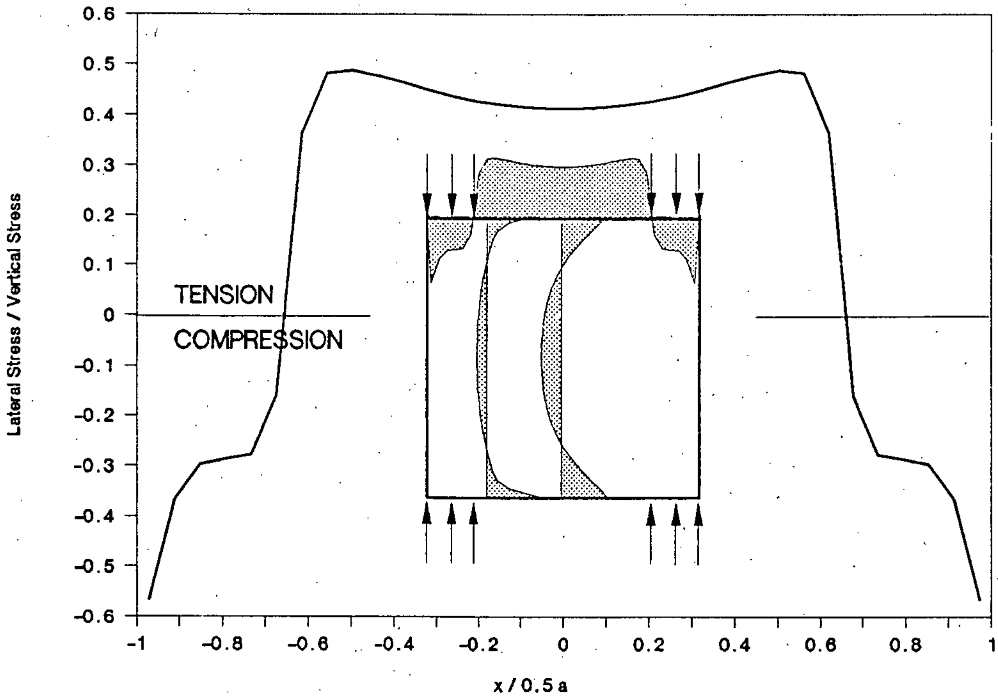

FIG. 5.5 Lateral Stress Distribution in a Web of Face-Shell Bedded Masonry under Uniaxial Compression: Variation across Top of Block, as well as Vertical Distribution on Centre Line and at Vertical Line where the Tension at the Top is a Maximum

compression and shear. This clearly explains why splitting initiates at these locations, and suggests, furthermore, that because of the beam bending mechanism, the crack will run through the web once it is initiated. Since the splitting occurs near the face-shell, after splitting, the force is transferred by the face-shell alone without effective lateral support. Thus vertical stability is unlikely to be maintained even if the face-shell is still not crushed. Therefore, in practice, we may consider that splitting signifies failure.

The deep beam bending mechanism is more obvious when face-shell bedded masonry is fully capped. The masonry block is loaded as depicted in Fig. 5.6. Unlike the face-shell capped prism, in this case the internal shear between face-shell and web cannot be neglected. If we assume that the compressive stress on the capping side is uniformly distributed and that the internal shear resultant introduced thereby acts on the midheight of the web, then the lateral tensile stress distribution is plotted in Fig. 5.7. In this figure, the result is compared with that of

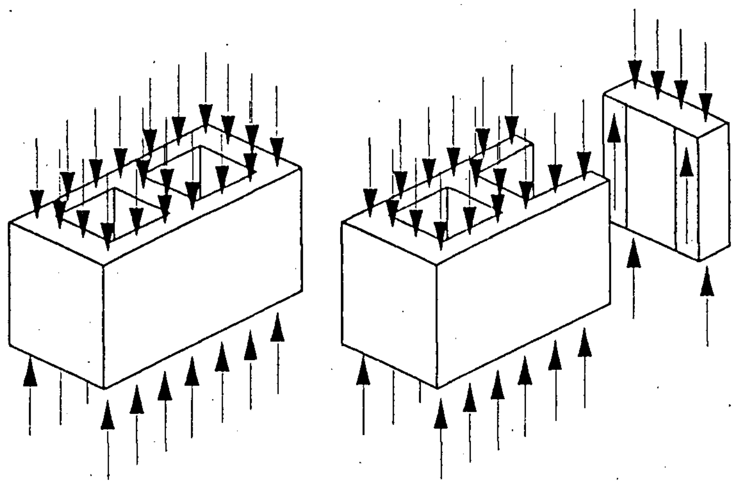

FIG. 5.6 Forces Acting on a Block with Full Capping and Face-Shell Bedding

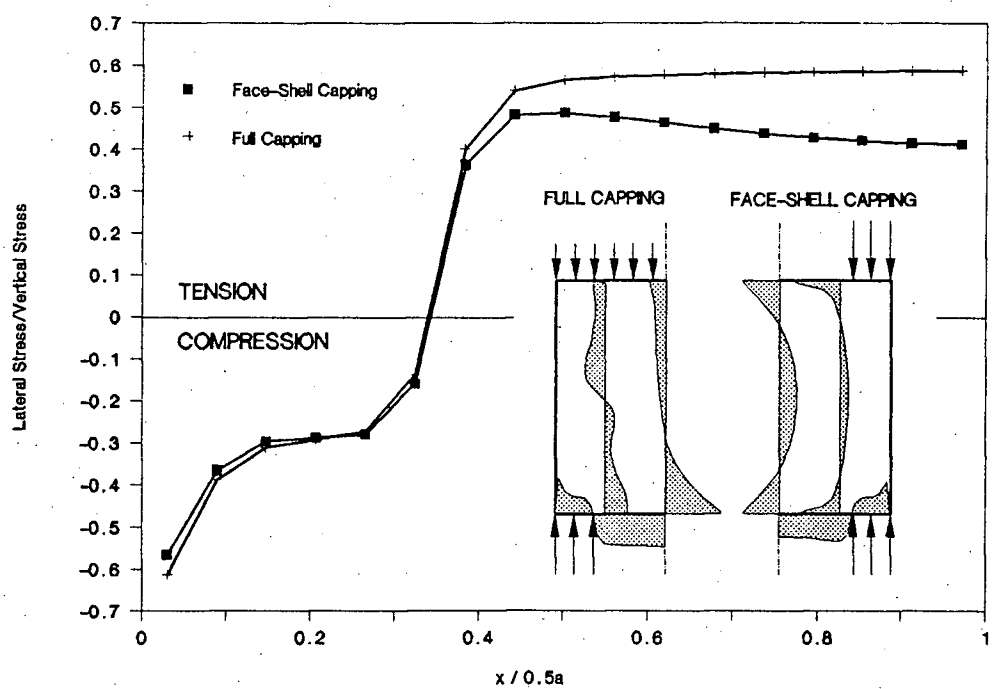

FIG. 5.7 Lateral Stress Distribution in a Web: Full Capping versus Face-Shell Capping; Variation across Bottom of Block, as well as Vertical Distribution on Centre Line and Quarter Line

the face-shell only capping conditions under the same total prism load.

Note that the entire web acts as a single deep beam in the top capped block. The maximum tensile stress is found at the bottom centre of the web. This tensile stress is not only higher than that of the face-shell capped prisms, but also extends to a larger depth. This explains why splitting is prone to occur at the centre of the web of fully capped prisms, and these prisms fail at a lower loads than their face-shell capped counterparts.

One practical implication is that plain concrete masonry should be either built totally fully bedded or totally face-shell beddéd. Mixed bedding patterns should be avoided. If a wall is going to be built by face-shell bedding, one must ensure that the whole wall is face-shell mortared, and detail the top and bottom of the wall so that the vertical load will be effectively transferred on the face-shell only. Otherwise one may inadvertantly sacrifice as much as half of the wall's capacity (see Table 5.1).

5.4 Some Comments on Joint Effect

The deep beam bending mechanism suggests that the mortar type should have a relatively minor effect on the capacity of face-shell bedded masonry, and thus it appears possible to estimate the capacity of such a system using the modulus of rupture of the masonry units. The known correlation between the compressive strength and the modulus of rupture of concrete suggests that the capacity of masonry should be in a form such as

$$f'_m = k\sqrt{f'_u} \qquad \text{(in Imperial units)} \qquad 5.1$$

or

$$\frac{f'_m}{f'_u} = \frac{k}{\sqrt{f'_u}} \qquad 5.2$$

where k is a constant. When $k = 40$, Eq. 5.2 is plotted in Fig. 5.8 with four groups of experimental data, which gives a reasonable correlation considering the scatter of the data.

However, experiments conducted by both Shrive (1982) and by the author by varying mortar strength have indicated that the effect of mortar type may not be totally neglected (cf. Table 4.1; the variation in the masonry capacity with mortar strength is also reflected in the scatter of the author's data in Fig. 5.8, which includes prisms with three different types of mortar). Again, it is noted that the stronger mortar does not necessarily make stronger masonry. In the tests conducted by the author, the strongest mortar made the weakest masonry prisms.

We may argue that although the deep beam mechanism dominates the failure, partial failure of the mortar joint may still occur at the failure stress. This is because the failure stress based on mortared area is still high compared with that of the fully bedded masonry. The outside edges of the mortar tend to fail and spall out, leaving a narrow strip of mortar down the centre of the face-shell. This partial joint failure will not only cause a local stress concentration in the vicinity of the joint, as studied in detail in the preceding chapter, but may also change the joint essentially from a flat-base to a hinge-like support, which provides little rotation constraint. The deep beam bending mechanism may be intensified by this support change. The above argument suggests that the adhesion of mortar joint to block unit is important to face-shell masonry capacity as well.

Eq. 5.2 gives an estimate of masonry capacity based on the unit strength. Further investigation is needed to include the joint effect quantitatively.

5.5 Summary

The behaviour of plain concrete masonry with face-shell bedding under concentric compression has been studied. The deep beam bending model for splitting in webs proposed by Shrive has been verified by experiments. The effect of capping conditions on capacity and failure mode has been investigated. Joint effect has also been discussed.

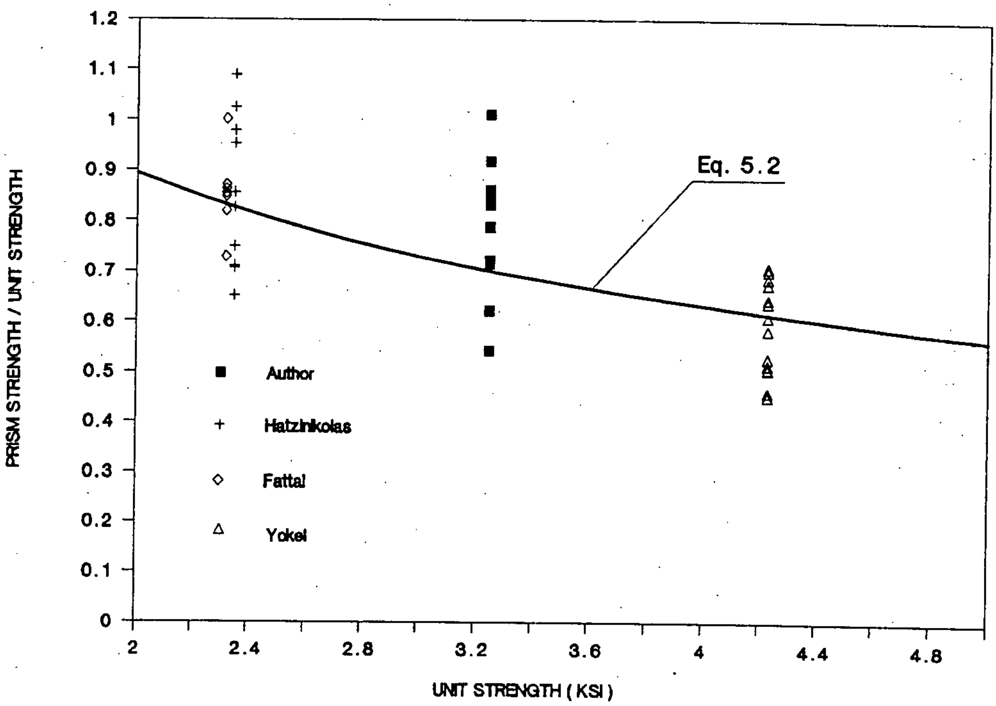

FIG. 5.8 Prism Strength versus Unit Strength for Face-Shell Bedded Masonry

CHAPTER VI

PLAIN MASONRY UNDER ECCENTRIC COMPRESSION

6.1 Failure Mode Transition

When plain masonry (whether fully mortared or face-shell mortared) is under eccentric compression, it fails in a rather different mode and at a higher apparent stress than it does under uniaxial compression.

5 groups of plain prisms were tested under eccentric compression. Most of the specimens exhibited shear type failure, i.e. failure is roughly characterized by an inclined fracture plane (or more precisely, a fracture zone in which material is highly cracked or crushed) separating the material. Because of this mode, the failure appeared to be relatively sudden.

All specimens failed on the loaded compression side, and failure was often localized in some part of the prism. Fig. 2.15 in Chapter II illustrates the typical failure pattern. Table 6.1 summarizes the failure loads. Figs. 6.1, 6.2 give the measured deformation curves. The apparent increase in strength phenomenon is depicted by comparing a theoretical P−M interaction curve

SPECIMEN1	e/t	1	2	3	4	AVG	COV
N18 (N-MORTAR)	1/6	150.5	107.0	120.0	121.0	124.6	12.8%
M20 (M-MORTAR)	1/3	77.5	79.0	86.5	95.0	84.5	8.2%
S21 (S-MORTAR)	1/3	96.0	90.0	100.0	93.0	94.8	3.9%
N19 (N-MORTAR)	1/3	83.0	81.0	85.0	69.0	79.5	7.8%
N22 (N-MORTAR)*	1/3	64.0	78.0	69.0	73.0	71.0	7.3%

Table 6.1 Failure Loads of Plain Prisms under Eccentric Load (kips)

* Face-shell Bedded

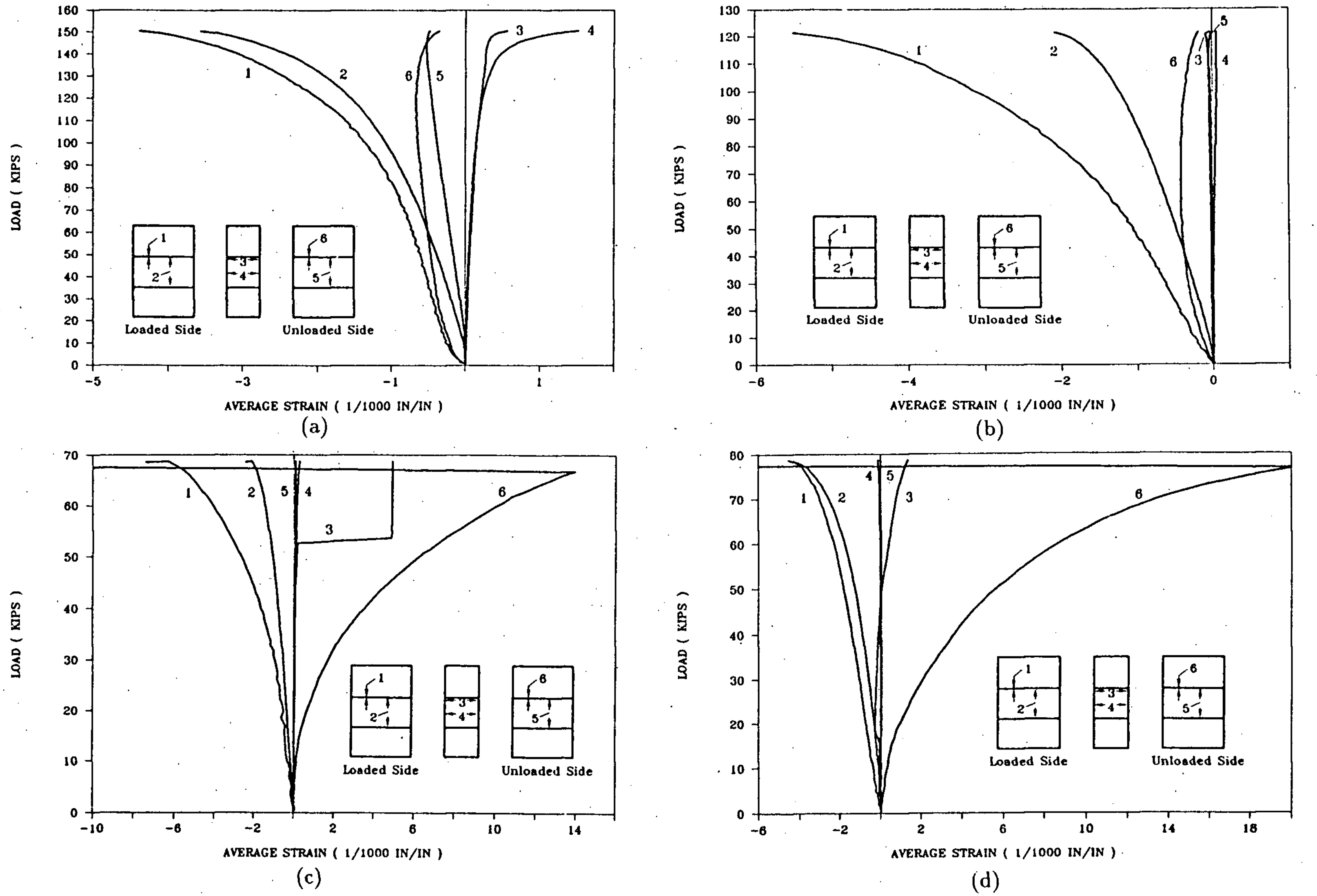

FIG. 6.1 Measured Deformations at Certain Locations of Plain Prisms under Eccentric Load:
a) N18-1, e=t/6; b) N18-4, e=t/6; c) N19-4, e=t/3; d) M20-2, e=t/3

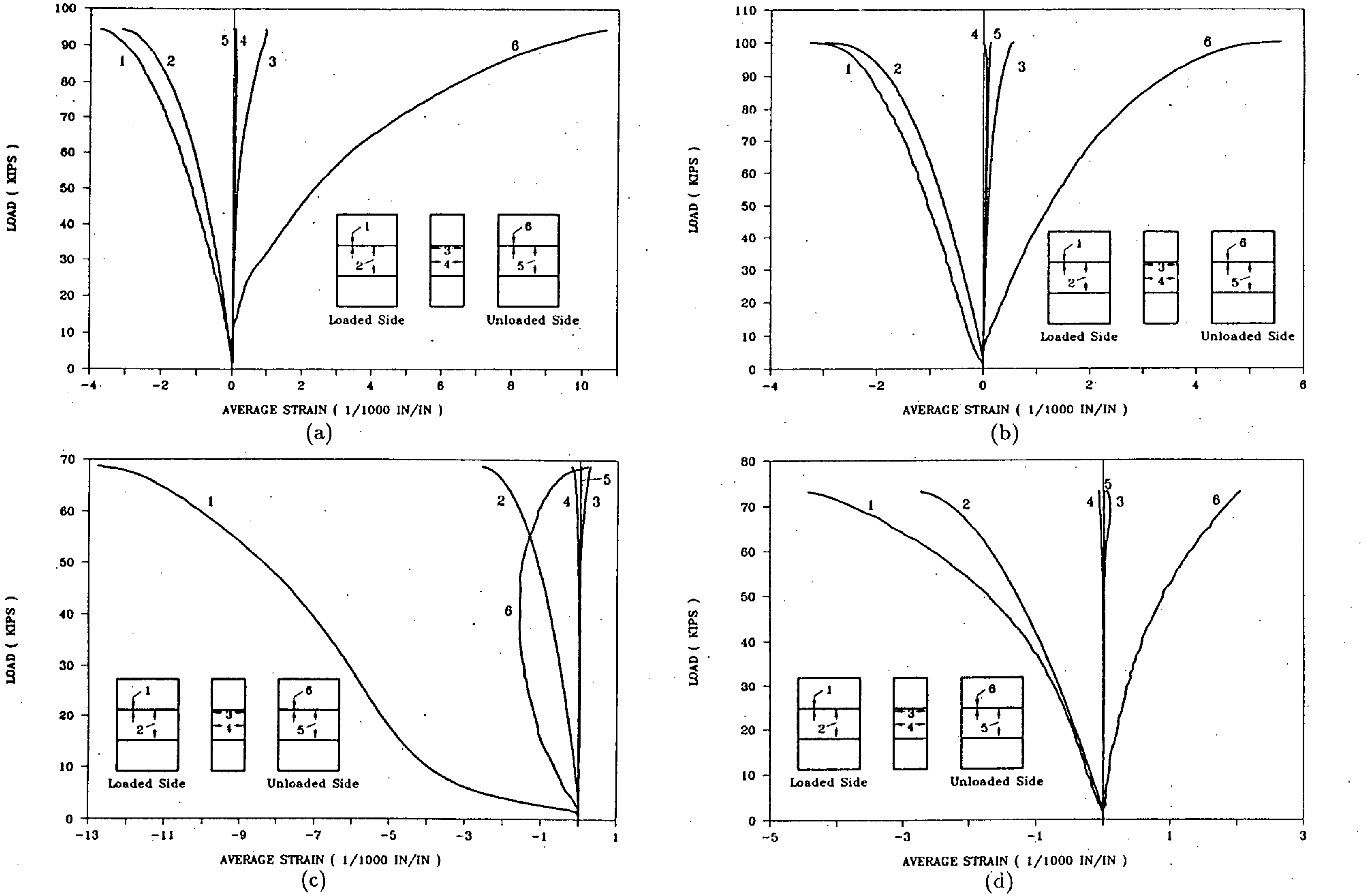

FIG. 6.2 Measured Deformations at Certain Locations of Plain Prisms under Eccentric Load: a) S21-4, e=t/3; b) S21-3, e=t/3; c) N22-2, e=t/3; d) N22-4, e=t/3

based on the uniaxial compressive strength with the eccentric compression test data, as shown by Fig. 4.1 in Chapter IV.

There are some differences in the detailed failure modes among the specimens. Vertical splitting in the web before or at failure of the loaded side was observed in some of the prisms with high eccentricity ($e=t/3$). A similar phenomenon was observed by Hatzinikolas et al in their experiments (1978), and it worth giving a brief explanation.

For those prisms which were under large eccentricity, the joints on the tension side of some specimens debonded before the compression side failed. (This is shown by the deformation measurement across the joint on the tension side, see Figs. 6.1, 6.2) Because of this debonding, the prisms were actually only loaded on the compression side, as depicted in Fig. 6.3. The resultant force acting on the compression side of the web is an axial force with a bending moment. Therefore, it is not surprising that some transverse tensile stress can develop in the web. For an ideal elastic case in which the compressive stress is triangularly distributed, a numerical study shows that the maximum magnitude of this transverse tensile stress can be as high as 25% of the maximum compressive stress, as depicted in Fig. 6.3.

However, it can be visualized that the splitting caused by this tensile stress does not directly lead to final failure of a prism, or of a low wall. This view is supported by the experimental observation that splitting can occur before the loaded face-shell fails, and that failure is essentially characterized by a shear mechanism. Nevertheless, it again implies the importance of sound adhesion in the joints. Although plain masonry is not usually designed to sustain load with high eccentricity, sound bond may ensure the wall's integrity in the case of the wall being accidentally loaded in the unfavorable condition (with tensile stress occurring on one side of the wall).

For the case of face-shell bedded masonry, with increasing eccentricity, the deep beam mechanism may no longer dominate the failure. A stress analysis, keeping the vertical compression stress on the loaded side constant, indicates that the magnitude of the lateral

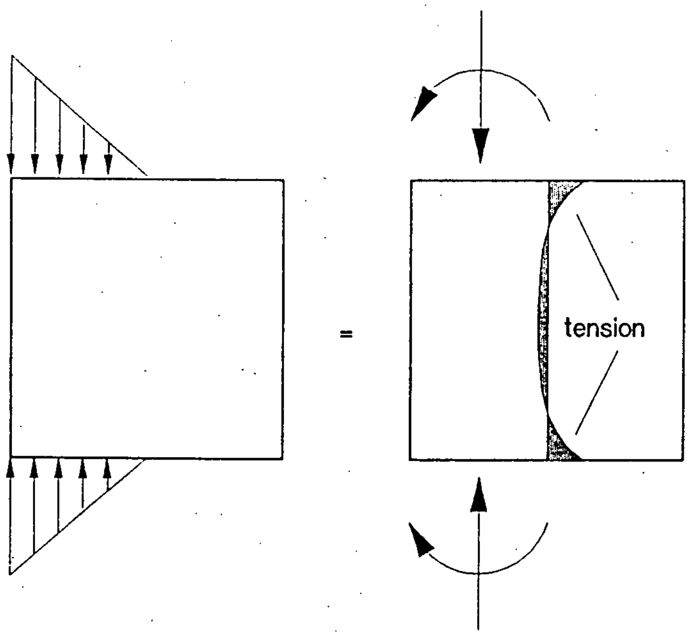

FIG. 6.3 Stress Distributions in a Cracked Section

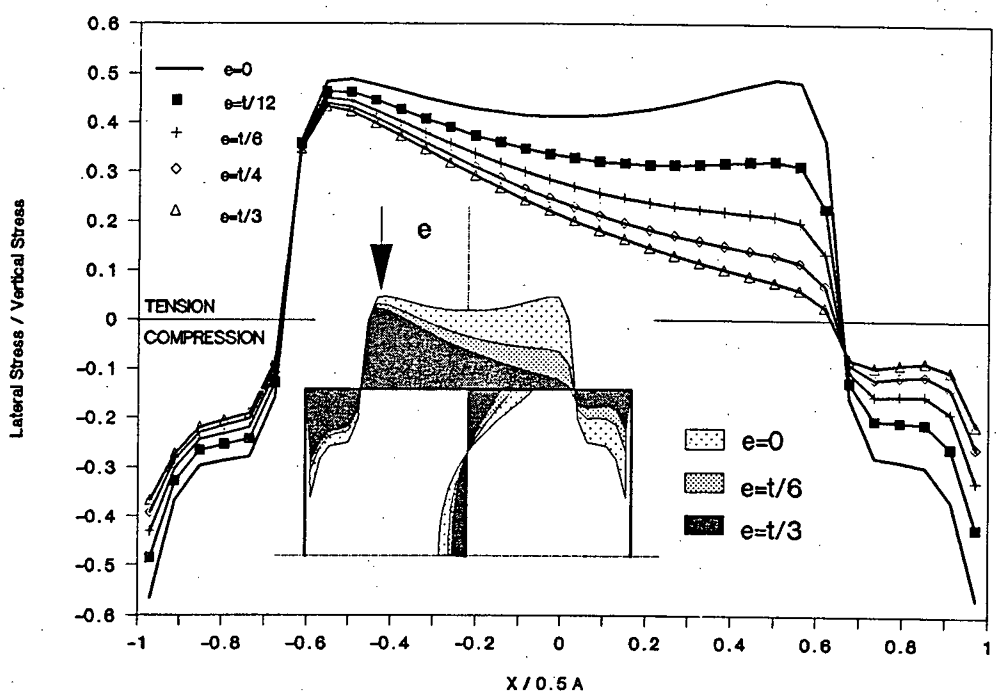

FIG. 6.4 Lateral Stress along Top of a Web with Face-Shell Bedding under Eccentric Load

tensile stress due to this mechanism is substantially reduced with increasing eccentricity, as shown in Fig. 6.4.

However, to fully explain the preference of the shear failure mode when masonry is under eccentric loading needs a thorough understanding of the failure of a concrete-like brittle material under various conditions. In Chapter III we have proposed a failure model explaining the splitting failure under uniaxial compression. However, it appears no easy extension can be made when the model mechanism is under a compressive stress with gradient. It could be that the uneven compression due to the stress gradient intensifies the friction and interlock mechanism between crack surfaces and thus prevents the splitting mode from occurring.

6.2 Effect of Joint Conditions

As shown in Table 6.1, under large eccentricity, change of mortar strength apparently has a relatively minor effect on the capacity of the prism. This may be explained as follows.

When plain concrete masonry is under highly eccentric compression, the compressive force is mainly transferred by the face-shell on the loaded side. Since there is a strain gradient across the face-shell, the stress distribution across it, at a point remote from the joint, must be hump shaped because of the nonlinearity of the material. This is quite different from that under uniaxial compression, where the stress would always be uniformly distributed in the absence of the joint, regardless of the development of material nonlinearity.

The hump shaped stress distribution suggests that the force would be largely transferred by the middle part of the face-shell. We know by the analysis of the preceding sections that the mortar joint can develop relatively high strength in its middle part (cf. Fig. 4.14). The presence of the joint, therefore, may not alter the normal stress distribution as much as the joint under uniaxial compression will do.

Moreover, because of the eccentric loading, the outer fiber of the loaded face-shell will deform more than the inner fibre will do. For loading with eccentricity equal to one third of the

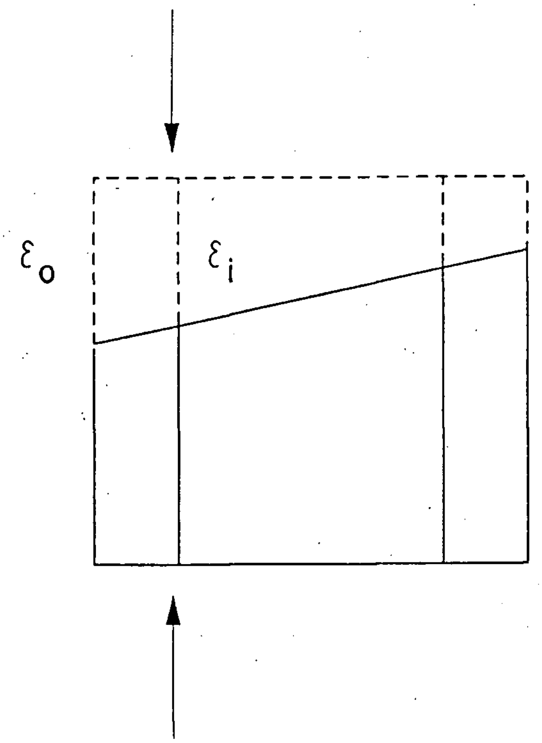

FIG. 6.5 Strain Distribution in a Section of Masonry under Eccentric Load

width of the prism, $\epsilon_i = 0.64\epsilon_o$, as depicted in Fig. 6.5. Here we neglect the tensile strength of concrete and assume $\epsilon_i = 0$ in the middle of the cross-section after the tensile part of the prism has debonded. When this strain is imposed on the joint, the joint is actually under a combination of uniaxial compression and bending. A stress analysis shows that the bending stresses will lend additional lateral confinement to the more compressed side of the joint and thus enhance the joint strength in that part. i.e., under eccentric compression the more compressed part of the joint will develop more strength. This ensures that the joint does not fail during the loading to the final stress distribution discussed above.

Thus, in practice we may neglect the joint conditions in designing walls under eccentric loading. This approach is further studied in the next chapter.

6.3 Summary

In this chapter, the behaviour of plain masonry under eccentric compression has been investigated. The eccentric behaviour differs from the concentric one not only in failure mechanism but also in the joint effect on the strength. In the following chapter, we will propose a design approach based on these findings, and conclude the study on plain concrete masonry .

CHAPTER VII

RECOMMENDED DESIGN APPROACH FOR PLAIN MASONRY

7.1 Recommendations on the Basis for Design

It has been demonstrated that under different load conditions plain masonry will fail by different modes.

Under uniaxial compression, masonry will fail by vertical splitting, but not due to the mechanism proposed by Hilsdorf. For face—shell bedded masonry, splitting can be attributed to a mechanism similar to deep beam bending.

Under eccentric loading, masonry tends to fail in a mode approximating shear failure. These two different failure modes will yield different apparent strengths. The joint conditions will affect the capacity of the masonry to a different extent under each of these two basic load patterns.

In practice, one wishes to estimate the capacity of masonry from the block unit compressive strength and the mortar cubic strength, since the latter are relatively easy to measure experimentally. The correlation given by Eqs. 4.27 or 4.28 and Eq. 5.2 may serve this purpose. However, when using these relations, one must keep in mind that some uncertainties are involved as was indicated in the development of the equations.

In particular, we have uncertainties in the failure criteria of the material itself, in the material properties other than strength, in the correlation between strengths, and last but not least, in the workmanship. These uncertainties are reflected in the scattered data of numerous experiments.

Therefore, it is recommended that in practice either we use the relations such as given by Eqs. 4.27 or 4.28 and Eq. 5.2 in a conservative manner or we retain the masonry prism test to estimate f'_m, the design base of plain concrete masonry under uniaxial compression.

However, for the case of eccentrically loaded masonry, an approach which differs from the traditional one will be recommended.

In the traditional approach, the eccentric capacity estimation is also based on the value f'_m associated with concentric loading. The apparent increase in strength is taken into account by a (strain gradient) factor. This factor as a function of eccentricity has been frequently studied through experiments (for example, Turkstra and Thomas 1978; Drysdale and Hamid 1983). In the current design code (CAN3-S304-M84 1984) the factor is given as a fixed value (1.3, reflected in the eccentricity coefficient C_e).

The usefulness of this approach depends on an assumed close and fixed correlation between the concentric capacity and the eccentric capacity. In the light of preceding studies, we know that this correlation is questionable since different failure mechanisms are involved.

In view of the failure mechanisms, the eccentric capacity of concrete masonry may be better correlated with the unit compressive strength f'_u instead of f'_m. As shown in Figs. 2.2 and 2.15 in Chapter II, the failure pattern of the unit block is very similar to that of prisms under eccentric compression.

Thus it is recommended here that the eccentric capacity estimation be directly based on the unit compressive strength f'_u, while the concentric capacity is based on the prism strength f'_m. The joint effect is neglected since apparently it is relatively minor for the case of eccentric loading. Although the apparent compressive strength of masonry may vary with the eccentricty, the variation is ignored for practical reasons. It is believed that this approach will yield better correlations since it is based on recognition of the failure mechanisms. Further, of course, this recommended approach considers the fact that it is not practical to test prisms under eccentric loading to assess the capacity.

The transitional point where the failure mode changes from splitting to shear failure needs to be indentified. It is suggested by the available experimental work that this occurres at a small eccentricity ($e < t/6$). This implies that the cross-section capacity curve is discontinuous somewhere between $e = t/6$ and $e = 0$. The detailed behaviour of the cross-section capacity in this range needs further investigation. At this point we recommend that this part of the curve be interpolated between the capacities at zero eccentricity and at $t/6$ eccentricity, but not to exceed the vertical load capacity of the zero eccentricity case. This is on the conservative side, as will be shown later, since the capacity at $t/12$ is also well correlated with the unit strength.

To examine this practical alternative of basing the eccentrically loaded capacity on the unit strength, we compare available test data with the recommended capacity curve. The capacity curves are generated by a conventional method, i.e. linear elastic behaviour and plane cross-section are assumed and the extreme fibre stress is set equal to the unit strength. The general expressions based on this method (for both grouted and ungrouted masonry) are derived in Chapter X. These expressions were checked against a computer program developed by Nathan (1985), which performs a rational analysis for beam columns based on material properties and cross-section geometry.

Since, under large eccentricity, masonry fails in a similar pattern regardless of the bedding conditions, experimental data for both bedding conditions (full and face-shell) are included. The comparison is illustrated in Figs. 7.1 to Fig. 7.11, which include the tests done by the author, by Fattal and Cattaneo (1976), by Hatzinikolas et al (1978) and by Drysdale and Hamid (1983). Tables 7.1 to 7.4 summarize the numerical results.

For the 58 cases compared, the average value of the ratio of failure load to predicted load is 1.026 with a coefficient of variation of 11.36%, corresponding to an expected ratio of 1.026 with 95% confidence limits equal to 0.996 and 1.056. The agreement is extremely good considering the scatter of the data and the erratic nature of the material.

Fig. 7.12 summarizes the comparison of the failure loads predicted by the recommended method with the experimental data. The coefficient of correlation is 0.956 and the majority of data points lie within the 99 percent confidence limits, which is highly significant.

The recommendations for design are concisely depicted in Fig. 7.13 by a $P-M$ capacity curve. Curve $O - B_1$, the masonry capacity under eccentric load, should be determined

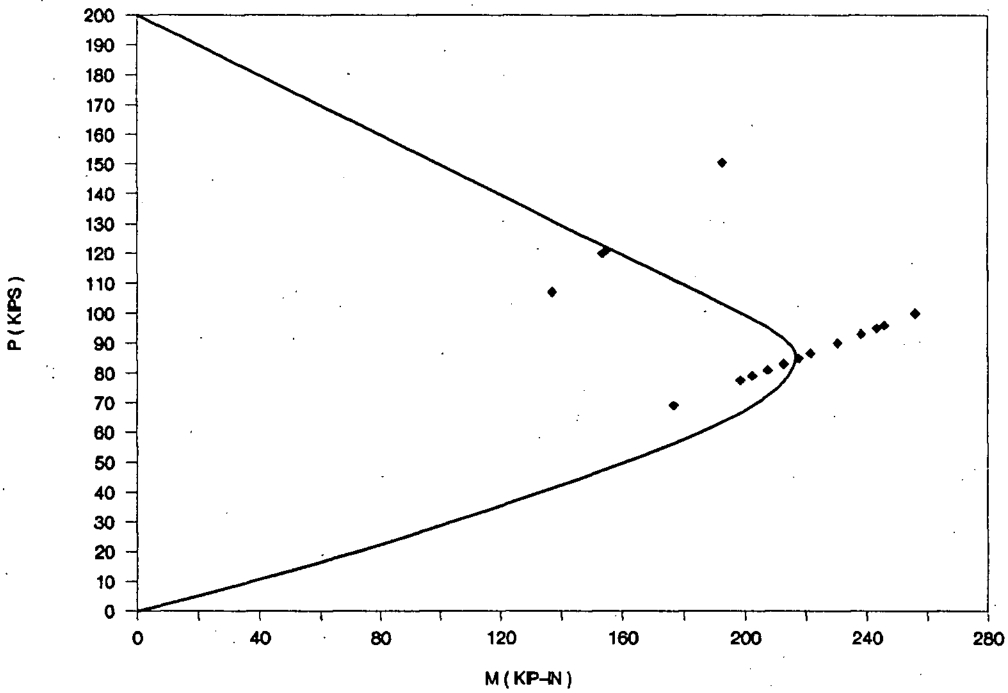

FIG. 7.1 Comparison between Recommended Approach and Experiments by the Author: N18, N19, M20 and S21

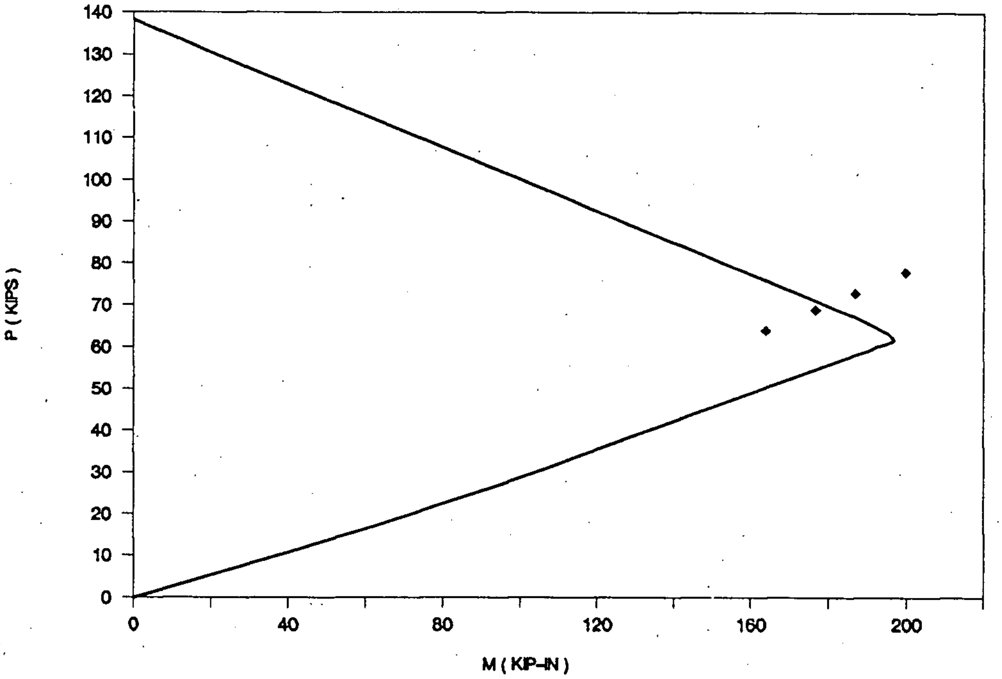

FIG. 7.2 Comparison between Recommended Approach and Experiments by the Author: N22 (Face-Shell Bedding)

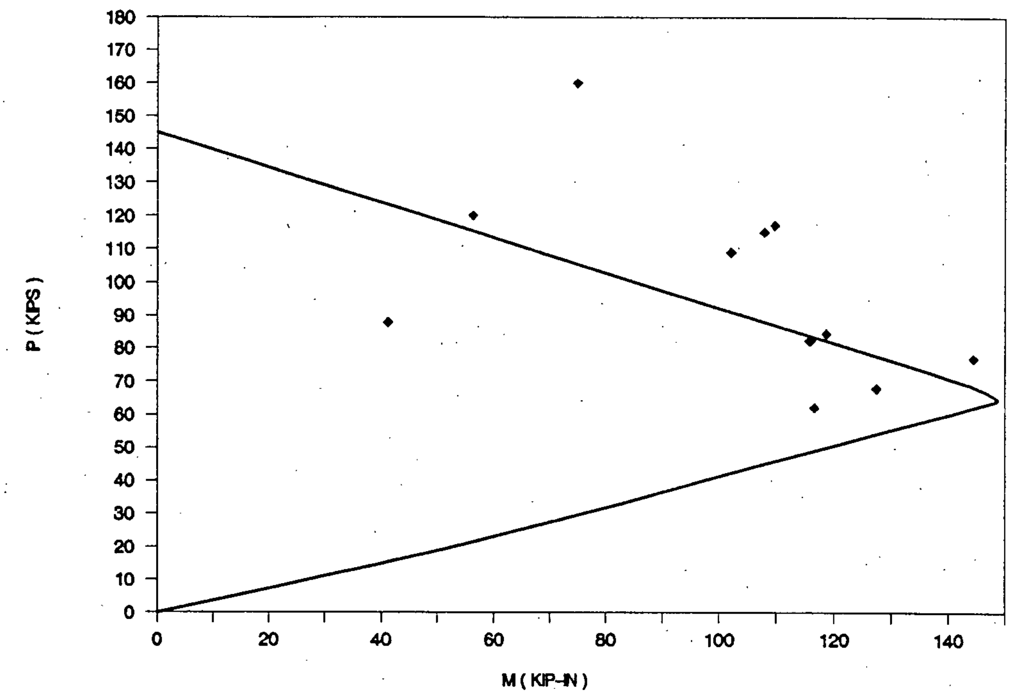

FIG. 7.3 Comparison between Recommended Approach and Experiments

by Fattal and Cattaneo

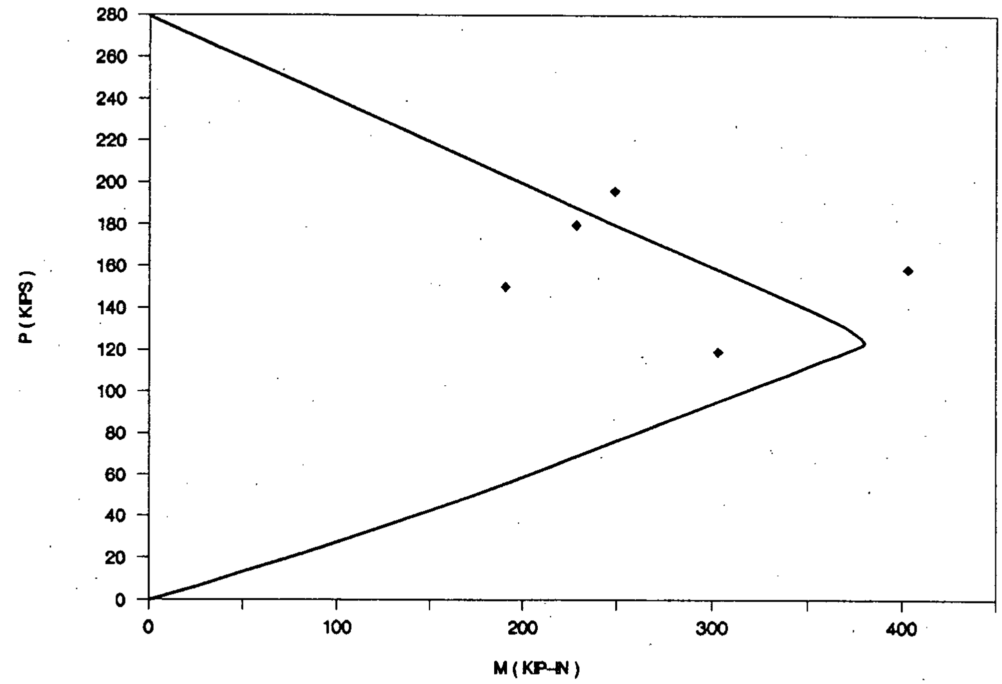

FIG. 7.4 Comparison between Recommended Approach and Experiments by Hatzinikolas et al

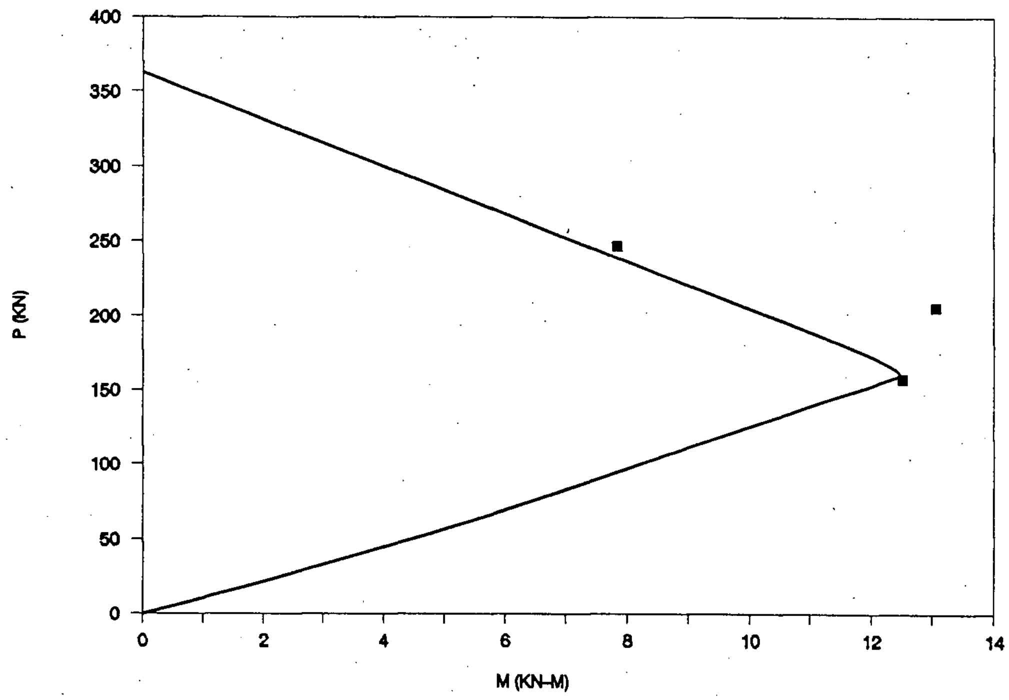

FIG. 7.5 Comparison between Recommended Approach and Experiments

by Drysdale and Hamid: Normal Block

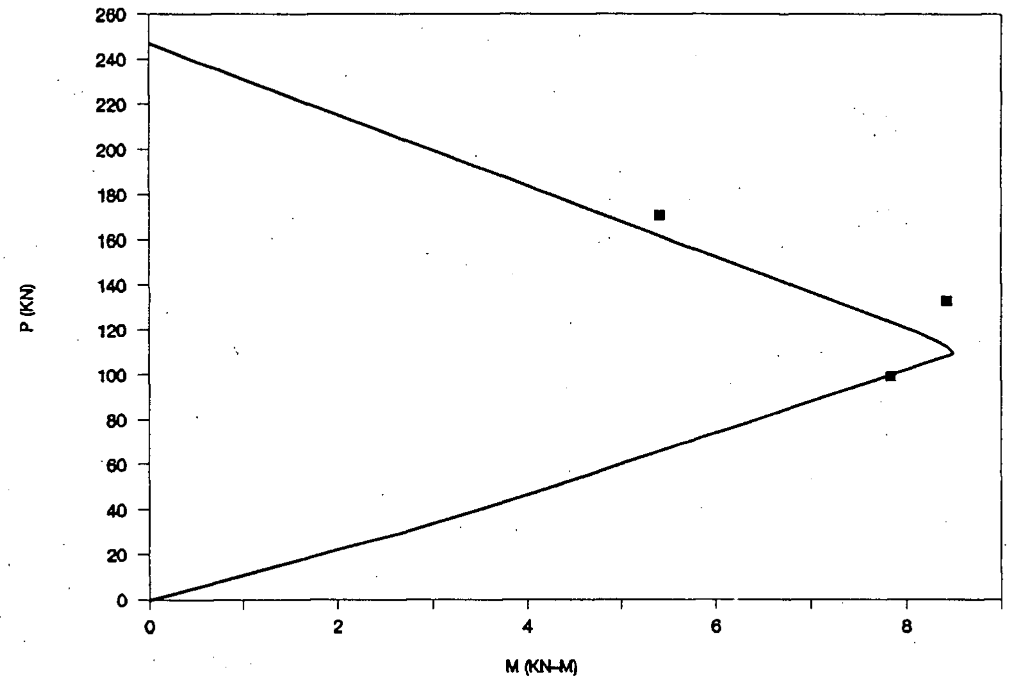

FIG. 7.6 Comparison between Recommended Approach and Experiments

by Drysdale and Hamid: Weak Block

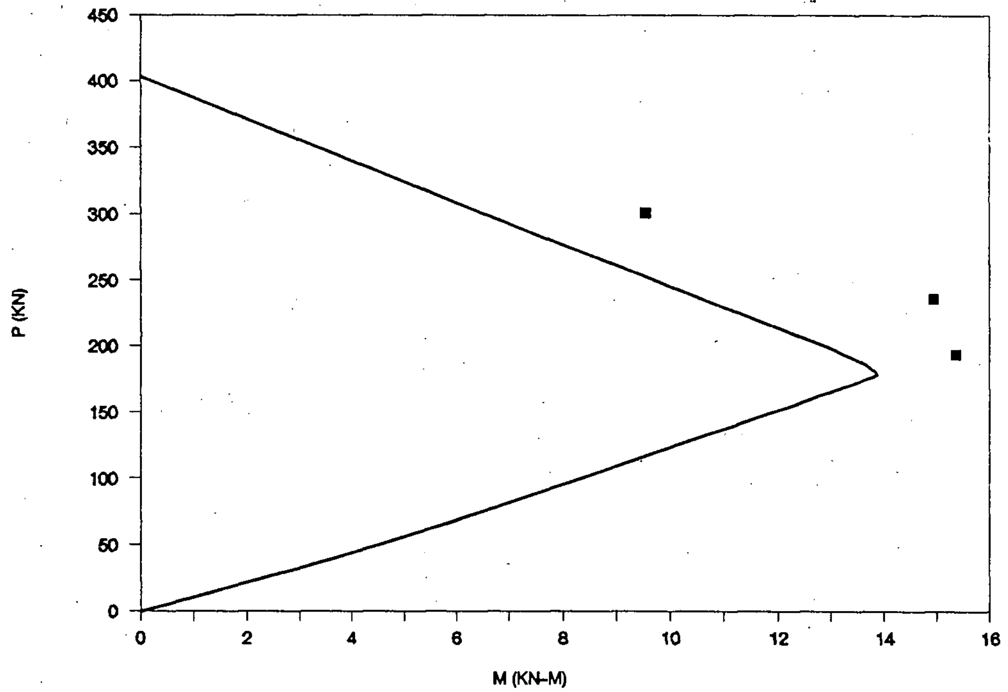

FIG. 7.7 Comparison between Recommended Approach and Experiments by Drysdale and Hamid: Strong Block

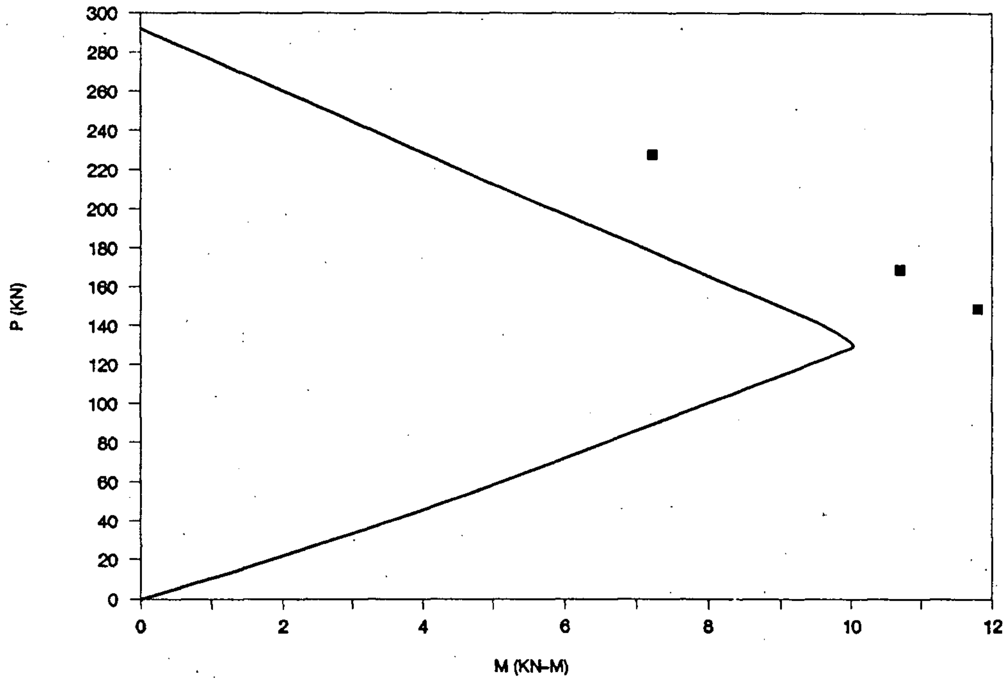

FIG. 7.8 Comparison between Recommended Approach and Experiments by Drysdale and Hamid: Light Weight Block

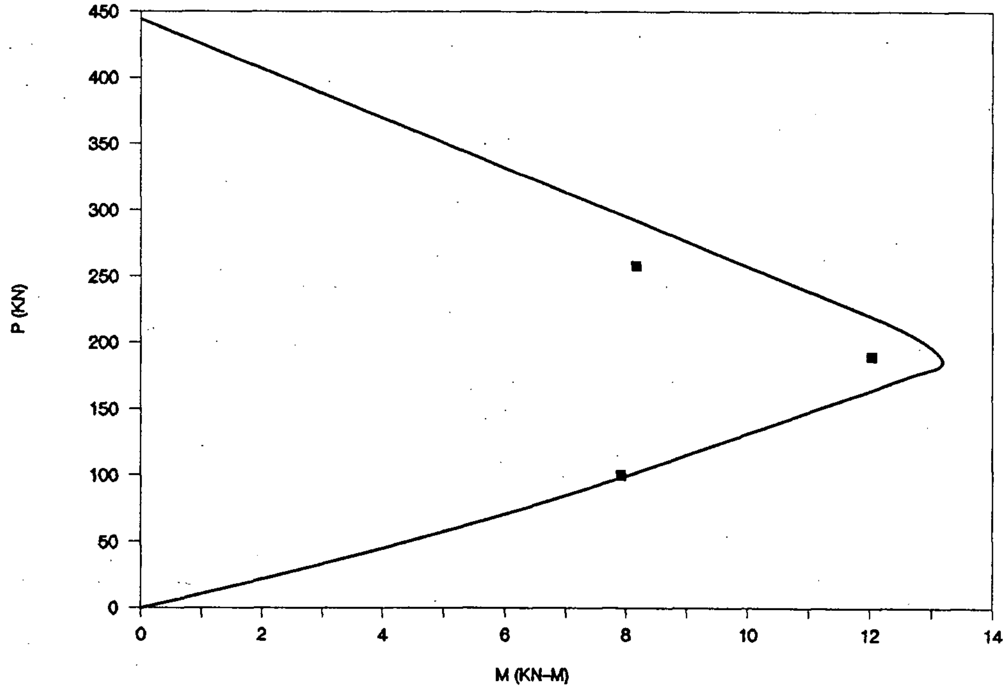

FIG. 7.9 Comparison between Recommended Approach and Experiments

by Drysdale and Hamid: 75% Solid Block

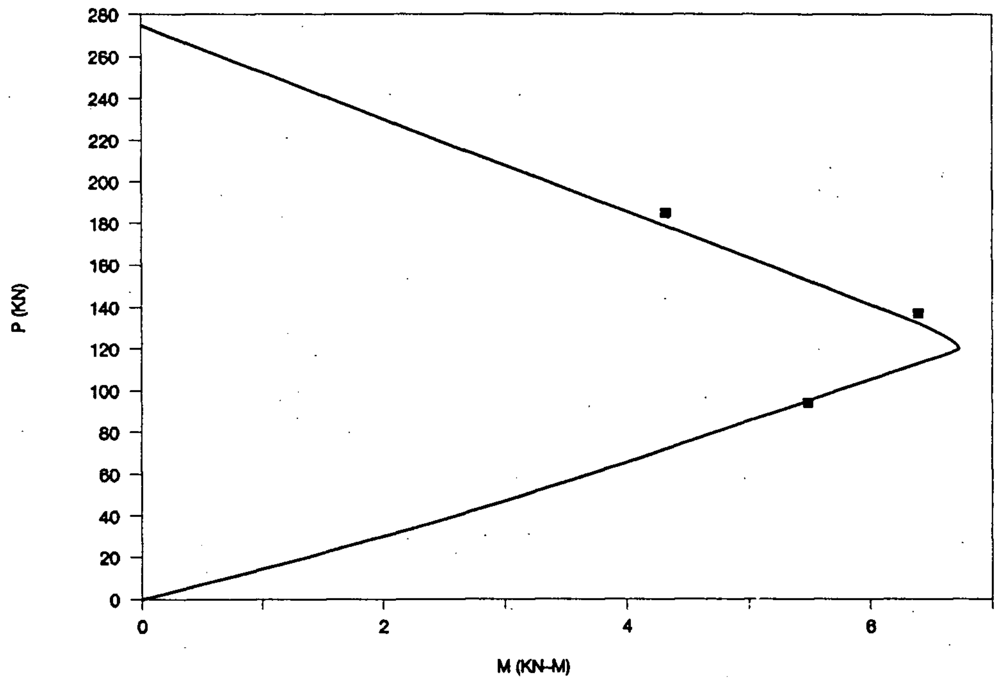

FIG. 7.10 Comparison between Recommended Approach and Experiments

by Drysdale and Hamid: 6 inch Block

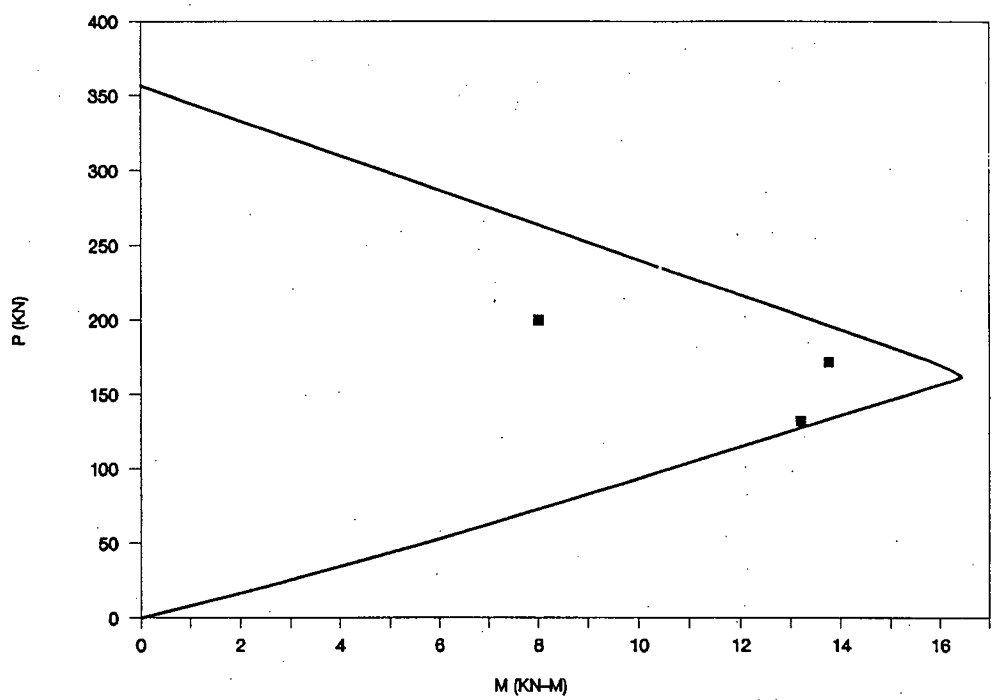

FIG. 7.11 Comparison between Recommended Approach and Experiments by Drysdale and Hamid: 10 inch Block

	N18 (e=1/6t) P_o=121.7kips (predicted)		N19 (e=1/3t) P_o= 84.4kips (predicted)		M20 (e=1/3t) P_o= 84.4kips (predicted)		S21 (e=1/3t) P_o= 84.4kips (predicted)		N22 (e=1/3t) P_o= 70.1kips (predicted)	
	P-kips	P/P_o	P-kips	P/P_o	P-kips	P/P_o	P-kips	P/P_o	P-kips	P/P_o
	150.5	1.24	83.0	0.98	77.5	0.92	96.0	1.14	64.0	0.91
	107.0	0.88	81.0	0.96	79.0	0.94	90.0	1.07	78.0	1.11
	120.0	0.99	85.0	1.01	86.5	1.02	100.0	1.18	69.0	0.98
	121.0	0.99	69.0	0.82	95.0	1.13	93.0	1.10	73.0	1.04
AVG	124.6	1.02	79.5	0.94	84.5	1.00	94.8	1.12	71.0	1.01
COV		12.8%		7.8%		8.2%		3.9%		7.3%

Table 7.1 Comparison with the Recommended Approach: Tests by Author

	e=1/12t P$_o$=116.3 kips		e=1/6t P$_o$=97.1 kips		e=1/4b P$_o$= 83.3 kips		e=1/3t P$_o$=72.9 kips	
	P(kips)	P/P$_o$	P(kips)	P/P$_o$	P(kips)	P/P$_o$	P(kips)	P/P$_o$
	120.0	1.03	115.1	1.19	82.5	0.99	62.2	0.85
	87.8	0.75	108.9	1.12	84.4	1.01	77.0	1.06
	160.0	1.38	117.1	1.21	82.3	0.99	68.0	0.93
AVG	122.6	1.05	113.7	1.17	83.1	1.00	69.1	0.95
COV		24.1%		3.1%		1.1%		8.8%

Table 7.2 Comparison with the Recommended Approach: Tests by Fattal et al

	e=1/6t P$_o$=185.4 kips		e=1/3t P$_o$=138.7 kips	
	P (kips)	P/P$_o$	P (kips)	P/P$_o$
	180.0	0.97	119.3	0.86
	196.0	1.06	158.7	1.14
	150.1	0.81		
AVG	175.4	0.95	139.0	1.00
COV		10.8%		14.2%

Table 7.3 Comparison with the Recommended Approach: Tests by Hatzinikolas et al

SPECIMEN	e/t	P (kN)	P (kips)	P_o(kips)	P/P_o
normal block	1/6	247	55.5	54.4	1.02
(NB)	1/3	206	46.3	40.8	1.13
	5/12	158	35.5	36.1	0.98
weak block	1/6	171	38.4	37.1	1.04
(WB)	1/3	133	29.9	28.0	1.07
	5/12	99	22.2	22.5	0.99
strong block	1/6	301	67.7	60.5	1.12
(SB)	1/3	236	53.1	45.4	1.17
	5/12	194	43.6	40.2	1.09
lightweight block	1/6	228	51.3	43.8	1.17
(LB)	1/3	169	38.0	32.8	1.16
	5/12	149	33.5	29.1	1.15
75% solid	1/6	258	58.0	62.8	0.92
(QB)	1/3	190	42.7	45.5	0.94
	5/12	100	22.5	22.2	1.01
6 inch block	1/6	185	41.6	40.7	1.02
(6"B)	1/3	137	30.8	30.3	1.02
	5/12	94	21.1	21.4	0.99
10 inch block	1/6	200	45.0	54.7	0.82
(10"B)	1/3	172	38.7	41.5	0.93
	5/12	132	29.7	28.7	1.03
AVG					1.04
COV					8.7%

Table 7.4 Comparison with the Recommended Approach: Tests by Drysdale et al

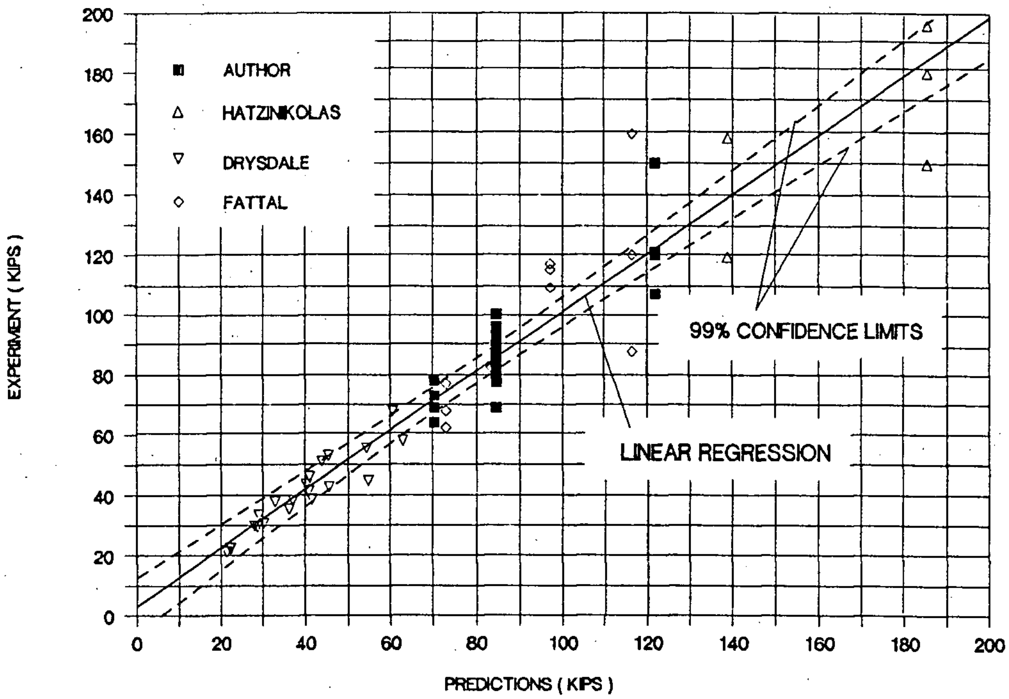

FIG. 7.12 Comparison between Recommended Approach and Experiments: Summary

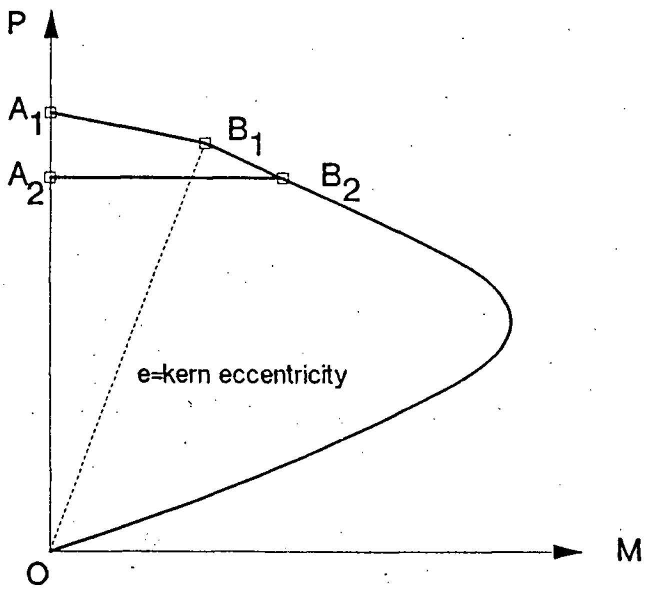

FIG. 7.13 Depiction of Recommended Approach

based on the masonry unit strength f'_u and the geomerty of the cross-section, where B_1 denotes the kern eccentricity capacity ($e = t/6$). A_1 or A_2, which stands for the concentric capacity, should be determined either by the prism test or by the correlation with the masonry unit strength f'_u and the mortar strength f'_j. The whole capacity curve is represented either by $A_1 - B_1 - O$ or by $A_2 - B_2 - O$ depending whether the concentric capacity is greater than the kern eccentricity capacity.

7.2 Discussion of The Current Design Code

The current design code (CAN3-S304-M84, 1984) permits two ways of designing walls for carrying in-plane axial compression and out of plane bending due to eccentricity of the vertical load. They are the so-called "coefficient method" and the "load deflection method". The former gives an additional alternative to determine the eccentricity coefficient. Therefore, one actually could develop three different $P-M$ design curves for the same member. We denote them by method 1, 2 and 3 for ease of discussion.

The basic information needed for design is f'_m, the ultimate compressive strength of masonry. The code specifies two methods to determine f'_m. Method A requires testing of at least five prisms in uniaxial compression. f'_m is then taken as the average strength minus 1.5 times the standard deviation of the sample. (This value may be reduced by a factor depending on whether the specified unit strength is consistent with the tested unit strength.) Method B allows one to test unit and mortar separately (the latter is to ensure that the specified mortar type is adequate) and f'_m is taken from the tabled value based on unit strength and mortar type.

The most obvious object of a design code is to ensure consistent reliability in structures. For flexural design of masonry walls, consistent reliability for various load combinations is required. The current code recognizes the apparent strength increase when walls are under eccentric loading, and some modifications are included in the conventional beam-column approach. This is reflected in method 1 by an increase in C_e, the eccentricity coefficient, of 30%

(this is fairly reasonable when compared with the author's experiments) when loading eccentricity is greater than $t/20$. For methods 2 and 3, this is reflected in the different allowable stresses that are used (compressive, flexural) in developing the $P-M$ interaction curve. Although the author has difficulty in understanding why the code allows quite different results by the three different methods for walls loaded with equal eccentricities, we will consider here the implications of present research with respect to these provisions.

First of all, it was concluded that the prism strength does not correlate well with the strengths of mortar and unit. This suggests that there is considerable uncertainty in the use of method B to avoid making axial prism tests. For the fully bedded prisms tested by the author, method A would give f'_m equal to 1760, 2625 and 1930 psi for prisms with M, S, and N type mortar respectively. Method B, which is based on the correlation between prism strength and strengths of unit and mortar, would give f'_m equal to 1855 psi for prisms with M and S type mortar and 1430 psi for prisms with type N mortar[2]. This is very inconsistent, especially in terms of the probability of non-exceedence of the strength value. f'_m determined by method A corresponds to a non-exceedence probability of about 6.7% for all three type mortar prisms, while f'_m determined by method B gives the non-exceedence probability of about 12% for M type mortar prism, 0.001% for S type and 0.03% for N type mortar prisms. The conclusion is clear: method B cannot be recommended, or it should be used very conservatively. The current code may already be on the very conservative side in most cases, but it can not prevent unfavorable results in some particular cases, such as the type M prism in the above example.

Second, the code requires that the design be based on f'_m. However, f'_m is the strength of masonry under uniaxial compression. It was concluded that, because of the different failure mechanisms, this strength does not correlate well with the flexural compressive strength, which

---

[2]Here we only have a sample size of 4 and we relax the 15% restriction on coefficient of variation for M type mortar masonry prism.

is much less dependent on the joint condition and bedding pattern. The code only takes account of the apparent increase in strength by allowing an increase in the design stress for masonry under eccentric loading of a fixed amount, i.e. 30% in method 1 and 20% in method 2 and 3 (some interpolation is involved in methods 2 and 3). This implies that a relationship is assumed between uniaxial strength and flexural strength of masonry which is independent of joint pattern and mortar type. In other words, since uniaxial compression strength depends largely on the joint condition and bedding pattern, the strength under eccentric loading also depends largely on these variables, according to the code. The study in the preceding sections indicates that this is not the case. The strength of masonry under eccentric compression may be better correlated with the unit compressive strength. Thus, inconsistency in the reliability of wall capacity as designed by the current code may be expected.

For example, for the 58 experimental cases studied above, including eccentrically loaded prisms of wall sections tested by the author and others, the flexural compressive stress at failure was calculated (based on the assumption that stress is linearly distributed in the cross-section), and listed in Table 7.5 to Table 7.8 and summarized in Fig. 7.14. The average ratio of the flexural strength to uniaxial compressive strength was 1.21 with a coefficient of variation equal to 13.3%.

Although the average 21 percent higher flexural compressive strength is close to the eccentric coefficient specified by the code (method 2 and method 3), the coefficient of variation is higher than that of the recommended method (11.4%). Fig. 7.14 shows the comparison between axial and flexural strengths for the reported tests, which has a coefficient of correlation of only 0.875, comparing unfavorably with that of 0.956 for the recommended method. The superiority of the recommended method over the code specified method is obvious in view of Figs. 7.12 and 7.14.

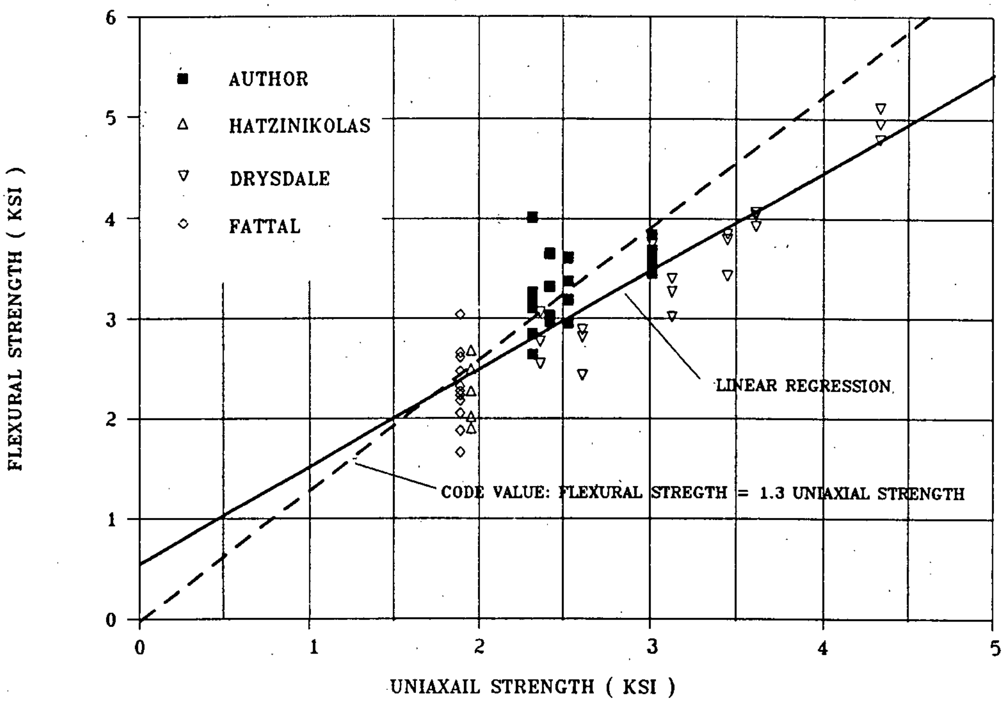

FIG. 7.14 Current Design Base: Uniaxial Strength versus Flexural Strength

	N18 (e=1/6t) f'_m=2.32 ksi (prism test)		N19 (e=1/3t) f'_m=2.32 ksi (prism test)		M20 (e=1/3t) f'_m=2.42 ksi (prism test)		S21 (e=1/3t) f'_m=3.02 ksi (prism test)		N22 (e=1/3t) f'_m=2.52 ksi (prism test)	
	f'_e(ksi)	f'_e/f'_m	f'_e(ksi)	f'_e/f'_m	f'_e(ksi)	f'_e/f'_m	f'_e(ksi)	f'_e/f'_m	f'_e(ksi)	f'_e/f'_m
	4.01	1.73	3.38	1.37	2.97	1.23	3.68	1.22	2.96	1.17
	2.85	1.23	3.11	1.34	3.03	1.25	3.45	1.15	3.60	1.43
	3.20	1.38	3.26	1.41	3.32	1.37	3.84	1.27	3.19	1.26
	3.22	1.39	2.65	1.14	3.65	1.51	3.57	1.18	3.37	1.34
AVG	3.32	1.43	3.05	1.31	3.24	1.34	3.63	1.21	3.28	1.30
COV		12.8%		7.8%		8.2%		3.9%		7.3%

Table 7.5 Flexural to Uniaxial Strength: Tests by Author

	e=1/12t $f'_m = 1.89$ ksi		e=1/6t $f'_m = 1.89$ ksi		e=1/4t $f'_m = 1.89$ ksi		e=1/3t $f'_m = 1.89$ ksi	
	f'_e(ksi)	f'_e/f'_m	f'_e(ksi)	f'_e/f'_m	f'_e(ksi)	f'_e/f'_m	f'_e(ksi)	f'_e/f'_m
	2.28	1.20	2.61	1.38	2.18	1.15	1.88	0.99
	1.67	0.88	2.47	1.31	2.23	1.18	2.33	1.23
	3.04	1.61	2.66	1.41	2.18	1.15	2.05	1.09
AVG	2.33	1.23	2.58	1.37	2.20	1.16	2.09	1.10
COV		24.1%		3.1%		1.1%		8.8%

Table 7.6 Flexural to Uniaxial Strength: Tests by Fattal et al

	e=1/6t $f'_m = 1.96$ ksi		e=1/3t $f'_m = 1.96$ ksi	
	f'_e (ksi)	f'_e/f'_m	f'_e (ksi)	f'_e/f'_m
	2.28	1.17	2.20	1.03
	2.49	1.28	2.68	1.37
	1.90	0.97		
AVG	2.22	1.14	2.35	1.20
COV		10.8%		14.2%

Table 7.7 Flexural to Uniaxial Strength: Tests by Hatzinikolas et al

SPECIMEN	e/t	f'_e (mpa)	f'_e (ksi)	f'_e/f'_m
normal block	1/6	28.0	4.06	1.12
(NB)	1/3	27.8	4.03	1.12
f'_m=24.9 mpa	5/12	27.0	3.91	1.08
weak block	1/6	19.4	2.81	1.08
(WB)	1/3	19.9	2.88	1.11
f'_m=18.0 mpa	5/12	16.8	2.43	0.93
strong block	1/6	34.0	4.93	1.14
(SB)	1/3	35.1	5.09	1.17
f'_m=29.9 mpa	5/12	32.9	4.77	1.10
lightweight block	1/6	25.8	3.74	1.24
(LB)	1/3	25.1	3.64	1.21
f'_m=20.8 mpa	5/12	25.3	3.67	1.22
75% solid	1/6	19.1	2.77	1.17
(QB)	1/3	17.6	2.55	1.08
f'_m=16.3 mpa	5/12	21.1	3.06	1.29
6 inch block	1/6	26.5	3.84	1.11
(6"B)	1/3	26.1	3.78	1.10
f'_m=23.8 mpa	5/12	23.6	3.42	0.99
10 inch block	1/6	20.8	3.01	0.96
(10"B)	1/3	23.4	3.39	1.08
f'_m=21.6 mpa	5/12	22.5	3.26	1.04
AVG				1.11
COV				7.7%

Table 7.8 Flexural to Uniaxial Strength: Tests by Drysdale et al

CHAPTER VIII

GROUTED MASONRY WITH FULL BEDDING

8.1 Introduction

In the west coast area of Canada, where earthquake resistance is a main concern in structural design, masonry walls and columns are required to be grouted and reinforced to improve structural continuity and ductility.

The axial capacity of grouted and reinforced masonry is of interest not only because it directly determines the design thickness of a wall providing axial and lateral load resistance in a multi—story building, but also, because it is closely related to the design ductility (Priestley and Hon 1983).

The methods for determining the compressive strength of grouted concrete masonry specified in the current code (CAN3-S304-M84, 1984) are essentially the same as those for plain concrete masonry, as reviewed in the preceding chapter. Method A, which requires a prism test, is not very practical. Since the failure load of a standard 8 inch grouted prism will usually be well above 300 kips, testing facilities with adequate capacity are extremely limited. Method B, which estimates the compressive strength based on the unit strength and mortar type, tends to be excessively conservative due to the uncertainties involved. The code does not correlate the masonry compressive strength with grout strength, but merely requires that the grout strength be at least equal to that of the block shell. On the one hand, this does not allow one to take advantage of high strength grouting, and on the other hand, it is a difficult specification to meet since the unit strength is often much higher than the specified value (cf. Tables 8.3—8.9). If the failure mechanism is dependent on the relative strengths, it will be correspondingly uncertain.

The axial behaviour of grouted concrete masonry has been studied both experimentally and analytically. Drysdale and Hamid (1979) first addressed the compatibility problem between masonry unit and grout based on their experimental observations. Akio Baba and Osamu Senbu (1986) proposed the concept of the grout efficiency, and found it varied considerably with different combinations of masonry unit and grout they tested. A few failure models have been suggested to predict the ultimate strength considering the interaction between unit, grout and mortar (Ahmad and Drysdale 1979, Priestley and Hon 1983). However, the internal forces of these models were entirely based on a state that all the three materials reach some assumed fracture criteria. This is not always a realistic description. Further, the fracture is not necessarily equivalent to ultimate state.

It is clear that a better understanding of the mechanical behaviour is needed and a more accurate estimate for masonry strength is desirable. In this study, the experimental behaviour of grouted masonry prisms is carefully examined and a better correlation of the masonry strength with the unit strength, grout strength and mortar strength is sought.

8.2 Experimental Observations

23 grouted prisms were tested under uniaxial compression, with various joint and grouting conditions. The failure loads of the prisms are summarized in Tables 8.1 and 8.2. The grout strengths, evaluated by testing in accordance with CSA Standard (A179—1976), are listed in Table 2.5.

The experiments indicate:

1) Both mortar strength and grout strength affect the prism strength. Apparently stronger mortar and grout make stronger masonry (see Tables 8.1 and 8.2). However, the increase in masonry capacity is minor, even with a substantial increase in the constituent strengths, as depicted in Fig. 8.1. This is especially true for grout, suggesting that the contribution of grout and block shell (including mortar joint) to the capacity of masonry is a function of their compatible deformations, and is not simply given by superposition of their individual capacities. This observation confirms that by Drysdale and Ahmad (1979).

2) Deformation measurements and direct observation (recorded by a video camera) indicate that almost all the prisms were cracked before final failure. Cracks were found in the webs as well as

in the face-shell, occurring at loads as low as 40% of the failure value, as evidenced by the recorded deformations in Figs. 8.2, 8.3 and 8.4. Similar observations have been reported by Sturgeon and Longworth (1985). Using acoustic measurement, Akio Baba and Osamu Senbu (1986) have also observed more detailed cracking process well before ultimate state for grouted prisms with bond beam concrete unit. This premature cracking may have been caused by the incompatibility between the grout and the block shell, as will be further studied below. However, closer inspection shows that the block shell still carried substantial load after cracking, indicating that premature cracking is not necessarily equivalent to failure. We know this mainly from two facts: a) The vertical deformation measurement of the block shell shows that the compressive strain remained at a high level after cracking had occurred (cf. Figs. 8.2-8.4). b) The capacity of the prism is usually substantially greater than that of grouting concrete alone.

3) Block shells are stiffer than concrete grout which in turn are stiffer than mortar. The peak strain is between 0.0015 to 0.002 for the block unit and 0.0025 to 0.003 for three types of grout (see Figs. 2.3, 2.4 and 2.6 in Chapter II). A similar phenomenon has been indicated by the research on concrete masonry in New Zealand (Priestley and Elder 1985). The Young's modulus of various concrete units (used in Japan) are also appearently higher than that of grout according to Akio Baba and Osamu Senbu (1986). The mortar even exhibited higher peak strains, which exceeded 0.005 (measured during the cube strength testing). The difference in the deformation properties is probably due to different material textures and curing conditions. This observation supports the view that compatibility plays an important role in concrete masonry capacity. The vertical deformation measurements, indeed, indicated that the block shells carried a larger share of load relative to the grout before they cracked; after cracking, the shell continued to carry a substantial portion of the load, although in some cases there was a slight decrease.

SPECIMEN	1	2	3	4	AVG	COV
M9 (NG, MJ)*	333.0	333.0	310.5		325.5	3.3%
S8 (NG, SJ)	303.0	264.0	321.0		296.0	8.0%
N13 (NG, NJ)			237.0	332.0	284.5	16.7%
N10 (NG, t_o=6/8")		302.0	300.0	273.5	291.8	4.5%
P11 (NG, t_o = 0)	274.0	234.0	312.5		273.5	11.7%
N17(NG,Face-Shell)		252.0	240.0	258.0	250.0	3.0%

Table 8.1 Failure Loads of Grouted Prisms (kips), with Variation in Joint Condition

* NG – Type N Grout; NJ – Type N Mortar Joint, etc.

SPECIMEN	1	2	3	4	AVG	COV
N12 (SG, NJ)		316.0	291.0	254.0	287.0	8.9%
N13 (NG, NJ)			237.0	332.0	284.5	16.7%
N14 (WG, NJ)		257.0	241.0	289.0	262.3	7.6%

Table 8.2 Failure Loads of Grouted Prisms (kips), with Variation in Grout

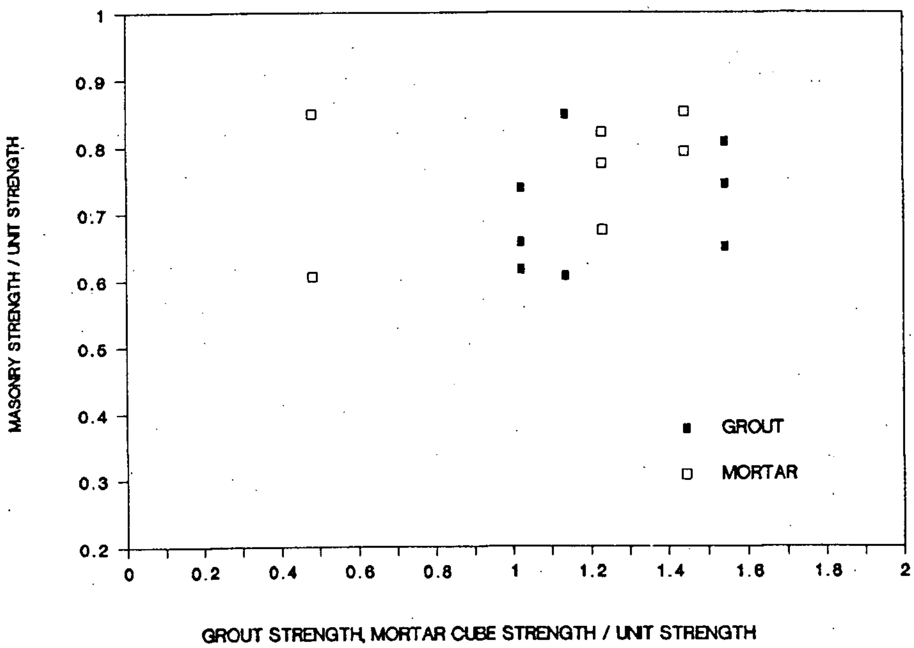

FIG. 8.1 Grouted Prism Strength Versus Mortar Strength and Grout Strength

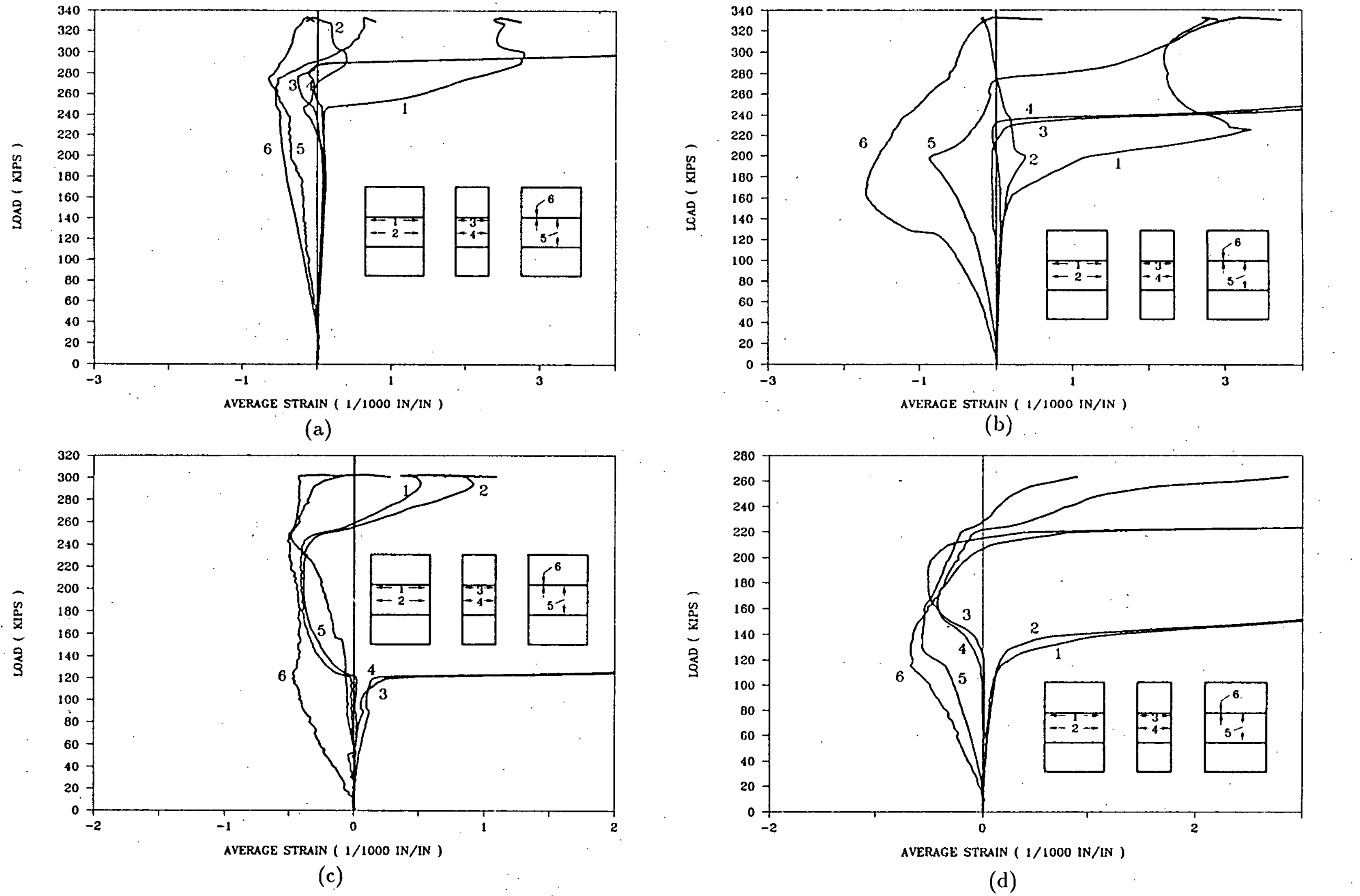

FIG. 8.2 Measured Deformations at Certain Locations of Grouted Prisms under Concentric Load: a) M9-1; b) M9-2; c) S8-1; d) S8-2

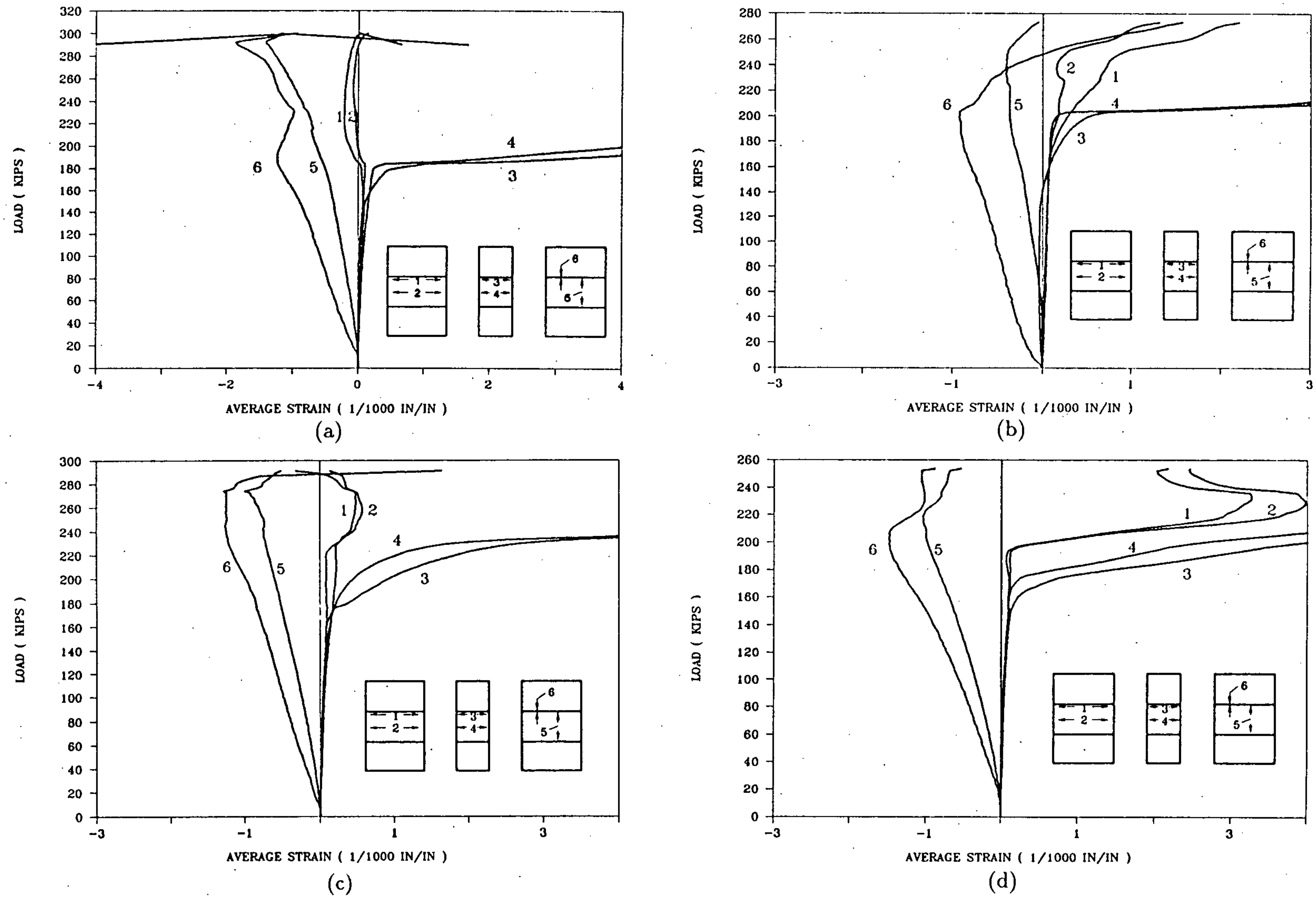

FIG. 8.3 Measured Deformations at Certain Locations of Grouted Prisms under Concentric Load: a) N10-3; b) N10-4; c) N12-2; d) N12-4

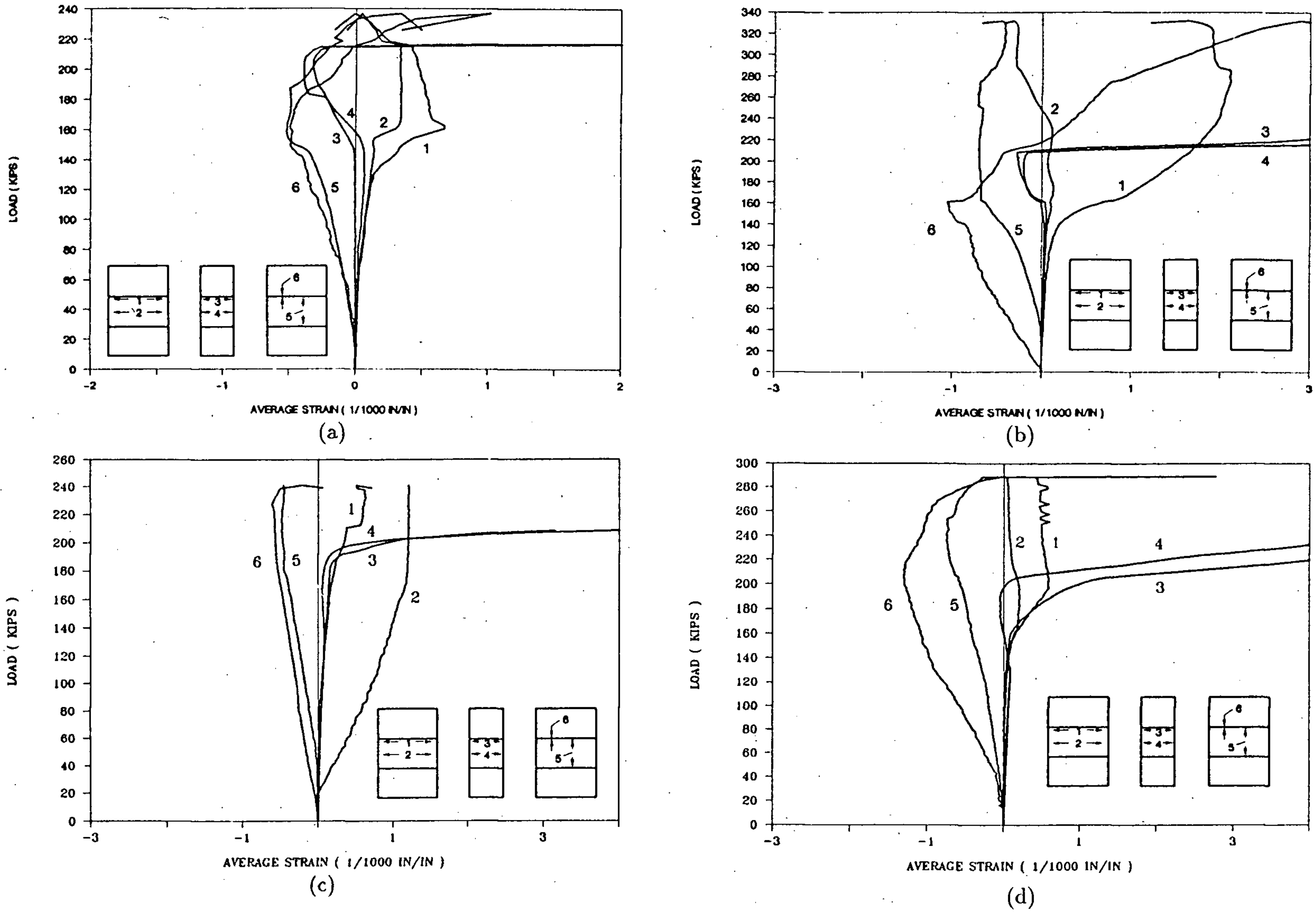

FIG. 8.4 Measured Deformations at Certain Locations of Grouted Prisms under Concentric Load: a) N13-3; b) N13-4; c) N14-3; d) N14-4

8.3 Analysis

Although there is considerable scatter in the strength data obtained by the author and in numerous previous studies, one conclusion can be drawn with certainty: that the capacity of the block unit and that of the grout are not simply additive. This obviously results from the difference in deformation properties of the materials, as discussed in the preceding paragraph. We consider two aspects of this deformation compatibility problem:

First, vertical compatibility. Since the grout and the block unit usually have different peak strains, as shown by experiment, they are not able to reach their full capacities at the same strain. From this viewpoint it is obvious that simple capacity addition is not valid. The efficiency of the grouting will depend on how close the deformation properties of the two materials are.

Second, horizontal (or cross-sectional) compatibility. This includes two parts. One is due to the different Poisson's effect of grout and block shell. The other is due to the geometry: for manufacturing reasons, the hollow core of a concrete masonry block is actually tapered with a release angle $1^\circ - 3^\circ$. This may introduce an additional cross-sectional compatibility problem when grout and block shell undergo different vertical strains.

The premature cracking observed in experiments is certainly caused by these cross-sectional incompatibilities.

Thus, a failure model of grouted masonry based on deformation compatibility will be closer to reality than one based on strength superposition. This will serve as a guideline for the following model development.

It may be useful to list all the notation applied in the model:

$A_g,\ A_n$ = gross area and net area of block unit, respectively;

$2a,\ 2b$ = width of block inner core and block unit, respectively;

$E_u,\ E_g,\ E_j$ = modulus of elasticity of block unit, grout, mortar joint, respectively;

f'_{mp}, f'_{mg} = compressive strength of plain masonry and grouted masonry, respectively;

f'_u, f'_g, f'_j = compressive strength of block unit, grout (prism strength), mortar (cube strength), respectively;

f'_{ut} = tensile strength of block unit;

h_o = height of block unit;

m_1, m_2 = modular ratio of E_u/E_g and E_u/E_j, respectively;

p = contact pressure between grout and block shell;

t_o = thickness of mortar joint;

α = release angle of block inner core;

ϵ_u, ϵ_g, ϵ_j = compressive strain in block unit, grout and mortar joint, respectively;

η = net area to gross area ratio of block unit A_n/A_g;

ν_u, ν_g, ν_j = Poisson's ratio of block unit, grout and mortar, respectively;

σ_m, σ_s = compressive stress in masonry (average) and in masonry shell, respectively;

σ_u, σ_g, σ_j = compressive stress in block unit, grout and mortar joint, respectively;

σ_{ut} = lateral tensile stress in block unit;

In general, the capacity of grouted masonry depends on many factors, most importantly:

* the strength of the materials f'_u, f'_{ut}, f'_g, f'_j

* the deformation properties of the materials E_u, E_g, E_j, ν_u, ν_g, ν_j

* geometric properties such as the shape of the block units, the thickness of the mortar joint, bond pattern, etc.

* workmanship, test method

To make the model practically useful, we neglect those effects which are not easy to quantify, such as workmanship or test method. We will also try to avoid explicitly including the deformation properties in the model, since they are difficult to measure. Further, we use η, the net to gross cross-sectional area ratio and α, the inner core release angle to characterize the geometry of a block unit. We will assume that the grout core is approximately square, and thus the model may be generally useful for grouted hollow concrete masonry with various dimensions.

It may be useful in the following derivation to first find some simple approximate relations between η and the dimensions of a masonry unit. By the definition and the assumption stated, we can write

$$\eta = 1 - \left(\frac{a}{b}\right)^2 \tag{8.1}$$

or

$$\frac{a}{b} = \sqrt{1 - \eta} \tag{8.2}$$

In the derivation, an expression for $(b-a)/a$ is needed. Eq. 8.1 can be rewritten as

$$\frac{b - a}{b} = \frac{\eta}{1 + a/b}$$

When a/b is expanded as $1 - \eta/2$ in view of Eq. 8.2, the above expression becomes

$$\frac{b - a}{b} \approx \frac{2\eta}{4 - \eta} \tag{8.3}$$

which gives good approximations even when η is as large as 0.6. Based on Eq. 8.3, it is easy to obtain

$$\frac{b - a}{a} \approx \frac{2\eta}{4 - 3\eta} \tag{8.4}$$

Although the determination of the stress state in grouted masonry is actually a three dimensional problem, which is further complicated by the inelastic behaviour of the materials,

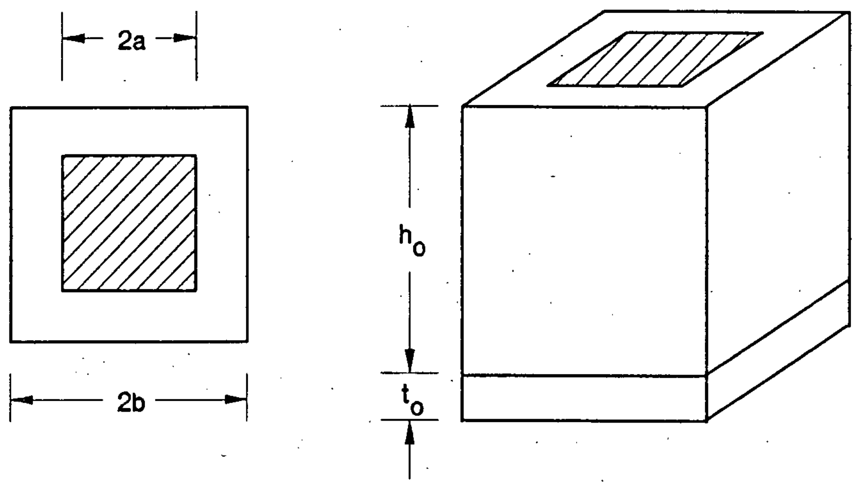

FIG. 8.5 A Grouted Masonry Prism with Square Cross-Section

for the sake of simplicity and practicality, we adopt a quasi-elastic approach. That is, we use the theory of elasticity and implicitly assume that the deformation properties involved are taken as secant or effective values. Further, we assume that stress and strain in the materials are uniform, or, in other words we treat the stress and strain in an average sense in each material.

For the prism shown in Fig. 8.5, the following relations can be written.

A) In Vertical Direction

Equilibrium:

$$\sigma_m = \eta\sigma_s + (1-\eta)\sigma_g \tag{8.5}$$

If the shear force between the block shell and grout is neglected, we have

$$\sigma_s = \sigma_u = \sigma_j$$

Compatibility:

$$\epsilon_g = \frac{\epsilon_u h_o + \epsilon_j t_o}{h_o + t_o} \approx \epsilon_u + \left(\frac{t_o}{h_o}\right)\epsilon_j \qquad 8.6$$

Stress–Strain Relation:

For grout we have

$$\epsilon_g = \frac{\sigma_g - 2\nu_g p}{E_g} \qquad 8.7$$

For the block shell, an expression for the vertical strain due to the contact pressure p is needed. This can be obtained by Betti's law. Referring to Fig. 8.5, we have

$$4(2a)h_o p \; \delta(\sigma_s) = A_n \sigma_s h_o \; \epsilon_u(p)$$

where $\delta(\sigma_s)$ is the lateral displacement due to the vertical stress, expressed as

$$\delta(\sigma_s) = \frac{\sigma_s \nu_u a}{E_u}$$

and $\epsilon_u(p)$ is the vertical strain in the unit due to the lateral pressure p. Upon substitution and rearranging, one finds

$$\epsilon_u(p) = \frac{2p\nu_u(1-\eta)}{\eta E_u}$$

Thus the vertical stress–strain relation of the block shell is

$$\epsilon_u = \frac{\sigma_s + 2p\nu_u(1-\eta)/\eta}{E_u} \tag{8.8}$$

The stress–strain relation for the mortar joint is

$$\epsilon_j = \frac{\sigma_s}{E_j} \tag{8.9}$$

B) In Lateral Direction

Equilibrium:

$$2ap = 2(b-a)\,\sigma_{ut}$$

or

$$\sigma_{ut} = \frac{ap}{b-a} \approx \frac{(4-3\eta)p}{2\eta} \tag{8.10}$$

in which the relation given by Eq. 8.4 has been used.

Compatibility:

$$\frac{(\nu_g\sigma_g - p)a}{E_g} = \frac{(\sigma_{ut}+\sigma_s\nu_u)a}{E_u}$$

where we assume that the lateral deformation of the block unit is the sum of the Poisson's effect and the stretch due to the lateral tensile stress in the block unit. If the lateral deformation due to the tapered core is included, which may be modeled as the grout acting as a wedge being driven into the block core, the compatibility condition can be rewritten as

$$\alpha\left(\frac{h_o}{a}\right)(\epsilon_g - \epsilon_u) + \frac{(\nu_g\sigma_g - p)}{E_g} = \frac{(\sigma_{ut}+\sigma_s\nu_u)}{E_u} \tag{8.11}$$

The above seven equations can be used to determine the stress and strain state in a grouted masonry prism when a vertical stress or strain is imposed.

C) Failure Conditions

There are several possible ways for a grouted concrete masonry assembly to fail. They include chiefly: a) Premature splitting of the block shell due to the incompatible material properties of the grout and the block, which give rise to tensions in the shell. b) If the assembly survives this condition, failure may occur when the sum of the shell and grout resistances reaches a maximum, at a deformation between their respective peak strains. c) The assembly may fail when the grout reaches its full capacity; at this point the substantial volume increase due to the internal cracking of the grout causes the block shell to fail. Whichever the case, the lower bound of the masonry strength should be always satisfied:

$$f'_{mg} \geq (1 - \eta) f'_g \qquad 8.12$$

which corresponds to the failure load being carried by the grout alone.

For normal range of η, failure condition c) requires that the peak strain of the grout be reached first. However this is unlikely to be the case, in view not only of the experiments by the author and of those done in New Zealand, which have indicated that the concrete block units were stiffer than grout, but also of the experimental observations by several other researchers that the grout core was intact even after masonry specimens had failed (Drysdale and Hamid 1979; Hatzinikolas et al 1978).

Failure condition a), of course, is governed by the block shell. However, to determine the failure load for condition b), a knowledge of the deformation properties of the materials over entire strain range is needed. Since this information is difficult to establish, as a practical alternative, we may inquire which material, block shell or grout, is closer to its full capacity at the point of failure of the assemblage. In the light of the study in Chapter II, one may tend to believe that the block shell, which is formed by fine aggregate concrete, would be "less ductile" than the grouting concrete in the post—peak range; thus the failure strain of masonry would be closer to the peak strain of the block shell, if the latter is assumed to be the stiffer component. Or in other words, masonry is likely to fail immediately after the full capacity of the block shell is reached, because the stress in the block shell will decrease drastically once its peak strain is exceeded. Although it is difficult to justify this assumption directly by experimental observation, it may be verified statistically, i.e. by correlating the masonry capacity with the block shell strength and with the grout strength. A multiple linear regression on the experimental data from 7 different sources (including the experiments conducted by the author) indicates that the masonry capacity is much more closely correlated to the block unit strength. Thus the assumption is supported by the statistical implications. Of course, this also strengthens the argument that failure condition c) is unlikely to occur.

Therefore, whether grouted masonry fails by condition a) or b), it is reasonable to assume the block shell will govern the failure state. We may only consider the solution for failure condition a), since condition b) may be included as a particular case. If the Coulomb-Navier failure criterion is assumed, one writes

$$\frac{\sigma_s}{f'_{mp}} + \frac{\sigma_{ut}}{f'_{ut}} = 1 \qquad 8.13$$

Eq. 8.5 to Eq. 8.11 with Eq. 8.13 can be used to find the 8 unknowns; namely ϵ_u, ϵ_g, ϵ_j, σ_s, σ_g, σ_m, p and σ_{ut}. The capacity of the grouted masonry, in terms of the masonry strength f'_{mg}, is equal to σ_m, since once Eq. 8.13 is included, the group of equations is actually solved at the critical condition.

Upon substituting and neglecting higher order terms, we get

$$f'_{mg} = \frac{\left[\eta+(1-\eta)\left(1+m_2\frac{t_o}{h_o}\right)\frac{1}{m_1}\right] f'_{mp}}{1 + \frac{4-3\eta}{4-\eta(3-2m_1)}\left[(\nu_g-\nu_u) + m_2\left(\alpha\frac{t_o}{a}+\nu_g\frac{t_o}{h_o}\right)\right]\frac{f'_{mp}}{f'_{ut}}} \tag{8.14}$$

It is interesting to examine the physical interpretation of this solution. The numerator represents the capacity of grouted masonry determined by considering only the vertical compatibility of the deformation properties. It means that without the difference in lateral properties, which will lead to failure condition b), the failure load of grouted masonry would be composed of two parts. One is the plain masonry strength times the net area of the block unit. The other is the product of the stress in the grout, which, due to the difference in stiffness, reaches $1/m_1$ times the stress in the block shell, with the grouted area. The factor $m_2 t_o/h_o$ takes account of the "softer" mortar joint, indicating that the latter tends to increase the stress in the grout.

The denominator accounts for the cross-sectional compatibility. It can be seen that the masonry strength f'_{mg} is an increasing function of η, indicating that the cross-sectional incompatibility becomes less important as the thickness of the block shell increases. The big square bracket contains some very small quantities. The term $(\nu_g-\nu_u)$, which is implicitly assumed to be greater than or equal to zero in the derivation, represents the incompatibility due to the difference in Poisson's effect of the two materials. The term $m_2\alpha(t_o/a)$ accounts for the incompatibility caused by the tapering of the core. The term $m_2\nu_g(t_o/h_o)$ implies the effect on the incompatibility of the softer mortar joint, which needs more detailed explanation.

Since the mortar is usually much softer than the block units, as indicated by experiment, the grout is actually strained more than the block unit in the vertical direction, due to the presence of the joint. Thus even if the block unit and grout have the same value of Poisson's ratio, the grout will expand more, laterally, than the block shell, causing additional cross-sectional incompatibility. It is clear that the masonry strength f'_{mg} is a decreasing function of these 3 terms appearing in the square bracket of the denominator.

Obviously, the denominator would reduce to unity if there were no lateral compatibility effect. In other words, the numerator predicts the ultimate failure load of failure condition b) when the prism survives failure condition a).

To make the model practically useful, some simplifications are necessary. Since the term $m_2 t_o/h_o$ is usually small compared with 1, e.g., for standard 8 inch block units, t_o/h_o is smaller than 0.05 and m_2, the secant modular ratio is around 3 according to the author's experiments (see Fig. 2.5 in Chapter II), we may neglect its variation by assuming $(1+m_2 t_o/h_o)$ in the numerator to be a constant slightly bigger than unity. By a similar argument, the term $\eta(3-2m_1)$ in the denominator can be neglected since it is small compared with the term 4. The variation of the term $\alpha t_o/a$ may also be ignored since it is small compared with $\nu_g(t_o/h_o)$; and for the geometry of a standard 8 inch block these two terms give approximated 0.015. Although it appears that the cross-sectional incompatibility would be mainly caused by the lateral expansion due to Poisson's effect on the grout, as believed by some researchers (Drysdale and Hamid 1979), we may neglect the variation of the term $(\nu_g-\nu_u)$ by replacing it with a constant ι, say, not exceeding 0.1. Due to the difference in the stiffness between grout and block shell, the block shell tends to be more stressed at failure. This view is also supported by the statistical argument stated above that masonry capacity is governed more by the block shell. Thus the effective ν_g will not increase as much as ν_u around the critical state due to internal cracking. The last term f'_{mp}/f'_{ut}, the ratio of the block shell strength to block unit tensile strength, may be assumed to be a constant ζ in the order of 10. Thus for the geometry of a standard 8 inch block, Eq. 8.14 can be simplified to

$$f'_{mg} = \frac{\left(\eta + (1-\eta)\frac{1}{m_1} \right) f'_{mp}}{1 + \zeta \left(\iota + 0.015 m_2 \right) \frac{4-3\eta}{4}} \qquad 8.15$$

Eq. 8.15 is based on fracture of the block shell, which may or may not lead to collapse of the masonry assemblage, as discussed earlier. Thus Eq. 8.15 predicts the load for failure condition a): fracture of block shell leads to final failure. However if the assembly survives this condition, the ultimate failure load is given by the numerator of Eq. 8.15 by neglecting cross-sectional incompatibility. Eq. 8.15 then corresponds to merely the cracking load of the block shell.

From the experiments conducted by the author and by numerous other researchers, it appears that either failure condition can occur. This poses the problem in practice as to which solution should be used in predicting masonry capacity. This question, again, may only be answered in a statistical sense. We may examine the available experimental data to see whether one of the two failure conditions has a probability of occurrence high enough to dominate the failure mode.

To correlate the available experimental data, expressions for f'_{mp}, m_1 and m_2 are needed. In view of the study in Chapter III, for normal joint thickness, the expression for f'_{mp} may be taken in the form as given by Eq. 4.28. i.e.

$$f'_{mp} = c_1 f'_u + c_2 f'_j \qquad 8.16$$

Further, the modular ratios may be related to the strength values as

$$m_1 = k_1 \sqrt{f'_u / f'_g} \qquad 8.17$$

and

$$m_2 = k_2 \sqrt{f'_u / f'_j} \qquad 8.18$$

where c_1, c_2, k_1 and k_2 are constants. The square root relation between the strength and the modulus of elasticity is adopted by many building codes.

We proceed to give an estimate for the constants involved in these relations. We will do this based on the 77 available data points from 7 different sources (Presents tests; Hamid and

Drysdale 1978; Boult 1979; Drysdale and Hamid 1979; Thurston 1981; Priestley and Elder 1982, 1985; Wong and Drysdale 1983). These actually include many more than 77 specimens because several of these data points were reported as average values. The data are summarized in Tables 8.3—8.9. The New Zealand results include f_j' values based on prisms. These have been converted to equivalent cube strength using the l'Hermite equation (Neville 1965).

The k values in Eq. 8.17 and Eq. 8.18 should make the equations yield the average values of m_1 and m_2 when the f_u', f_g' and f_j' take their mean values. According to the data, the ratios of the average unit strength to grout strength and to mortar strength are 1.04 and 1.5 respectively. The average value of m_1, according to the experimental results by the author and by the New Zealand researchers, may be taken as 1.32. The mean value of m_2 may be taken to be 3 as mentioned earlier. This leads to $k_1 = 1.29$ and $k_2 = 2.54$. Further c_1 and c_2 may be awarded the values given by Eq. 4.28.

For failure condition a) Eq. 8.15 is used while for failure condition b) only the numerator of the equation is applied. The results are also summarized in Table 8.3—8.9.

It appears that predicted failure loads based on failure condition a) substantially underestimate those obtained by experiments. The results based on condition b), however, correlate well with the experimental data, although it appears that they overestimate strength in the lower range. The correlation coefficient for the former is 0.894, while for the latter is 0.918. These results are plotted in Figs. 8.6 and 8.7 as predictions versus experiments. It is clear that the difference between the two methods is significant.

Thus, it may be concluded, based on the above study and on the available experimental data from various sources that, under normal construction conditions, the strength of grouted masonry is mainly governed by the vertical compatibility of the grout and block shell. Further, since the block shell is stiffer in the pre-peak range of strain, and less ductile in the post-peak range than grout, the masonry will tend to fail when the full capacity of the block shell is reached; thus the capacity of masonry is more closely correlated with block unit strength than with grout strength.

It should be noted that the above conclusion does not eliminate the possibility that the failure may occur in the form of condition c), and, especially condition a). It only means that failure condition b) has a predominant probability of governing.

η	f'_u	f'_j	f'_g	f'_{mg}	a	b	c
0.51	3.25	1.57	3.70	1.97	1.57	2.30	2.22
0.51	3.25	1.57	3.70	2.76	1.57	2.30	2.22
0.51	3.25	4.00	3.70	2.52	1.97	2.72	2.52
0.51	3.25	4.00	3.70	2.20	1.97	2.72	2.52
0.51	3.25	4.00	3.70	2.67	1.97	2.72	2.52
0.51	3.25	4.69	3.70	2.77	2.07	2.84	2.61
0.51	3.25	4.69	3.70	2.77	2.07	2.84	2.61
0.51	3.25	4.69	3.70	2.58	2.07	2.84	2.61
0.51	3.25	1.57	5.02	2.63	1.68	2.46	2.48
0.51	3.25	1.57	5.02	2.42	1.68	2.46	2.48
0.51	3.25	1.57	5.02	2.11	1.68	2.46	2.48
0.51	3.25	1.57	3.33	2.14	1.53	2.24	2.14
0.51	3.25	1.57	3.33	2.00	1.53	2.24	2.14
0.51	3.25	1.57	3.33	2.40	1.53	2.24	2.14

Table 8.3 Grouted Prisms, Tests by the Author

f'_{mg} — Experimental value of prism strength

a — Theoretical prediction of prism strength by failure condition a)

b — Theoretical prediction of prism strength by failure condition b)

c — Theoretical prediction of prism strength by failure condition c)

(All in ksi, same for the following tables)

η	f'_u	f'_j	f'_g	f'_{mg}	a	b	c
0.62	2.85	2.06	1.80	1.51	1.45	1.99	1.61
0.62	2.85	2.06	1.80	1.55	1.45	1.99	1.61
0.62	2.85	2.06	1.80	2.01	1.45	1.99	1.61
0.62	2.85	2.06	1.80	1.45	1.45	1.99	1.61
0.62	2.85	2.06	1.80	1.67	1.45	1.99	1.61
0.62	2.85	2.63	2.07	1.77	1.57	2.12	1.75
0.62	2.85	2.63	2.07	1.78	1.57	2.12	1.75
0.62	2.85	2.63	2.07	1.67	1.57	2.12	1.75
0.62	2.85	2.63	2.07	1.78	1.57	2.12	1.75
0.62	2.85	0.82	2.07	1.49	1.25	1.82	1.48
0.62	2.85	0.82	2.07	1.59	1.25	1.82	1.48
0.62	2.85	0.82	2.07	1.43	1.25	1.82	1.48
0.62	2.85	0.82	2.07	1.51	1.25	1.82	1.48
0.62	2.85	2.29	2.52	1.83	1.56	2.13	1.79
0.62	2.85	2.29	2.52	1.86	1.56	2.13	1.79
0.62	2.85	2.29	2.52	2.06	1.56	2.13	1.79
0.62	2.85	2.29	2.52	1.75	1.56	2.13	1.79
0.62	2.85	2.29	2.52	1.78	1.56	2.13	1.79
0.62	2.85	1.95	3.65	2.12	1.60	2.20	1.94
0.62	2.85	1.95	3.65	1.96	1.60	2.20	1.94
0.62	2.85	1.95	3.65	1.78	1.60	2.20	1.94
0.62	2.85	1.95	3.65	1.90	1.60	2.20	1.94
0.62	2.85	1.95	2.05	1.77	1.46	2.01	1.65
0.62	2.85	1.95	2.05	1.78	1.46	2.01	1.65
0.62	2.85	1.95	2.05	1.67	1.46	2.01	1.65
0.62	2.85	1.95	2.05	1.78	1.46	2.01	1.65
0.62	2.85	1.97	5.52	1.99	1.74	2.38	2.20
0.62	2.85	1.97	5.52	2.30	1.74	2.38	2.20
0.62	2.85	1.97	5.52	2.28	1.74	2.38	2.20
0.62	2.85	1.97	5.52	2.23	1.74	2.38	2.20

Table 8.4 Grouted Prisms, Tests by Hamid and Drysdale

η	f'_u	f'_j	f'_g	f'_{mg}	a	b	c
0.62	2.85	2.50	2.21	1.64	1.57	2.12	1.76
0.62	2.85	0.83	2.53	1.51	1.29	1.88	1.58
0.62	2.85	2.06	2.21	1.64	1.50	2.05	1.70
0.62	2.85	2.64	2.53	1.75	1.62	2.19	1.85
0.62	2.85	2.29	3.09	1.86	1.62	2.20	1.90
0.62	2.85	1.96	4.48	1.94	1.67	2.29	2.06
0.62	2.85	1.96	2.52	1.75	1.51	2.07	1.74
0.62	2.85	1.97	6.85	2.20	1.81	2.49	2.37
0.59	4.67	2.06	2.87	2.45	2.10	2.99	2.73
0.59	4.67	2.06	2.87	2.38	2.10	2.99	2.73
0.70	3.19	2.06	3.19	1.91	1.79	2.39	1.99
0.69	3.08	2.06	3.19	2.05	1.74	2.32	1.94
0.63	2.92	2.06	2.87	1.76	1.59	2.17	1.85
0.73	2.90	2.06	3.19	2.13	1.71	2.24	1.81
0.61	2.27	2.06	3.10	1.34	1.37	1.86	1.56
0.62	2.85	1.86	2.39	1.73	1.48	2.04	1.70
0.62	2.85	1.86	2.39	1.93	1.48	2.04	1.70

Table 8.5 Grouted Prisms, Tests by Drysdale Hamid

η	f'_u	f'_j	f'_g	f'_{mg}	a	b	c
0.51	2.78	2.72	4.93	2.16	1.75	2.45	2.35
0.51	2.78	2.72	4.93	2.10	1.75	2.45	2.35

Table 8.6 Grouted Prisms, Tests by Wong and Drysdale

η	f'_u	f'_j	f'_g	f'_{mg}	a	b	c
0.55	5.54	2.24	4.03	3.91	2.43	3.55	3.47
0.55	5.54	2.24	4.03	3.77	2.43	3.55	3.47
0.55	5.54	2.24	4.03	3.93	2.43	3.55	3.47
0.61	5.54	1.70	5.30	3.90	2.54	3.70	3.59

Table 8.7 Grouted Prisms, Tests by Priestley and Elder

η	f'_u	f'_j	f'_g	f'_{mg}	a	b	c
0.55	5.80	2.20	2.25	2.61	2.28	3.34	3.07
0.55	5.80	2.20	2.25	2.77	2.28	3.34	3.07
0.55	5.80	2.20	2.25	2.99	2.28	3.34	3.07
0.48	5.28	2.20	2.25	2.61	1.99	2.98	2.84
0.48	5.28	2.20	2.25	2.58	1.99	2.98	2.84
0.48	5.28	2.20	2.25	2.99	1.99	2.98	2.84

Table 8.8 Grouted Prisms, Tests by Boult

η	f'_u	f'_j	f'_g	f'_{mg}	a	b	c
0.52	2.41	2.79	3.75	2.12	1.54	2.13	1.93
0.52	2.41	2.79	3.75	2.16	1.54	2.13	1.93
0.61	2.83	2.79	3.75	1.68	1.74	2.35	2.07
0.54	4.12	2.79	3.75	2.70	2.08	2.93	2.80

Table 8.9 Grouted Prisms, Tests by Thurston

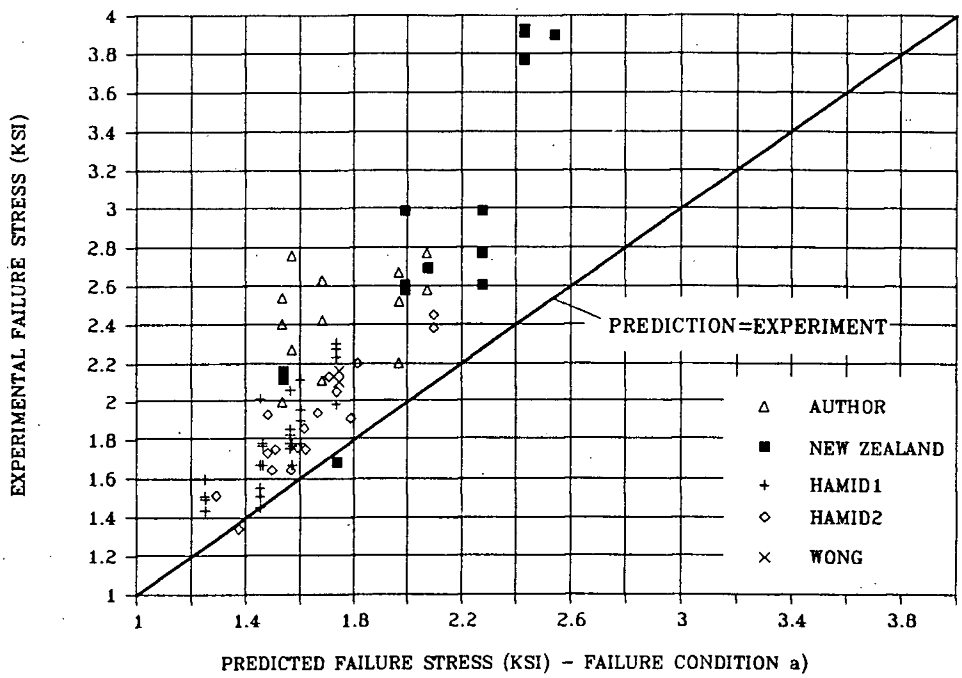

FIG. 8.6 Model Prediction versus Experiments, Based on Failure Condition a)

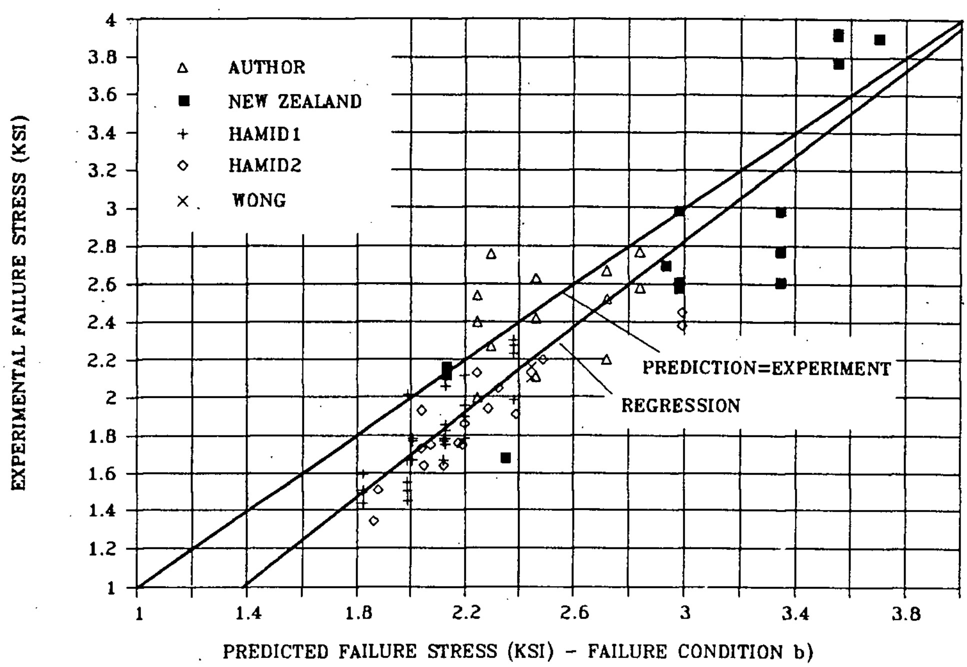

FIG. 8.7 Model Prediction versus Experiments, Based on Failure Condition b)

Therefore, it is not surprising to see that the prediction based on condition b) appears to overestimate the masonry capacity in the lower strength range, since if masonry fails in condition a), i.e. as the result of the premature failure of block shell, it will lead to a lower failure load.

It is clear that although we could use the numerator of Eq. 8.15 directly to estimate the grouted masonry capacity based on unit strength, grout strength, mortar strength and area ratio, some discrepancy should be expected since occasionally failure conditions other than condition b) may occur. Moreover, it is not desirable in practice to overestimate the masonry capacity. Therefore the equation may need empirical modification.

One modification may be to adjust the coefficient in the equation to best fit the available experimental data. Substituting Eqs. 8.16-8.18 and neglecting small quantities, the numerator of Eq. 8.15 may be expanded in the form of

$$f'_{mg} = A\eta f'_u + B(1-\eta)\sqrt{f'_g f'_u} + C\eta f'_j + D \qquad \text{(in ksi)} \qquad 8.19$$

A multiple regression analysis of the data gives:

$A = 0.53$

$B = 0.94$

$C = 0.24$

$D = -0.45$

Eq. 8.19 together with the lower bound given by Eq. 8.12 may be used to give an estimate for the ultimate capacity of grouted masonry. This estimate is also listed in Table 8.3—8.9 and plotted in Fig. 8.8 versus the data base. The relation has a correlation coefficient of 0.934, which is significant. However, the data used to evaluate parameters certainly do not all refer to failure condition b), and the correlation is affected by additional uncertainties such as workmanship and test method; and this is probably why a number of points fall outside the 99 percent confidence limit (see Fig. 8.8).

The model equation clearly reflects the fact that masonry capacity is not very sensitive to the grout strength, as observed by Drysdale and Hamid (1979) and by the author (see Tables 8.3, 8.5). The masonry strength is better correlated with the square root of the grout strength, based on the deformation compatibility. Indeed, linear regression on the basis of Eq. 8.19 in which $\sqrt{f_g' f_u'}$ is replaced by f_g', a form often seen in literature, indicates that it leads not only to a lower correlation coefficient of 0.907 but also to a much higher D value, which is not desirable.

The above analysis suggests that Eq. 8.15 may be used to estimate the cracking load of concrete grouted masonry. Unfortunately, no experimental data are available in terms of cracking loads except those recorded by the author. For these very limited data, the comparison is listed in Table 8.10 and plotted in Fig. 8.9, in which Eq. 4.16 is scaled down by a factor of 0.92. The cracking loads for the specimens with varying joint thickness are also included. Except for two data points (S8) the agreement is reasonable, considering the cracking load is a rather random event. The correlation coefficient for this case is 0.618, while prediction of failure loads it is 0.563, indicating that the load estimated by Eq. 8.15 is indeed more closely correlated with the cracking load than with the ultimate load.

One practical implication of the above study is that one should consider the cracking load estimated by Eq. 8.15 as the lower limit load in design, since block shell cracking is, in any case, not a desired event under normal service conditions. This usually can be achieved, since, in most small masonry buildings, the axial load levels are low and therefore the actual value of allowable stress is not critical. (It is noted that the cracking load estimated by Eq. 8.15 is around 70% of the ultimate load estimated by Eq. 8.19 or by the numerator of Eq. 8.15.) However, the ultimate load estimated by the model can be used as the final limit load under severe service conditions. For example, under earthquake loading, the axial capacity of masonry

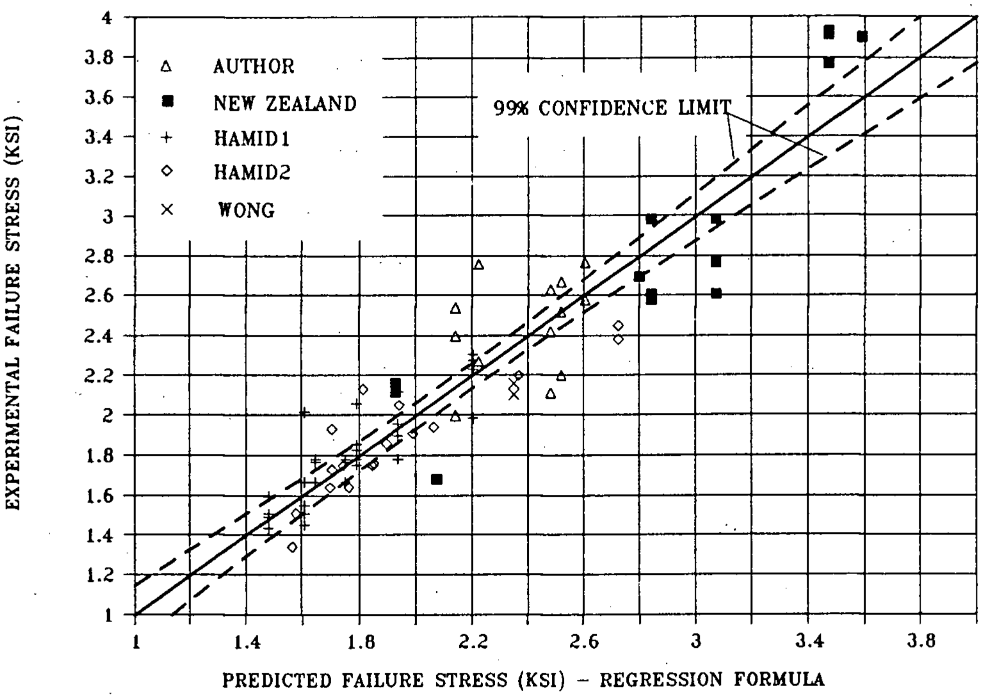

FIG. 8.8 Model Prediction versus Experiments, Based on Modified Equation

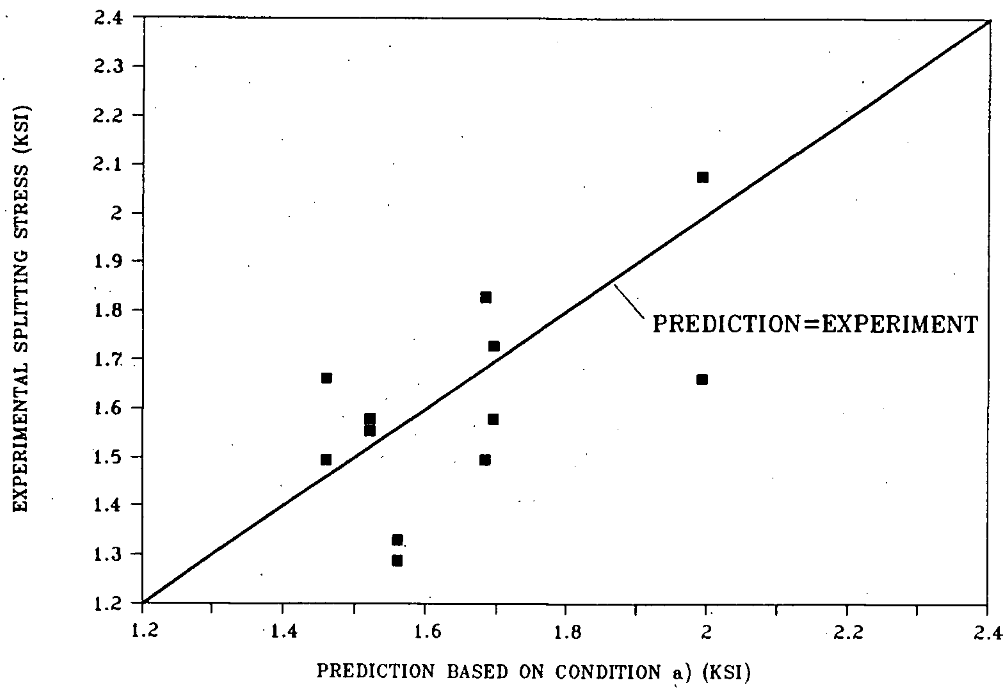

FIG. 8.9 Model Prediction versus Cracking Loads, Based on Failure Condition a)

can become critical not only because of the ductility requirement but also because of the inertia force itself. One may then take advantage of the higher ultimate strength by allowing a higher allowable stress based on Eq. 8.19. This is economical and certainly agrees with the risk philosophy commonly adopted in the earthquake engineering design, that some damage, even structural damage, is acceptable in the major event, but not collapse.

Finally, of course, the validity of Eq. 8.19 as a predictor of cracking loads needs further investigation. Many more experimental data are required in this respect.

8.4 Summary

In this chapter, the axial behaviour of grouted concrete masonry with full bedding has been investigated. Three possible failure conditions have been studied. A failure model based on internal deformation compatibilities has been proposed.

SPECIMEN	ult. load(kips)	crk. load(kips)	f'_{mg} (ksi)	f_{ck}(ksi)	Prediction (ksi)
S8-1	303.0	120.0	2.52	1.00	1.90
S8-2	264.0	130.0	2.20	1.08	1.90
N13-3	237.0	155.0	1.97	1.29	1.56
N13-4	332.0	160.0	2.76	1.33	1.56
M9-1	333.0	250.0	2.77	2.08	1.99
M9-2	333.0	200.0	2.77	1.66	1.99
N12-3	291.0	220.0	2.42	1.83	1.68
N12-4	254.0	180.0	2.11	1.50	1.68
N14-3	241.0	187.0	2.00	1.55	1.52
N14-4	289.0	190.0	2.40	1.58	1.52
N10-3	300.0	180.0	2.49	1.50	1.46
N10-4	273.0	200.0	2.27	1.66	1.46
P11-1	302.0	190.0	2.51	1.58	1.70
P11-2	300.0	208.0	2.49	1.73	1.70

Table 8.10 Model Prediction versus Cracking Loads, Tests by the Author

CHAPTER IX

GROUTED MASONRY WITH FACE-SHELL BEDDING

It is clear by the analysis in Chapter V, that under uniaxial compression face-shell bedded masonry will fail prematurely by a deep beam mechanism at a low load.

When face-shell bedded masonry is grouted, the deep beam bending mechanism will still be activated as the vertical force will be shared by the block shell and grout. This was shown by the experiments conducted by the author (see Fig. 9.1). The webs of the face-shell bedded and grouted prisms cracked vertically at a very low load owing to this mechanism. The vertical strain in the block shell drops much faster than that of the fully bedded counterparts, implying the hinging mechanism of the block shell studied in Chapter V.

However, the author's tests indicate that the cracking of the block shell due to the beam bending mechanism will not lead to ultimate failure of the masonry if the residual capacity of the grout is greater than the cracking load. Thus we may use

$$f'_{mg} = (1 - \eta) f'_g \qquad 9.1$$

as a lower bound or as a conservative estimate of the grouted masonry compressive strength.

For the author's tests, Eq. 9.1 underestimates the prism capacity by about 10%, as shown in Table 9.1, indicating a very low grouting efficiency. At failure, the load was only effectively sustained by the grout, as implied by the deformation measurement (see Fig. 9.1).

Eq. 9.1 underestimates the failure loads of the prisms tested by Drysdale and Hamid (1983) by a larger margin, indicating a higher grouting efficiency in their specimens. However, it seems reasonable in practical design to neglect the capacity of the block shell since this may not be a reliable quantity in view of the beam bending mechanism.

SPECIMEN		η	f_g' (ksi)	P (kips)	f_{mg}' (ksi)	$(1-\eta)f_g'$
A)	N17	0.51	3.70	252	2.09	1.81
	N–GROUT	0.51	3.70	240	2.00	1.81
	N–MORTAR	0.51	3.70	258	2.14	1.81
B)	NB GN	0.56	3.06	123	2.09	1.36
	NB GW	0.56	1.99	121	2.05	0.88
	NB GS	0.56	5.94	131	2.22	2.64
	WB GN	0.56	3.06	93.5	1.59	1.36
	SB GN	0.56	3.06	128	2.18	1.36
	QB GN	0.75	3.06	124	2.10	0.76
	6"B GN	0.51	3.06	86.6	1.99	1.50
	10"B GN	0.54	3.06	123	1.65	1.41

Table 9.1 Grouted Masonry with Face-Shell Bedding

A) – Tests by the author

B) – Tests by Drysdale and Hamid (1983)

The problem that remains unanswered is whether the cracking load should be used to govern the design. If so, more experimental work is needed and more attention should be directed to this value, since there have so far been few experiments monitoring premature cracking.

According to the author's tests, face-shell bedded, grouted masonry has a very low grouting efficiency, which may be even lower in terms of the cracking loads. This is because the two constituents do not work together properly. It appears that in the early stages of loading, the block unit takes a big share of the load as implied by the vertical strain measurements (cf. Fig. 9.1 and Fig. 5.3, locations 5 and 6). However, after the block shell is cracked, almost the whole load is passed to the grout. This is not desirable from a structural point of view.

It is clear that for grouted masonry full bedding is recommended, although, as indicated above, in practice that effective full bedding is sometimes difficult to achieve because of the web alignment. It is also obvious that the deformation properties of the two materials play an important role. Low grouting efficiency is inevitable unless there is a fundamental improvement in material design such that the deformation properties of grout and unit are more compatible.

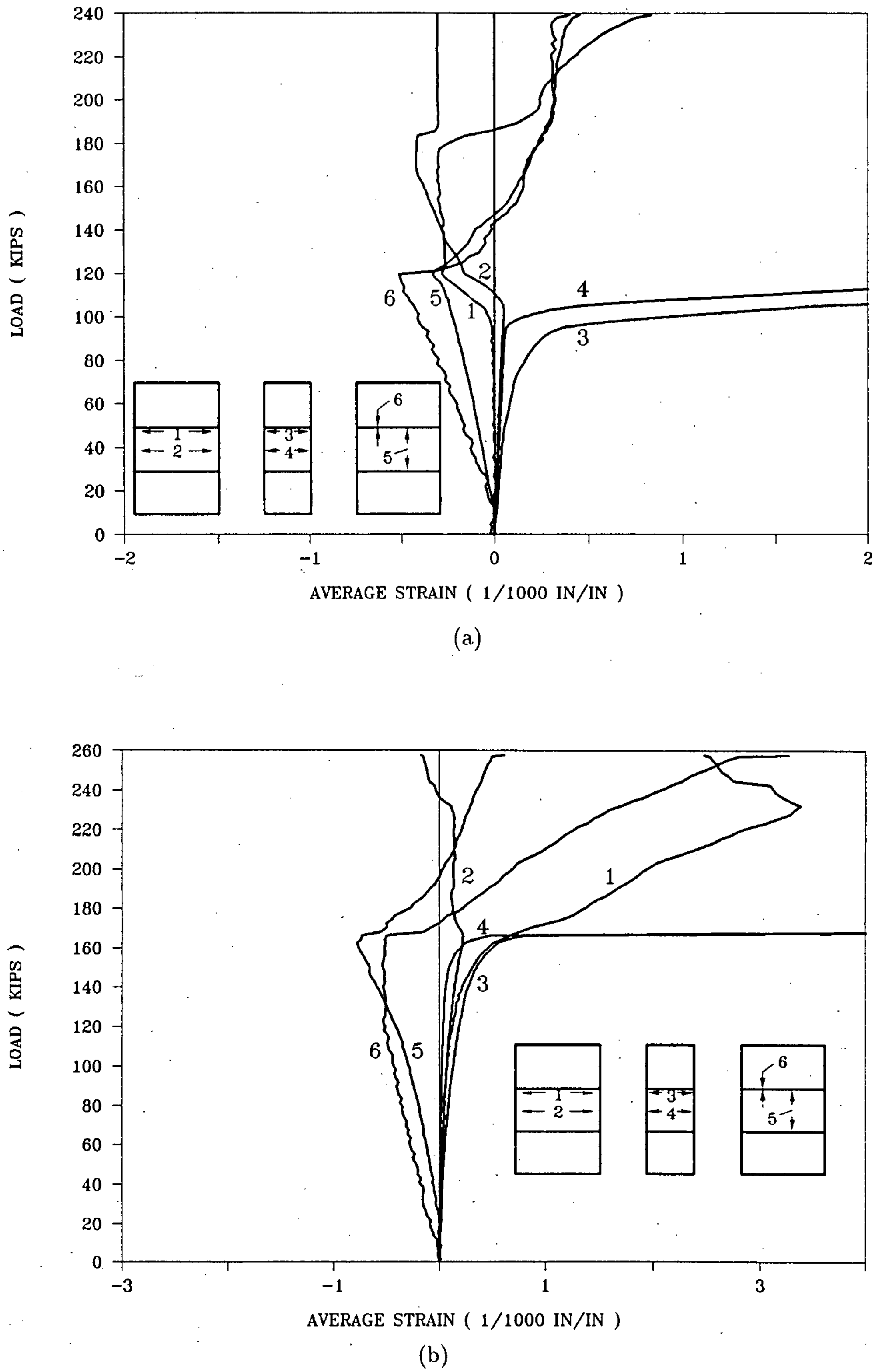

FIG. 9.1 Measured Deformations at Certain Locations of Grouted, Face-Shell Bedded Prisms under Concentric Compression: a) N17-3; b) N17-4

CHAPTER X

GROUTED AND REINFORCED MASONRY UNDER ECCENTRIC LOADING

10.1 General Remarks

Probably the biggest advantage of concrete masonry over traditional brickwork is that the concrete block units are hollow and can thus be vertically reinforced to improve the bending capacity. Bending capacity is essential for walls designed to sustain eccentric load or vertical force combined with laterally distributed pressure. This is obvious since theoretically the capacity of plain brickwork will be drastically reduced if the load falls outside the kern, and the wall can not support any load when the eccentricity reaches half the wall depth. With reinforcement, the improved bending capacity enables modern masonry structures to become taller and thinner, while preserving the traditional beauty of these structures.

Therefore, eccentrically loaded reinforced concrete masonry, which must be grouted, is of interest. In this chapter, experimental observations are first reviewed and the findings in the preceding chapters are placed in this context. Some useful relations will then be developed.

10.2 Experimental Observations

To study the basic behaviour of reinforced concrete masonry under compression and bending, 12 grouted prisms (without reinforcement) were tested under eccentric loading. The failure loads of these specimens are listed in Table 10.1 and the deformation measurements are plotted in Figs. 10.1 and 10.2. The failure process was recorded by a video camera for better observation.

The experiments indicate that under eccentric load, the joint condition and grouting condition do not have a significant influence on the masonry capacity (compare also the failure loads of plain ungrouted concrete masonry under eccentric load in Table 6.1). This is expected since the force shared by the grout diminishes with increasing eccentricity. In other words, the

SPECIMEN	e/t	1	2	3	4	AVG	COV
N26 (NJ,NG)	1/6	178.0	196.0	164.0	200.0	184.5	7.8%
M26 (MJ,NG)	1/3	106.0	92.0	82.0	128.5	102.1	17.1%
S25 (SJ,NG)	1/3	108.0	93.0	101.0	127.0	107.3	11.7%

NG — Type N Grout; NJ — Type N Mortar Joint, etc.

Table 10.1 Failure Loads of Grouted Prisms under Eccentric Load (kips)

capacity of eccentrically loaded masonry is even more strongly governed by the capacity of the block shell.

The failure modes again were characterized by shear, i.e by spalling mixed with crushing of the block shell on the loaded side, as shown in Fig. 2.16. This phenomenon was more obvious for the specimens under larger eccentricity ($e = t/3$).

The grout did not prevent the debonding of the mortar joints on the unloaded side, as indicated by the substantial deformation measured across the joint (LVDT #6) for the case of $e = t/3$, although it appears that the vertical continuity was improved by the grouting as the opening of the joints was smaller compared with their ungrouted counterparts. The face-shell on the unloaded side did not transfer load essentially for the whole loading range, as shown by the strain measured at location 5, indicating that debonding took place as soon as the specimen was loaded.

Before final failure, no premature vertical cracks were observed during the tests (see also the deformation measurements at locations 3 and 4 as shown in Figs. 10.1 and 10.2), which is in sharp contrast to what was observed for the prisms under uniaxial loading, suggesting that the cross-sectional incompatibility is not a problem for grouted masonry under eccentric loading. This is another supporting indication that the contribution of the grout to the capacity is

(a)

(b)

(c)

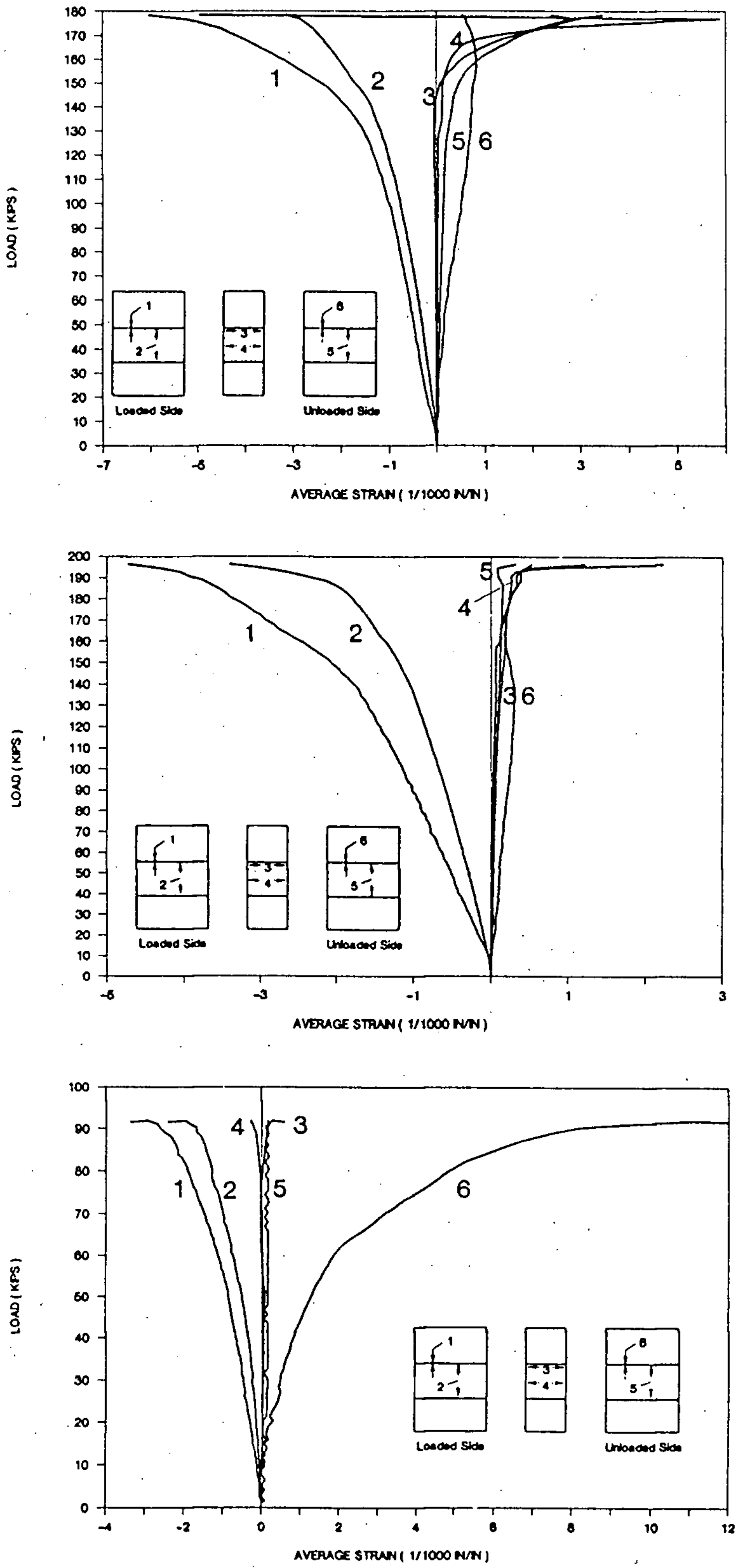

FIG. 10.1 Measured Deformations at Certain Locations of Grouted Prisms under Eccentric Compression: a) N26-1, e=t/6; b) N26-2, e=t/6; c) M26-2, e=t/3

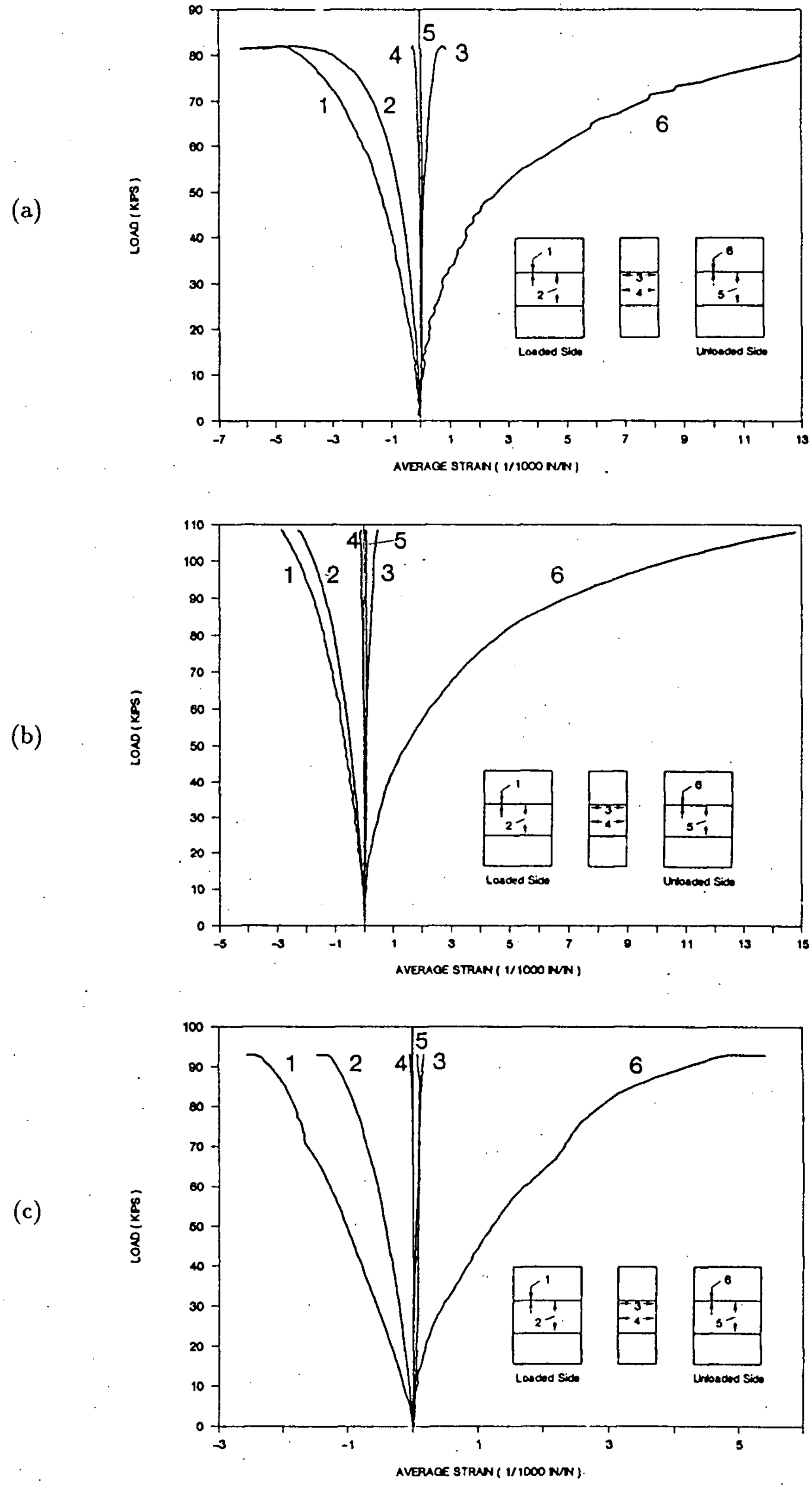

FIG. 10.2 Measured Deformations at Certain Locations of Grouted Prisms under Eccentric Compression: a) M26-3, e=t/3; b) S25-1, e=t/3; c) S25-1, e=t/3

relatively minor when the masonry is under eccentric loading.

These observations are essentially the same as those for plain concrete masonry. This encourages us to approach the problem as we did for plain concrete masonry under eccentric loading. That is, failure is assumed to be governed by the block shell and capacity estimation is based on the unit strength rather than on the uniaxial prism strength. The force shared by the grout at failure is estimated by considering the vertical deformation compatibility.

10.3 Theoretical Considerations

The capacity of reinforced concrete masonry under eccentric load will be expressed here in terms of the traditional force-moment curve. Such a relationship depends not only on the material properties of the masonry constituents, including block unit, grout, reinforcing steel and mortar, but also on its geometry, which is further complicated by various bedding and grouting combinations.

To make the situation simpler, attempts will be made to quantify the material properties, the geometry, the bedding and grouting conditions by some parameters, expressed mainly in terms of the modulus and dimensional ratios. The usefulness of such parameters will be illustrated.

For example, if linear-elastic behaviour is assumed, the forces shared by the block shell, grout, and the reinforcing steel can be calculated based on deformation modulus ratios.

A linear stress-strain relationship may be a good approximation for concrete masonry as indicated by various experiments, including those by the author, which show that nonlinearity before failure appears to be rather limited. The analyses in the preceding chapters based on this assumption do yield reasonable estimations for the masonry capacity.

Further, if linear strain along the cross-section (plane sections remaining plane) is assumed, the internal force P and moment M can be readily expressed in terms of the outer fibre stresses σ_1, σ_2 or the crack depth c (depending whether the cross-section is cracked or not), as shown in Fig. 10.3.

Note, in the following expressions, the contribution of the vertical reinforcement, which plays an important role when the cross-section is cracked, is included. This has been neglected in the analysis for grouted masonry under uniaxial compression, since the contribution is unreliable unless the steel is tied against buckling. Moreover, for normal steel ratios, the contribution in sustaining compressive force is small compared to the concrete materials, even it is included. This is especially true for the case of eccentric loading. However, in the following expressions, the force shared by the reinforcement will be included for continuity. The reinforcing steel is assumed to be placed in the middle of the cross-section as is the common practice.

When the eccentricity e is small, the cross-section remains uncracked, so the force and the moment can be expressed as (see Fig. 10.3)

$$P = \sigma_1 bl\left(1 + \frac{\sigma_2}{\sigma_1} \right)\left(1 - \lambda\frac{a}{b} + n\rho \right) \qquad 10.1$$

$$M = \frac{\sigma_1 b^2}{3} l\left(1 - \frac{\sigma_2}{\sigma_1} \right)\left(1 - \lambda\left(\frac{a}{b}\right)^3 \right) \qquad 10.2$$

where b is the half thickness (b=$t/2$) of the masonry, a is the half width of the inner core of block unit; and l is the length of the wall. σ_1 and σ_2, as have been mentioned, denote the maximum and minimum extreme fiber stresses (in compression) respectively. ρ represents the steel ratio with respect to the gross cross-sectional area, and n stands for the modular ratio; i.e. the elastic modulus of steel to that of the masonry block shell.

The parameter λ is introduced here to characterize the grouting, bedding conditions and cross-sectional geometry in the transverse direction:

$$\lambda = 1 - \frac{w}{l} - \frac{1}{m_g}\frac{w_g}{l} \qquad 10.3$$

where w and w_g are the sum of the mortared web dimension and grout dimension along the wall length, respectively (see Fig. 10.4). m_g is the modular ratio: the elastic modulus of the block shell to that of the grout, approximated as:

$$m_g = \frac{m_1}{1 + m_2 \frac{t_o}{h_o}} \qquad 10.4$$

Recall that m_1 and m_2 are the modular ratios of unit to grout, and unit to mortar joint, respectively. h_o is the height of the masonry unit and t_o is the thickness of the mortar joint.

Thus whether the masonry is fully bedded or not, and whether it is plain or fully or partially grouted, can be expressed through the parameter λ. For example, $\lambda = 0$ corresponds to the case of a solid section; $w_g = 0$, $\lambda = (1 - w/l)$ stands for the case of ungrouted masonry; similarly, $w = 0$, $\lambda = (1 - w_g/m_g l)$ is for the face-shell bedded masonry; $\lambda = 1$, when $w = w_g$

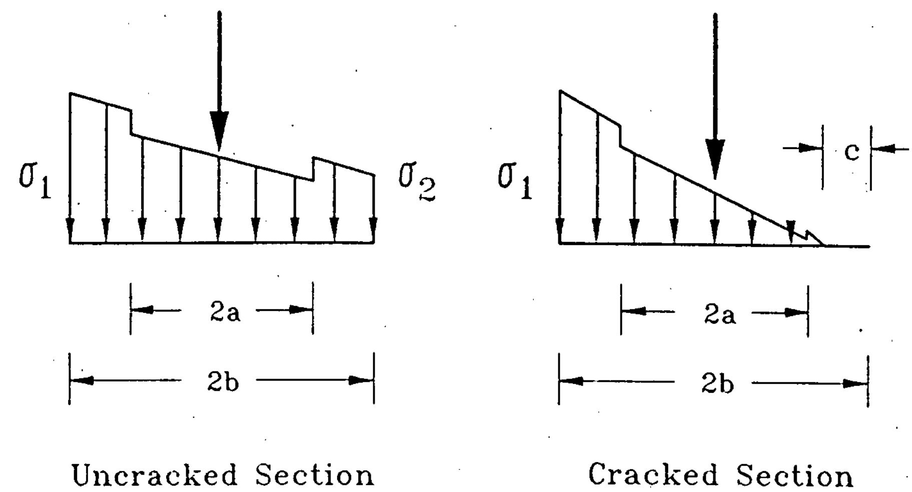

$$P = \int_0^{2b} \sigma \, dx \qquad M = \int_0^{2b} x\sigma \, dx \qquad P = \int_0^{2b-c} \sigma \, dx \qquad M = \int_0^{2b-c} x\sigma \, dx$$

FIG. 10.3 Assumed Stress Distribution of an Uncracked Section and a Cracked Section

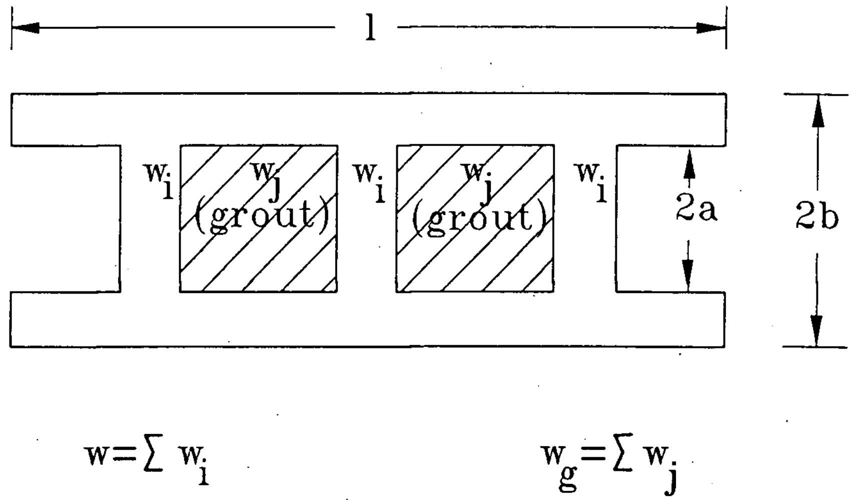

FIG. 10.4 A Typical Section of a Grouted Wall

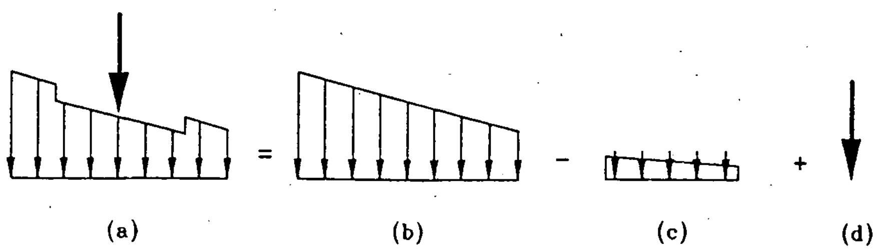

FIG. 10.5 Stress Distribution along a Section and Its Composition

= 0, of course, represents the case of the face-shell bedded, ungrouted masonry. By this means, all the combinations can be included and the relations derived here are generally useful; they have, incidentally, been applied in Chapter VI for plain concrete masonry.

Eq.10.1 and Eq.10.2 are obtained based on the principle of superposition. Due to the difference in deformation modulus of the masonry block shell, grout, and reinforcing steel, the stress distribution along the cross-section must be discontinuous at the boundaries of these materials as depicted in Fig. 10.5(a). This stress distribution, in an average sense along the wall length, can be decomposed into the stress distributions as shown in Fig. 10.5(b), (c) and (d), where distribution (b) corresponds to a solid section and distribution (c) represents the difference in stress distributions between a solid section and a grouted section. The point force depicted in Fig. 10.5(d), of course, stands for the contribution of the reinforcing steel. Clearly, distribution (c) is weighted by parameter λ and distribution (d) by $n\rho$. These parameters are combined with the cross-section factor a/b in Eq. 10.1 and Eq. 10.2.

The same principle is used in the derivation of the following equations. If the tensile resistance of the cross-section is neglected, the cross-section will crack (by observation, cracks always occur at the mortar joints, see Fig. 10.1 and Fig. 10.2) when $\sigma_2/\sigma_1 < 0$ (positive for compression). It can be shown that for $0 \leq c \leq b - a$

$$P = \sigma_1 bl\left(\left(1 - \frac{c}{2b} \right) - 2\left(\lambda\frac{a}{b} - n\rho\right) \frac{1 - c/b}{2 - c/b} \right) \qquad 10.5$$

$$M = \frac{\sigma_1 b^2 l}{(2 - c/b)} \left\{ \left(\frac{2}{3} - \frac{1}{2}\left(\frac{c}{b}\right)^2 + \frac{1}{6}\left(\frac{c}{b}\right)^3 \right) - \frac{2}{3}\lambda\left(\frac{a}{b}\right)^3 \right\} \qquad 10.6$$

where c denotes the crack length (see Fig. 10.3).

Similarly, for $b - a \leq c \leq b + a$

$$P = \sigma_1 bl\left(\left(1 - \frac{c}{2b} \right) - \lambda \frac{(1 + a/b - c/b)^2}{2(2 - c/b)} + 2n\rho \frac{1-c/b}{2-c/b} \right) \qquad 10.7$$

$$M = \frac{\sigma_1 b^2 l}{2 - c/b} \left\{ \left(\frac{2}{3} - \frac{1}{2}\left(\frac{c}{b}\right)^2 + \frac{1}{6}\left(\frac{c}{b}\right)^3 \right) \right.$$

$$\left. - \lambda \left(\frac{2}{3}\left(\frac{a}{b}\right)^3 - \frac{1}{6}\left(1 - \frac{a}{b} - \frac{c}{b}\right)^2 \left(1 + 2\frac{a}{b} - \frac{c}{b}\right) \right) \right\} \qquad 10.8$$

Finally, for $b + a \leq c \leq 2b$

$$P = \sigma_1 b l \left(\left(1 - \frac{c}{2b} \right) + 2n\rho \, \frac{1 - c/b}{2 - c/b} \right) \qquad 10.9$$

$$M = \frac{\sigma_1 b^2 l}{6} \left(2 + \frac{c}{b} - \left(\frac{c}{b}\right)^2 \right) \qquad 10.10$$

Again, if the masonry unit strength is used to define the critical state, as for plain concrete masonry under eccentric loading, we readily obtain the short wall capacity curve by letting the extreme fibre stress σ_1 be equal to f'_u, the unit compressive strength. That is, the $P-M$ curve can be developed by varying σ_2/σ_1 from unity to zero, when $\sigma_2 \geq 0$; and by stepping c from 0 to $2b$, when the cross-section has cracked.

Note that in the above expressions, the reinforcing steel is implicitly assumed not to reach its yield strength. By experimental observations, we know that the compressive failure strain for concrete masonry is usually small (less than 0.002), so that this assumption may be good as long as the eccentricity e is not too small. For concentric loads, Eq. 10.1 may overestimate the failure load, because the steel could yield. However, this part of the capacity curve is not of interest here since the concentric capacity is treated separately, as in Chapter VII and VIII. Moreover, as mentioned earlier, the contribution to the compressive capacity of the reinforcing steel is usually small compared to that of the surrounding cross-section.

However, if the crack extends beyond the half depth of the wall, the reinforcing steel may yield in tension. This may happen when the crack depth at the balanced load

$$c_b = \left[2 - \frac{1}{1+\frac{f_y}{nf_u}} \right] b \qquad 10.11$$

is less than that corresponding to the pure moment capacity (the c which makes Eq. 10.7 or Eq. 10.9 vanish); f_y here is the yield strength of the steel. Although yielding of the steel is not desirable and is not allowed in the current design code, for analysis, we may replace the term $2n\rho(1-c/b)/(2-c/b)$ in Eq. 10.7 or Eq. 10.9 by $2\rho f_y/\sigma_1$ to include this situation.

10.4 Comparison of Theory with Experiments

In summary, the capacity curve for concrete masonry is determined by the following parameters: f_u' , f_y, m_1, m_2, $n\rho$, a, b, l, w, w_g and t_o/h_o, which can all be measured. However, for practical reasons, the modulus ratios m_1 and m_2 may be related to the corresponding strength ratios. In the following comparison, the same square root correlation is used as in Chapter VII.

The $P-M$ curves generated for the author's specimens and those tested by Drysdale and Hamid (1983) are plotted in Fig. 10.6 to Fig 10.15 with the experimental data. The plot is nondimensionalized by dividing vertical load by $P_o = f_u' tl$, the nominal axial capacity; and moments by $M_k = P_o t/6$, the moment capacity when P_o is applied at the kern eccentricity of a solid section.

For most cases, the agreement is reasonably good. For the experiments by Drysdale and Hamid, the curves appear to underestimate the bending capacity of the specimens tested at the biggest eccentricity consistently, although by a small amount. This is probably caused by the assumption that the cross-section does not resist any tensile force, which is closer to reality for plain masonry than for grouted masonry.

No efforts are made here to compare the results numerically, since a number of the data points are obtained at large eccentricity when the loading path $M=eP$ is almost parallel to the lower boundaries of the capacity curves. In this situation small experimental errors can lead to large numerical variations in load or moment.

The model based on linear strain and stress appears to give reasonable predictions. The comparison again supports the assumption that the capacity of eccentrically loaded masonry is more closely correlated with the unit strength than with the concentric capacity. Thus in practical design, it may be again recommended that the concentric capacity and the eccentric capacity be treated separately, as in the case of plain masonry. The expressions developed here provide convenient ways to estimate the eccentric capacity of concrete masonry with various grouting and bedding conditions.

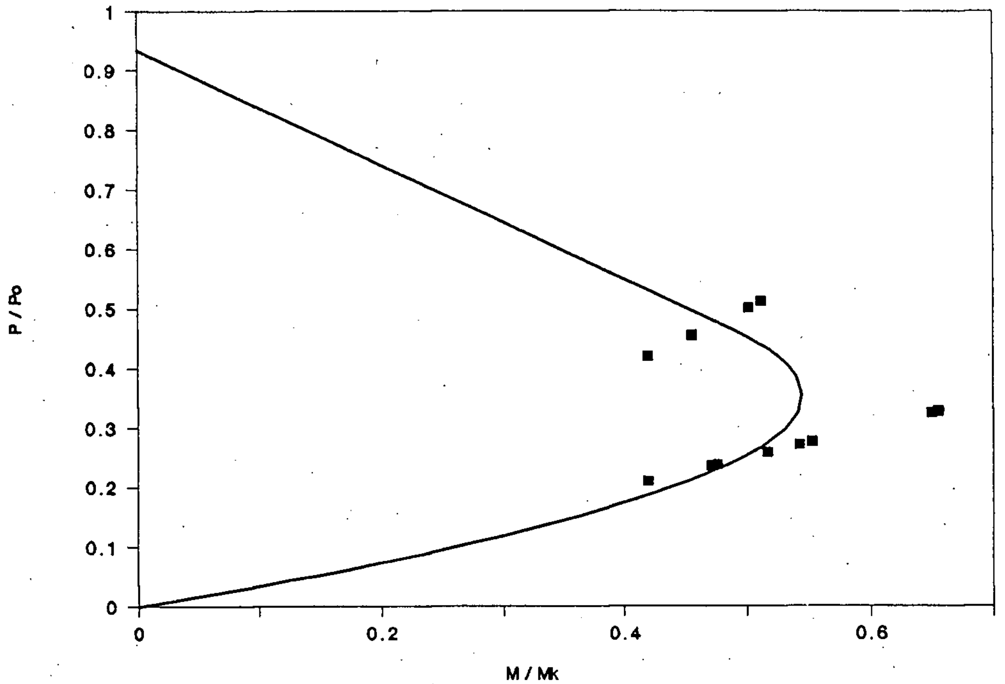

FIG. 10.6 Comparison of Predicted Interaction Curve with Experiments by the Author: N26, M26, S25

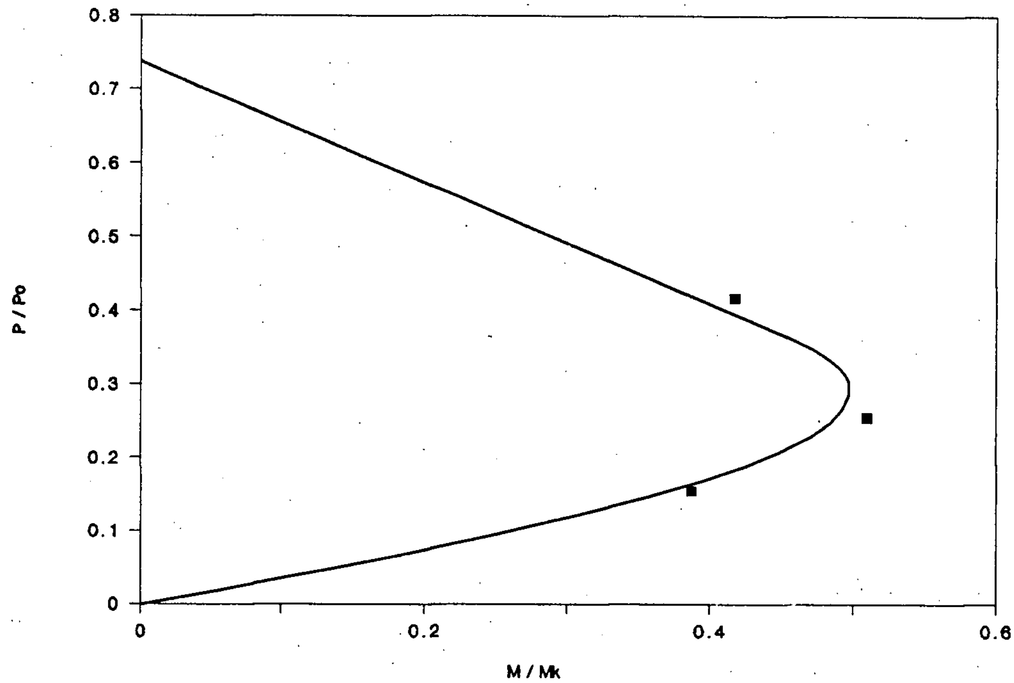

FIG. 10.7 Comparison of Predicted Interaction Curve with Experiments by Drysdale and Hamid: Normal Block, Type N Grout

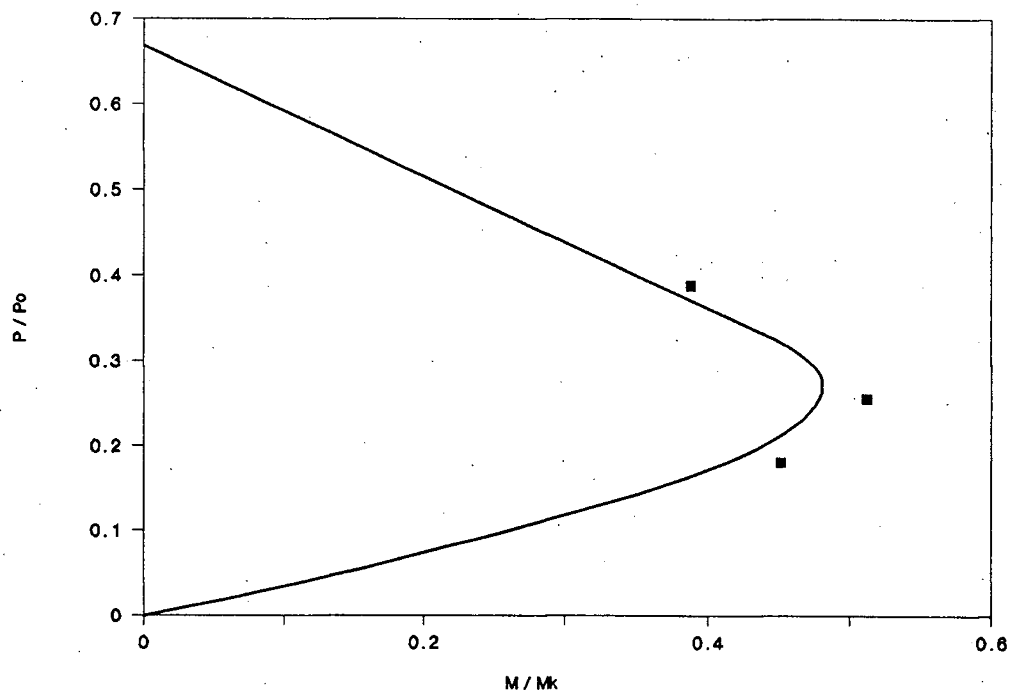

FIG. 10.8 Comparison of Predicted Interaction Curve with Experiments by Drysdale and Hamid: Normal Block, Type W Grout

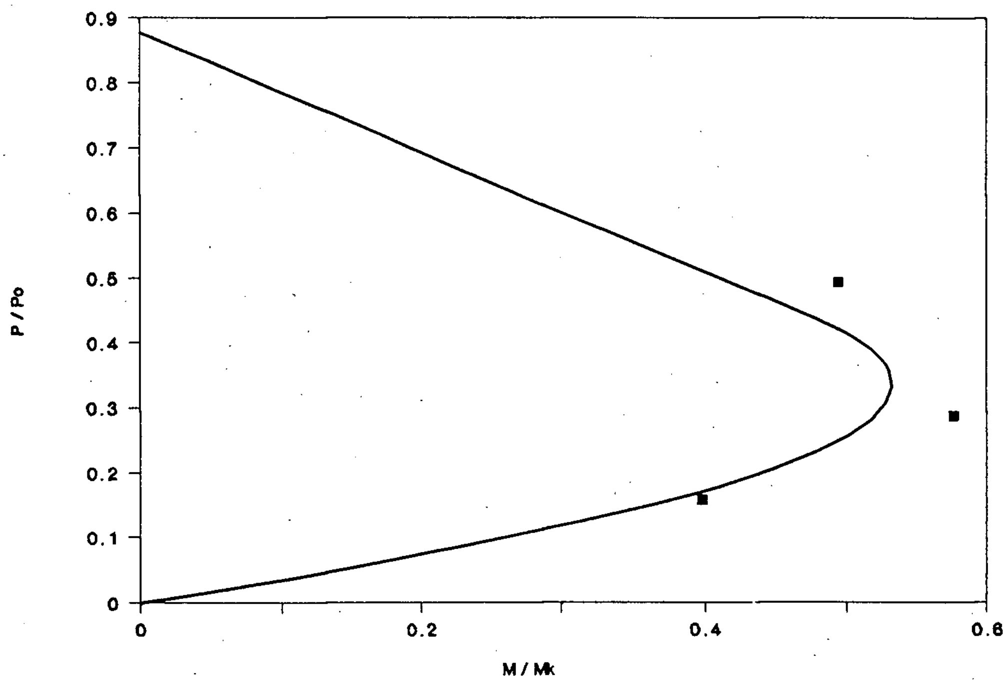

FIG. 10.9 Comparison of Predicted Interaction Curve with Experiments by Drysdale and Hamid: Normal Block, Type S Grout

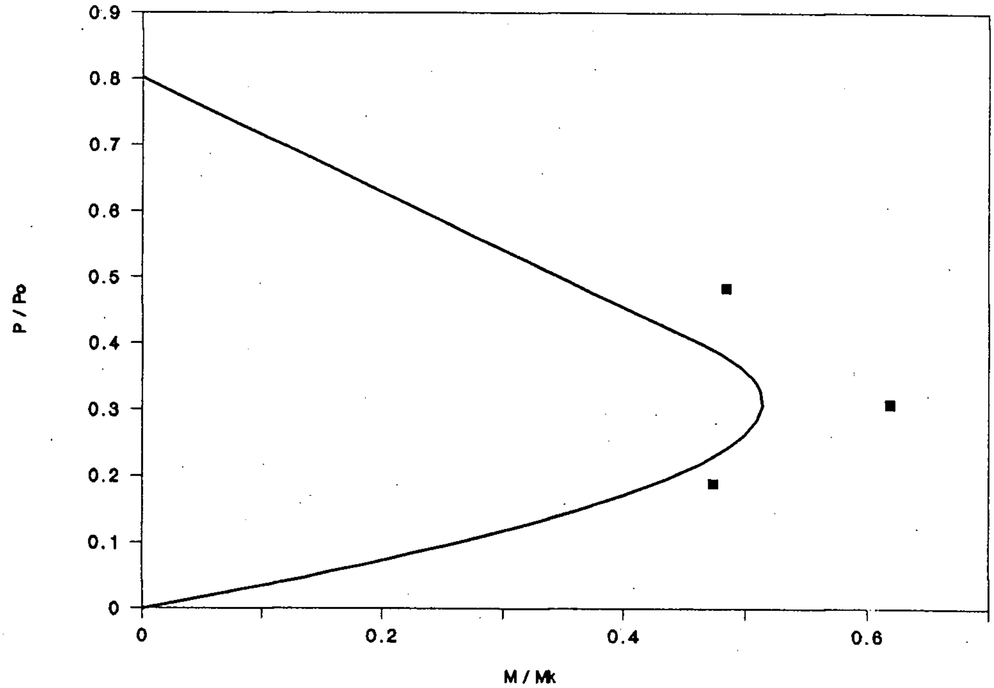

FIG. 10.10 Comparison of Predicted Interaction Curve with Experiments by Drysdale and Hamid: Weak Block, Type N Grout

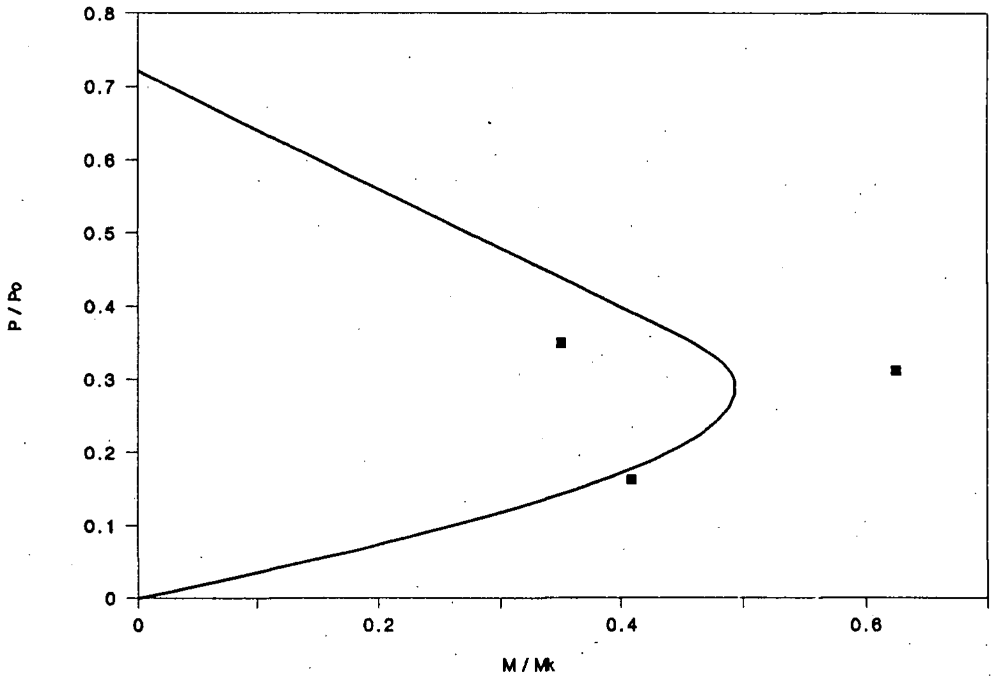

FIG. 10.11 Comparison of Predicted Interaction Curve with Experiments by Drysdale and Hamid: Strong Block, Type N Grout

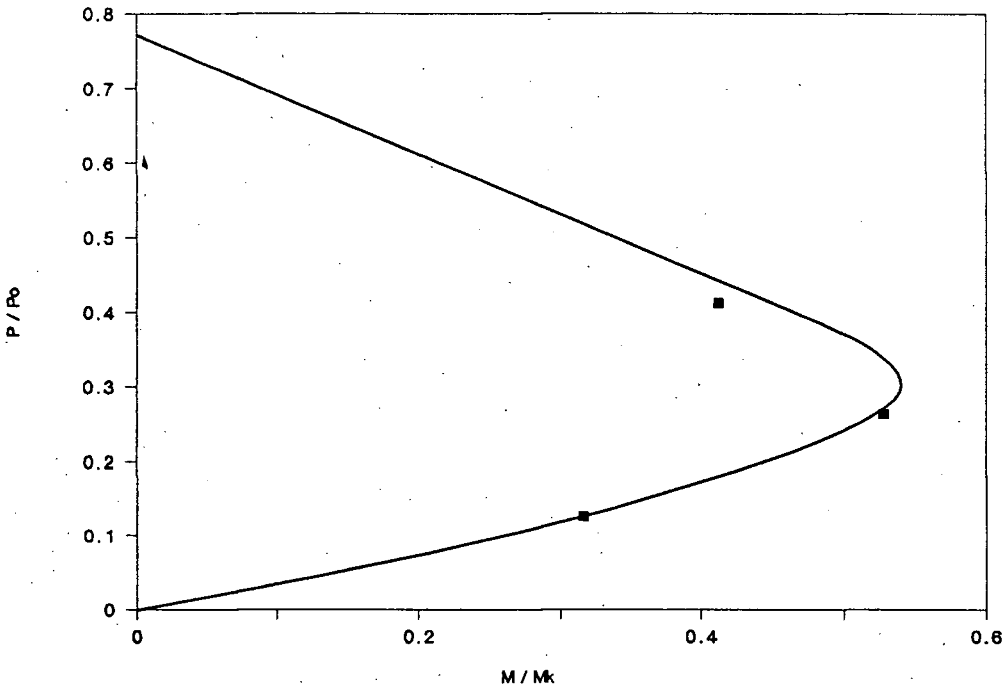

FIG. 10.12 Comparison of Predicted Interaction Curve with Experiments by Drysdale and Hamid: 75% Solid Block, Type N Grout

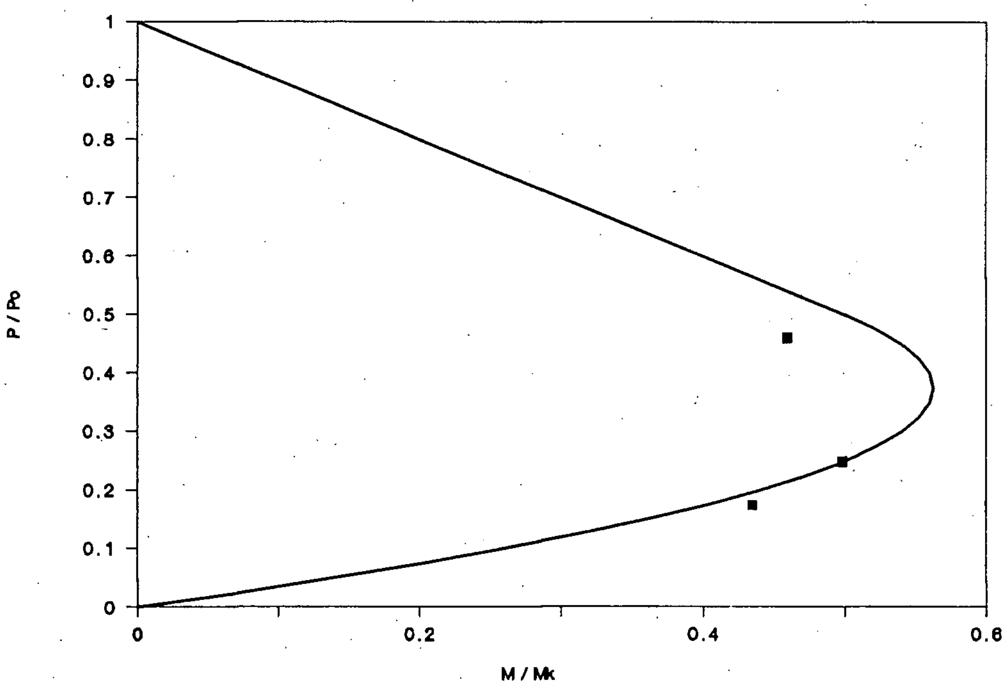

FIG. 10.13 Comparison of Predicted Interaction Curve with Experiments by Drysdale and Hamid: Full Block

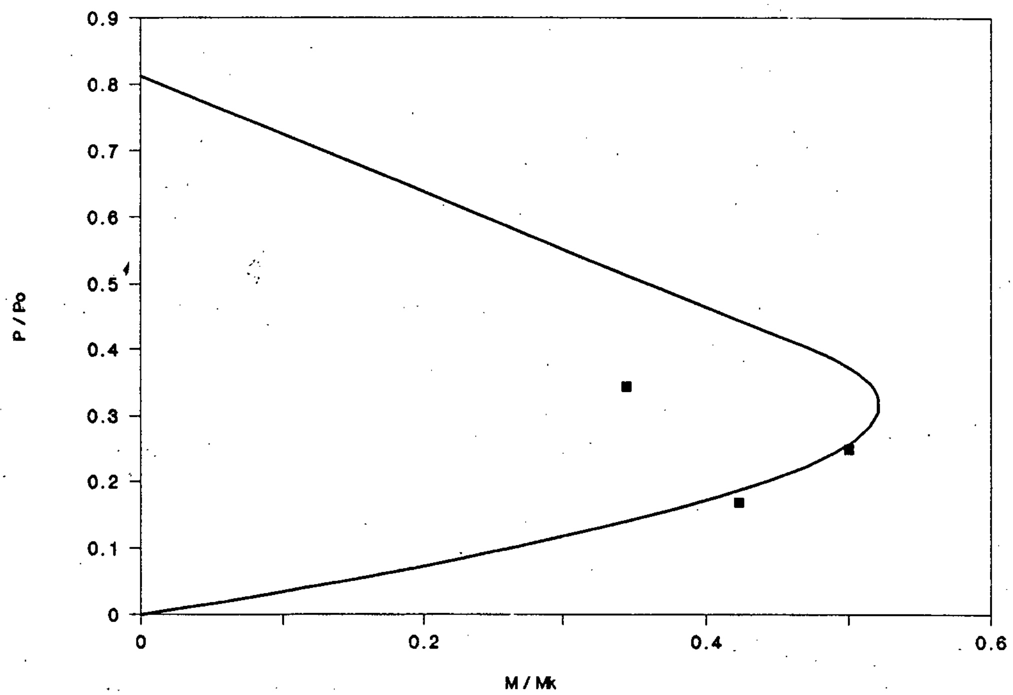

FIG. 10.14 Comparison of Predicted Interaction Curve with Experiments by Drysdale and Hamid: 6 inch Block, Type N Grout

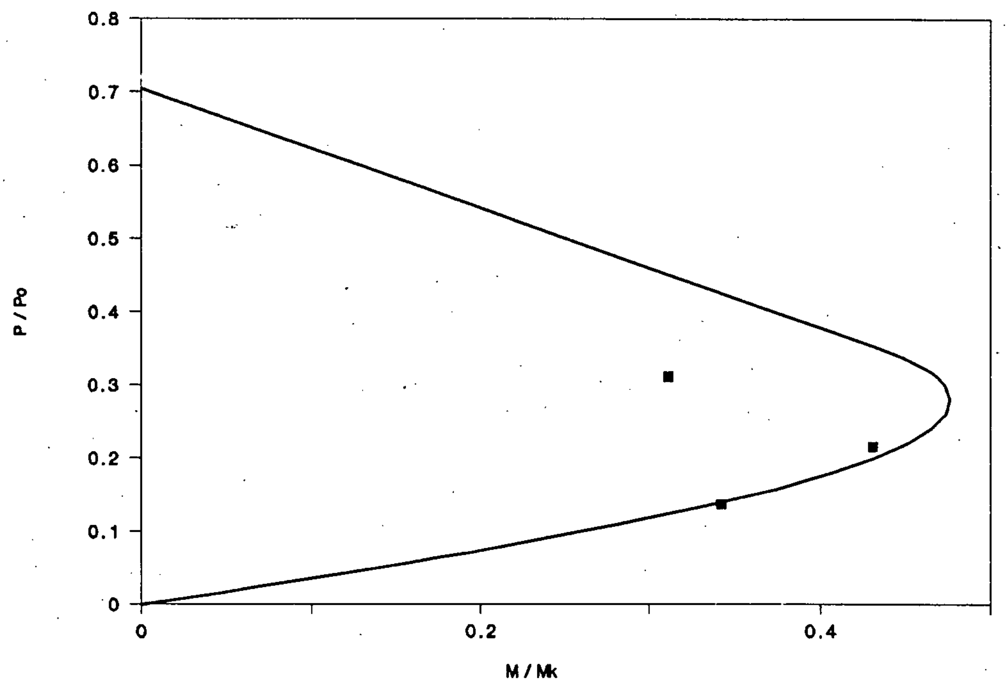

FIG. 10.15 Comparison of Predicted Interaction Curve with Experiments by Drysdale and Hamid: 10 inch Block, Type N Grout

CHAPTER XI

SLENDERNESS OF CONCRETE MASONRY

11.1 Introduction

Modern masonry structures are becoming taller, not only in terms of the elevation of the building, but also in terms of storey heights. Besides advances in engineering knowledge, changes in the masonry constituents have contributed to this development. Structural behaviour is greatly improved by high strength concrete units with steel reinforcement.

Tall, slender concrete masonry can be seen in many places, such as apartment highrises, department stores, warehouses, supermarkets, gymnasiums and auditoriums. The benefits of building taller and more slender masonry are obvious; besides space savings, material and construction costs are reduced. As the wall becomes lighter, smaller footings are required and lower seismic forces are induced. These are important reasons why modern masonry structures find a place in today's competitive building market.

However, the development of tall, slender masonry is still largely hampered by a limited understanding of the mechanical behaviour, and probably by an historic prejudice that masonry is not sound when it is tall. This is reflected in the stringent slenderness requirements in the current masonry design code (CAN3-S304-M84, 1984).

In the last two decades, reinforced slender walls have been studied extensively. Some experiments have shown excellent flexural performance; for example, the tests conducted in the early 80's by ACI Southern California Chapter (Athey 1982), which lead to some limited relaxations of the slenderness requirements in building codes. However, since full scale wall tests are very expensive and time consuming, it is very difficult to observe the behaviour under various load combinations. The analysis of slenderness effects have so far been largely limited to the traditional approach, i.e. the moment magnifier method has been applied and thus an effective rigidity of the member has had to be assumed. In this chapter, a more rational analysis will be presented in the context of these experimental observations, and of the findings in the preceding chapters, which have been focused on the short wall or column capacity. This will follow a brief review of background information.

11.2 Background Information Review

The slenderness effects discussed here refer to masonry under eccentric load. Walls under concentric loading are not of practical concern since a minimum eccentricity has always to be assumed ($0.1t$ or 25 mm, specified by the current design code (CAN3-S304-M84, 1984)) to take account of member imperfections and alignment error.

When a slender member carries an eccentric load, it is important to bear in mind that it may suffer loss of capacity either due to material failure or by instability. This particular point has been clearly explained by Nathan (1977). Fig. 11.1 shows the interaction curve for a column subject to a compressive load with equal end eccentricities. The line O—A defines the relationship between load and end moment. However, due to the slenderness, the midheight moment is magnified by the member deflection, and the corresponding load-moment path is defined by O—B. Material failure occurres at point B, when the end conditions are as indicated at point C. Theoretically, if the moment—curvature ralationship of the beam column remains linear, material failure always governs the behaviour, since the midspan deflection will be unbounded when the Euler load is approached. The moment magnifier method perfectly predicts this failure mode. When the member develops some nonlinearity in its moment—curvature relationship, the method is still a valid approximation provided an appropriate effective cross-sectional rigidity is used. However, when the cross-section has developed substantial nonlinearity, usually at greater eccentricities, the midspan moment increases with deflection to a point such as D in Fig. 11.1, and the member becomes unstable in the sense that equlibrium cannot be maintained even though the material of the cross-section is still sound.

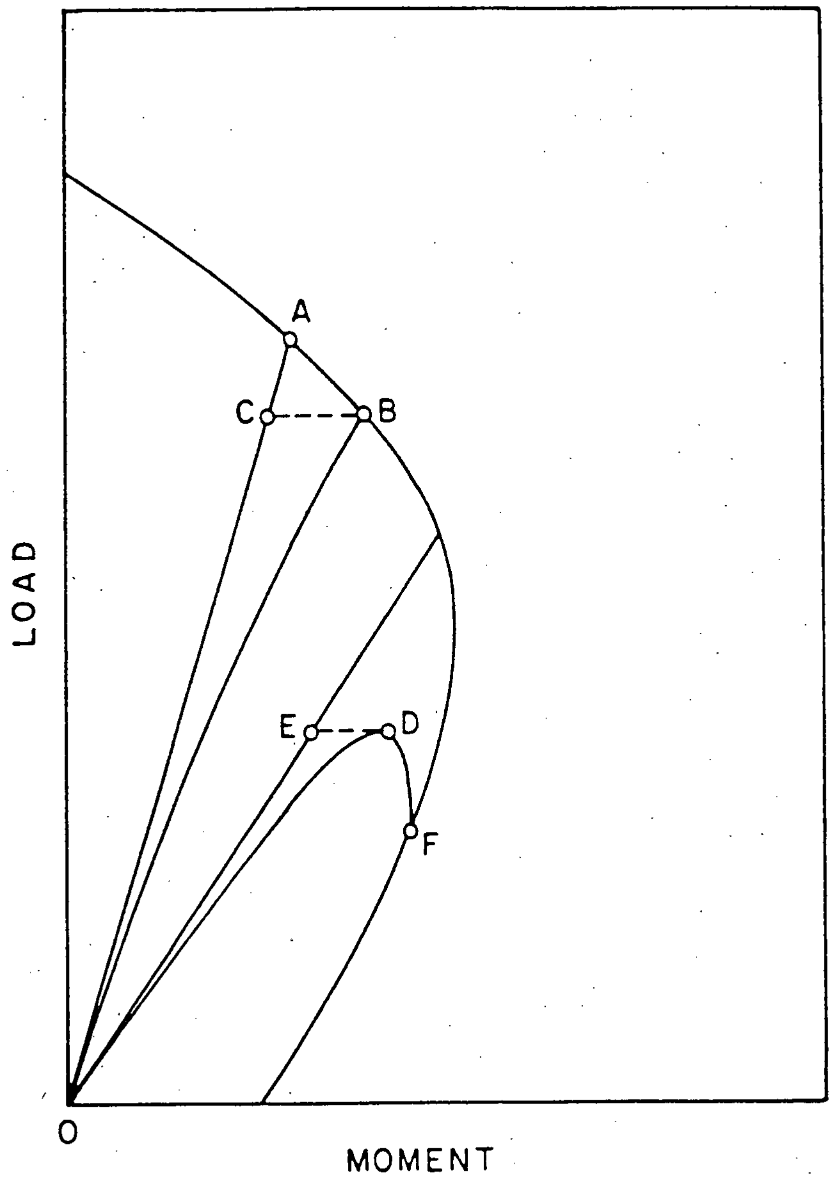

FIG. 11.1 A Load–Moment Interaction Curve and Loading Paths of a Compression Member

The member will fail at this point, corresponding to end condition E, unless the load can be shed by other means, to lead to material failure at point F. The moment magnifier procedure, in which the design moment is compared with the short column moment, no longer applies rigorously to this situation. The procedure adopted in the current code (CAN3-S304-M84, 1984) is, at best, an artificial empirical device for the member governed by instability.

It is clear that for the moment magnifier method (albeit in an artificial way) to be applied succesfully to the design problem, the key issue is how to estimate the nonlinear development of the cross-section. As in a concrete column, the nonlinear development of a masonry member is due to material nonlinearity as well as to the cracking of the cross-section. To estimate these effects accurately is difficult since they are coupled with the magnitude as well as the eccentricity of the load. Therefore it is not surprising that the current design process is subject to many limitations, since these effects cannot be included in a single assumed "effective cross-sectional rigidity". Further, after the cross-section has cracked, the rigidity is a variable along the member height rather than a single constant represented by the "effective rigidity"; the physical picture of the simplification is not clear.

To include all the nonlinear effects, a rational analysis with some numerical procedures is often necessary. For analysis of concrete beam columns, Nathan (1985) has developed a computer program based on some well established principles. By numerical integration, it first finds force-moment-curvature relationships for any cross-sectional geometry, and for materials with any constitutive law. An iteration scheme is then used to give the column deflection curve which matches to any boundary conditions. It is of course very general and useful, and may be applicable to concrete masonry with a few modifications. On the other hand, Suwalski and Drysdale (1986) have used a finite element model to directly analyze the slenderness influence of the capacity of concrete masonry.

These approaches are useful in the sense that they may include all the factors which affect the behaviour. However, at the same time, they require more input parameters, which, in design practice, often must be assumed rather than measured. It appears that with these approaches, the walls must be studied individually, and it is difficult to perform a parametric study which may yield some simplified relations governed by some key factors.

In the following analysis, some assumptions will be made based on the observed characteristics of concrete masonry. With these assumptions, some analytical relations will be developed to explicitly reveal some key factors representing the masonry slenderness effect. This will be shown to lead to a relatively simple but yet rational approach to the problem. This approach will be shown to be easily adapted to design analysis. The usefulness and limitations of this approach will then be discussed.

11.3 Masonry Characteristics and Some Assumptions

Compared with concrete columns, concrete masonry is more prone to crack when the cross-section is subjected to tension because of the material discontinuity at the mortar joint. This is clearly evident from the deformation measurements across the joints. (see Figs. 10.1, 10.2, also see Figs. 6.1 and 6.2 for plain masonry). Similar observations were also reported by Fattal et al (1976) and by Hatzinikolas et al (1978). Thus for all practical purposes this tensile bond can be assumed to be zero. And since the bed joints are evenly spaced, it is reasonable to treat the problem in an average sense, which is necessary to lead to a continuous formulation along the member height.

Another significant observation, mentioned many times earlier, is that material nonlinearity is rather limited up to the failure stress, and the linear stress-strain material relation is a valid approximation (also see Yokel and Dikkers 1971, Hatzinikolas et al 1978, Warwaruk et al 1986). The linear material and the zero tensile bond assumptions are equivalent to supposing that the nonlinearity in the moment—curvature relationship of a concrete masonry member is mainly due to the cracking of the cross-section. Indeed, the cross-sectional rigidity, which is proportional to the third power of the section depth, will decrease drastically as the depth is reduced by crack extension.

The third assumption is that of the plane section remaining plane, corresponding to a linear strain distribution across the section. This is a commonly accepted assumption, however rigorously speaking, it implies, in the context of the first assumption, an infinitesimal cracking spacing when the side of a cross-section is subject to tension. Since the tension cracks occur only at the mortar joints, the materials between two cracked joints must transfer some tension force and thus alter the plane sections. Therefore the linear strain distribution may be a good approximation only when the crack depth is not big compared to the unit height.

With these main assumptions, it is possible to establish relatively compact relationships governing the mechanical behaviour of a masonry member under various loading conditions, and thus it is easier to perform some parametric studies on slenderness effects. The equations governing the cross-sectional behaviour derived in the preceding chapter are still valid and will be quoted without further comments.

11.4 Differential Equations Governing Concrete Masonry with Cracked Section

Equal end eccentricities will first be investigated, and the approach will then be extended to more general loading conditions. Different differential equations are used to describe the behaviour, depending on whether the cross-section has cracked and how deep the crack extends.

Fig. 11.2 depicts the most general case: a concrete masonry member under eccentric load with uncracked sections at the two ends and, due to deflection, a cracked section in the middle range. Note, $\acute{c}$ represents the crack length or cracked sectional depth. M, F, and C denote the cross-section at midspan, the cross-section at which the crack extends to the flange (face-shell) depth and the cross-section at which the crack begins to extend, respectively. The variables subscripted with these letters (in lower case) stand for the corresponding values at these cross-sections.

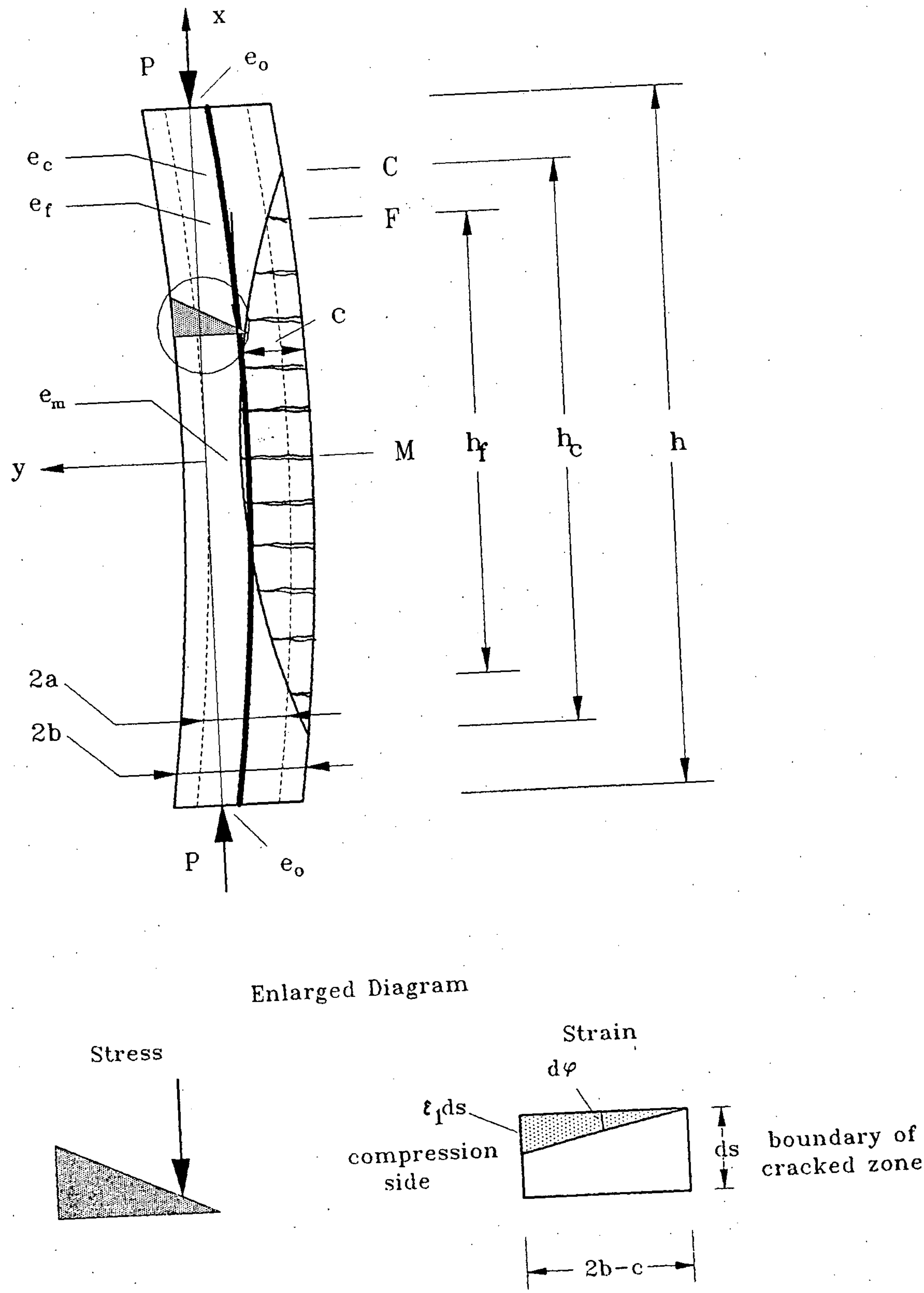

FIG. 11.2 A Cross-Section View of A Reinforced Concrete Wall under Eccentric Compression

By symmetry, we need only study the upper half of the masonry wall. For the end portion of the wall, cracking does not take place. Referring to the selected coordinates in which the x axis coincides with the thrust line and y lies through the symmetric section, we have, for the curve defining the compression face

$$EI\,\frac{d^2y}{dx^2} - P(b-y) = 0 \qquad h_c/2 < x < h/2 \tag{11.1}$$

with boundary conditions:

$$y(h/2) = b - e_o \tag{11.2}$$

at the end; and

$$y(h_c/2) = b - e_c \tag{11.3}$$

with

$$\frac{dy}{dx}\left(\frac{h_c}{2}\right) = \varphi_c \tag{11.4}$$

at the C—cross-section; where e_c is the virtual loading eccentricity and φ_c is the rotation at this cross-section. Note, for this loading condition, the end eccentricity e_o is smaller than the cracking eccentricity e_c.

When Eq. 11.1 is integrated and matched to the boundary conditions (see appendix), we obtain

$$\sqrt{\frac{P}{\xi P_{cr}}}\,\frac{1-h_c/h}{2}\pi = \sin^{-1}\frac{e_c}{\sqrt{e_c^2 + \frac{EI}{P}\,\varphi_c^2}} - \sin^{-1}\frac{e_o}{\sqrt{e_c^2 + \frac{EI}{P}\,\varphi_c^2}} \tag{11.5}$$

where P_{cr} is the Euler load corresponding to the gross section:

$$P_{cr} = \frac{\pi^2 EI_g}{h^2} = \frac{\pi^2 Elt^3}{12h^2} \tag{11.6}$$

and ξ is the ratio of the moment of interia of the net cross-section to that of the gross-section

$$\xi = \frac{I}{I_g} = 1 - \lambda\left(\frac{a}{b}\right)^3 \tag{11.7}$$

in which λ and a/b are defined as in the preceding chapter. For a given cross-section, e_c can be written as

$$e_c = \frac{M_c}{P_c} = \frac{1 - \lambda\left(\frac{a}{b}\right)^3}{3\left(1 - \lambda\frac{a}{b} + n\rho\right)} b \tag{11.9}$$

in which M_c and P_c are expressed through Eqs. 10.1 and 10.2 with σ_2 being set equal to zero by neglecting the tensile resistance of the cross-section.

Eq. 11.5 gives the relation between load P and two unknowns, namely h_c and φ_c, which will be found by the equations governing the cracked section as shown further below.

The differential equation for the cracked section can be derived by first considering the geometric relation. As shown by the enlarged diagram in Fig. 11.2, the cross-section will rotate due to the uneven compression which produces the outer fiber strain ϵ_1 at the compression face but zero at the boundary between cracked and uncracked zones. The change of the rotation of a small section, therefore, can be approximated as

$$d\varphi = \frac{\epsilon_1 ds}{2b - c} \approx \frac{\epsilon_1 dx}{2b - c} \tag{11.10}$$

By recognizing

$$\varphi \approx \frac{dy}{dx} \qquad 11.11$$

it follows that

$$\frac{d^2y}{dx^2} = \frac{\epsilon_1}{2b - c} \qquad 11.12$$

The assumed linear stress-strain relation allows us to write

$$\epsilon_1 = \frac{\sigma_1}{E} \qquad 11.13$$

Finally, σ_1 can be expressed in terms of the load P and the cross-sectional parameters by the equilibrium condition, either through Eq. 10.5 or Eq. 10.7, depending on whether the crack has extended beyond the flange. Thus for $0 < c < b-a$, we have

$$\frac{d^2y}{dx^2} = \frac{P}{2Eb^2l\left(\left(1 - \frac{c}{2b}\right)^2 - \left(\lambda\frac{a}{b} - n\rho\right)\left(1 - \frac{c}{b}\right)\right)} \qquad 11.14$$

with y being related to the parametric variable c by the geometric relation (see Fig. 11.2):

$$y = b - e = b - \frac{\left(1 - \frac{c}{2b}\right)^2\left(1 + \frac{c}{b}\right) - \lambda\left(\frac{a}{b}\right)^3}{3\left(\left(1 - \frac{c}{2b}\right)^2 - \left(\lambda\frac{a}{b} - n\rho\right)\left(1 - \frac{c}{b}\right)\right)}\, b \qquad 11.15$$

by recognizing $e = M/P$ and relations given by Eqs. 10.5 and 10.6.

Similarly, for $b-a < c < b+a$ we obtain

$$\frac{d^2y}{dx^2} = \frac{P}{2Eb^2l\left(\left(1 - \frac{c}{2b}\right)^2 - \frac{\lambda}{4}\left(1 + \frac{a}{b} - \frac{c}{b}\right)^2 + n\rho\left(1 - \frac{c}{b}\right)\right)} \qquad 11.16$$

and

$$y = b - \frac{\left(1-\frac{c}{2b}\right)^2\left(1+\frac{c}{b}\right) - \lambda\left(\left(\frac{a}{b}\right)^3 - \frac{1}{4}\left(1-\frac{a}{b}-\frac{c}{b}\right)^2\left(1+2\frac{a}{b}-\frac{c}{b}\right)\right)}{3\left(\left(1-\frac{c}{2b}\right)^2 - \frac{\lambda}{4}\left(1+\frac{a}{b}-\frac{c}{b}\right)^2 + n\rho\left(1-\frac{c}{b}\right)\right)}\, b \qquad 11.17$$

in view of Eqs. 10.7 and 10.8.

It is not intended to include the case of $b+a< c < 2b$, since it is of little practical significance when the crack extends so deep; although it poses no further difficulties.

With the relations given by Eqs. 11.15 and 11.17, Eq. 11.14 and Eq. 11.16 can be integrated, by some manipulations presented in the appendix, in closed form to give the slope

$$\frac{dy}{dx} = \sqrt{\frac{P}{Ebl}\left(C_1 - \Omega_1(c)\right)} \qquad 11.18$$

for $0 < c < b-a$, in which C_1 is a constant of integration and Ω_1 is a function of c expressed as

$$\Omega_1(c) = \frac{4\left(1-\frac{c}{2b}\right)^3 - \lambda\left(\frac{a}{b}\right)^3 - 3\left(\lambda\frac{a}{b} - n\rho\right)\left(1-\frac{c}{b}\right)^2}{6\left(\left(1-\frac{c}{2b}\right)^2 - \left(\lambda\frac{a}{b} - n\rho\right)\left(1-\frac{c}{b}\right)\right)^2} \qquad 11.19$$

And similarly for $b-a< c < b+a$

$$\frac{dy}{dx} = \sqrt{\frac{P}{Ebl}\left(C_2 - \Omega_2(c)\right)} \qquad 11.20$$

with

$$\Omega_2(c) = \frac{4\left(1-\frac{c}{2b}\right)^3 - \lambda\left(\frac{a}{b}\right)^3 - \frac{\lambda}{2}\left(1-\frac{a}{b}-\frac{c}{b}\right)^3 - 3\left(\lambda\frac{a}{b} - n\rho\right)\left(1-\frac{c}{b}\right)^2}{6\left(\left(1-\frac{c}{2b}\right)^2 - \frac{\lambda}{4}\left(1+\frac{a}{b}-\frac{c}{b}\right)^2 + n\rho\left(1-\frac{c}{b}\right)\right)^2} \qquad 11.21$$

The constants of integration C_1 and C_2 can be determined by matching to the known conditions on the rotation. By symmetry, we have

$$\frac{dy}{dx}(c_m) = 0 \qquad 11.22$$

which leads to

$$C_2 = \Omega_2(c_m) \qquad 11.23$$

where c_m denotes the midspan crack length. Thus the rotation at section F is

$$\varphi_f = \sqrt{\frac{P}{Ebl}\left(\Omega_2(c_m) - \Omega_2(c_f)\right)} \qquad 11.24$$

which also leads, by continuity of the rotation, to an expression for C_1

$$C_1 = \Omega_2(c_m) - \Omega_2(c_f) + \Omega_1(c_f) \qquad 11.25$$

where $c_f = b-a$, the crack length at section F.

Eqs. 11.18 and 11.20 can then be rearranged and integrated along the wall height to give

$$\sqrt{\frac{P}{P_{cr}}}\,\frac{h_c/h-h_f/h}{2}\pi = \sqrt{\frac{3}{2}}\int_{c_f}^{c_c} \frac{dy}{b\sqrt{C_1-\Omega_1(c)}} \qquad 11.26$$

for $0 < c < b$–a, where $c_c = 0$, the crack length at section C; and

$$\sqrt{\frac{P}{P_{cr}}}\frac{h_f/h}{2}\pi = \sqrt{\frac{3}{2}}\int_{c_m}^{c_f}\frac{dy}{b\sqrt{C_2-\Omega_2(c)}} \qquad 11.27$$

for $b-a< c < b+a$. dy can be expressed in terms of dc by differentiation of Eq. 11.15 or Eq. 11.17 within their specified domains. Thus, for given a c_m the right hand sides of Eqs. 11.26 and 11.27 can be integrated numerically.

Further, the rotation at section C, which is contained in Eq. 11.5, can be readily obtained in view of Eq. 11.18

$$\varphi_c = \sqrt{\frac{P}{Ebl}\Big(\Omega_2(c_m) - \Omega_2(c_f) + \Omega_1(c_f) - \Omega_1(c_c)\Big)} \qquad 11.28$$

Finally, by summing Eqs. 11.26, 11.27 and 11.5, a definitive relation between the applied load P and the midspan crack depth c_m is reached

$$\frac{P}{P_{cr}} = \frac{4}{\pi^2}\Bigg\{\sqrt{\frac{3}{2}}\int_{c_m/b}^{c_f/b}\frac{dy/dc}{\sqrt{\Omega_2(c_m)-\Omega_2(c)}}\,d\Big(\frac{c}{b}\Big)$$

$$+\sqrt{\frac{3}{2}}\int_{c_f/b}^{c_c/b}\frac{dy/dc}{\sqrt{\Omega_2(c_m)-\Omega_2(c_f)+\Omega_1(c_f)-\Omega_1(c)}}\,d\Big(\frac{c}{b}\Big)$$

$$+\sqrt{\xi}\Bigg(\sin^{-1}\frac{e_c/b}{\sqrt{\left(\frac{e_c}{b}\right)^2+\frac{2}{3}\xi\Big(\Omega_2(c_m)-\Omega_2(c_f)+\Omega_1(c_f)-\Omega_1(c_c)\Big)}}$$

$$-\sin^{-1}\frac{e_o/b}{\sqrt{\left(\frac{e_c}{b}\right)^2+\frac{2}{3}\xi\Big(\Omega_2(c_m)-\Omega_2(c_f)+\Omega_1(c_f)-\Omega_1(c_c)\Big)}}\Bigg)\Bigg\}^2 \qquad 11.29$$

This equation implicitly defines the force—deflection relation of a concrete masonry wall through the parametric variable c_m, which can be used to study the slenderness effects and the stability of the wall.

By examining Eq. 11.29, one finds that the three terms on the right hand side actually represent the capacity contributions of three sections of the masonry wall, namely, the cracked section in which the crack has extended into the grout core, the cracked section in which the crack extends within the face-shell, and the uncracked section. Therefore, by adding or subtracting the contributions, the results can be extended to more general loading cases.

For (equal) end eccentricities e_o larger than cracking eccentricity e_c, the cracked zone will extend over the entire height, and Eq. 11.29 reduces to

$$\frac{P}{P_{cr}} = \frac{6}{\pi^2}\left(\int_{c_m/b}^{c_f/b} \frac{dy/dc}{\sqrt{\Omega_2(c_m) - \Omega_2(c)}}\, d\left(\frac{c}{b}\right) \right.$$

$$\left. + \int_{c_f/b}^{c_o/b} \frac{dy/dc}{\sqrt{\Omega_2(c_m) - \Omega_2(c_f) + \Omega_1(c_f) - \Omega_1(c)}}\, d\left(\frac{c}{b}\right)\right)^2 \qquad 11.30$$

where c_o is the end cracking corresponding to e_o, found through Eqs. 10.5 and 10.6.

If e_o is greater than the flange cracking eccentricity e_f, Eq. 11.30 further reduces to

$$\frac{P}{P_{cr}} = \frac{6}{\pi^2}\left(\int_{c_m/b}^{c_o/b} \frac{dy/dc}{\sqrt{\Omega_2(c_m) - \Omega_2(c)}}\, d\left(\frac{c}{b}\right) \right)^2 \qquad 11.31$$

where c_o is determined through Eqs. 10.7 and 10.8.

Similarly, when the midspan cracking c_m is less than the flange cracking c_f, which may happen when e_o is less than e_f, Eq. 11.29 and Eq. 11.30 become

$$\frac{P}{P_{cr}} = \frac{4}{\pi^2}\left\{ \sqrt{\frac{3}{2}} \int_{c_m/b}^{c_c/b} \frac{dy/dc}{\sqrt{\Omega_1(c_m) - \Omega_1(c)}}\, d\left(\frac{c}{b}\right) \right.$$

$$+\sqrt{\xi}\left(\sin^{-1}\frac{e_c/b}{\sqrt{\left(\frac{e_c}{b}\right)^2+\frac{2}{3}\xi\left(\Omega_1(c_m)-\Omega_1(c_c)\right)}}-\sin^{-1}\frac{e_o/b}{\sqrt{\left(\frac{e_c}{b}\right)^2+\frac{2}{3}\xi\left(\Omega_1(c_m)-\Omega_1(c_c)\right)}}\right)\Bigg\}^2 \qquad 11.32$$

and

$$\frac{P}{P_{cr}} = \frac{6}{\pi^2}\left(\int_{c_m/b}^{c_o/b}\frac{dy/dc}{\sqrt{\Omega_1(c_m)-\Omega_1(c)}}\,d\left(\frac{c}{b}\right)\right)^2 \qquad 11.33$$

respectively. Thus, all the possible combinations for equal eccentricity loading are included.

By the same principle, the results can also be extended to the case of unequal eccentricity loading. According to Nathan (1972), the configuration of a column loaded with arbitrary eccentricities can be represented by a portion of a wave of an imaginary, infinitely long column under the action of the axial load, as shown in Fig. 11.3. Without loss of generality, we assume that the magnitude of the bottom eccentricity is not less than that of the top one. Thus the maximum deflection from the thrust line always lies in the lower portion of the column. This point, at which $dy/dx=0$, corresponds to the midspan of the case of equal eccentricity loading studied above. The column loaded with arbitrary eccentricities then is actually composed of a portion symmetrical about the maximum deflection point, with an extension at the top end as far as the appropriate value of eccentricity. From this viewpoint, the corresponding capacity contributions can easily be evaluated and summed to give the force—cracking relation.

It should be indicated that for the case of double curvature loading (e_t/e_b negative), there are apparently two possible equilibrium configurations depicted by sections AB and AC in Fig. 11.3. However, as far as the lowest buckling load is concerned, the configuration AB will be under consideration. This configuration should also be realized for the case of anti-symmetric loading ($e_t/e_b=-1$). This has been shown by the experiments (Hatzinikolas et al, 1978; Fattal

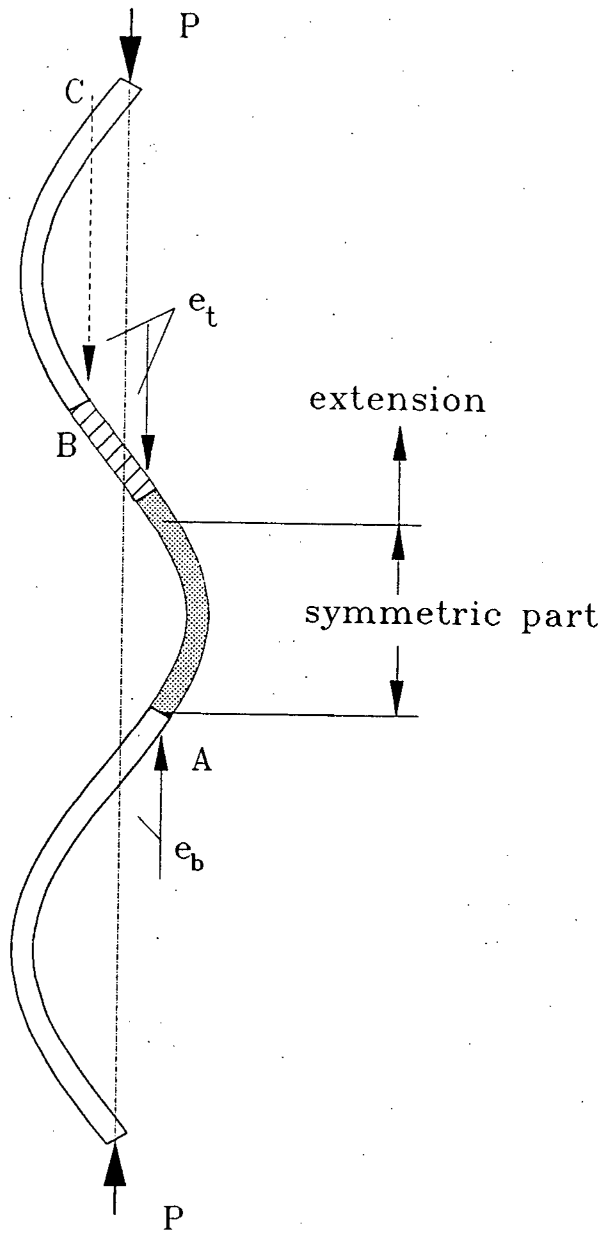

FIG. 11.3 Column Deflection Curve

et al 1976), and a theoretical explanation will be presented in appendix.

Consider two most general cases. First $0 < e_t < e_b < e_c$; the corresponding relation is

$$\frac{P}{P_{cr}} = \frac{4}{\pi^2} \left\{ \sqrt{\frac{3}{2}} \int_{c_m/b}^{c_f/b} \frac{dy/dc}{\sqrt{\Omega_2(c_m) - \Omega_2(c)}} d\left(\frac{c}{b}\right) \right.$$

$$+ \sqrt{\frac{3}{2}} \int_{c_f/b}^{c_c/b} \frac{dy/dc}{\sqrt{\Omega_2(c_m) - \Omega_2(c_f) + \Omega_1(c_f) - \Omega_1(c)}} d\left(\frac{c}{b}\right)$$

$$+ \sqrt{\xi} \left(\sin^{-1} \frac{e_c/b}{\sqrt{\left(\frac{e_c}{b}\right)^2 + \frac{2}{3}\xi \left(\Omega_2(c_m) - \Omega_2(c_f) + \Omega_1(c_f) - \Omega_1(c_c)\right)}} \right.$$

$$\left. - \sin^{-1} \frac{e_b/b}{\sqrt{\left(\frac{e_c}{b}\right)^2 + \frac{2}{3}\xi \left(\Omega_2(c_m) - \Omega_2(c_f) + \Omega_1(c_f) - \Omega_1(c_c)\right)}} \right)$$

$$+ \frac{1}{2}\sqrt{\xi} \left(\sin^{-1} \frac{e_b/b}{\sqrt{\left(\frac{e_c}{b}\right)^2 + \frac{2}{3}\xi \left(\Omega_2(c_m) - \Omega_2(c_f) + \Omega_1(c_f) - \Omega_1(c_c)\right)}} \right.$$

$$\left.\left. - \sin^{-1} \frac{e_t/b}{\sqrt{\left(\frac{e_c}{b}\right)^2 + \frac{2}{3}\xi \left(\Omega_2(c_m) - \Omega_2(c_f) + \Omega_1(c_f) - \Omega_1(c_c)\right)}} \right) \right\}^2 \qquad 11.34$$

The second case is when $e_b > e_f > 0$, $e_t < 0$, but $e_b > |e_t| > e_f$, the relation becomes

$$\frac{P}{P_{cr}} = \frac{4}{\pi^2} \left\{ \sqrt{\frac{3}{2}} \left(\int_{c_m/b}^{c_b/b} \frac{dy/dc}{\sqrt{\Omega_2(c_m) - \Omega_2(c)}} d\left(\frac{c}{b}\right) \right. \right.$$

$$+ \frac{1}{2} \int_{c_b/b}^{c_f/b} \frac{dy/dc}{\sqrt{\Omega_2(c_m) - \Omega_2(c)}} d\Big(\frac{c}{b}\Big) + \frac{1}{2} \int_{c_t/b}^{c_f/b} \frac{dy/dc}{\sqrt{\Omega_2(c_m) - \Omega_2(c)}} d\Big(\frac{c}{b}\Big)$$

$$+ \int_{c_f/b}^{c_c/b} \frac{dy/dc}{\sqrt{\Omega_2(c_m) - \Omega_2(c_f) + \Omega_1(c_f) - \Omega_1(c)}} d\Big(\frac{c}{b}\Big)\Bigg)$$

$$+ \sqrt{\xi} \sin^{-1} \frac{e_c/b}{\sqrt{\Big(\frac{e_c}{b}\Big)^2 + \frac{2}{3}\xi\Big(\Omega_2(c_m) - \Omega_2(c_f) + \Omega_1(c_f) - \Omega_1(c_c)\Big)}} \Bigg\}^2 \qquad 11.35$$

where c_b and c_t are the crack depths corresponding to e_b and e_t, respectively. In these two loading conditions, the cracking c_m is assumed to be greater than c_f.

These results are readily generalized to any other load combinations for unequal end eccentricity loading.

A computer program written in FORTRAN-G was developed based on the equations derived above. A listing of the program is given in an appendix.

11.5 Results and Applications

The algorithm developed above will be used to study two main aspects of concrete masonry wall behaviour, namely the stability, and the force—deflection relation; the latter also affects the wall capacity. The focus will be on the case of equal eccentricity loading.

According to the model, the buckling load of concrete masonry can be found by stepping c_m from zero to some critical depth, at which the load P reaches a maximum. This is illustrated by the $c_m - P$ relationship for a plain, solid section ($\lambda = a/b = n\rho = 0$) loaded at the kern eccentricity ($e_o = t/6$), as shown in Fig. 11.4. On the horizontal axis, the value $c_m/t = 0$ represents an undeflected member. Thus this corresponds to no axial load or $P/P_{cr} = 0$. Obviously, no load could be maintained if the whole cross-section were cracked, $c_m/t = 1$. Thus

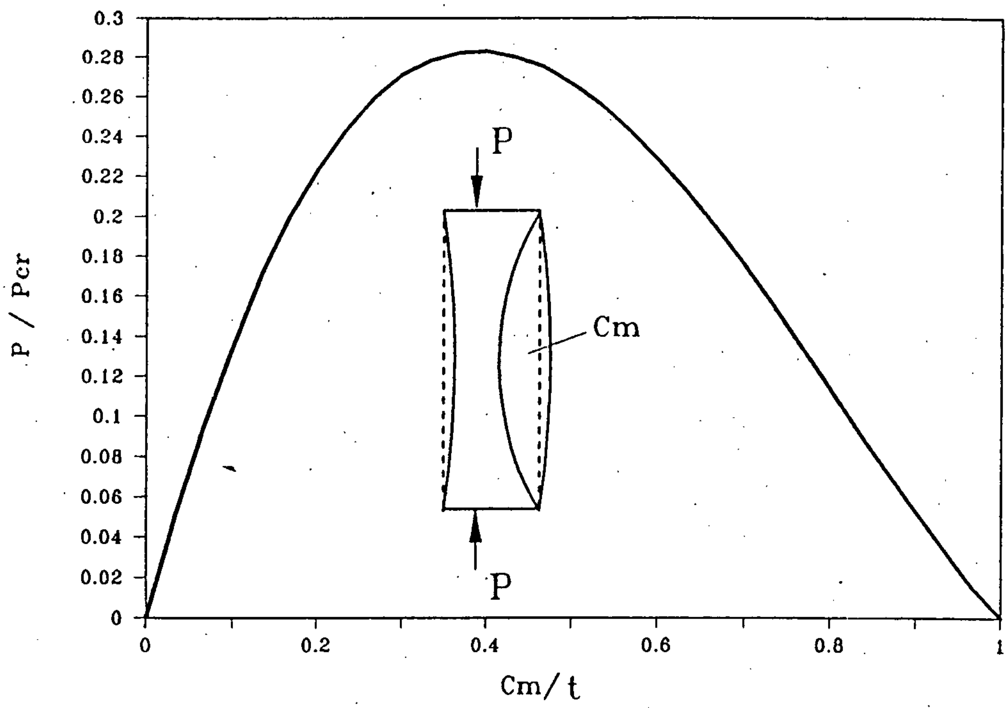

FIG. 11.4 Critical Load versus Crack Depth at Middle Section of a Plain, Solid Member Loaded at e=t/6

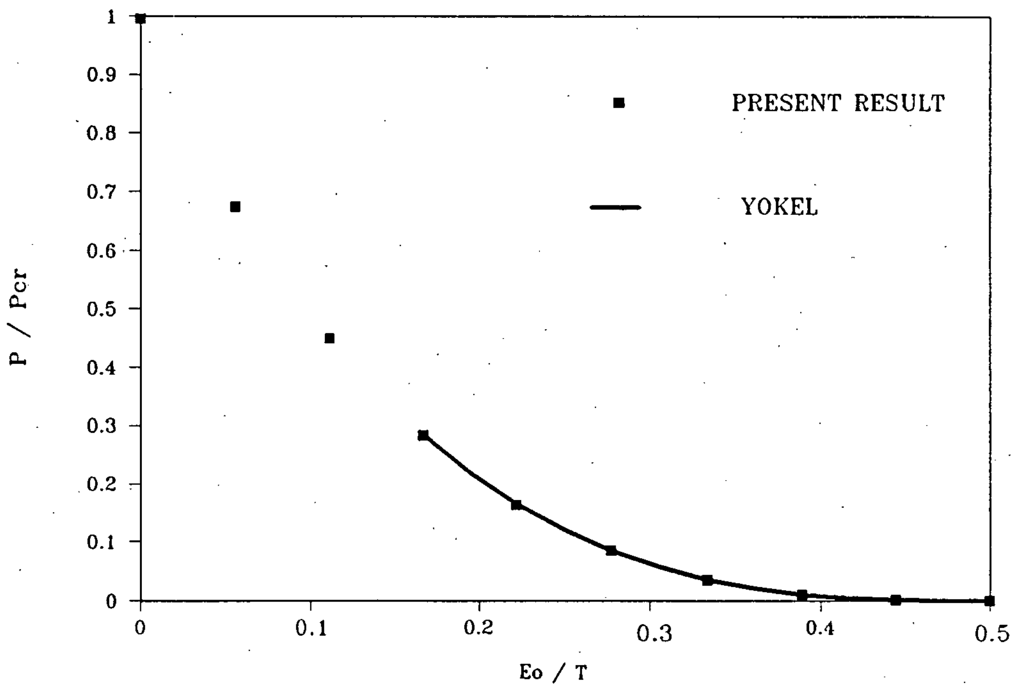

FIG. 11.5 Critical Load versus Loading Eccentricity for a Solid Section

this point also corresponds to the value $P/P_{cr}=0$. When P is applied and increased, deflection will increase together with the crack depth. Assuming there is no compression failure during the loading stage, the load P will reach a maximum corresponding to some crack depth ($c_m/t \approx 0.4$ and $P/P_{cr} \approx 0.28$ for this case). Any further increase of P beyond this point will cause the member to collapse. It is clear that the relation before this critical point, $dP/dc_m > 0$, represents stable equilibrium. Beyond this point, $dP/dc_m < 0$ represents unstable equilibrium. At the point, $dP/dc_m = 0$; $P=P_{max}$ of course, stands for the buckling load.

Obviously, the cross-sectional cracking of a member will depend heavily on the loading eccentricity and so, therefore, will the buckling load. For a plain, solid section, the buckling load is plotted against the eccentricity in discrete form in Fig. 11.5. At the point where $e_o/t=0$, when the member is loaded concentrically, $P/P_{cr}=1$, and the buckling load coincides with the Euler load. The buckling load decreases drastically with increase in eccentrcity. When $e_o/t=0.5$, $P/P_{cr}=0$, i.e., no load can be sustained if the load is applied at the edge of a member with no tension resistance.

The classic problem of the buckling of a plain, solid member with no tension resistance was first investigated by Royen (1937). The problem and its application to brickwork have been subsquently studied by Chapman and Slatford (1957), Sahlin (1971), Yokel (1971), Hatzinikolas (1978). In Fig. 11.5, the results obtained by the algorithm are compared with a closed form solution for loading eccentricity larger than $t/6$ given by Yokel. For the range compared, the results are essentially identical.

The following are some of the interesting predictions given by the algorithm. As shown by Fig. 11.6 for the solid section ($\lambda=a/b=0$, $n\rho$ varies), while the buckling loads corresponding to small eccentricities are essentially unaffected, the stability of the wall is greatly improved with increase of the reinforcement ratio at large eccentricities. The rather flat tails at large eccentricities imply that the capacity of reinforced walls is largely governed by the bending rigidity.

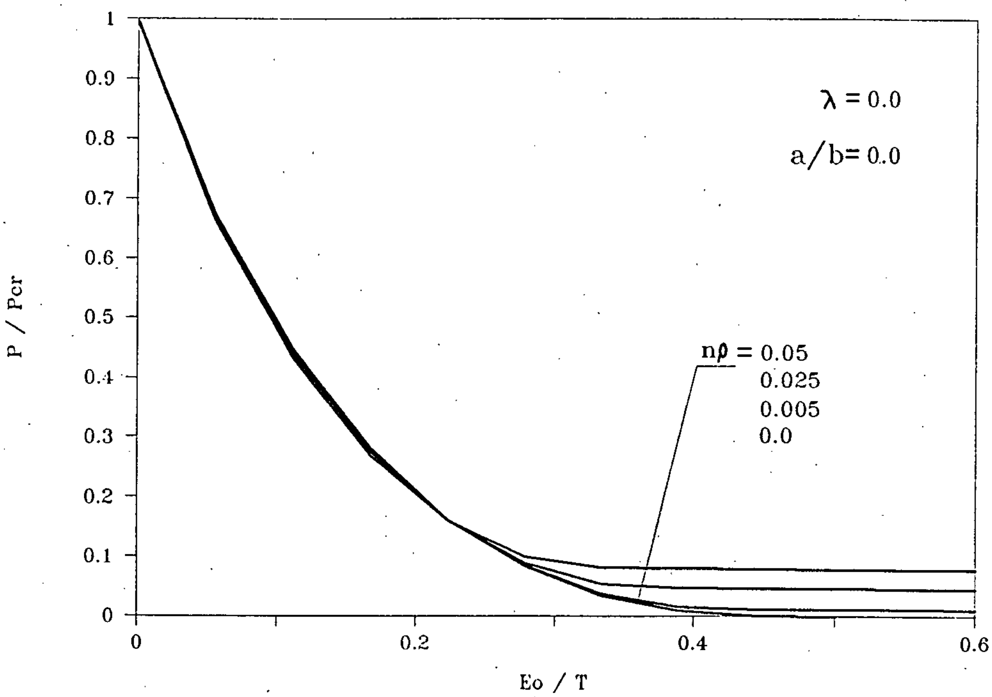

FIG. 11.6 Critical Load versus Loading Eccentricity: $\lambda = a/b = 0$, $n\rho$ Varies

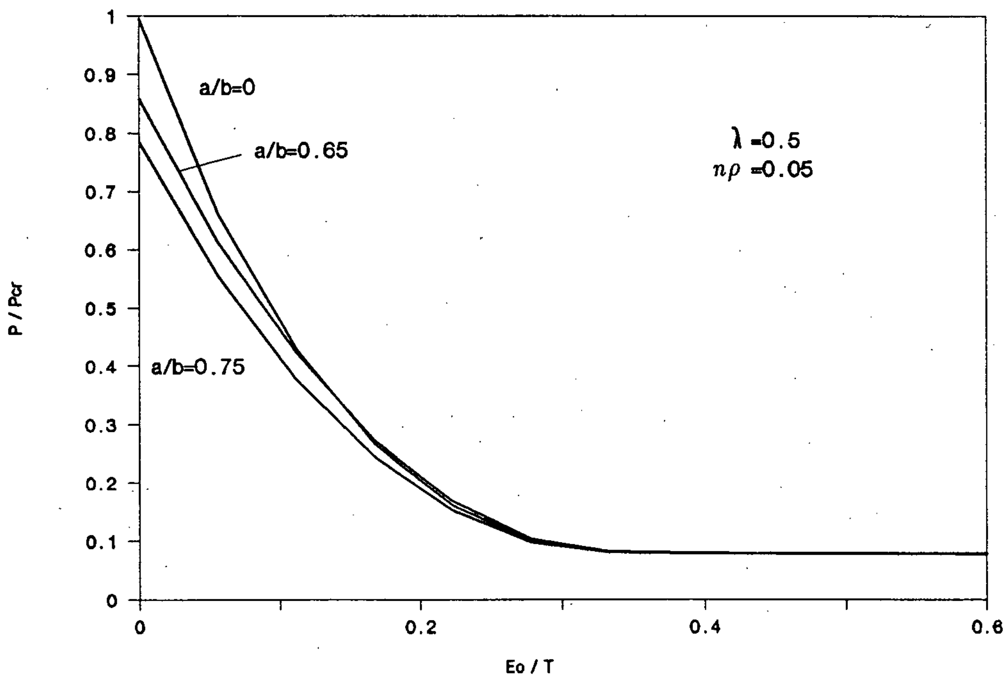

FIG. 11.7 Critical Load versus Loading Eccentricity: $\lambda = 0.5$, $n\rho = 0.05$, a/b Varies

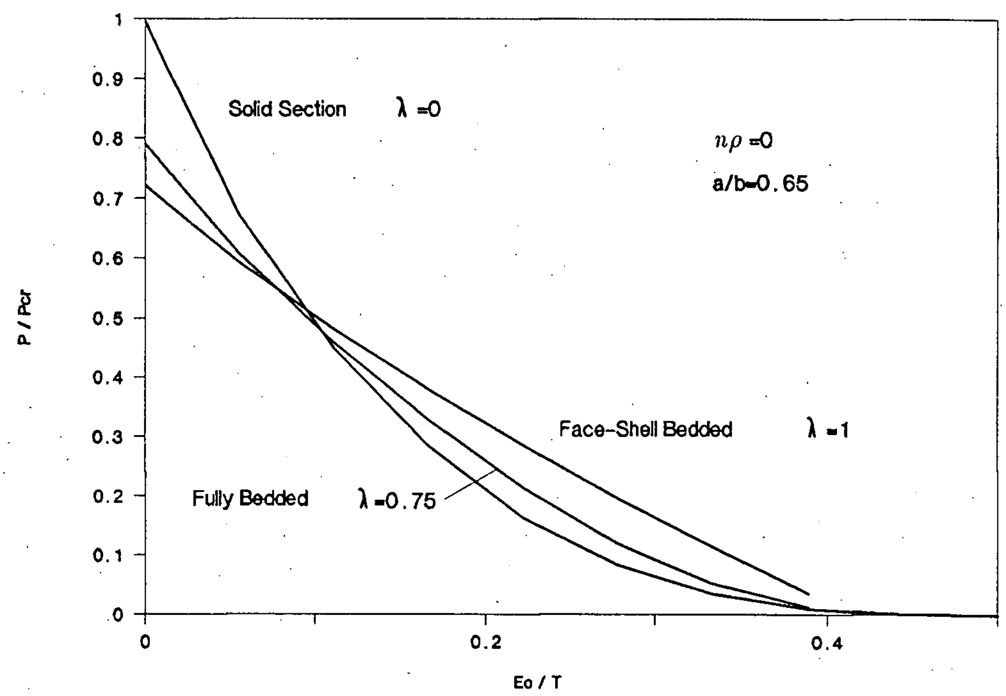

FIG. 11.8 Critical Load versus Loading Eccentricity: a/b=0.65, $n\rho$=0, λ Varies

In contrast, the variation of a/b only affects the stability at small eccentricities as shown by Fig. 11.7 (λ=0.5, corresponding to a partially grouted wall; $n\rho$=0.05; a/b=0, 0.65, 0.75). The effect of changes in λ is illustrated through an example comparing different bedding conditions. Fig. 11.8 shows the buckling loads for a typical 8 inch plain section (a/b=0.65; $n\rho$=0. λ=1 for face-shell bedding and λ= 0.75 for full bedding; λ=0 represents a solid, or fully grouted section, included here as a reference). Although the buckling load of the solid section is higher at very small eccentricities, it drops rapidly as the eccentricity increases and soon becomes the lowest. Face-shell bedded masonry, on the contrary, has lower buckling loads at small eccentricities but remains relatively higher at larger eccentricities. A fully bedded section falls in between. Since buckling usually only governs failure at larger eccentricities, one may conclude that in terms of stability, face-shell bedded masonry is better than its fully bedded counterpart which is in turn better than a solid section. This is not surprising considering that face-shell bedded masonry is least prone to crack under eccentric loading. We may infer, in the context of the strength studies presented in the preceding chapters, that face-shell bedded masonry is more likely to be governed by strength than by stability.

The present approach is compared with some of the existing data obtained from full scale concrete wall tests. These include eleven 137 inch and 105 inch high walls (8×40×128 inch and 8×40×96 inch nominal) with different reinforcement tested under equal end eccentricities by Hatzinikolas et al (1978).

As discussed at the begining of the chapter, tall masonry walls may lose strength either by material failure or by instabilily. The examination of the 137 inch high wall with 3#3 reinforcing steel ($n\rho$=0.027) provides an excellent illustration of this point.

In Fig. 11.9, the load—moment interaction curve is developed by the equations given in Chapter X. The straight lines radiating from the origin define the end conditions for different loading eccentricities. These experimental lines are terminated by the data points and paired with the predicted curves representing the load—moment relationships at midheight. It is clear that the moment is magnified due to the slenderness. When the cross-section remains uncracked, usually under small eccentricities with low load magnitude, the magnifier is given by the linear solution:

$$\delta = \sec\left(\sqrt{\frac{P}{\xi P_{cr}}}\,\frac{\pi}{2} \right) \approx \frac{1}{1 - \frac{P}{\xi P_{cr}}} \qquad 11.36$$

Recall that P_{cr} represents the Euler load for the gross section which must be adjusted by ξ for particular conditions. When the cross-section is cracked, the magnifier $\delta = e_m/e_o$ is calculated, by the algorithm, for every midspan crack depth c_m. It is interesting to note that for the case of the smallest eccentricity $e_o = t/6$, as depicted by the lines with the steepest initial slope, the point defining the end conditions is within the $P-M$ capacity curve while the corresponding point representing the midspan conditions (moment has been magnified) is outside but fairly

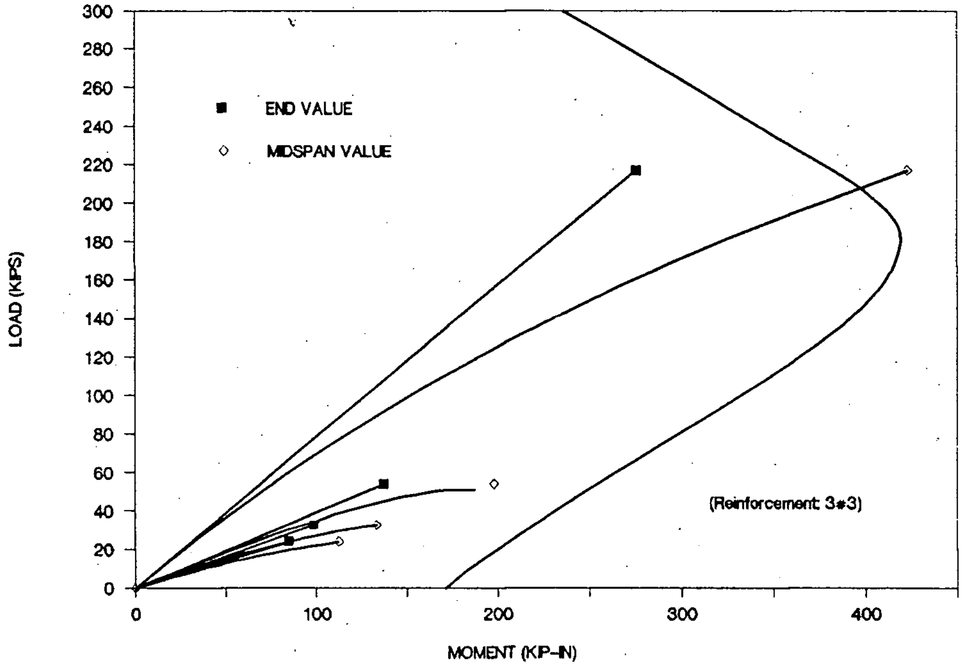

FIG. 11.9 Theoretical P−M Interaction Curve and Loading Paths Compared with Experiments by Hatzinikolas et al: 137 inch High Wall with Reinforcement 3#3

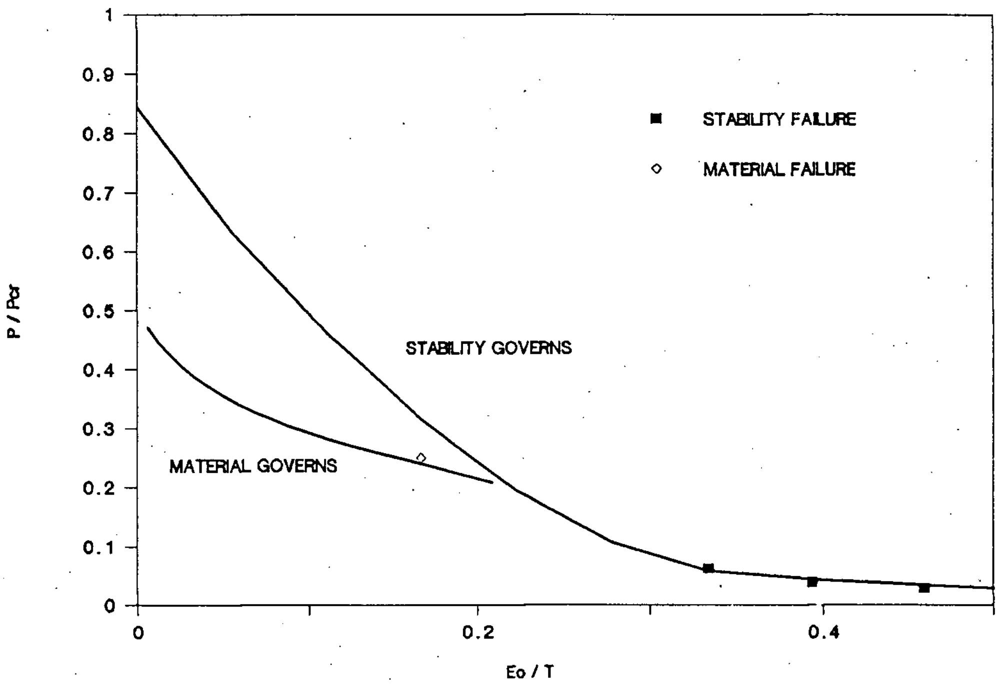

FIG. 11.10 Theoretical Load−Eccentricity Curve Compared with Experiments by Hatzinikolas et al: 137 inch High Wall with Reinforcement 3#3. The Points Show the Experimental Results while the Continuous Lines Show the Prediction

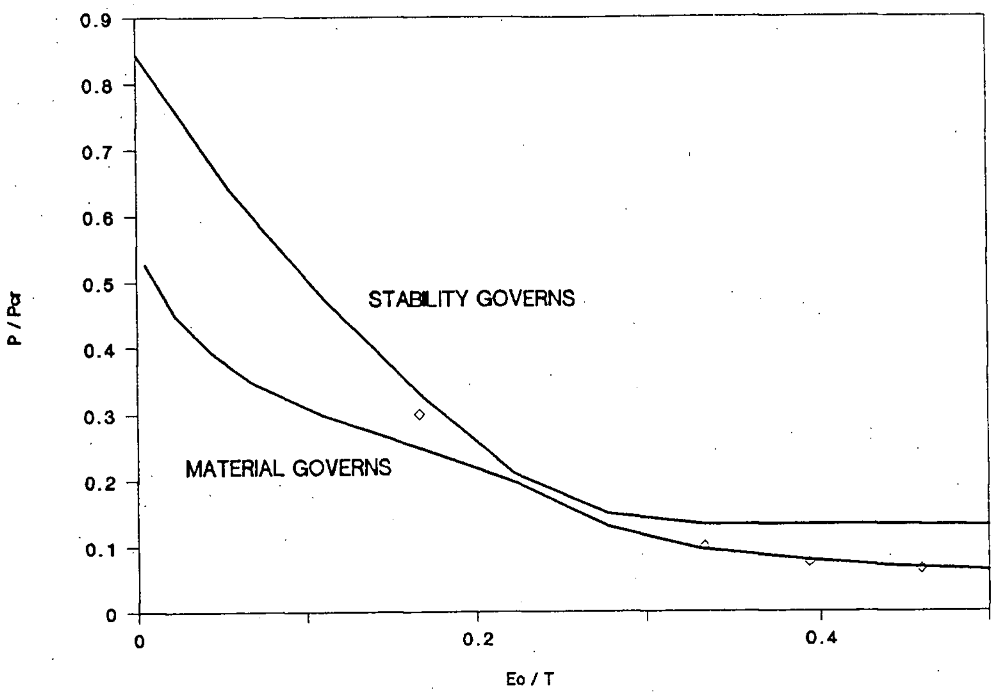

FIG. 11.11 Theoretical Load–Eccentricity Curve Compared with Experiments by Hatzinikolas et al: 137 inch High Wall with Reinforcement 3#6

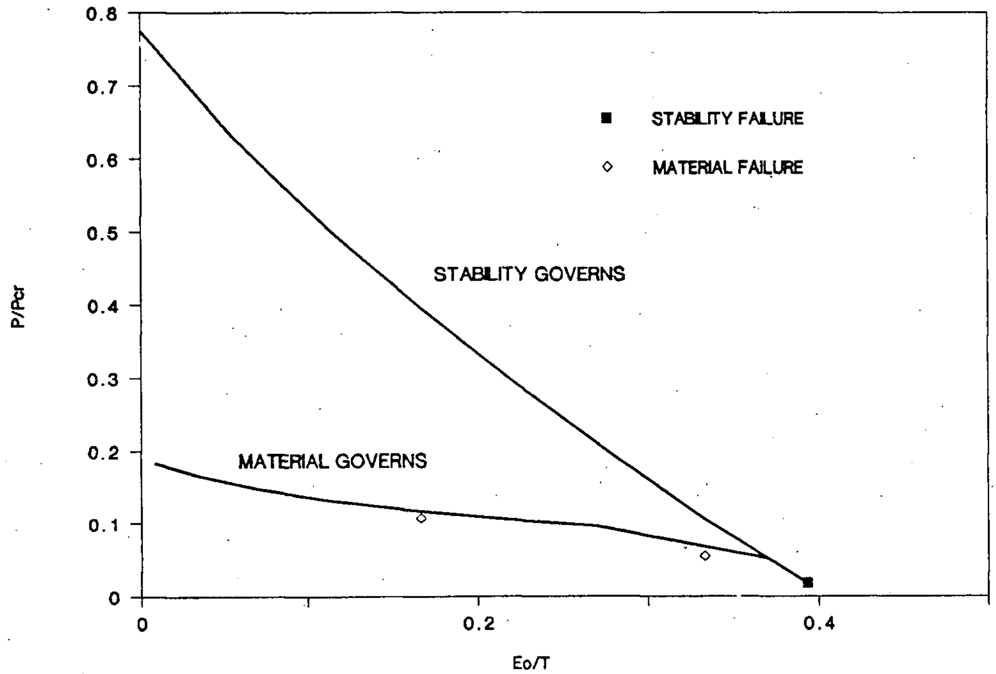

FIG. 11.12 Theoretical Load–Eccentricity Curve Compared with Experiments by Hatzinikolas et al: 105 inch High Plain Wall

close to the curve. This indicates material failure since the cross-sectional capacity is reached at midspan. However, for the cases of larger eccentricities ($e_o=t/3$, $e_o=3$ in and $e_o=3.5$ in), all the end points are well within the capacity curve. The maximun force for equilibrium is reached while the cross-sectional capacity is not exceeded as shown by the curves defining the midspan conditions. It is clear that these are the cases of instability failure. (At instability, the midheight load path should reach a horizontal tangent. It is seen that this is approximately true of the predicted curves.)

The comparison in terms of the failure loads may be better illustrated by plotting P/P_{cr} against e_o/t as shown in Fig. 11.10. The plot includes two curves, one of which represents instability failure generated by the algorithm similar to the curve in Fig. 11.5. The other defines material failure, which is converted and shrunk (by the slenderness effect) from the $P-M$ capacity curve given in Fig. 11.9. It is clear that when loading eccentricity is small, the wall is governed by material failure. When the eccentricity is great, the wall will fail by instability. The agreement with the experiments in terms of the failure loads is very good.

As expected, an increase of the reinforcement will overcome the brittleness of the wall and prevent instability failure. Fig. 11.11 shows the $P-e$ relationship for walls of the same configuration as the ones studied above but with heavier reinforcement (3#6, $n\rho=0.108$). Material failure governs for the whole eccentricity range as illustrated in the plot.

When walls are lower, material failure will again govern the behaviour, as shown in Fig. 11.12 for the case of the 105 inch high plain concrete wall with smaller eccentricities. We see again, by comparing Figs. 11.10, 11.11 and 11.12, that behaviour under large eccentricities is significantly enhanced by an increase in the reinforcement.

11.6 Usefulness and Limitations

The analysis presented leads to a very attractive approach to the slenderness of concrete masonry. For a given wall, i.e. when the dimensions and the parameters f'_u, E, λ, a/b and $n\rho$ of the wall are known, the $P-M$ cross-sectional capacity curve and the curve defining the relationship between buckling load and eccentricity (such as the one in Fig. 11.5) can be developed. The designer must first ensure that the design load at the design eccentricity does not exceed the buckling value. He is then required to make sure that the design load and the design moment at midspan (or the point of maximum deflection for unequal eccentricities) lie inside the $P-M$ capacity curve so that material failure will not happen. The end moment is magnified to give the midspan moment. The magnifier, which varies with P/P_{cr}, is a byproduct of the derivation of the buckling curve.

The attractiveness of the approach lies in the fact that the buckling curve as a function of the loading eccentricity is uncoupled from the specific material properties and dimensions of a wall. The curve is dependent only on the three cross-sectional parameters: namely, λ, the extent of the grout and the bedding; a/b, the hollowness of the block unit; and $n\rho$, the reinforcement parameters. Thus, for any combinations of these parameters, the curve may be pre-prepared. A designer is then only required to work with these prepared curves and the $P-M$ cross-sectional capacity bound, which can be developed for a specific wall by equations given in Chapter X or by any other simplified means, to determine if the wall is adequate. Without performing a special, costly analysis for an individual wall, the designer is able to approach the problem with assured accuracy. This approach, the author believes, is much more rational than the current design analysis at the cost of very limited additional effort.

The independence of the buckling load from the specific material properties and dimensions of a wall arises from the assumption of linear material relationships. Further, the validity of the approach is also based on the assumption that plane sections remain plane. The approach is good as long as these assumptions are still close to reality; otherwise it is subject to limitations.

Substantial nonlinearity may be caused by the yielding of the reinforcing steel in tension. This may happen when the necessary condition specified in Chapter X (see the context of Eq. 10.11) is satisfied, which usually corresponds to a low steel ratio. Although the steel yielding can be incorporated in the algorithm without much difficulty, by changing the $n\rho$ value for appropriate sections at which the yield strain is exceeded, the advantage of simplicity is lost. If this happens it appears that the wall must be studied individually.

However, further investigation indicates that when the steel ratio is low, the behaviour of the wall will be governed mainly by the surrounding concrete. Buckling usually takes place before the yield strain is reached, as in the 3#3 reinforced walls studied above. Indeed, yielding of the steel was never observed in the experiments (Hatzinikolas et al 1978), and the proposed procedures do give very good predictions, as shown above.

Further, for very low steel ratios, the changing of $n\rho$ in the algorithm makes very little difference if the loading eccentricity is not too large. Anyhow, the steel yielding in tension corresponding to large deflections is unfavorable and may be prevented through design requirements.

The presented procedure tends to overestimate the deflections for walls with heavy reinforcement, as is seen with the 3#9 ($n\rho$=0.245) reinforced walls tested by Hatzinikolas et al (1978). This is believed to be mainly caused by the violation of the plane section assumption. With heavy reinforcement, a wall tends to allow development of deeper crackings in its midspan region. Since the cracks occur usually only at the bed joints, the compressive strains between two joints, i.e., within a block unit, will depart correspondingly from the linear distribution as the crack depths increase. As indicated, the model assumes a linear strain distribution corresponding to an infinitesimal cracking spacing, which, of course, underestimates the rigidity of the cross-section. The underestimation may be substantial when crack depth is large compared to crack spacing (unit height), leading to erroneous results.

The nonlinearity of concrete may also affect the accuracy of the approach. However, the assumption of linear material tends to overestimate the rigidity of the cross-section.

For the cases compared, the approach gives good results for reinforcement up to

$n\rho=0.108$, which corresponds to a steel ratio up to about 1% with respect to the gross cross-sectional area. This covers most of the normal design reinforcement range. Thus the approach will be useful for many design cases without major modifications.

11.7 Some Simplifications

To examine material failure, the method uses the moment magnifier which is produced by the algorithm during generation of the buckling load curve. For a given cross-section, the magnifier is a function of the loading eccentricity as well as the magnitude of the load. For a plain solid section ($\lambda=a/b=n\rho=0$), the relationship is plotted in Fig. 11.13.

In the figure, the two curves running from the origin through the upper right part represent the linear solutions for a member with an uncracked section; the lower one is exact and the upper one is the commonly adopted approximation (see Eq. 11.36). The four lower curves define the magnifier for four different eccentricities. For the smallest eccentricity ($e_o=1/9t$), the curve coincides with the linear solution when the load is small. It begins to depart therefrom at about $P/P_{cr}=0.32$, indicating that the cross-section has started to crack and that nonlinearity in moment-curvature has started to develop at this point. Three other curves, which correspond to loading eccentricities equal to or larger than the kern eccentricity ($e_k=1/6t$), depart from the linear solution at the origin. This indicates that the cross-section begins to crack as soon as the member is loaded. As expected, the nonlinearity leads to a larger magnifier, as clearly illustrated in the plot. Due to the nonlinearity, the member, if it does not fail materially first, will eventually buckle, and therefore these curves are terminated at the buckling load P_k.

Fig. 11.14 shows a similar plot for a member with reinforcement ($\lambda=a/b=0$, $n\rho=0.05$). It appears that the ductility of the member at the greater eccentricities, in the sense of the deflection development before instability, is greatly improved by the reinforcement.

For design purposes, the procedure can be simplified. The magnifier curve for a given eccentricity may be characterized by two parameters, the buckling load, P_k, and the

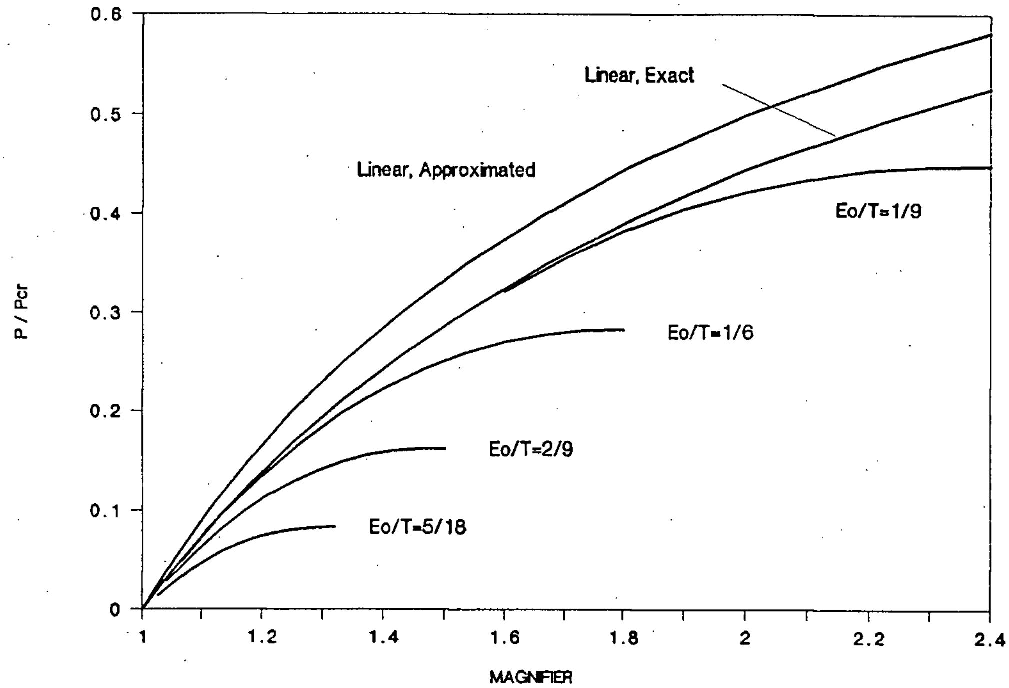

FIG. 11.13 Moment Magnifier versus Load for a Plain Section

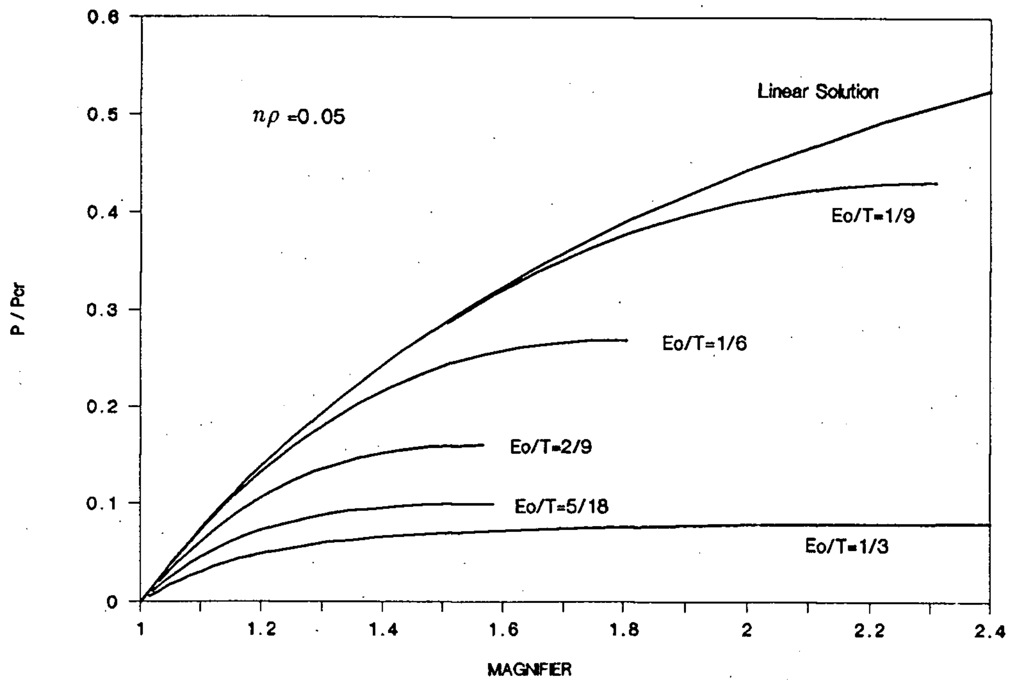

FIG. 11.14 Moment Magnifier versus Load for a Reinforced Section

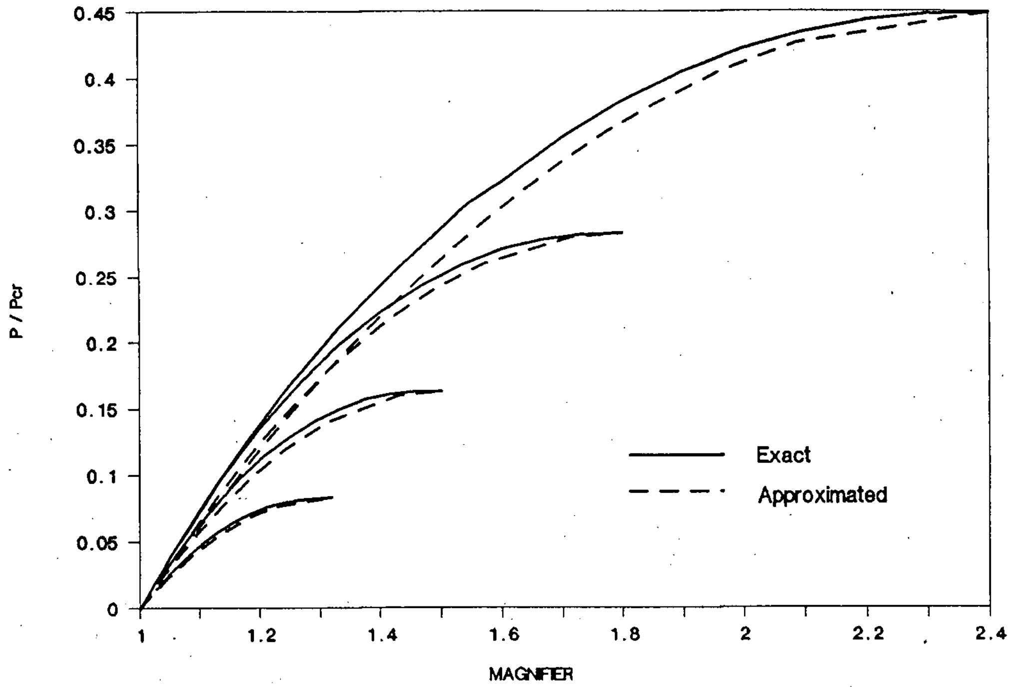

FIG. 11.15 Moment Magnifier: Exact versus Approximation

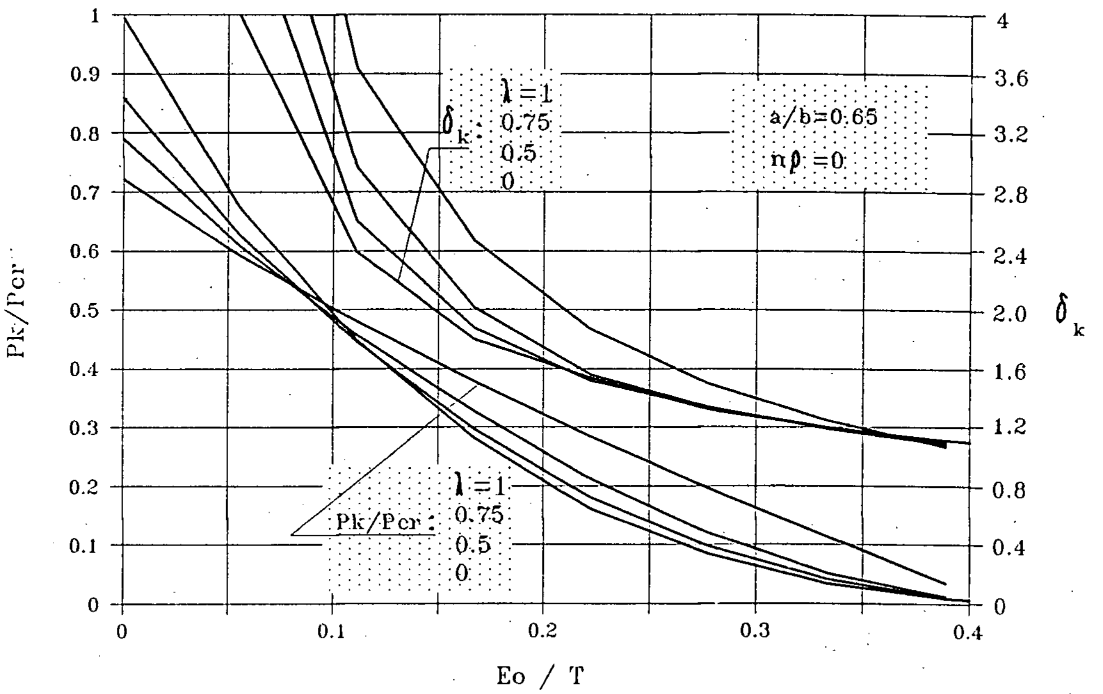

FIG. 11.16 Critical Load and Critical Moment Magnifier Versus Eccentricity: for Purpose of Design Analysis

corresponding magnifier δ_k. If the curve can be constructed by some means to end with a horizontal tangent at this point, it may be accurate enough for design. For this purpose we introduce the form

$$\delta = \left[1 - \left(1 - \frac{1}{\delta_k}\right)\sqrt{1-\frac{P}{P_k}}\;\right]\delta_k \qquad 11.37$$

which passes through the origin and reaches the end point with zero slope. This gives satisfactory fitting for the plain section case, as shown in Fig. 11.15. For a reinforced cross-section at large eccentricity, the curve may be truncated at the beginning of the flat plateau to yield a good fit (cf. Fig. 11.14). This will lead to limited errors since usually values well below the buckling load are of interest.

Through this simplification, we only need to know the buckling load P_k and the corresponding magnifier δ_k for a given cross-section at given eccentricity. These two parameters can be pre-determined and exhibited in the form of tables, or graphs such as the one shown in Fig. 11.16. The figure is for a plain section with different cross-sectional factors λ. Note that two scales are used for the ordinate so that P_k and δ_k can be plotted in the same graph.

For commercially available block units, the range of variation in a/b is small. The parameter λ varies from about 0 up to 1; $n\rho$ also has an upper limit (of 0.1 for the time being). Thus the combinations of these three parameters are limited and it is not impractical to prepare tables or graphs of P_k and δ_k for design purposes.

Finally, it may be worth repeating the approach which has been developed and which is strongly recommended for design purposes:

1) Select the wall cross-section, and, using the material properties and dimensions construct the $P-M$ cross-sectional capacity curve (or choose a pre-prepared one). This is a well developed procedure except that it is recommended that the curve be based on the unit strength. (The equations in Chapter X may be used.)

2) Calculate the Euler load for the gross section P_{cr}.

3) Determine parameters λ, a/b and $n\rho$. (these may have been determined in the first step) According to these three parameters, choose an appropriate pre-prepared buckling load graph (such as the one shown in Fig. 11.16) or table. Examine the stability by checking whether the design load (P/P_{cr}) is below the buckling load (P_k/P_{cr}) at the design eccentricity (e_o/t). If not, repeat from step 1.

4) To check material failure, read P_k and δ_k at the design eccentricity (interpolation often necessary), and calculate the moment magnifier δ by using Eq. 11.37.

5) Magnify the design end moment by δ and ensure that material failure will not occur by checking if this moment combined with the design load falls within the $P-M$ cross-sectional curve. If not, repeat from step 1.

The recommended design approach, the author believes, can be extended to the case of unequal eccentricities (which is included in the algorithm) without much difficulty.

CHAPTER XII

SUMMARY AND CONCLUSIONS

1) The mechanical properties of concrete masonry subject to axial compression and out plane bending have been investigated experimentally, by testing block prisms with various bedding and grouting conditions under various eccentricities.

2) Splitting failure has been examined and Hilsdorf's model has been revised in the light of both experimental and analytical work. It is concluded that the splitting failure mode of concrete masonry under axial compression cannot simply be attributed to the lower stiffness of the mortar joints.

3) Brittle failure under uniaxial compression has been investigated at the fundamental level. A qualitative model was proposed to explain the splitting failure, and to reveal some of the characteristics of concrete and other brittle materials under axial compression.

4) The joint effect on masonry strength can be attributed to the distortion of the uniform compressive stress in the vicinity of the joint.

5) The deep beam bending model proposed by Shrive for failure of face-shell bedded masonry under axial compression has been reviewed and verified experimentally.

6) Based on the failure mechanism and joint effect study, it is concluded that concentric and eccentric capacities should be treated differently. It is shown that eccentric capacity can be satisfactorily predicted on the basis of masonry unit compressive strength.

7) The behaviour of grouted masonry is highly governed by the deformation properties of the masonry constituents. Premature cracking is caused by the incompatibility between block shell and grout. The ultimate capacity is more strongly governed by the strength of the block shell.

8) Based on the above observations, an analytical model considering vertical as well as cross-sectional deformation interaction has been presented which gives satisfactory predictions for ultimate capacity and cracking loads.

9) Based on the observations and studies on the masonry prism characteristics, a theoretical model has been developed to study the slenderness and the stability of concrete masonry walls. Compared with experiments, the model gives very good predictions for low and moderate reinforcement ratios.

10) The geometry, grouting, and bedding conditions and the reinforcement are quantified by a few parameters, and the model is presented in a relatively simple form. It is demonstrated that this simple, rational approach can easily be adapted to the design and analysis of slender walls.

REFERENCES

Akio Baba and Osamu Senbu (1986). Influencing factors on prism strength of grouted masonry and fracture mechanism under uniaxial loading. *Proc. of 4th canadian Masonry Symposium.* 1078-1092.

Ashby, M. F. and Cooksley, S. D. (1986). "The failure of brittle solids containing small cracks under compressive stress states." *Acta metall*, Vol. 34, No. 3, 497-510.

Athey, J. W. (1982, Edt.) *Report of the task committee on slender walls.* ACI. Southern California Chapter and the Structural Engineers Association of Southern California, Los Angeles, California.

Bažant, Z. P. (1985) "Mechanics of fracture and progressive cracking in concrete structures." In *Fracture mechanics of concrete*, Ed. by Sih and Ditommaso, Martinus Nijhoff Publishers.

Beyer, W. H. (1986, Edt). *CRC Standard Mathematical Tables 27th Ed.* CRC Press, p245.

Bhargava, J. and Rehnstorm, A. (1975). High speed photography for fracture studies of concrete. *Cement and Concrete Research*, 5, 239-248.

Biolzi, L. (1988). Evaluation of compressive strength of masonry walls by limit analysis. *ASCE J. of Structural Engineering*, Vol. 114, No. 10, Oct. 2179-2189.

Boult, B. F. (1979). Concrete masonry prism testing, *J. of A. C. I., V.76, No.4, April* 513-536.

Brace, W. F., and Bombolakis, E. G. (1963). "A note on brittle crack growth in compression." *J. Geophys. Res.* 68, 3709-3713.

Brace, W. F., and Byerlee, J. D. (1966). *Proc. of the 8th Rock Mech. Sym.* Univ. of Minnesota, AIME, New York. 58-81.

Brady, B. H. G. and Brown, E. T. (1985). *Rock mechanics for underground mining*, George Allen & Unwin.

Broek, D. (1978). *Elementary engineering fracture mechanics*, Sijthoff & Noordhoff.

Chapman, J. C. and Slatford, J. (1957). The elastic buckling of brittle columns. *Paper* 6147, *Proceedings of the Institution of Civil Engineers*, *London*, *vol.*6 *Jan.* 107-125

Crouch, S. L. and Starfield, A. M. (1983). *Boundary element methods in solid mechanics*, George Allen& Unwin press.

CSA Standard A179M, (1976). *Mortar and Grout for Unit Masonry.*

CSA Standard CAN3-S304-M84, (1984). *Masonry Design for Buildings.*

Drysdale, R. G. and Hamid, A. A. (1979). Behaviour of concrete block masonry under axial compression. *A.C.I. J./ June*, 707-721.

Drysdale, R. G. and Hamid, A. A. (1983). Capacity of concrete block masonry prisms under eccentric compressive loading. *A.C.I J. Mar.-April* 102-108.

Fairhurst, C. and Cook, N. G. W. (1966) "The phenomenon of rock splitting parallel to the direction of maximum compression in the neighbour hood of a surface." In *Proc.* 1*st Congr. Int. Soc. Rock Mech.*, *Lisbon*, Vol. 1, 687-692.

Fattal, S. G. and Cattaneo, L. E. (1976). Structural performance of masonry walls under compression and flexure. *Nat. Bur. Std.* (*U.S*), *Bldg. Sci. Ser.* 73.

Goodier, J. N. (1968). Mathematical theory of equilibrium cracks. *Fracture II*, H. Liebowitz (Ed.), Academic Press, New York and London, 56-65.

Griffith, A. A. (1921). *Phil. Trans. R. Soc. Lond. A*221, 163-198.

Hamid, A. A. (1978). *Behaviour characteristics of concrete masonry.* Ph.D. thesis, Macmaster University.

Hamid, A. A. and Drysdale, R. G., and Heidebrecht, A. C. (1978). Effect of grouting on the strength characteristics of concrete block masonry, *Proc.* 9*th. American Masonry Conf. U. of Colorado*, *Boulder*, *Cal.*, *Aug.*

Hamid, A. A. and Drysdale, R. G. (1979). Suggested failure criteria for grouted concrete masonry under axial compression. *ACI J.* Oct. 1047-1061.

Hamid, A. A. and Chukwunenye A. O. (1986). Compression behaviour of concrete masonry prisms. *ASCE J. of Structural Engineering*, Vol 112, No. 3 Mar. 605-613.

Hatzinikolas, M., Longworth, J. and Warwaruk, J. (1978). Concrete masonry walls. *Structural Engineering Report No.*70 Department of Civil Engineering, University of Alberta.

Hilsdorf, H. K. (1969). Investigation into the failure mechanism of brick masonry loaded in axial compression. *Proc., Int. Conf. on Masonry Structural Systems*, Austin, Tex., 34-41.

Hoek, E., and Bieniawski, Z. T. (1965). "Brittle fracture propagation in rock under compression." *Int. J. Frac.* 1, 137-155.

Horii, H. and Nemat-Nasser, S. (1985). "Compression-induced microcrack growth in brittle solids: axial splitting and shear failure." *J. of Geophy. Res.* Vol. 90, No. B4, 3105-3125.

Horii, H. and Nemat-Nasser, S. (1986). "Brittle failure in compression." *Phil. Trans. R. Soc. Lond.*, A319, 337-374.

Hsu, T. T. C.; Slate, F. O.; Sturman, G. M.; Winter, G. (1963). "Microcracking of plain concrete and the shape of the stress-strain curve." *ACI J. Proceedings* Vol. 60, No.2, Feb., 209-224.

Irwin, G. R. (1957). Analysis of stress and strain near the end of a crack traversing a plate. *J. Appl. Mech.* 24, 361-364.

Kachanov, M. L. (1982). "A microcrack model of rock inelasticity, part II: propagation of microcracks." *Mechanics Mater.* 1, 29-41.

Kendall, K. (1978). Complexities of compression failure. *Proc. R. Soc. Lond.* A.361, 245-263.

Kotsovos, M. D. (1979). "Fracture process of concrete under general stress states." *Matériaux et Constructions, Materials and Structures*, Nov.-Dec., Vol.12, No.72, 431-437.

Kotsovos, M. D. and Newman, J. B. (1981) Fracture mechanics and concrete behaviour. *Magazine of Concrete Research*, Vol.33, No. 115, June, 103-112.

Kotsovos, M. D. (1983). Effect of testing techniques on the post-ultimate behaviour of concrete in compression. *Matériaux et Constructions, Materials and Structures*, Jan.-Feb., Vol.16, No.91, 3-12.

Maurenbrecher, A. H. P. (1980). The effect of test procedures on the compressive strength of masonry prisms. *Proc. 2nd Can. Masonry Conf., Ottawa.* 39.

McClintock, F. A. and Walsh, J. B. (1963) "Friction on Griffith cracks in rocks under pressure." In *Proc. 4th U. S. Nat. Congr. Appl. Mech.* 1962, Vol. 2, 1015-1021. New York: ASME.

Mindess, S. (1983). The application of fracture mechanics to cement and concrete: A historic review. *Fracture Mechanics of Concrete* F. H. Wittmann (Ed.), Elsevier, 1-25.

Nathan, N. D. (1972). Slenderness of prestressed concrete beam-columns. *PCI J., Vol.* 17, #6. Nov.-Dec. 45-57.

Nathan, N. D. and Alcock, W. J. (1977). Moment magnification tests of prestressed concrete columns. *PCI J., Vol.* 22, #4. July-Aug.

Nathan, N. D. (1985). A computer program for rational analysis of beam columns. *Research Report*, Department of Civil Engineering, the University of British Columbia.

Nemat-Nasser, S. and Horii, H. (1982). "Compressive-induced nonplanar crack extension with application to splitting, exfoliation, and rockburst." *J. of Geophy. Res.* Vol. 87, No. B8, 6805-6821.

Neville, A. M., (1965). A general relation for strengths of concrete specimens of different shapes and sizes, *J. of A.C.I. Oct.*, 1095-1109.

Obert, L. (1972). "Brittle fracture of rocks." *Fracture VII* H. Liebowitz (Ed.), Academic Press, New York and London, 93-155.

Panasjuk, V. V. (1976). Stress distribution around cracks in plate andshells. *Naukova Dumka*, Kiev, 444.

Park, R. and Pauley, T. (1975). *Reinforced concrete structures.* Wiley, New York.

Paterson, M. S. (1978) *Experimental rock deformation — the brittle field.* Springer, Berlin.

Priestley, M. J. N. and McG. Elder, D. (1982). Seismic behaviour of slender concrete masonry shear walls. *Research report ISSN* 0110-3326, Department of Civil Engineering. University of Canterbury.

Priestley, M. J. N. and Hon, C. Y. (1983). Prediction of masonry compressive strength from constituent properties. *Research Report*, Department of Civili Engineering, University of Canterbury.

Priestley, M. J. N., and Elder, D. M. (1985). Stress strain curves for unconfined and confined concrete masonry, *J. of A.C.I.*, *V.*80, *No.*3, *May/June*, 192-201.

Royen, N. (1937). Knickfestigkeit Exzentrisch Beanspruchter Säulen Aus Baustoff, *der Nur Gegen Druck Widerstandsfähig Ist. Der Bauingenieur*, *vol.* 18, *p*444.

Sahlin, S. (1971). *Structural masonry.* Englewood Cliffs, N. J., Prentice Hall.

Sammis, C. G. and Ashby, M. F. (1986) "The failure of brittle porous solids under compressive stress states." *Acta metall* Vol. 34, No. 3, 511-526.

Santiago, D. S. and Hilsdorf, H. K. (1973). "Fracture mechanics of concrete under compressive load." *Cement and Concrete Research.* Vol.3, 363-388.

Seldenrath, I. T. R. and Gramberg, I. J. (1958). "Stress-strain relations and breakage of rocks." *Mechanical properties of non-metallic brittle materials* Walton (Ed.).

Shrive, N. G. and Jessop, E. L. (1980). Anisotropy in extruded clay units and its effect on masonry behaviour. *Proc. 2nd Canadian Masonry Symposium*, 39-50.

Shrive, N. G. (1982) The failure Mechanism of face-shell bedded (ungrouted and unreinforced) masonry. International *J. of Masonry construction*, *Vol.*2 *No.*3.

Shrive, N. G. (1982). An examination of the failure mechanism of masonry piers, prisms and walls subjected to compression. *Proc. of the British Ceramic Society*, *No.* 30, ed. by H.W.H. West.

Shrive, N. G. (1983). A fundamental approach to the fracture of masonry. *Proc. 3rd Canadian Masonry Symposium*, 4-1,4-16.

Stafford-Smith, B. and Carter, C. (1971). Distribution of stresses in masonry wall subjected to vertical loading. *Proc 2nd Int. Br. Mas. Conf.*, *Brit. Cer. Res. Ass.*, *Stroke-on-Trent*, 119-

124.

Steif, P. S., (1984). "Crack extension under compressive loading." *Engng. Fract. Mech.* 20, 463-473.

Sturgeon, G.R. and Longworth, J. (1985). Reinforced concrete block masonry columns, *Proc. Third North American Masonry Conference.* 20-1, 20-16.

Suwalski, P. D. and Drysdale, R. G. (1986). Influence of slenderness of the capacity of concrete block walls. *Proc. of 4th Canadian Masonry Symposium.* 122-135.

Thurston, S. J., Cyclic Racking (1981) Tests of reinforced concrete masonry shear walls, *M. W. D. Central Labs. Report No.* 5-81/8.

Timoshenko, S. and Krieger, S. W. (1959), *Theory of Plates and Shells* Sec. Edt. McGRAW-HILL book company.

Troxell, G. E, Davis, H. E. and Kelly, J. W. (1968) *Composition and properties fo concrete*, 2nd edt. Mcgraw-Hill Civil Eng. Series.

Turkstra, C. J, and Thomas, G. R. (1978). Strain gradient effects in masonry, *Research Report*, Department of Civil Engineering, McGill University.

Wang, P. T., Shah, S. P. and Naaman, A. E. (1978). Stress-strain curves of normal and lightweight concrete in compression. *ACI J.* Nov. 603-611.

Wong, H. E. and Drysdale, R. G. (1983) Compression characteristics of concrete block masonry prisms *ASTM. STP* 871, 167-177.

Warwaruk, J.; Longworth, J. and Feeg, C. (1986). Response of masonry column using standard wall units. *Proc. of 4th Canadian Masonry Symposium.* 894-909.

Wawersik, W. H. and Fairhurst, C. (1970). A study of brittle rock fracture in laboratory compression experiments. *Int. J. Rock Mech. Min. Sci.* 7, 561-575.

Xu, Z. (1979). *A concise course of elasticity*, 1979. Qinghua University (in Chinese).

Yokel, F. Y. and Dikkers, R. D. (1971). Strength of load bearing masonry walls. *Journal of the Structural Division, Proceedings of the ASCE* May, 1593-1609.

Yokel, F. Y. (1971) Stability and load capacity of member with no tensile strength. *Journal of the Structural Division, Proceedings of the ASCE July*, 8253-1925

Zaitsev, Y. (1983) "Crack propagation in a composite material." *Fracture Mechanics of Concrete F. H. Wittmann (Ed.)*, Elsevier, 251-299.

Ziegeldorf, S, (1983). "Phenomenological aspects of the fracture of concrete" *Fracture Mechanics of Concrete* F. H. Wittmann (Ed.), Elsevier, 31-41.

APPENDICES

APPENDIX A. Expressions for dU and dR in Chapter III

The strain energy for a linear-elastic body with volume $\mathcal{V}$ is

$$U = \frac{1}{2} \int_{\mathcal{V}} \sigma_{ij}\epsilon_{ij} \; d\mathcal{V} \tag{A1}$$

For a cracked body, as long as the cracks have not gone through the body, so that the region is still connected, general energy relations should hold as for a solid body. Without loss of generality, consider an elastic body containing a single crack, as shown in Fig. A.1. At the equilibrium state, we have

$$\int_{\Gamma_1} T_i u_i \; ds + \int_{\Gamma_2} Q_i v_i \; ds = \int_{\mathcal{V}} \sigma_{ij}\epsilon_{ij} \; d\mathcal{V}$$

$$= 2U \qquad \text{(in view of Eq. A1)} \tag{A2}$$

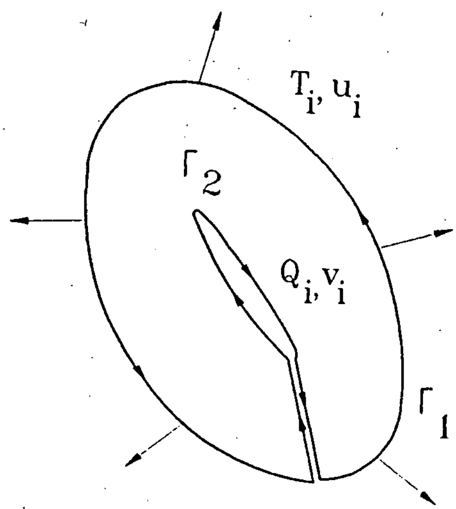

FIG. A1 An Elastic Body Containing a Single Crack

as a result of the application of the divergence theorem, equilibrium and compatibility conditions; where T_i, u_i and Q_i, v_i denote the tractions and associated displacements on the external boundary Γ_1 and internal Γ_2 (crack surface), respectively. Note the integral path we have chosen; the repeated path does not contribute.

If the surface of the crack is free, then $Q_i = 0$. If the opposite surfaces of the crack slide against each other, as is the case in the model, then $Q_n \neq 0$ and $v_t \neq 0$, but $Q_t = v_n = 0$, so that $Q_i v_i = 0$; where subscripts n and t denote normal and tangential components respectively. Therefore, it is always true that

$$U = \frac{1}{2} \int_{\Gamma_1} T_i u_i \, ds \tag{A3}$$

regardless of how this crack extends within the material. Of course, for our model this is

$$U = \frac{1}{2} F\Delta \tag{A4}$$

If friction between the crack surfaces is included, the situation becomes more complicated. Restricting attention to our model, we have $Q_t = f$, the friction force, which can be related to the applied force when crack surfaces are sliding against each other:

$$f = \sigma\mu \sin^2\alpha = \frac{F}{w}\mu \sin^2\alpha \tag{A5}$$

(Recall that w is the specimen width and F is the applied force). v_t may be approximated by the geometric relation between the crack opening and the sliding displacement, as shown in Fig. A2

$$v_t \approx \delta/\sin\alpha \tag{A6}$$

In view of Eq. A2, the expression for the strain energy becomes

$$U = \frac{1}{2} \left(F\Delta - 2a\, M\, f\, \delta/\sin\alpha \right) \tag{A7}$$

The negative sign preceding the second term indicates that the friction force is in the opposite

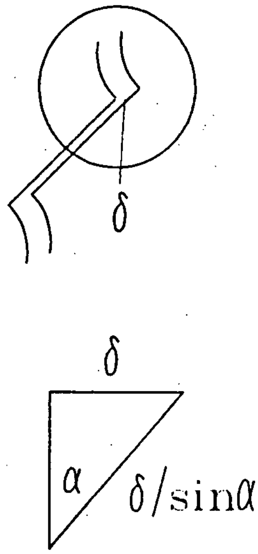

FIG. A2 Geometric Relation between Crack Opening and Sliding Displacement

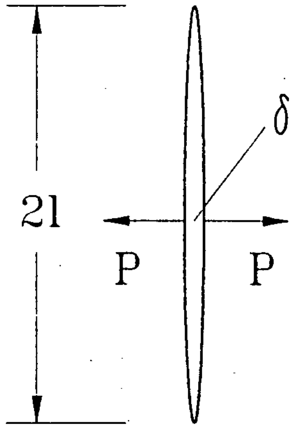

FIG. A3 A Crack Extended by a Pair of Splitting Forces

direction to that of the sliding displacement.

An expression for the crack opening δ is still needed. Consider a crack with initial length $2l_o$ being extended to $2l$ under the action of a pair of forces P, as shown in Fig. A3. According to the energy theorems concerning the formation and extension of cracks in the elastic solid (Goodier 1968), we have

$$\frac{1}{2} P\delta = 2 \int_{l_o}^{l} G_I \, dl \qquad \text{A8}$$

Rearranging the equation and noting Eq. 3.5, we obtain

$$\delta = \int_{l_o}^{l} \frac{4P(1-\nu^2)}{Eb\sin(\pi l/b)}\, dl = \frac{4P(1-\nu^2)}{\pi E} \log\left(\frac{\tan(\pi l/2b)}{\tan(\pi l_o/2b)}\right) \qquad \text{A9}$$

Eq. 3.13 follows when Eq. A5 and Eq. A9 are subsituted into Eq. A7

It should be noted that in a later stage of the post-peak branch, when the crack opening width is decreasing, the friction force will change direction, and the sign preceding μ contained in the expression should be changed.

When crack surfaces are sliding against each other, the energy dissipated by friction is

$$dR = 2a\ M\, f\, dv_t = 2a\ M\ \mu\sigma \sin\alpha\ d\delta \qquad \text{A10}$$

Eq. 3.17 follows when Eq. A9 is differentiated and substituted into this expression.

APPENDIX B. Solution of equation 3.10

After making the appropriate substitutions and rearranging, some cancellation occurs and Eq. 3.10 reduces to

$$F\Delta' - F'\Delta = 4M\ G_{IC}\left(1 + \frac{2\mu sin\alpha}{k}\right) \qquad \text{A11}$$

which is solved by the method of variation of parameters, as shown further below. Letting $\Delta = H(l)F(l)$ and substituting, it follows that

$$H' = 4M\ G_{IC}\left(1 + \frac{2\mu sin\alpha}{k}\right)\frac{1}{F^2} \qquad (\text{ recall } F = \sigma w)$$

$$= 4M\ G_{IC}\left(1 + \frac{2\mu \sin\alpha}{k}\right)\left(\frac{ka}{w\ K_{IC}}\right)^2 \frac{1}{b\sin(\pi l/b)} \qquad \text{A12}$$

in which relations given by Eq. 3.2 and Eq. 3.4 are applied. Eq. A12 is then integrated and matched to the initial condition given by Eq. 3.18. The solution takes the form as given by Eq. 3.22 when the relations defined by Eqs. 3.6, 3.19, 3.20 and 3.21 are used.

The solution is valid for the whole range except the friction transitional interval, in which the friction force is changing magnitude as well as direction; the relation given by Eq. A5 does not then hold. Certainly, after the transitional interval, the sign preceding μ should be changed.

The starting point of this transitional interval may be found by setting $d\delta$ equal to zero. This condition follows by differentiating Eq. A9:

$$1 + \frac{\cos\Theta}{2} \log \frac{\tan(\Theta/2)}{\tan(\Theta_o/2)} = 0 \qquad \text{A13}$$

(recall $\Theta = \text{arc } \sin(\sigma/f_c')^2$, $\Theta_o = \text{arc } \sin(\sigma_o/f_c')^2$, and recognize also arc $\sin(\sigma/f_c')^2 = \pi l/b$) We define this starting point by Θ_1 or σ_1 (quantities at this point denoted with subspript 1). During the transitional interval, the expression for the tensile splitting force becomes

$$P = 2a \, (\, \sigma \sin\alpha \, \cos\alpha \, - \, f \,) \, \sin\alpha \qquad \text{A14}$$

The crack extension condition is still governed by Eq. 3.4. Recognizing that during this interval the crack opening remains constant, we have an extra condition

$$\frac{4P_1(1-\nu^2)}{\pi E} \log \frac{\tan(\Theta_1/2)}{\tan(\Theta_o/2)} = \delta_1 = \text{constant} \qquad \text{A15}$$

Two cases need to be discussed. First we assume l increases during the interval. It is obvious then that Eq. 3.4 and Eq. A15 can not be satisfied simultaneously. Further inspection indicates that the force defined by Eq. A15 is always higher than that defined by Eq. 3.4. This actually implies that the crack will extend immediately and the material will fail almost at the instant the starting point is reached.

In the second case, if we assume that the applied load retreats so fast that l or P remains unchanged during the interval, then both Eq. 3.4 and Eq. A15 are satisfied, and the friction force f can be found by using the relation given by Eq. A14. In view of Eq. A7, the strain energy is then expressed as

$$U = \frac{1}{2}\left[F\Delta - 2a\, M\left(\sigma \sin\alpha \cos\alpha - \frac{P_1}{2a\,\sin\alpha}\right)\frac{\delta_1}{\sin\alpha}\right] \qquad \text{A16}$$

Further since $P = P_1$ remains constant, the finish point, defined as σ_2, can be found by equating the expression for P at the beginning point to that at the finish point, as

$$\sigma_2 = \frac{\cos\alpha - \mu\sin\alpha}{\cos\alpha + \mu\sin\alpha}\,\sigma_1 \qquad \text{A17}$$

Since $d\delta = dl = 0$, the differential equation of the energy relation reduces to

$$dV - dU = 0 \qquad \sigma_1 < \sigma < \sigma_2 \qquad \text{A18}$$

After substituting Eq. 3.11 and Eq. A16 , the solution of Eq. A18 turns out to be a linear relation between stress and strain:

$$\epsilon = \frac{a\,\delta_1 \cos\alpha}{2b^2} + C\sigma \qquad \text{A19}$$

where C is an integral constant found by the conditions at the starting point. This relation is used in plotting Fig. 3.9.

APPENDIX C. Solution of equation 4.1

A series solution can be formed by the eigen functions of the problem:

$$u(x,y) = \sum_{n=1}^{\infty} X_n(x) \ \sin(\alpha_n y) \qquad \text{A20}$$

which satisfies boundary conditions specified by Eqs. 4.3 and 4.4; where $X_n(x)$ is a function of x and $\alpha_n = n\pi/t_o$. When A20 is substituted into Eq. 4.1, it follows that

$$X_n''(x) - \kappa^2\alpha_n^2 \ X_n(x) = 0 \qquad n=1,2 \cdots\cdots \infty \qquad \text{A21}$$

Recall that $\kappa = \sqrt{(1-\nu)/2}$. A21 is integrated and substituted back into A20, which, when boundary condition Eq. 4.2 is applied, reduces to

$$u(x,y) = \sum_{n=1}^{\infty} A_n \sinh(\kappa\alpha_n x) \sin(\alpha_n y) \qquad \text{A22}$$

where A_n is a constant, which is then found by matching A23 to the boundary condition Eq. 4.5:

$$\sum_{n=1}^{\infty} A_n \kappa\alpha_n \cosh\left(\frac{\kappa\alpha_n a}{2}\right) \sin(\alpha_n y) = \frac{1-\nu^2}{E} \ q$$

$$A_n = \frac{2}{t_o\kappa\alpha_n \cosh\left(\frac{\kappa\alpha_n a}{2}\right)} \int_0^{t_o} \frac{1-\nu^2}{E} \ q \sin(\alpha_n y) \ dy$$

$$= \begin{cases} \dfrac{4(1-\nu^2)qt_o}{n^2\pi^2\kappa E \cosh\left(\frac{\kappa\alpha_n a}{2}\right)} & \text{when } n \text{ is odd} \\ 0 & \text{when } n \text{ is even} \end{cases} \qquad \text{A23}$$

Eq. 4.6 follows when A23 is substuted into A22.

APPENDIX D. Coefficients A_m, B_m in stress function Φ specified by equation 4.11

Eq. 4.11 is actually a summation of Levy's type solutions for plate bending (Timoshenko and Krieger, 1959), so it is clear that

$$\nabla^4 \Phi = 0 \tag{A24}$$

And it is also obvious that Eq. 4.11 is constructed acoording to the diametrically symmetric properties of the problem, so that only boundary conditions at x=0 and y=0 need to be considered.

Referring to Fig. 4.7, if we integrate the boundary data we have

$$\Phi = c_1 y + c_2 \tag{A25}$$

with

$$\Phi_x = c_3 \tag{A26}$$

at the boundary $x = 0$; and

$$\Phi = c_4 x + c_5 \tag{A27}$$

with

$$\Phi_y(x) = \int \tau_{xy}(x,0)\ dx + c_6$$

$$= \frac{4qt_o}{\pi^2} \sum_{n=1}^{\infty} \frac{\cosh[(2n\text{-}1)\kappa\pi(x - a/2)/t_o]}{(2n\text{-}1)^2 \cosh[(2n\text{-}1)\kappa\pi a/2t_o]} + c_6 \tag{A28}$$

at $y = 0$; where c_1 to c_6 are constants of integration. Note in A28, τ_{xy} is specified by Eq. 4.7 but with the shifted origin. c_1 and c_4 must vanish for symmetry of the problem. Thus Φ is constant along the boundaries, and Eq. 4.11 assumes $c_2 = c_5 = 0$ by the fact that it is immaterial to add a constant to Φ. Further, the slopes defined by A26 and A28 must also vanish at the origin ($x = y = 0$) because of the constancy. This leads to $c_3 = 0$ and

$$c_6 = -\frac{qt_o}{2} \qquad \text{A29}$$

When Eq. 4.11 is differentiated and set equal to the boundary conditions, we obtain two equations:

$$\sum_{m=1}^{\infty} \left[A_m \mathfrak{Y}_m(y) + \frac{2}{b} B_m b_m \sin\left(\frac{m\pi}{b} y\right) \right] = 0 \qquad \text{A30}$$

and

$$\sum_{m=1}^{\infty} \left[\frac{2}{a} A_m a_m \sin\left(\frac{m\pi}{a} x\right) + B_m \mathfrak{X}_m(x) \right] = \Phi_y(x) \qquad \text{A31}$$

where

$$\mathfrak{X}_m(x) = \frac{m\pi}{b} \left(\frac{m\pi(x-a/2)}{b} \sinh \frac{m\pi(x-a/2)}{b} - \beta_m \tanh\beta_m \cosh\frac{m\pi(x-a/2)}{b} \right)$$

$$\mathfrak{Y}_m(y) = \frac{m\pi}{a} \left(\frac{m\pi(y-b/2)}{a} \sinh \frac{m\pi(y-b/2)}{a} - \alpha_m \tanh\alpha_m \cosh\frac{m\pi(y-b/2)}{a} \right)$$

$$a_m = \frac{m\pi}{2} \left((\alpha_m \tanh\alpha_m - 1)\sinh\alpha_m - \alpha_m \cosh\alpha_m \right)$$

$$b_m = \frac{m\pi}{2} \left((\beta_m \tanh\beta_m - 1)\sinh\beta_m - \beta_m \cosh\beta_m \right)$$

and $\Phi_y(x)$ is given by A28. By orthogonality, A30 and A31 become two linear system equations, which can be written symbolically

$$k^a_{mn} A_n + B_m = 0 \tag{A32}$$

$$A_m + k^b_{mn} B_n = C_m \qquad m,\ n = 1,\ 2 \cdots\cdots \infty \tag{A33}$$

where

$$k^a_{mn} = \frac{1}{b_m} \int_0^b \mathcal{Y}_n(y) \sin\frac{m\pi y}{b}\, dy$$

$$k^b_{mn} = \frac{1}{a_m} \int_0^a \mathfrak{X}_n(x) \sin\frac{m\pi x}{a}\, dx$$

$$C_m = \frac{1}{a_m} \int_0^a \Phi_y(x) \sin\frac{m\pi x}{a}\, dx$$

Therefore, for finite size N, it is always possible to solve for A_m and B_m, m=1, 2, ⋯⋯ N:

$$\{A\} = \Big[\, [\,\mathrm{I}\,] - [k^b][k^a] \Big]^{-1} \{C\} \tag{A34}$$

$$\{B\} = -[\, k^a]\, \{A\} \tag{A35}$$

in view of A32 and A33; where [I] is an identity matrix of size N, and hence to obtain an approximation for Φ. In Chapter IV, N=8 was used.

APPENDIX E. Derivation of equation 11.5

The general solution for Eq. 11.1 is

$$y = A \sin\left(\sqrt{\frac{P}{EI}}\left(x - \frac{h}{2}\right)\right) + B\cos\left(\sqrt{\frac{P}{EI}}\left(x - \frac{h}{2}\right)\right) + b \tag{A36}$$

$B = -e_o$ for the boundary condition at the top. When the boundary conditions at section C are applied, we obtain following two relations

$$A \sin\left(\sqrt{\frac{P}{EI}}\left(\frac{h-h_c}{2}\right)\right) + e_o \cos\left(\sqrt{\frac{P}{EI}}\left(\frac{h-h_c}{2}\right)\right) = e_c \tag{A37}$$

$$\sqrt{\frac{P}{EI}}\left[A\cos\left(\sqrt{\frac{P}{EI}}\left(\frac{h-h_c}{2}\right)\right) - e_o \sin\left(\sqrt{\frac{P}{EI}}\left(\frac{h-h_c}{2}\right)\right)\right] = \varphi_c \tag{A38}$$

which lead to

$$A^2 + e_o^2 = e_c^2 + \varphi_c^2 \frac{EI}{P} \tag{A39}$$

Further, when A37 is multiplied by $\left(A^2 + e_o^2\right)^{-1/2}$, it can be rewritten as

$$\sin\left[\sqrt{\frac{P}{\xi P_{cr}}}\left(\frac{1-h_c/h}{2}\right)\pi + \sin^{-1}\frac{e_o}{\sqrt{A^2 + e_o^2}}\right] = \frac{e_c}{\sqrt{A^2 + e_o^2}} \tag{A40}$$

or

$$\sqrt{\frac{P}{\xi P_{cr}}}\left(\frac{1-h_c/h}{2}\right)\pi = \sin^{-1}\frac{e_c}{\sqrt{A^2 + e_o^2}} - \sin^{-1}\frac{e_o}{\sqrt{A^2 + e_o^2}} \tag{A41}$$

Equation 11.5 follows when the relation given by A39 is used.

APPENDIX F. Integration of equations 11.14 and 11.16

By letting

$$F_1(c) = \frac{1}{3}\left[\left(1 - \frac{c}{2b}\right)^2\left(1 + \frac{c}{b}\right) - \lambda\left(\frac{a}{b}\right)^3\right] \qquad \text{A42}$$

and

$$G_1(c) = \left(1 - \frac{c}{2b}\right)^2 - \left(\lambda\frac{a}{b} - n\rho\right)\left(1 - \frac{c}{b}\right) \qquad \text{A43}$$

Eqs. 11.14 and 11.15 can be written as

$$\frac{d^2y}{dx^2} = \frac{P}{2Eb^2l\, G_1(c)} \qquad \text{A44}$$

and

$$\frac{y}{b} = 1 - \frac{F_1(c)}{G_1(c)} \qquad \text{A45}$$

A45 defines the relationship between y and c, which must be used in integration of A44. By recognizing

$$\frac{d}{dx}\left(\frac{dy}{dx}\right)^2 = 2\left(\frac{dy}{dx}\right)\frac{d^2y}{dx^2} \qquad \text{A46}$$

A44 becomes

$$\left(\frac{dy}{dx}\right)^2 = \frac{P}{Ebl}\int \frac{1}{G_1(c)}\, d\left(\frac{y}{b}\right) \qquad \text{A47}$$

A45 is then substituted into A47, which becomes, after integration by parts

$$\left(\frac{dy}{dx}\right)^2 = -\frac{P}{2Ebl}\left[\frac{F_1(c)}{G_1^2(c)} + \int \frac{F_1'(c)}{G_1^2(c)}\,dc\right] \qquad \text{A48}$$

where

$$F_1'(c) = \frac{dF_1(c)}{dc} = \frac{1}{4b}\left[\left(\frac{c}{b}\right)^2 - 2\left(\frac{c}{b}\right)\right] \qquad \text{A49}$$

in view of A42. Now the problem becomes to integrate

$$I_1 = \int \frac{F_1'(c)}{G_1^2(c)}\,dc \qquad \text{A50}$$

It is seen that the integrand is a rational function of c. The denominator is formed by the square of the G_1 function, which, in view of A43, is quadratic in c. The numerator can be broken into two terms. Thus the integral can be carried out by any standard approach, for example, see CRC Standard Mathematical Tables 27th Ed. p245 (Beyer 1986). After appropriate calculation, the result turns out to be rather simple:

$$I_1 = \frac{1 - c/b}{G_1(c)} \qquad \text{A51}$$

When A51 is substituted back into A48 with a constant of integration, we obtain

$$\left(\frac{dy}{dx}\right)^2 = \frac{P}{Ebl}\left(C_1 - \Omega_1(c)\right) \qquad \text{A52}$$

where $\Omega_1(c)$ is defined by Eq. 11.19. Eq. 11.18 takes the positive square root of A52 referring to Fig. 11.2.

A similar approach is used to integrate Eq. 11.16. However, the equivalent F and G functions become

$$F_2(c) = \frac{1}{3}\left[\left(1-\frac{c}{2b}\right)^2\left(1+\frac{c}{b}\right) - \lambda\left(\left(\frac{a}{b}\right)^3 - \frac{1}{4}\left(1-\frac{a}{b}-\frac{c}{b}\right)^2\left(1+2\frac{a}{b}-\frac{c}{b}\right)\right)\right] \quad \text{A53}$$

and

$$G_2(c) = \left(1-\frac{c}{2b}\right)^2 - \frac{\lambda}{4}\left(1+\frac{a}{b}-\frac{c}{b}\right)^2 + n\rho\left(1-\frac{c}{b}\right) \quad \text{A54}$$

The integrand of the equivalent integral

$$I_2 = \int \frac{F_2'(c)}{G_2^2(c)}\,dc \quad \text{A55}$$

is also a rational function. However, $F'(c)$ contains three terms by differentiation of A53:

$$F_2'(c) = \frac{1}{4b}\left[(1-\lambda)\left(\frac{c}{b}\right)^2 - 2(1-\lambda)\left(\frac{c}{b}\right) - \lambda\left(1-\left(\frac{a}{b}\right)^2\right)\right] \quad \text{A56}$$

After a lengthy but controllable calculation, it turns out again in similar form to A51

$$I_2 = \frac{1-c/b}{G_2(c)} \quad \text{A57}$$

Eq. 11.20 follows after appropriate substitutions.

APPENDIX G. Configuration of a column loaded with double curvature bending

We try to shed some light on the problem by investigating an elastic column. Fig. A4 shows a column loaded with top eccentricity e_t and bottom eccentricity e_b, which will deflect according to

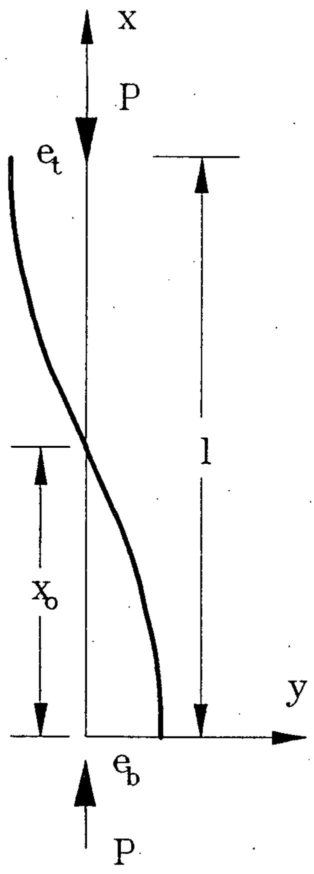

FIG. A4 A Column Loaded with Double Curvature Bending

$$y = \frac{e_t - e_b \cos kl}{\sin kl} \sin kx + e_b \cos kx \qquad \text{A58}$$

where $k = \sqrt{P/EI}$.

A58 must vanish at the inflection point x_o, which leads to

$$\tan kx_o = \frac{\sin kl}{\cos kl - e_t/e_b} \qquad \text{A59}$$

It is clear that when $e_t/e_b = -1$, i.e. the column is loaded anti-symmetrically, $x_o = l/2$. However, we will show that this configuration is not stable when the Euler load is approached. For this purpose we introduce a small perturbation ϵ to the loading conditions

$$e_t/e_b = -(1-\epsilon) \qquad (\epsilon \geq 0) \qquad \text{A60}$$

and examine the sensitivity of the deflected configuration. When A60 is substituted into A59, we obtain

$$F = (\cos kl + 1 - \epsilon)\tan kx_o - \sin kl = 0 \qquad \text{A61}$$

The sensitivity of the configuration to the perturbation is reflected in the derivative of x_o with respect to ϵ

$$\left.\frac{dx_o}{d\epsilon}\right|_{\epsilon=0} = -\left.\frac{F_\epsilon}{F_{x_o}}\right|_{\epsilon=0} = \frac{\sin 2kx_o}{2k(1+\cos kl)} = \frac{\sin kl}{2k(1+\cos kl)} \qquad \text{A62}$$

It is seen that when the load P is relatively low, the derivative will be small. However, when P approaches the Euler load, $kl \to \pi$, it becomes unbounded (note A62 is in an indeterminate form, L'Hospital's rule has been applied once). The high sensitivity is obvious. That is, when the Euler load is approached, the column will have a very high tendency to depart from its original anti-symmetric configuration.

In reality, it is always reasonable to assume some imperfection reflected in the small quantity ϵ. Thus A61 can be rewritten as

$$\frac{x_o}{l} = \begin{cases} \dfrac{1}{kl}\tan^{-1}\left(\dfrac{\tan(kl/2)}{1-\epsilon\Big/\left(2\cos^2(kl/2)\right)}\right) & 1-\epsilon\Big/\left(2\cos^2(kl/2)\right) \geq 0 \\ \dfrac{1}{kl}\left[\pi + \tan^{-1}\left(\dfrac{\tan(kl/2)}{1-\epsilon\Big/\left(2\cos^2(kl/2)\right)}\right)\right] & 1-\epsilon\Big/\left(2\cos^2(kl/2)\right) < 0 \end{cases} \qquad \text{A63}$$

It is seen by the second equation of A63 that

$$\lim_{P\to P_{cr}} \frac{x_o}{l} = \lim_{kl\to\pi} \frac{x_o}{l} = 1 \qquad \text{A64}$$

That is, the column will assume its lowest buckling configuration, for any small imperfection ϵ, when the Euler load is approached.

For a nonlinear column, the situation becomes much more complicated. It appears that a similar tendency would control the behaviour. For design purposes, it is reasonable to assume, conservatively, that this would happen.

APPENDIX H. Electronic Circuit Used in Detecting Macroscopic Splitting (Part)

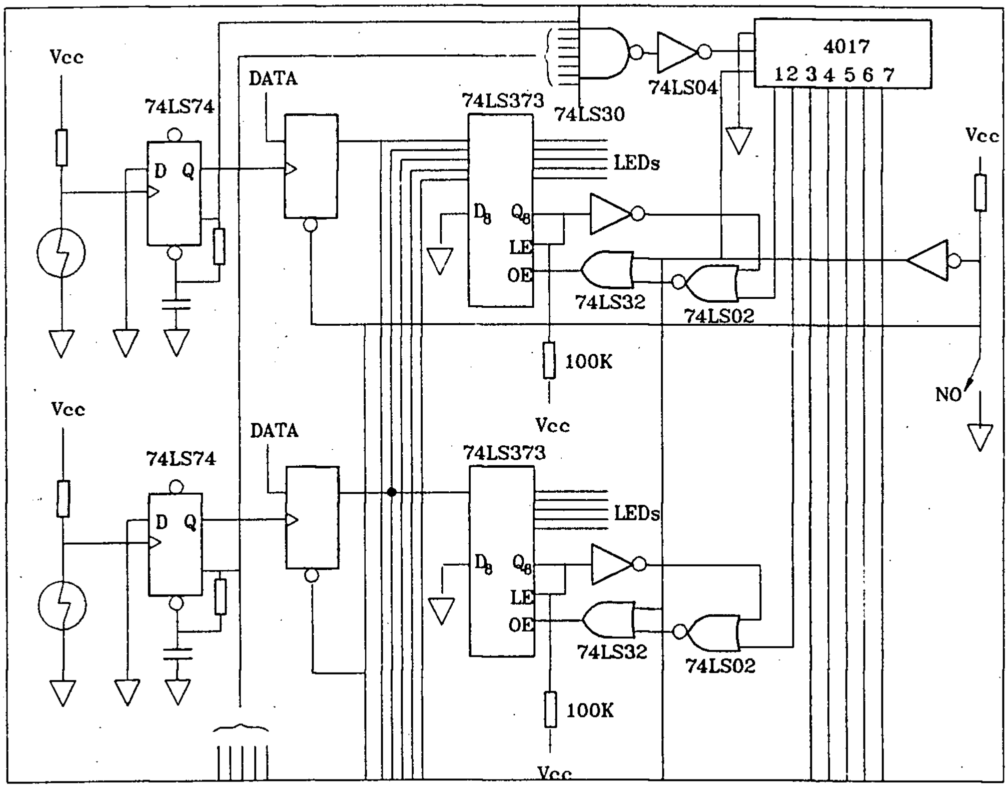

APPENDIX J. Computer Program Calculating Buckling Load and Moment Magnifier of Concrete Masonry

```
C
C   PROGRAM TO EVALUATE MAXIMUM BUCKLING LOAD OF REINFORCED MASONRY
C
      EXTERNAL F1,F2,F3,F4
      COMMON RO,RC,RS,EO,EC,EF,EE,D1,D2
      DIMENSION TITLE(20)
C
C   *****************************************************************
C
C                NOTATION OF VARIABLES
C
C   RO = CROSS-SECTIONAL FACTOR
C   RC = A/B CORE RATIO
C   RS = STEEL RATIO
C   EO = (EQUAL) END ECCENTRICITY
C   EA = SMALLER END ECCENTRICITY
C   EB = LARGER END ECCENTRICITY (EB.GE.ABS(EA))
C   EC = CRACKING ( KERN ) ECCENTRICITY
C   EF = ECCENTRICITY CORRESPONDING TO FLANGE CRACKING
C   D1,D2 = INTERGAL CONSTANTS
C
C   NOTE: ALL ECCENTRICITIES ARE TAKEN AS RATIOS TO HALF DEPTH OF CROSS-SECTION
C
C   *****************************************************************
C
C
C
C     DEFINE PARAMETERS
C
      READ(5,1)(TITLE(I),I=1,20)
      WRITE(6,2)(TITLE(I),I=1,20)
1     FORMAT(20A4)
2     FORMAT(//,1H1,/,24X,20A4,/)
      READ(5,3)RO,RC,RS,EA,EB
3     FORMAT(5F10.5)
      IF(RC.LT.0.0.OR.RS.LT.0.0.OR.EB.LT.ABS(EA))STOP 1
C
      PI=4.*ATAN(1.)
      DRT=SQRT(1.5)
      RST=1.+RS
      CF=1.-RC
      CU=1.+RC
      IF(RC.EQ.0.0.OR.RO.EQ.0.0)CU=2.
      CV=(RST-0.25*RO*CU*CU)/(RST-0.5*RO*CU)
      IF(RO.NE.1.0)CV=2./(1.-RO)*(RST-0.5*RO*CU-SQRT(RST*(RS-
     .RO*RC)+0.25*RO*CU*CU))
      CMU=AMIN1((CV-0.001),CU)
      EC=E1(0.)
      EF=E1(CF)
      EU=E2(CV-0.001)
      IF(CV.GT.CU)EU=E2(CU)
C
      WRITE(6,4)RO,RC,RS,EC,EF,EU
4     FORMAT(/,T25,'CROSS-SECTIONAL PROPERTIES',//,'SEC. FACTOR = ',
     .F8.3,5X,'CORE RATIO = ',F8.3,5X,'STEEL RATIO = ',F8.3,///,
     .'EC/B = ',F8.3,5X,'EF/B = ',F8.3,5X,'EU/B = ',F8.3)
C
      WRITE(6,5)EA,EB
5     FORMAT(/,T25,'LOADING CONDITIONS',//,'EA/B = ',F8.3,5X,'EB/B = '
```

```
     . ,F8.3,///,T25,'CM/B',11X,'P/PCR',10X,'EM/EO',10X,'ERROR')
      EO=EB
C
C     EVALUATE BUCKLING LOAD
C
      PM=0.0
      DM=0.0
      IF(EO.GT.EC)GO TO 200
C
C   END ECCENTRICITY EB LESS THAN CRACKING ECCENTRICITY
C
      CD=CMU/30.
      CM=0.0
      DO 500 I=1,29
      CM=CM+CD
      IF(CM.GT.CF)GO TO 110
      D1=O1(CM)
      TH=D1-O1(0.)
      CML=CM-5.E-6
C
C   SUB-FUNCTION CADRE PERFORMS NUMERICAL INTEGRATION
C
      S1=CADRE(F1,CML,0.0,0.0001,0.,ERROR)
      SQ=Q(TH,EC,EO)
      IF(EA.NE.EO)SQ=SQ+0.5*Q(TH,EO,EA)
      P=4./(PI*PI)*(DRT*S1+SQ)**2
      IF(P.LE.PM)GO TO 1000
      PM=P
      IF(EO.NE.0.0)DM=E1(CM)/EO
      GO TO 505
110   IF((CM-CD).LE.CF)PM=0.0
      D1=O2(CM)-O2(CF)+O1(CF)
      D2=O2(CM)
      TH=D1-O1(0.)
      CML=CM-2.E-6
      S1=CADRE(F1,CF,0.0,0.0001,0.,ERROR)
      S2=CADRE(F2,CML,CF,0.0001,0.,ERROR)
      SQ=Q(TH,EC,EO)
      IF(EA.NE.EO)SQ=SQ+0.5*Q(TH,EO,EA)
      P=4./(PI*PI)*(DRT*(S1+S2)+SQ)**2
      IF(P.LE.PM)GO TO 1000
      PM=P
      IF(EO.NE.0.0)DM=E2(CM)/EO
505   WRITE(6,470)CM,P,DM,ERROR
500   CONTINUE
      WRITE(6,555)
      GO TO 1000
200   IF(EO.GE.EF)GO TO 300
C
C   END ECCENTRICITY EB LARGER THAN CRACKING ECCENTRICITY
C   BUT LESS THAN FLANGE CRACKING ECCENTRICITY
C
      C0=0.0
      C1=0.0
      CL=CF
      ER=0.0001
      EE=EO
C
```

```
C     SUBROUTINE ROOT FINDS CO FOR GIVEN EO
C
      CALL ROOT(CO,CL,F3,ER)
      EE=ABS(EA)
      IF(EA.NE.EO.AND.EE.GT.EC)CALL ROOT(C1,CL,F3,ER)
      CD=(CMU-CO)/30.
      CM=CO
      DO 510 J=1,29
      CM=CM+CD
      IF(CM.GT.CF)GO TO 210
      D1=O1(CM)
      IF(EA.LE.EC)TH=D1-O1(0.)
      CML=CM-2.E-6
      S1=CADRE(F1,CML,CO,0.0001,0.,ERROR)
      IF(EA.NE.EO.AND.EA.GT.EC)S1=S1+0.5*CADRE(F1,CO,C1,0.0001,0.,ERR)
      IF(EA.LE.EC.AND.EA.GE.-EC)S1=S1+0.5*CADRE(F1,CO,0.,.0001,0.,ERR)
     .+0.5/DRT*Q(TH,EC,EA)
      IF(EA.LT.-EC)S1=S1+0.5*CADRE(F1,CO,0.,0.0001,0.,ERR)+0.5/DRT*
     .Q(TH,EC,-EC)+0.5*CADRE(F1,C1,0.0,0.0001,0.0,ERR)
      P=6./(PI*PI)*S1*S1
      IF(P.LE.PM)GO TO 1000
      PM=P
      DM=E1(CM)/EO
      GO TO 515
210   IF((CM-CD).LE.CF)PM=0.0
      D1=O2(CM)-O2(CF)+O1(CF)
      D2=O2(CM)
      IF(EA.LE.EC)TH=D1-O1(0.)
      CML=CM-2.E-6
      S1=CADRE(F1,CF,CO,0.0001,0.,ERROR)
      S2=CADRE(F2,CML,CF,0.0001,0.,ERROR)
      SS=S1+S2
      IF(EA.NE.EO.AND.EA.GT.EC)SS=SS+0.5*CADRE(F1,CO,C1,0.0001,0.,ERR)
      IF(EA.LE.EC.AND.EA.GE.-EC)SS=SS+0.5*CADRE(F1,CO,0.,.0001,0.,ERR)
     .+0.5/DRT*Q(TH,EC,EA)
      IF(EA.LT.-EC)SS=SS+0.5*CADRE(F1,CO,0.,0.0001,0.,ERR)+0.5/DRT*
     .Q(TH,EC,-EC)+0.5*CADRE(F1,C1,0.0,0.0001,0.0,ERR)
      P=6./(PI*PI)*SS**2
      IF(P.LE.PM)GO TO 1000
      PM=P
      DM=E2(CM)/EO
515   WRITE(6,470)CM,P,DM,ERROR
510   CONTINUE
      WRITE(6,555)
      GO TO 1000
300   IF(EO.GE.EU)GO TO 900
C
C   END ECCENTRICITY EB LARGER THAN FLANGE GRACKING ECCENTRICITY
C
      CO=CF
      C1=CF
      C2=0.0
      CL=CMU
      CL2=CF
      ER=0.0001
      EE=EO
      CALL ROOT(CO,CL,F4,ER)
      EE=ABS(EA)
```

```
      IF(EA.NE.EO.AND.EE.GT.EF)CALL ROOT(C1,CL,F4,ER)
      IF(EE.LE.EF.AND.EE.GT.EC)CALL ROOT(C2,CL2,F3,ER)
      CD=(CMU-CO)/30.0
      CM=CO
      DO 520 K=1,29
      CM=CM+CD
      IF(EA.LE.EF)D1=O2(CM)-O2(CF)+O1(CF)
      D2=O2(CM)
      IF(EA.LE.EC)TH=D1-O1(0.)
      CML=CM-2.E-6
      S2=CADRE(F2,CML,CO,0.0001,0.,ERROR)
      IF(EA.NE.EO.AND.EA.GE.EF)S2=S2+0.5*CADRE(F2,CO,C1,0.0001,0.,ERR)
      IF(EA.LT.EF.AND.EA.GE.EC)S2=S2+0.5*CADRE(F2,CO,CF,0.0001,0.,ERR)
     .+0.5*CADRE(F1,CF,C2,0.0001,0.,ERR)
      IF(EA.LT.EC.AND.EA.GE.-EC)S2=S2+.5*CADRE(F2,CO,CF,0.0001,0.,ERR)
     .+0.5*CADRE(F1,CF,0.,0.0001,0.,ERR)+0.5/DRT*Q(TH,EC,EA)
      IF(EA.LT.-EC.AND.EA.GE.-EF)S2=S2+.5*CADRE(F2,CO,CF,.0001,0.,ERR)
     .+0.5*CADRE(F1,CF,0.,0.0001,0.,ERR)+0.5/DRT*Q(TH,EC,-EC)
     .+0.5*CADRE(F1,C2,0.,0.0001,0.,ERR)
      IF(EA.LT.-EF)S2=S2+0.5*CADRE(F2,CO,CF,0.0001,0.,ERR)+CADRE(F1,CF
     .,0.0,0.0001,0.,ERR)+0.5/DRT*Q(TH,EC,-EC)+0.5*CADRE(F2,C1,CF,
     .0.0001,0.,ERR)
      P=6./(PI*PI)*S2*S2
      IF(P.LE.PM)GO TO 1000
      PM=P
      DM=E2(CM)/EO
      WRITE(6,470)CM,P,DM,ERROR
470   FORMAT(T20,3(F10.3,5X),G12.3)
520   CONTINUE
      WRITE(6,555)
555   FORMAT(T20,'(MAXIMUM LOAD NOT REACHED FOR THE CRACKING RANGE)')
      GO TO 1000
900   WRITE(6,920)
920   FORMAT(T20,'THE ECCENTRICITY IS TOO BIG FOR THE CROSS-SECTION')
1000  STOP
      END
C
C     ***************************************************************
C
C     FUNCTION DEFINING INTERGRAND 1
C
      FUNCTION F1(C)
      COMMON RO,RC,RS,EO,EC,EF,EE,D1,D2
      T1=1.-0.5*C
      T2=1.-C
      T3=RO*RC-RS
      T4=T1*T1-T2*T3
      YP=(0.5*C*T1-(T1-T3)*E1(C))/T4
      DEN=D1-O1(C)
      IF(DEN.LE.0.)DEN=D1*1.E-6
      F1=YP/SQRT(DEN)
      RETURN
      END
C
C     FUNCTION DEFINING INTERGRAND 2
C
      FUNCTION F2(C)
      COMMON RO,RC,RS,EO,EC,EF,EE,D1,D2
```

```
      T1=1.-0.5*C
      T2=1.-C
      T3=1.+RC-C
      T4=T1*T1-0.25*RO*T3*T3+RS*T2
      YP=(0.5*(1.-RO)*T1*C+0.25*RO*(1.-RC*RC)
     .-(T1-0.5*RO*T3+RS)*E2(C))/T4
      DEN=D2-O2(C)
      IF(DEN.LE.O.)DEN=D2*1.E-6
      F2=YP/SQRT(DEN)
      RETURN
      END
C
C     FUNCTION DEFINING CRACKING ECCENTRICTY 1
C
      FUNCTION F3(C)
      COMMON RO,RC,RS,EO,EC,EF,EE,D1,D2
      F3=EE-E1(C)
      RETURN
      END
C
C     FUNCTION DEFINING CRACKING ECCENTRICTY 2
C
      FUNCTION F4(C)
      COMMON RO,RC,RS,EO,EC,EF,EE,D1,D2
      F4=EE-E2(C)
      RETURN
      END
C
C     FUNCTION DEFINING THE TERM IN INTERGRAND 1
C
      FUNCTION O1(C)
      COMMON RO,RC,RS,EO,EC,EF,EE,D1,D2
      T1=1.-0.5*C
      T2=1.-C
      T3=RO*RC-RS
      O1=(4.*T1*T1*T1-RO*RC*RC*RC-3.*T3*T2*T2)
     ./6./(T1*T1-T3*T2)**2
      RETURN
      END
C
C     FUNCTION DEFINING THE TERM IN INTERGRAND 2
C
      FUNCTION O2(C)
      COMMON RO,RC,RS,EO,EC,EF,EE,D1,D2
      T1=1.-0.5*C
      T2=1.-C
      T3=1.-RC-C
      T4=1.+RC-C
      T5=RO*RC-RS
      O2=(4.*T1*T1*T1-RO*RC*RC*RC-0.5*RO*T3*T3*T3-3.*T5*T2*T2)
     ./6./(T1*T1-0.25*RO*T4*T4+RS*T2)**2
      RETURN
      END
C
C     INVERSING SIN FUNCTIONS
C
      FUNCTION Q(TH,EV,EU)
      COMMON RO,RC,RS,EO,EC,EF,EE,D1,D2
```

```
      T=1.-RO*RC*RC*RC
      TD=SQRT(EC*EC+2./3.*T*TH)
      Q=SQRT(T)*(ASIN(EV/TD)-ASIN(EU/TD))
      RETURN
      END
C
C     FUNCTION DEFINING CRACKING ECCENTRICITY 1
C
      FUNCTION E1(C)
      COMMON RO,RC,RS,EO,EC,EF,EE,D1,D2
      T1=(1.-0.5*C)*(1.-0.5*C)
      E1=(T1*(1.+C)-RO*RC*RC*RC)/3./(T1-(RO*RC-RS)*(1.-C))
      RETURN
      END
C
C     FUNCTION DEFINING CRACKING ECCENTRICITY 2
C
      FUNCTION E2(C)
      COMMON RO,RC,RS,EO,EC,EF,EE,D1,D2
      T1=(1.-0.5*C)*(1.-0.5*C)
      T2=(1.-RC-C)*(1.-RC-C)
      T3=(1.+RC-C)*(1.+RC-C)
      E2=(T1*(1.+C)-RO*(RC*RC*RC-0.25*T2*(1.+2.*RC-C)))
     ./3./(T1-0.25*RO*T3+RS*(1.-C))
      RETURN
      END
C
C     SUBROUTINE FINDING ZERO OF FUNCTION F
C
      SUBROUTINE ROOT(A,B,F,TL)
      Y1=F(A)
      Y2=F(B)
      IF(Y1*Y2.GT.0.OR.Y1-Y2.EQ.0.OR.TL.LE.0.OR.A.GE.B)STOP 2
20    X=0.5*(A+B)
      Y=F(X)
      IF(Y*Y1.GT.0.)A=X
      IF(Y*Y1.LE.0.)B=X
      IF((B-A).GT.TL)GO TO 20
      A=X
      RETURN
      END
```